The Modeling, Design and Demonstration of Electrostatic Synchronous Machines

by

Baoyun Ge

A dissertation submitted in partial fulfillment of
the requirements for the degree of

Doctor of Philosophy

(Electrical and Computer Engineering)

at the

UNIVERSITY OF WISCONSIN–MADISON

2018

Date of final oral examination: 05/08/2018

The dissertation is approved by the following members of the Final Oral Committee:

Daniel C. Ludois, Assistant Professor, Electrical and Computer Engineering
Thomas M. Jahns, Professor, Electrical and Computer Engineering
Giri Venkataramanan, Professor, Electrical and Computer Engineering
Daniel Klingenberg, Professor, Chemical and Biological Engineering

To my parents and fiancée.

ACKNOWLEDGMENTS

The hardest arithmetic to master is that which enables us to count our blessings.

— Eric Hoffer

I would like to express the deepest appreciation to my advisor, Professor Daniel C. Ludois, who has the attitude and the substance of a genius. Without his patient instruction, I cannot finish the work. I still remember that the first time we met, I just had this electrostatic motor idea from ECE 713 class and he already founded a company on this. With the development of the research project, I gradually sensed how much effort one needs to devote and how much knowledge one needs to possess in order to realize an idea. Prof. Ludois not only has endless emerging ideas but also is diligent and profound knowledgable. Hereby I give him my sincerely respect.

I would like to thank Professor Thomas M. Jahns, Professor Giri Venkataramanan and Professor Daniel Klingenberg for agreeing to be members of my final defense exam committee and spending their valuable time on reviewing and making suggestions on this thesis.

I would like to thank Professor Thomas M. Jahns. His invaluable lectures in ECE 411, ECE 711 and ECE 713 are the solid foundations of my research project. I also want to thanks for the opportunity of working with him as a teaching assistant in ECE 411. His rigorous scholarship truly impressed me during the lecture and office hour discussion.

I would like to thank Professor Donald W. Novotny. I watched his recorded lecture ECE 511 and I love the way he derived equations, explained physics and made jokes in the lecture. I also had the opportunity to discuss with him when I started to derive the dq-axis model of the electrostatic machine. I appreciate his insights contributing to this thesis.

I would like to thank the team from C-Motive: Justin Reed, Graham Reitz and Bill Butrymowicz. Justin's meticulousness, Graham's optimism and Bill's handful skills helped me a lot on the way of building the separately excited machine. Moreover, I deeply admire their spirit as great explorers and adventurers bringing the electrostatic motor technology into the world.

I would like to thank machine specialist Tom Wirth at Engineering Center Building. The over 500 hours machining in the shop is a great experience. Without him, I could not machine those

scary looking electrostatic motors. I will always remember his words: “Everyone is always good at something!”

I would like to thank friends and colleagues in UW: Yutong Zhu, Adam Shea, Hao Jiang, James McFarland, Parikshith Channegowda, Mahima Gupta, Jiyao Wang, Yang Xu, Kevin Frankforter, Kang Wang, Silong Li, Yingjie Li, Ruxiu Zhao, Le Chang, Hang Dai, Hao Ding, Ryan Knippel, Skyler Hagen, Andy Schroedermeier, Wanjun Zhang and many others. I also would like to thank my undergraduate advisors: Yunkai Huang, Shuhua Fang and Ying Fan and old friend Ying Pang.

Especially, I would like to thank Jiejian Dai, Aditya Ghule and Peter Killeen for their assistance in the experimental work. I also would like to thank Seth McElhinney, Aditya Ghule, Wenbo Liu, Mingda Liu and Jianning Dong who were very kind to do proof reading for some of the chapters in this thesis. I also would like to thank Helene Demont, who is very thoughtful and offered lots of help in these years.

Finally, I would like to thank my family: parents, sister, brother in law and my fiancée for being so much patient and very supportive along my PhD career.

CONTENTS

LIST OF TABLES

LIST OF FIGURES

NOMENCLATURE

Symbols (Unless otherwise illustrated in the context)

a	Constant complex vector	$e^{j2\pi/3}\,[\cdot]$
d	Depth into the paper	[m]
g	Gap distance	[m]
i	Transient current	[A]
j	Imaginary unit	$[\cdot]$
r	Resistance or radius	[Ω] or [m]
v	Transient voltage	[V]
z	Complex rectangular coordinate, $x + jy$	[m]
γ	Torque angle	[rad]
ε_0	Vacuum permittivity	$8.85 \times 10^{-12}\,[\mathrm{F/m}]$
ε_r	Relative permittivity	$[\cdot]$
ζ	Complex polar coordinate, $re^{j\theta}$	[m]
μ_0	Vacuum permeability	$4\pi \times 10^{-7}\,[\mathrm{H/m}]$
μ_r	Relative permeability	$[\cdot]$
σ	Shear stress	$[\mathrm{N/m^2}]$
p	Pressure	$[\mathrm{N/m^2}]$
ω_e	Excitation angular frequency	[rad/s]
ω_r	Electrical rotating angular frequency	[rad/s]

ω_{rm}	Mechanical rotating angular frequency	[rad/s]
$\mathscr{E}_e$	Elastance	[1/F]
B	Magnetic flux density	[T]
C	Capacitance	[F]
D	Electric displacement field strength	[C/m^2]
E	Electric field strength	[V/m]
G	Conductance	[S]
H	Magnetic field intensity	[A/m]
I	Steady state current	[A]
L	Inductance	[H]
P	Pole number	[$\cdot$]
Q	Transient/Steady state charage	[C]
V	Steady state voltage	[V]

Embellishments

i_{lk}	Leakage current
$(\cdot)^A$	Asymptote of the variable $(\cdot)$
$(\cdot)_{abcs}$	Vector form of three phase variables $(\cdot)_{as}, (\cdot)_{bs}, (\cdot)_{cs}$
$\underline{(\cdot)}_{abcs}$	Complex vector form of the three phase variable $(\cdot)$, i.e. $(2/3)\left((\cdot)_{as} + a(\cdot)_{bs} + a^2(\cdot)_{cs}\right)$
$\underline{(\cdot)}_{qds}$	Complex vector form of the stator dq-axis variable $(\cdot)$ in the arbitrary reference frame
$\underline{(\cdot)}_{qdr}$	Complex vector form of the rotor dq-axis variable $(\cdot)$ in the arbitrary reference frame

$\underline{(\cdot)}^{r}_{qds}$ Complex vector form of the stator dq-axis variable $(\cdot)$ in the rotor reference frame

$\underline{(\cdot)}^{r}_{qdr}$ Complex vector form of the rotor dq-axis variable $(\cdot)$ in the rotor reference frame

$p\,(\cdot)$ Derivative with respect to time, i.e. $\partial\,(\cdot)\,/\partial t$

$\mathfrak{R}[(\cdot)]$ Real part of the complex vector $(\cdot)$

$\mathfrak{I}[(\cdot)]$ Imaginary part of the complex vector $(\cdot)$

Abbreviations

2D Two dimensional

3D Three dimensional

BLDC Brushless Direct Current

CAD Computer aided design

CSI Current source inverter

EMF Electromotive force

FD Finite difference

FE Finite element

FEA Finite element analysis

FOC Field oriented control

HPG High pressure gas

HTC High throughput computing

HV High voltage

HVAC High voltage alternating current

HVDC High voltage direct current

MEMS	Microelectromechanical system
MMF	Magnetomotive force
OTS	Off the shelf
PCB	Printed circuit board
PM	Permanent magnet
SEM	Synchronous electrostatic machine
THD	Total harmonic distortion
UHV	Ultra high vacuum
VSI	Voltage source inverter

Color Code (Unless otherwise illustrated in the context)

- Red, stator phase A electrode or HV terminal for single phase machines
- Yellow, stator phase B electrode
- Blue, stator phase C electrode
- Light gray, rotor positive electrode
- Black, rotor negative electrode
- Green, ground
- Green brown, PCB substrate

ABSTRACT

This research focuses on fluid filled electrostatic synchronous machines, an emerging family of machines that hold promising specific and volumetric torque density. The contributions of the research are three thrusts: dielectric liquid selection, circuit modeling and electrostatic design/optimization.

Effective electromechanical power conversion using electrostatics requires dielectric liquids whose permittivity and breakdown field strength can facilitate adequate electric shear stress beyond the capabilities of media such as air or vacuum. This research discusses design points for practical electrostatic force production and evaluates available off-the-shelf dielectric liquid in terms of electric pressure and shear capability.

Circuit models of the proposed machines were developed to understand torque production as well as form a basis for vector control. Unlike magnetic machines where the conduction paths are confined within windings, the current field in the proposed machine is co-located with the electrostatic field. This research blends the electrical behavior of the dielectric fluid into the dq-axis model. The resultant torque equation is parsed into field, saliency and induction torque. Each component of the torque equation is expressed as functions of few key capacitances for the optimization purpose and maximum torque per volt is derived.

Effective electromechanical power conversion using electrostatics also requires optimal geometric design. This research proposes an asymptotical approach incorporating conformal mapping techniques with field analysis to obtain the lower and upper bounds of the torque production, the trend of which can be correlated with the machine geometric parameters. This could be regarded as the sizing process in the well established machine design practices. A finer optimization routine is then implemented by solving electrostatic field analytically.

The theoretical contributions were verified by an axial flux prototype machine constructed of cascaded printed circuit boards. This construction approach is low cost and scalable, thereby demonstrating a path for industrial development. Building the machine from composites and plastics plated with conductor allows it to be lightweight with improved torque density, which is a big advantage over traditional magnetic magnetic machines in terms of manufacturing costs and materials sustainability.

1 INTRODUCTION

Whether or not there is about the instrument and its history that which would ever give it a claim to any measure or serious interest, it is at least an electric motor most unique. A motor without magnetism, wiring, or any iron in its make up. A motor that runs by the action of the direct push and pull of the pure unconverted electricity itself.

— H. B. Dailey (1880)

1.1 Motivation

Recently, efforts towards more sustainable electric machinery (motors and generators) designs have received prominent interest [1–3]. Manufacturing traditional electromagnetic machines demands large quantities of specific natural resources, namely a suitable pathway for magnetic flux, such as silicon steel and a conductor of electric current, such as copper or aluminum. In the last 20 years different types of permanent magnets (PM) have been widely incorporated into electric machinery to enable higher performance, e.g. NdFeB magnets in hybrid vehicles, wind turbines, aerospace, mining, etc. The sustainability, cost and manufacturing of these materials drives design [4].

The future availability of copper (Cu), neodymium (Nd), dysprosium (Dy), Boron (B), Samarium (Sm) and Cobalt (Co) is uncertain. Figure 1.1 highlights the threat these elements pose to manufacturing supply chain [5]. Past markets had a reflecting volatile history. For example, the price of neodymium rose rapidly in 2011 to nearly 25 times the price in 2009 and is currently recovering [6]. Parallel to this, the recycling rate of those rare earth materials is less than 10%, which makes them even scarcer [7]. What is more, those magnets often include dysprosium as well to achieve higher temperature operation — making their formulation more exotic still [4]. The price of copper (for windings) has also risen to a new equilibrium of $3 \sim 4$ times higher than a decade ago [8]. Aside from the cost of raw materials, manufacturing (especially stamping, winding, and magnet insertion) a machine can be a labor/tooling intense process, especially for PM machines.

Even though major corporations and universities have realized the problem stated above and started to undertake the task of reducing and even eliminating the usage of rare earth materials [9]

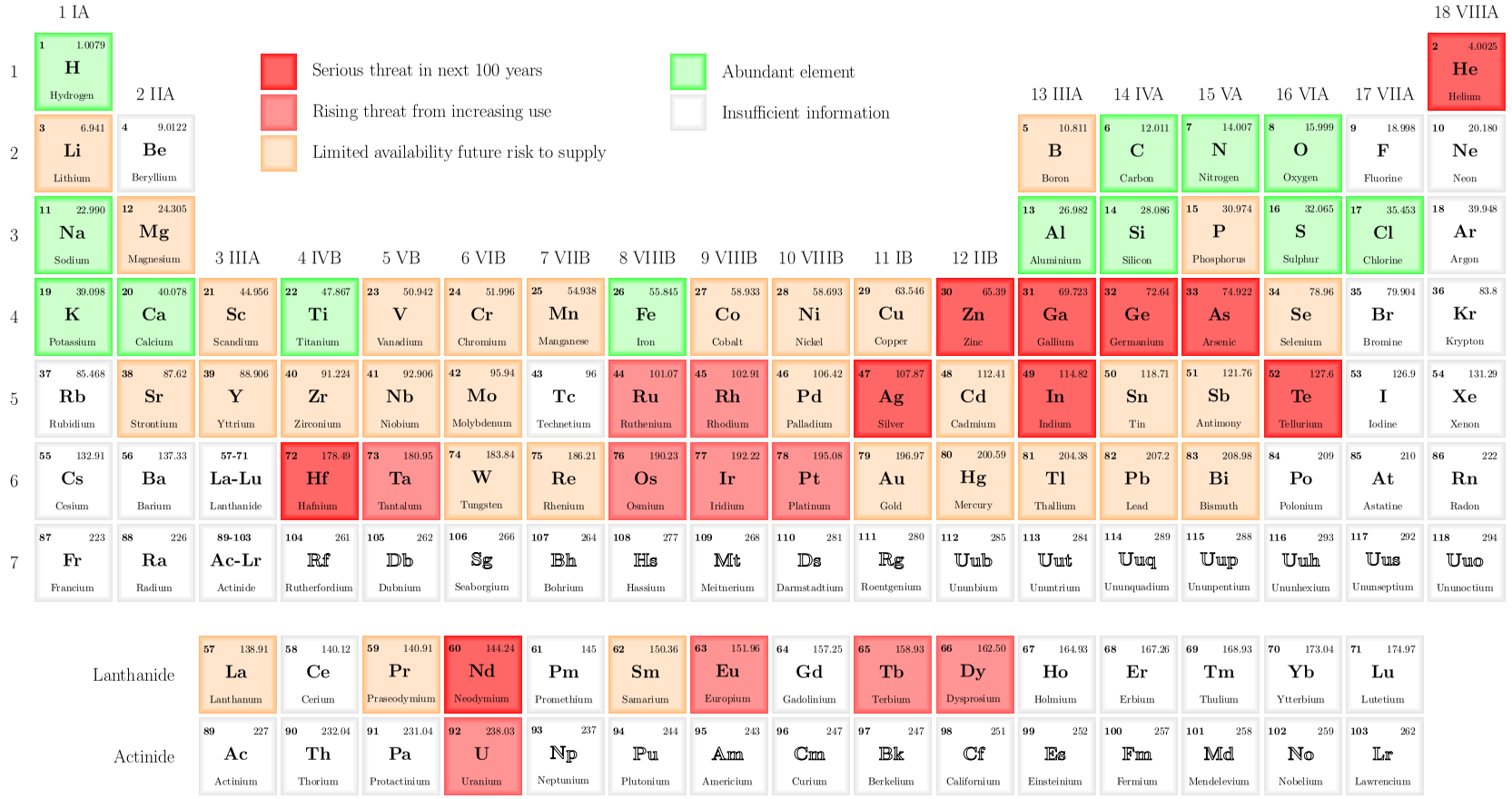

Figure 1.1: The periodic table with elements highlighted according to their resource criticality [5].

(and if copper is assumed to be fairly available in the near future), traditional electromagnetic machines still suffer from another drawback — relatively low specific torque density, i.e. torque per weight metric (Newton-meter per kilogram, N-m/kg), for some applications like aerospace, aircraft carrier, electric vehicle, drone, etc., where weight is the enemy of cruise time and some other applications like wind turbine, cooling tower fan, robot arm, etc., where more weight causes more mechanical structural design. Those materials mentioned above, i.e. silicon steel (Fe), copper (Cu) and permanent magnet (Nd, Fe, B, Dy, Sm, Co, etc.), however, are all heavy materials comparing to others used in the system, which can be observed from Figure 1.1.

Figures 1.2 and 1.3 plot the specific torque density over base operating speed for premium efficiency induction machines and servo type PM machines respectively. Specific torque density of electromagnetic machines increases as the base speed decreases, power level increases and cooling condition becomes better. It is noteworthy that the specific torque density showing in the plots will be sacrificed if cooling facilities are counted. Specifically for the low speed applications we are targeting here, electromagnetic machines set out two paths: (1) high speed machines pairing with gearbox; From the system viewpoint, the existence of gearbox will further burden the weight crisis and also gearbox is not an option for some critical applications as will be illustrated later. (2) direct drive low speed machines. This may be suitable for large horsepower applications as scatter points shown in the upper left corner in Figure 1.3. However, for integer horsepower low speed applications, high pole count causes crowding issues in electromagnetic machines, which will lower down the specific torque density even though it is not reflected in the plots.

The third drawback that traditional electromagnetic machine cannot steer clear of is low efficiency at low speed and especially standstill (position and hold) applications. This can be immediately understood simply because to provide rated torque at low speed, a traditional electromagnetic machine (current energizing device) needs to constantly pumping current through the winding, which however causes "rated losses." Given the fact that applications like heavy lifting drones, in wheel motor, cooling tower fan, direct drive wind turbine and industrial robots are rapidly growing, magnetic machines may not be acceptable economically and environmentally.

Overall, these demand electromagnetic machines be highly optimized, to the point where

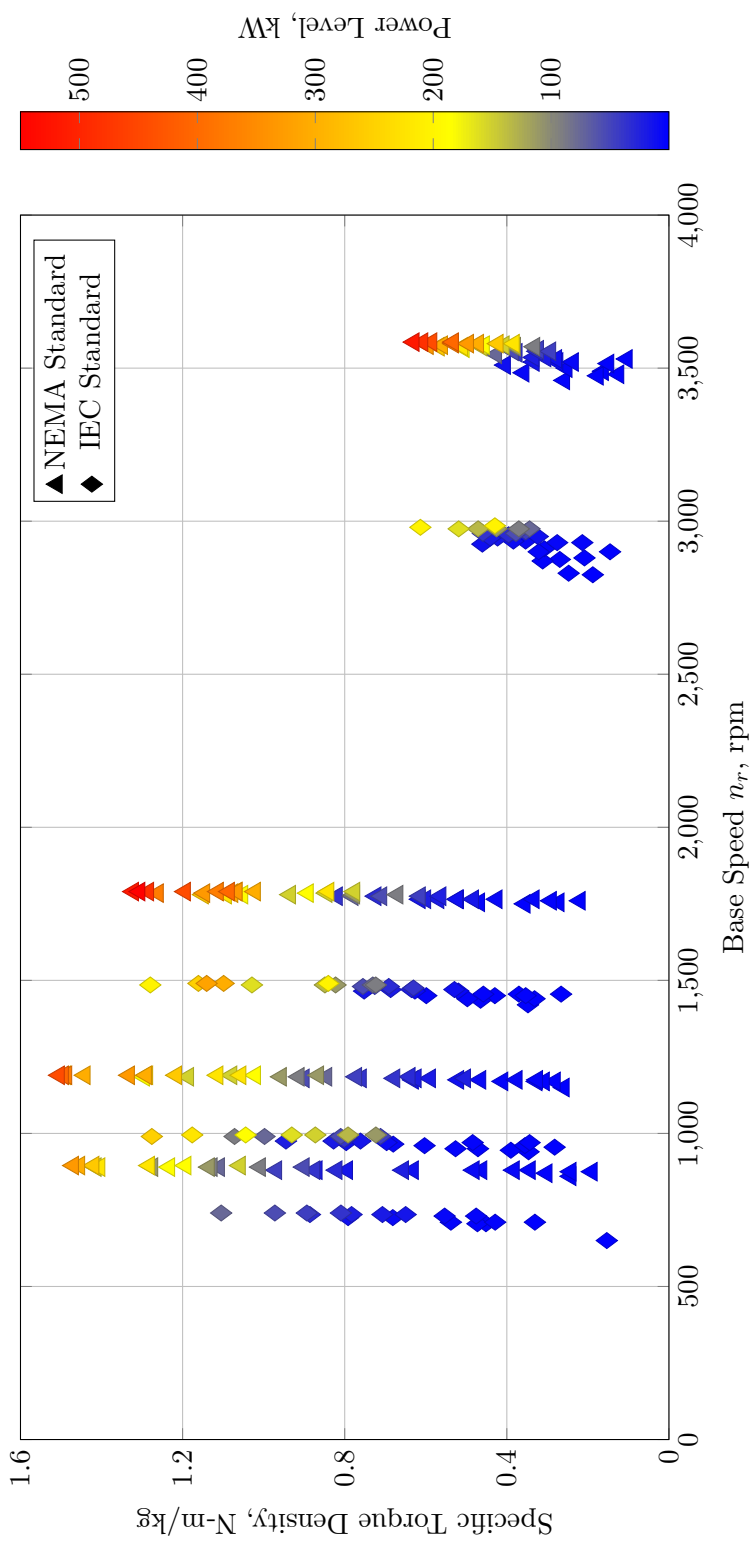

Figure 1.2: Specific torque density of induction machines meeting premium efficiency standards as a function of base speed [11].

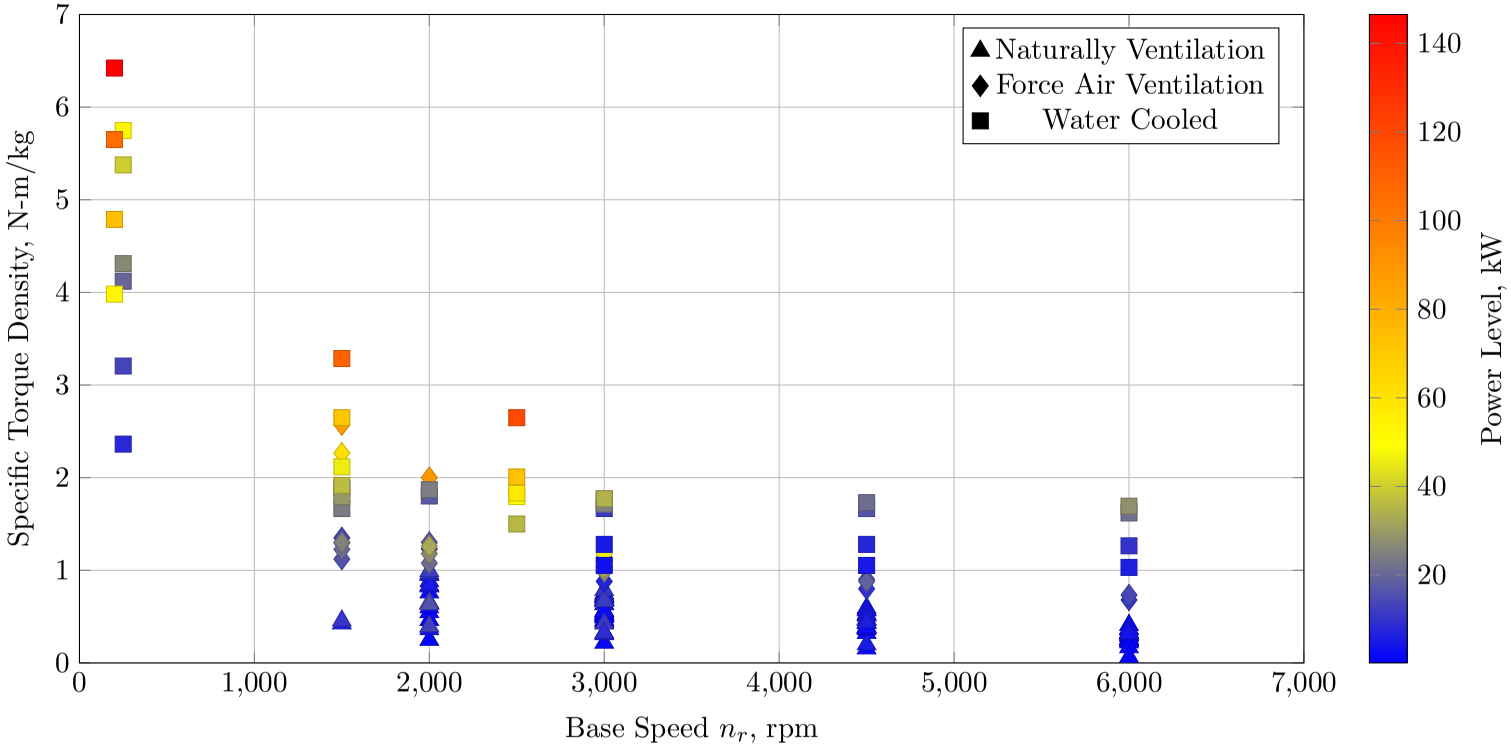

Figure 1.3: Specific torque density of PM machines with different types of cooling conditions as a function of base speed [12].

machines are asymptotically approaching theoretical performance limits (flux density has been pushed against saturation limit $B_{sat} \approx 2\,\mathrm{T}$ and current density has been pushed against whatever the cooling condition is given [10]). This prompts the question: if electromagnetic machines are approaching their limit, *is there another avenue using different torque mechanisms that should receive attention?*

To manufacture a weight and cost efficient electric machine, the fundamental materials used for traditional electric machine, including silicon steel, copper and permanent magnet, should be changed. Plastics, which has a density of $\sim 1.2 \times 10^3\,\mathrm{kg/m^3}$ [13], may be considered since they are not only light weight but also easy to manufacture with low cost thanks to injection mold and 3D printing technologies, and are readily recycled as well. However, an electric machine still requires conductors to fulfill electromechanical power conversion. Aluminum, which has a density of $2.7 \times 10^3\,\mathrm{kg/m^3}$, may fit since it is cheaper, lighter and more abundant than copper (refer to Figure 1.1). The combination of plastics and aluminum seems to lead to ironless electromagnetic machine with aluminum windings. However, the third deficiency mentioned above, low efficiency caused by conduction loss, still presents to such machine. Furthermore, ironless electromagnetic machines are usually used in high speed application due to the low coupling inductance. Comparing to copper, aluminum is not a good conductor for a current energizing device either. Nevertheless, it is a good one for a voltage energizing device, like an electrostatic apparatus, where the electric field resides between the conductors to coordinate surface charge, rather than to drive currents within the conductors. To further take advantage of this property and embrace the plastic machine concept, plastic material may be manufactured in such a way to occupy the space where originally dominated by the flux conductor and to function as the mechanical structure. This seems to suggest an electrostatic machine with partial metalization on the surface of dielectric (plastic, ceramic, composite, etc.) substrates. It is also worth to mention that in an electrostatic machine, the amount of conductors used is almost negligible and hence it is still a significant reduction even if copper is utilized. Consequently, *this research here proposes electrostatics as a ripening path for significant machine development.*

1.2 Electrostatic Machine Introduction

In general, an electric machine is understood as an electromechanical device converting electrical power to mechanical power or vice versa. The electromechanical energy conversion, which takes place through the medium of magnetic or electric field [14], can be classified into two types accordingly. The first type, widely applied in our daily life and industry as mentioned above, creates force as a result of magnetic field acting on current carrying conductors. The corresponding machine is well known as an *"electromagnetic machine."* The second type, rarely seen but rapidly developed over the last half century, creates force as a result of electric field acting on charges residing on conductors or permanently polarized dielectrics. The corresponding machine is called an *"electrostatic machine."*

An intuitive terminology for these two types of machine may be "magnetic machine" and "electric machine." However, as you may have already foreseen that "electric machine" confuses with the general electric machine concept. Another proper terminology for "electromagnetic machine" is "magnetostatic machine", which seems to make more sense because of the duality between the two types of machine. To follow the convention, "electromagnetic machine" will be used throughout this thesis to describe the conventional machinery. Maybe in the future, "electromagnetic machine" will be properly named after a hybrid machine producing force through the coupling between electric and magnetic field.

It is interesting that the first electric machine ever made is actually an electrostatic machine (an electric carousel) made by Benjamin Franklin [15], given the fact that the electrostatic machine is not studied throughly compared to its cousin — electromagnetic machine. A rough comparison will tell the reason. The density of the field energy stored in the isotropic medium (dielectric or magnetic material) can be expressed by the following two equations:

$$w_e = \frac{1}{2}\varepsilon_0\varepsilon_r E^2 \tag{1.1}$$

$$w_m = \frac{1}{2}\frac{B^2}{\mu_0\mu_r} \tag{1.2}$$

in which ε_0, μ_0 are the permittivity and permeability of vacuum, ε_r and μ_r are the relative permittivity and relative permeability of the medium where the field locates, E and B are the

magnitude of electric and magnetic field intensity respectively. Generally, for medium of air,

$$\text{Air Dielectric}: \quad \varepsilon_r \approx 1, \quad E_{bk} \approx 3 \times 10^6 \,\text{V/m}$$

$$\text{Air Magnetic}: \quad \mu_r \approx 1, \quad B_{sat,Fe} \approx 2 \,\text{T}$$

in which E_{bk} stands for the breakdown strength of the air dielectric and $B_{sat,Fe}$ for the maximum magnetic field before the back iron gets saturated. Substitute these into eq. (1.1) and eq. (1.2),

$$\text{Air Dielectric}: \quad w_{e,\ \max} \approx 39.8 \,\text{J/m}^3$$

$$\text{Air Magnetic}: \quad w_{m,\ \max} \approx 1.59 \times 10^6 \,\text{J/m}^3$$

This five orders of lower magnitude in energy density inhibits the electrostatic machine from being received too much attention in macro scale application. However, electrostatic machine is indeed frequently used and dominant in the microelectromechanical system (MEMS) (the reasons are summarized in Section 2.1). The previous rough calculation does not tell the whole story. In order to bridge (at least reducing) the gap of five orders of deficiency, this research proposes to fill the gap space between stator and rotor with dielectric liquids possessing higher dielectric strength and dielectric constant, a concept to be explored in detail.

To put things into perspective, the three deficiencies facing by electromagnetic machines can be potentially solved by electrostatic machines:

- **High Material Cost:** As a rough comparison, Table 1.1 demonstrates that the embodied energy (the energy used to produce the raw material prior to manufacturing) for manufacturing an electrostatic machine is much less than an electromagnetic one with similar torque rating, if torque density (Newton-meter per liter, N-m/L) is assumed to be the same. Furthermore, it can be observed from Figure 1.1 that all the elements consisting of an electrostatic machine are abundant.

- **Low Specific Torque Density:** Table 1.1 also indicates that the specific torque density of an electrostatic machine has the potential to be much higher than (4 ~ 5x) that of an electromagnetic one with similar torque rating, *if the volumetric torque density is assumed to be the same.* The goals of this research here is exceeding first integer horsepower induction

Table 1.1: Comparison of Material's Embodied Energy in Electric Machines.

Materials Used in Electromagnetic Machines	Weight Specific Embodied Energy, MJ/kg	Density, kg/m^3	Volumetric Embodied Energy, GJ/m^3
Steel	25 ~ 40	7650	191 ~ 306
Copper	42 ~ 100	8960	376 ~ 896
NdFeB	250 ~ 400 †	7500	1875 ~ 3000
SmCo	250 ~ 400 †	8400	2100 ~ 3360
Materials Used in Electrostatic Machines	Weight Specific Embodied Energy, MJ/kg	Density, kg/m^3	Volumetric Embodied Energy, GJ/m^3
Plastic	~ 90	1200	~ 108
Aluminum	~ 170	2700	~ 459
Dielectric Liquid	~ 29 ‡	880	~ 26

† This is a conservative estimate. ‡ This is an estimate from biodiesel oil fuel, which is made of vegetable oil — a major source of biodegradable transformer oil [16, 17].

machines' specific torque density and then PM machines' respectively with an implying goal of achieving same volumetric torque density as electromagnetic machines.

- **Low Efficiency:** This may not be as obvious as the above two aspects since using dielectric liquids brings in higher viscous drag loss. However, with careful selection of modern dielectric liquids and design of machine structures, the dielectric leakage and viscous drag losses may be well controlled under the conduction and core losses level of an electromagnetic machine of similar ratings respectively for low speed applications.

1.3 Organization of Thesis

- Chapter 2 provides the background on the current state of electrostatic machines development in both macro-scale and micro-scale applications as well as identifies the research opportunities for low speed high torque applications.

- Chapter 3, serving as the cornerstone of the following chapters, presents the energy conversion principles in electrostatic field system including two-conductor for single phase machine and multi-conductor for multi-phase machine.

- Chapter 4 explores the opportunity of utilizing dielectric liquid to reduce the magnitude difference in energy density, which inhibits the electrostatic machine from being widely applied from the first place.

- Chapter 5 derives the dq-axis theory for three phase electrostatic machine, including both synchronous and induction machines. From the machine design perspective, the theory provides the information of which capacitance quantities should be used for optimization.

- Chapter 6 proposes a systematic design approach for three phase synchronous electrostatic machines with field excitation. The design considerations of the key parameters and the scalability of the machine are also discussed.

- Chapter 7 presents two methods for analytically determining the capacitance coupling of the the proposed machine, which is essential for design optimization.

- Chapter 8 documents the experimental results of a prototype three phase synchronous electrostatic machine with field excitation. They are compared with the predicted ones to verify the design tools.

- Chapter 9 summarizes the contributions and proposes the future work.

2 A REVIEW OF THE STATE OF THE ART

If you want the present to be different from the past, study the past.

— Baruch Spinoza

I believe that the justification of art is the internal combustion it ignites in the hearts of men and not its shallow, externalized, public manifestations. The purpose of art is not the release of a momentary ejection of adrenalin but is, rather, the gradual, lifelong construction of a state of wonder and serenity.

— Glenn Gould (1962)

In order to discover the research opportunities of the electrostatic machine with high torque density in low speed applications, a literature review of the past and current work is summarized in two major categories: MEMS and macro scale. Based on the previous work, the state of the art material and manufacturing development, research opportunities are then identified.

2.1 Electrostatic Machine at MEMS Scale

Electrostatic machines at MEMS scale have a power level of milliwatt and size range of micrometer to millimeter. They are extensively used due to their relatively simple structure that accommodates easier manufacturing and greater power density when compared to their electromagnetic counterparts [18–21]. Electrostatic machines have the following five distinct advantages at the MEMS scale [4]:

1) Voltage across micro scale distances produce extremely large electric fields, thus high force or torque.

2) No "back-iron," electric field lines terminate on charge and do not require a core material to re-direct them.

3) No permeable material or "windings" required, only conducting surfaces supported on insulators.

4) Force or torque is driven by voltage, not current (nearly zero losses at stall).

5) No magnetic material is presented in the system, which make it compatible for applications like magnetic resonance imaging [22].

Machine Types

Different types of electrostatic actuators and machines have been developed for MEMS applications, namely stepping motor, synchronous variable capacitance machine, electrostatic induction machine and wobble machine. While electrostatic, these MEMS machines are miniature counterparts exhibiting duality to electromagnetic machines found in macro-scale everyday uses.

Stepping & Synchronous Machine: The design, fabrication and operation of a stepping motor and a synchronous variable capacitance machine are first introduced by L. S. Fan et al. [23] in 1988 and Y. C. Tai et al. [24] in 1989 using integrated circuit manufacturing processes. Referring to Figure 2.1a, if yellow electrodes are energized in the next cycle, the nearest misaligned rotor electrodes will tend to move into the aligned position. The rotor rotates in a stepping fashion as the stator electrodes are energized sequentially. As for the synchronous machine in Figure 2.1b, the rotor rotates in a continuous and smooth fashion since the stator potential wave rotates synchronously with the rotor as the name suggests. L. S. Fan et al. also applied similar manufacturing processes to integrated movable micromechanical structures for applications like sensors and actuators [25]. R. X. Gao et al. extended the former radial flux synchronous machine to an axial flux one, which was fabricated using modified printed circuit board (PCB) techniques [26, 27]. So far in the micromotor structures, the rotor or mover has been passively induced and energized by the stator excitation or vice versa. T. Niino et al. proposed a dual excitation multiphase electrostatic motor which possessed two potential advantages: (1) it can generate repulsive torque/force reducing frictional force that hinders the rotor's or mover's smooth movement; (2) it is torque denser, lighter and more compact [28].

Electrostatic Induction Machine: In 1989, S. F. Bart et al. first introduced an axial flux type electrostatic induction micromotors, which is based on free electric image charge induced in the rotor plate and lagging behind the traveling potential wave due to *charge relaxation* [29]. The

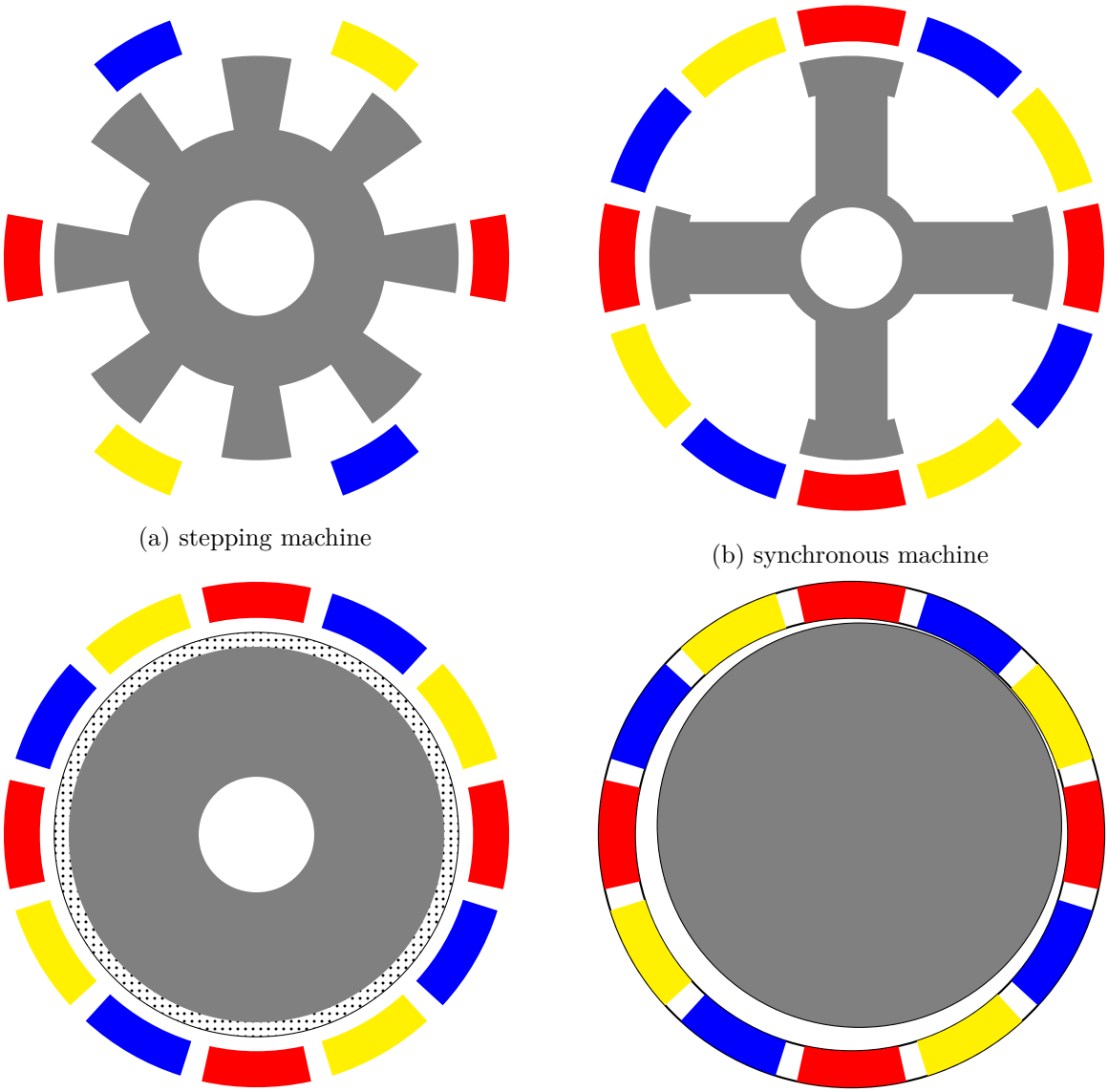

(a) stepping machine

(b) synchronous machine

(c) induction machine

(d) wobble machine

Figure 2.1: Basic types of electrostatic machines in MEMS applications, classified according to working principles.

rotor must be coated with a material (as shown in Figure 2.1c) possessing high dielectric constant but low electrical conductivity. The manufacturing and control advantages of such machine are immediately realized giving the fact that neither the saliency nor the rotor position feedback is required. The fabrication process and testing of this type is well documented in [30].

Wobble Machine: In 1989, S. C. Jacobsen et al. proposed an eccentric-motion electrostatic micro-actuator — wobble motor (Figure 2.1d) to reduce the large friction force presenting in the previous types due to the extremely small gap, especially salient ones [31]. An outer rotor configuration was suggested in [32] to: (1) increase the torque production because it has a significant larger radius; (2) easily drive passive structures, which are directly, lubricantly, or magnetically coupled to the rotor. Interestingly, the rotor in a wobble machine can be made of either an electrically well conductive material (with insulation) or the same dielectric material used in the induction machine.

Machine Design

Even though electrostatic machines are much simpler in structure compared to their electromagnetic counterparts, the design and analysis are usually carried out numerically [33, 34] for electrostatic micromotors (except for few special cases) due to the difficulties of calculating capacitance values even for structures as simple as multiple parallel plates.

W. S. N. Trimmer et al. first published the design considerations for micromachined electric actuators based on a primitive parallel plate model involving no fringing effect, i.e. the capacitance is strictly proportional to the facing area and inverse proportional to the gap distance [35]. This model can be applied to both the stepping and synchronous machines.

A comprehensive modeling of the electrostatic induction machine was documented by J. R. Melcher in his famous book *Continuum Electromechanics* [36], where the stator potential wave is assumed to be ideally sinusoidal. It was implemented by S. F. Bart et al. despite the arrangement of the stator electrodes is discrete and the resulting stator potential wave is not sinusoidal [29]. S. F. Nagle et al. made an in depth analysis based on those work with a particular attention paid to parameters that strongly affect the performance [30]. A lumped parametric model, which is

similar to the circuit model of the electromagnetic induction machine, was introduced by F. J. Santana et al. [33]. They also analyzed the spatial harmonics presented in an electrostatic induction micromotor [37], which is rarely studied in the MEMS research society.

Another major task in the electrostatic machine design is the bearing design due to the extremely limited space prohibiting the use of conventional bearings. It is documented in but not limited to [38], [39], [40], [41] and [42].

2.2 Electrostatic Machine at Macro Scale

Even though electrostatic machines are widely used at MEMS scale, those primitive types introduced above except the wobble machine were prototyped at macro scale quite earlier. Nevertheless, there are rarely few research at macro scale undertaken by universities and corporations and major thrusts by past notable researchers are reviewed here.

Electrostatic machine at macro scale was pioneered by J. G. Trump. In his thesis *Vacuum Electrostatic Engineering* [43], he reported ten types of axial flux electrostatic machine working at AC or DC, motor or generator modes utilizing the ultra high vacuum (UHV) as the essential insulating medium. The two major benefits of the UHV insulation were identified as:

- The electrostatic force acting on electrodes is a quadratic function of the voltage gradient across them and breakdown strength of tens of millions of volts per millimeter in UHV was reported at that time, which was hundreds to thousands higher than that in air; (Notice that this would bridge the gap of energy density between electrostatic and electromagnetic as mentioned in Section 1.2.)

- A vacuum eliminates the viscous drag, dielectric losses and weight caused by any non-vacuum media;

and the two major advantages of the electrostatic machine over the electromagnetic machine were claimed as:

- Electrostatic force can be maintained with no power loss since it only requires the presence and not the motion of electricity, while electromagnetic force need to pay continuous power loss since it requires the continuous movement of electricity;
- Electromagnetic machines require heavy materials such as iron and copper while electrostatic machines can be made of light conductive material such as aluminum.

One of the types was built and tested in the lab. It is a two pole design with a synchronous speed of 3600 rpm and the maximum power developed by this machine was 55 W at a peak voltage of 73 kV. Limited by the manufacturing technology, this machine was unable to demonstrate the superior advantages over the electromagnetic machine. However, the developed theory and the reported design considerations were invaluable to following researchers. S. F. Philp of the General Electric company proposed a paper design — a 7 MW, 200 kV machine of the same type [44]. Even though the theoretical calculation shows superior performance, he was never be able to build one. A Japanese company Shinsei also successfully developed a radial flux DC type 100 W, 10,000 rpm electrostatic machine with a specific power density of 500 W/kg [45]. R. O'Donnell et al. demonstrated that using electrostatic field to generate a HVDC output with a minimum power conditioning is preferred over the conventional generator-transformer-rectifier system in efficiency and weight perspectives [46].

The second thrust using gases under a high pressure to drive the breakdown strength up and consequently increase the energy density of an electrostatic machine was lead by N. J. Felici [47]. The supporting theory is Paschen's Law, which states that the breakdown strength of a gas dielectric is a function of the gas pressure as shown in Figure 2.2. This approach has resulted an axial flux type generator with a maximum power of 750 W at 250 kV. It is noteworthy to list the major lessons he learned from the ten years research on electrostatic machine:

- Comparing to the axial flux type machine, the radial flux type with only one pair of stator and rotor, i.e. one gap, could not provide sufficient surface area that would be of some use.
- For the axial flux type machine, the difficulties of exceeding powers of more than a few hundred watts were mainly caused by the mechanical construction.

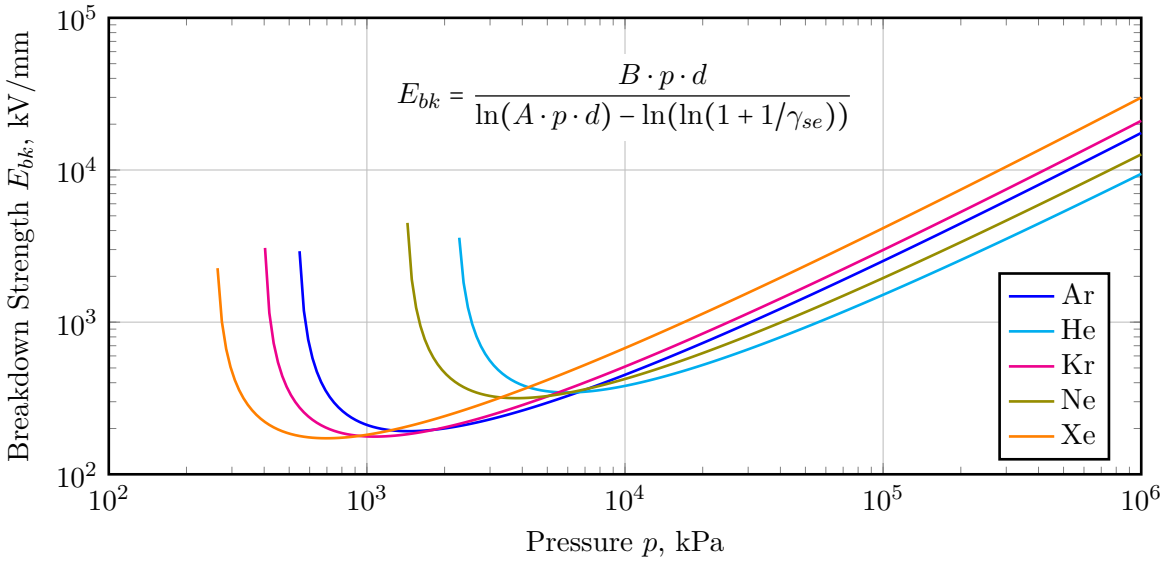

Figure 2.2: Paschen's curve obtained for argon, helium, krypton, neon and xenon. Parameters A and B are taken from [49], d is the separation distance between electrodes and γ_{se} is the secondary electron emission coefficient at the cathode and is set to 0.01.

- The thickness of the electrodes is of great importance in the torque production. (He determined the optimum ratio between the gap distance and the electrode thickness as $1:1$ or $1:2$ that assures a uniform dielectric stress on the ambient medium.)

There are actually quite few followers continued on this approach. R. A. Vanslette mentioned the usage of the high pressure gas (HPG) in his electrostatic hysterisis machine using ferroelectric materials without any further investigation [48].

The third thrust switched to the electrostatic induction machine was majorly carried out by P. T. Krein [50]. However, the unsuccessfulness of building a torque meter with resolution less than 0.001 N-m left few documented torque characteristics of the machines he built. Nevertheless, he was able to demonstrate the following valuable contributions:

- The electric field theory including the equivalent circuit model he derived is a useful tool for studying the electrostatic induction machine excluding the corona machine. Specifically, using the slip value to characterize the output torque was significant.

- The effects of harmonics can be easily analyzed by applying superposition on the circuit model.
- Time harmonics are not necessarily detrimental and thus designing motors for square wave excitation offers a simple means of increasing the torque. Space harmonics are detrimental, but even the simple flat electrodes produce very low harmonics above the second.

Parallel to those major strikes, B. Bollée worked on both synchronous and electrostatic induction machines with air dielectric in *Philips Research Laboratories* [51]. Without being able to achieve significant power out of electrostatic machines due to the limited breakdown strength, he realized that electrostatic machines may compete with electromagnetic ones either in cases where very small machines are required or operated in UHV. The former was confirmed by the MEMS society and the latter, however, is still not appreciated by the macro scale applications. In 2011, D. Ludois of University of Wisconsin-Madison patented an electrostatic machine whose electrode surfaces are really close together via hydrodynamic fluid bearing [52]. The fluid in the machine serves two purposes, i.e. hydrodynamic lifting and electric shear stress enhancing. This idea was partially realized and demonstrated by D. Ludois et al. via building a capacitive power transfer system, which successfully delivered 100 W through a 125 μm gap at a peak voltage of 80 V [53]. In 2016, The author himself demonstrated a single phase switched type electrostatic machine using 3D printing and metal plating techniques [54]. The machine has a comparable torque density to NEMA standard induction machines of similar size. In 2017, a start-up company called *C-Motive Technologies* presented a single phase axial flux type electrostatic machine using printed circuit boards (PCBs) as the main torque producing components, which shows its advantages in terms of manufacturing, flexbility and scalability [55]. Table 2.1 summarizes the key metrics of the work mentioned above and the gray highlighted work are ludois group affiliated.

An interested reader can refer to O. Jefimenko's book *Electrostatic Motors: Their History, Types and Principles of Operation* for a more comprehensive historical view of the electrostatic machine development at macro scale [15].

Table 2.1: Key Metrics of Rotational Electrostatic Machines Built by Prior Researchers.

Metric	**Insulation Medium**	**Power**, W	**Speed**, rpm	**Maximum Torque**, N-m	**Voltage**, kV	**Torque per Volt^2**, N-m/kV^2	Type †	Year	Scale ‡
J. G. Trump [43]	UHV	5.5E+1	3.6E3	1.5E-1	7.3E+1	2.7E-5	Sync	1933	L
N. J. Felici [47]	HPG	5.0E+2	7.5E2	6.4E+0	2.5E+2	1.0E-4	Sync	1947	L
R. A. Vanslette [48]	HPG	1.0E-2	1.5E3	7.5E-5	4.0E+0	4.7E-6	Hyst	1965	L
B. Bollée [51]	Air	1.0E-4	2.0E2	4.8E-6	2.2E-1	9.9E-5	Sync	1969	L
B. Bollée [51]	Air	2.0E-4	6.0E2	3.2E-6	2.2E-1	6.6E-5	Indu	1969	L
P. T. Krein [50]	Air	2.0E-1	5.4E2	3.5E-3	1.2E+1	2.4E-5	Coro	1982	L
S. F. Bart et al. [29]	Air	7.9E-7	1.0E4	7.5E-10	1.0E-1	7.5E-8	Indu	1989	S
T. Niino et al. [28]	Air	3.6E-3	2.0E2	6.9E-4	1.8E+0	2.1E-4	Sync	1995	S
S. F. Nagle et al. [30]	Air	5.8E-2	2.7E5	2.0E-6	9.0E-2	2.5E-4	Indu	2005	S
Shinsei Corp. [45, 56]	UHV	1.0E+2	1.0E4	1.0E-1	1.0E+2	1.0E-5	DC	2007	L
B. Ge et al. [54]	Liquid	2.0E+1	5.0E2	1.2E+0	7.0E+0	2.4E-2	Swit	2016	L
G. Reitz et al. [55]	Liquid	3.0E+1	5.0E2	2.0E+0	9.0E+0	2.5E-2	Swit	2017	L

† Sync — Synchronous Machine, Hyst — Hysteresis Machine, Indu — Induction Machine, Coro — Corona Machine, DC — DC Machine.

‡ L — Macro Scale, S — MEMS Scale.

2.3 Research Opportunities

Research opportunities are now identified based on previous researchers' work and are boldfaced below. *Notice that what is bold is not currently presented by other authors in the literature.*

Manufacturing

Either the axial flux or the radial flux type electrostatic machine has its own limitations. Wall thickness and metal plating with galvanic isolation are critical in the radial flux one, i.e. a thin wall is preferred by torque production but sufficient thickness to assure gap distance integrity is crucial [53]. Also, the three phase metal plating is currently not avaiable in the market and requires more engineering effort. Thus,

- **a multi-gap axial flux type electrostatic machine may be prototyped to demonstrate the competitive performance of electrostatic machine in low speed applications without the mechanical complexities of an radial flux design**.

What is more, there is no three phase electrostatic machine has been demonstrated before at macro scale, while in electromagnetic machine, three phase is preferred over single phase and field excitation is preferred over without field excitation in terms of torque production, therefore

- **a multiphase electrostatic machine with field excitation, taking advantage of the PCB substrate providing the galvanic insulation, may be built to exploit the torque capability within certain amount of volume.**

Furthermore, the electric flux still penetrates the substrate material, which in turn affects the design,

- **the influence of the substrate's dielectric properties on the torque production may be studied.**

Insulation Medium

The electrostatic machine using either UHV or HPG produce relatively low torque per volt and must spin at considerable speed, often in the range of 10k-500k rpm, to develop power because of: (1) the breakdown strength can only be enhanced to a practical limit of $20 \sim 40\,\mathrm{kV/mm}$ for many electrodes [57, 58]; (2) the relative permittivity of the insulating medium in either case is low (slightly larger than unity), as the space between the molecules dominates. Additionally, it is difficult to maintain UHV or HPG conditions in a rotating environment with shaft seals, let along justify the cost for a fractional or integer horsepower machine.

Other than those two medium, dielectric insulating liquids, such as transformer oils, may be considered and they have been engineered throughout these years for the purpose of heat dissipation in electrical equipment [59, 60]. Although not fully formed, the concept of filling the gap with dielectric liquids was first hinted by R. A. Vanslette [48] and N. Felici [61]. To explore such a concept,

- **those liquids may be purchased and directly used for the proof of concept prototyping.**

As a first step towards high performance electrostatic machine in low speed applications,

- **those liquids may be benchmarked in terms of relative permittivity, breakdown strength, electrical conductivity and viscosity;**
- **quantitative analysis of those characteristics on the performance of electrostatic machine may be carried out.**

Machine Modeling

From either the design or the control perspective, a circuit model for electrostatic machine is necessary. P. T. Krein created one for the electrostatic induction machine by solving the electric field [50]. Even though same routine cannot be applied to other types of electrostatic machine,

- **a general circuit model, which breaks down the torque production mechanism into three parts: field, elastance (refer to Section 3.5) and induction, for the synchronous electrostatic machine with field excitation may be derived.**

For the purpose of sizing the proposed machine based on the torque requirement,

- **a torque model, which relates the torque production as a function of the key geometric parameters, may be developed.**

Machine Optimization

Most of the optimization work done on the electrostatic machine was based on the assumption of the linear proportionality between capacitance and the facing area. Part of the reason is the calculation of capacitance is much harder than that of inductance even in simple structures. However, this assumption is not accurate especially when the electrodes are misaligned. In order to quickly and accurately predict the machine performance,

- **analytically determined capacitance calculation may be developed.**

What is more,

- **the impact of pole count, electrode thickness, electrode width, etc., may be investigated thoroughly.**

3 ELECTROMECHANICAL ENERGY CONVERSION PRINCIPLES IN ELECTROSTATIC FIELD SYSTEMS

If we never experience the chill of a dark winter, it is very unlikely that we will ever cherish the warmth of a bright summer's day. Nothing stimulates our appetite for the simple joys of life more than the starvation caused by sadness or desperation. In order to complete our amazing life journey successfully, it is vital that we turn each and every dark tear into a pearl of wisdom, and find the blessing in every curse.

— Anthon St. Maarten (2012)

3.1 Introduction

The energy conversion between electrical and mechanical forms is called electromechanical energy conversion. It can take place through the medium of magnetic or electric fields. To understand the nature of electrostatic energy conversion, a simple parallel plate capacitor is used to derive electrostatic force and torque. Also the duality of magnetic and electric fields is discussed in terms of force, flux linkage, energy, reluctance and elastance, etc.

This chapter serves as the cornerstone of the following chapters. It is also dedicated to give the author's respect to A. E. Fitzgerald and his book *Electric Machinery*, which enlightened the author's electric machine world.

3.2 Forces and Torques in Electrostatic Field Systems

Energy conversion is usually associated with work, which is the result of displacement in the direction of a force. In an electromagnetic field, the total force experienced by a charge q is called the *Lorentz force*:

$$\mathbf{F} = q(\mathbf{E} + \mathbf{v} \times \mathbf{B}), \tag{3.1}$$

in which $\mathbf{v}$ is velocity of the charge, $\mathbf{E}$ and $\mathbf{B}$ are the electric and magnetic field experienced by the charge [14]. Lorentz force can be separated into the force due to the electric field,

$$\mathbf{F}_e = q\mathbf{E}, \tag{3.2}$$

and the force due to the magnetic field,

$$\mathbf{F}_m = q\mathbf{v} \times \mathbf{B}. \tag{3.3}$$

In a conventional electric machine, the magnetic or electric field which crosses the air gap is usually quasi-static since the rotating shaft and electrical frequencies are tied together, meaning that the magnetic field produced by the "slowly" varying electric field is almost negligible and vice versa. Thus in a normal electric machine, the Lorentz force is usually reduced to either eq. (3.2) or eq. (3.3).

In electrostatic field systems, eq. (3.2) indicates that the force experienced by the charge is proportional to the charge amount q and electric field intensity $\mathbf{E}$, and, the force direction is exactly the same as the fields. In magnetostatic field systems, eq. (3.3) indicates that the force experienced by the charge is proportional to the charge magnitude q, magnetic field intensity $\mathbf{B}$, charge velocity $\mathbf{v}$ and also the angle between $\mathbf{v}$ and $\mathbf{B}$. The direction is determined by the right hand rule.

Provided that the normal field is much stronger than the tangential field (Section 4.2), it seems that force can be more easily produced in an magnetostatic field system because the magnetic field can be perpendicular to the motion (force) direction while the electric field must be in line with the motion (force) direction in an electrostatic field system. However, eq. (3.3) is not very useful in this comparison simply because charge usually flows inside wires and magnetic fields tend to detour through low reluctance paths — back iron, which cannot be co-located with wires. Chapter 4 will give a more convincing comparison through the Maxwell stress tensor.

For both field force $\mathbf{F}_e$ and $\mathbf{F}_m$, the torque experienced by the charge is simply

$$\tau = \mathbf{r} \times \mathbf{F},$$

in which $\mathbf{r}$ is the position vector relative to the axis of rotation.

3.3 Charge Linkage, Capacitance and Energy

Equation (3.2) is not a practical way to calculate the electrostatic force even in a simple electromechanical device: usually the charge and electric field distribution are unknown in the system and solving them using numerical tools like *finite element* (FE) analysis is quite time consuming. A systematic closed-form approach based on energy method [14] is implemented in the subsequent two sections to determine the resultant electrostatic force and torque.

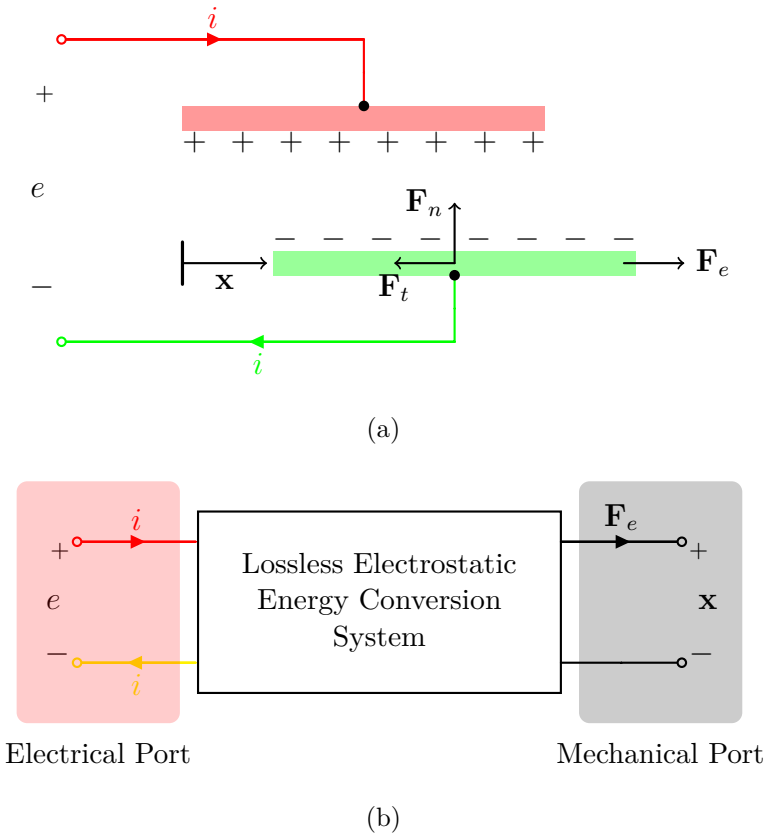

Figure 3.1: Diagram of (a) a parallel plate capacitor (b) a simple lossless electrostatic energy conversion system.

Referring to a simple lossless electrostatic energy conversion system (a parallel plate capacitor) in Figure 3.1a, an electrostatic energy conversion system usually consists of electrical signal at one terminal — voltage e across the system terminal and current i flowing through the system. It also has the mechanically stationary part (stator), translational/rotational part (mover or rotor)

and mechanical work at another terminal. This is the resultant force $\mathbf{F}_e$ on the moving part and displacement $\mathbf{x}$ of the moving part, which is shown in Figure 3.1b. At the electrical port, because of *Kirchhoff's current law*, the current flowing in equals the current flowing out of the lossless system. However, at the mechanical port, the resultant force $\mathbf{F}_e$ does not circulate in a similar way.

Following the polarity convention defined in Figure 3.1a, the power absorbed from the electrical port is

$$p_e = e \cdot i,$$

and the power delivered to the mechanical port is

$$p_m = \mathbf{F}_e \cdot \frac{d\mathbf{x}}{dt}.$$

The electrostatic system itself functions as an energy bank, which exchanges energy with both the electrical and mechanical ports. The total stored energy is defined as W_e. From conservation of energy in this lossless system,

$$\frac{dW_e}{dt} = e\,i - \mathbf{F}_e \cdot \frac{d\mathbf{x}}{dt}. \tag{3.4}$$

In order to solve $\mathbf{F}_e$ in eq. (3.4), the total stored energy W_e as a function of the state of the electrostatic system needs to be known. An easy way to explore this is to set $d\mathbf{x}/dt = 0$ for now, which corresponds to no energy conversion between the mechanical port and the system; all the power from the electrical port is stored inside the system. Thus the net energy gained in the time interval $[t_1, t_2]$ is

$$\Delta W_e = \int_{t_1}^{t_2} e\,i\,dt.$$

It is not hard to observe that $i\,dt$ is the charge accumulating on the parallel plates. Also, there is a linear relationship between the terminal voltage and the total charge $q = Ce$, where C is the *capacitance* of the system. By changing the integration variable to the charge q residing in the system, and applying the linearity relation, the above equation turns into:

$$\Delta W_e = \int_{q_1}^{q_2} \frac{q}{C}\,dq = \frac{1}{2C}\left(q_2^2 - q_1^2\right), \tag{3.5}$$

in which q_1 and q_2 are the amount of charge at times t_1 and t_2. If W_e is chosen to equal zero when there is no charge in the system (no electric field), then eq. (3.5) suggests that at any given charge

state q, the total stored energy is

$$W_e = \frac{q^2}{2C} = \frac{1}{2}Ce^2. \tag{3.6}$$

Equation (3.6) can be applied to a general electrostatic energy conversion system, even though it is derived from a parallel plate capacitor. Recall that for a magnetostatic energy conversion system, the total stored energy is

$$W_m = \frac{\lambda^2}{2L} = \frac{1}{2}Li^2, \tag{3.7}$$

in which λ is the flux linkage linking through stator and mover/rotor parts, L is the inductance of the system and i is the current flowing in the flux-generating windings [14]. The duality between eq. (3.6) and eq. (3.7) reveals some observations about the electrostatic system:

(1) Capacitance is the energy storage element. The larger the capacitance, more powerful the system;

(2) Charge functions as a linkage, which is established by electrostatic induction, between stator and mover/rotor parts;

(3) From the control perspective, an electrostatic machine is naturally a voltage regulating device.

In the end of this section, the widely accepted relation $q = Ce$ will be reconsidered. Capacitance C is usually determined by the geometry of the electrostatic system. For a capacitor with large aspect ratio (overlapping length over gap distance g), the capacitance can be approximated by

$$C = \frac{\varepsilon S}{g},$$

in which ε is the permittivity of the dielectric material between the plates, and S is the facing area (plate depth times overlapping distance). The facing area is usually a function of the displacement of mover/rotor in the system, like $\mathbf{x}$ in Figure 3.1a. In the above derivation $\mathbf{x}$ is set to zero, so C can be treated as constant. In Section 4.5, the capacitance is shown as a nonlinear function of the charge (similar to the nonlinear relation between inductance and magnetic flux) and the nonlinearity is minor, which gives us more confidence on the above derivation.

3.4 Determination of Electrostatic Force and Torque

Substitute eq. (3.6) into eq. (3.4) and multiply both sides by dt,

$$\frac{1}{2}\, d\left(Ce^2\right) = ei\, dt - \mathbf{F}_e \cdot d\mathbf{x}.$$

Even though capacitance C is treated as a constant in the last section while developing an expression for total stored energy, it can be varying now simply because the displacement $\mathbf{x}$ is free to change. By applying $i\, dt = dq = d\left(Ce\right)$ and using the basic calculus identity $d(uv) = u\, dv + v\, du$, the above equation leads to

$$\mathbf{F}_e \cdot d\mathbf{x} = \frac{1}{2} e^2\, dC,$$

which further suggests that the force F_e in the direction of movement $d\mathbf{x}$ (speed direction) is

$$F_e = \frac{1}{2} e^2 \frac{dC}{dx}. \tag{3.8}$$

Hereby another analytical expression to calculate the electrostatic force is found. Interested readers might ask: do we still need the capacitance as a function of x to get the force value? Indeed, if the FE tool is used, eq. (3.8) has no advantages over eq. (3.2) because capacitance is calculated through charge distribution in such case. As will be seen later in Chapter 7, an analytical approach that bypasses the need to calculate charge distribution, can calculate the capacitance dramatically faster than FE approach.

For a rotating device, the resultant torque T_e exerting on the rotor can be derived in a similar way. The end result is given directly as:

$$T_e = \frac{1}{2} e^2 \frac{dC}{d\theta}, \tag{3.9}$$

in which θ is the rotor mechanical displacement angle.

It is interesting that eq. (3.8) and eq. (3.9) do not include any de term while the energy expression eq. (3.6) are functions of both C and e. In fact the energy change caused by de is *immediately* balanced by the electrical port as can be revealed by the equation simplification process. However, the terminal voltage e does play a quadratic role in the resultant force. This intuition inspires the design and control of a single phase electrostatic machine, which is shown in Section 3.5 and [54].

Furthermore, if voltage e was kept constant and the rotor rotated integer electrical cycles, there would be no average torque developed at all. That is to say, the voltage excitation has to possess AC components to obtain net average torque.

3.5 Duality of Magnetostatic and Electrostatic

After getting the complete set of equations for the electrostatic energy conversion system, it is amazing that a beautiful duality between magnetostatic and electrostatic shows up. Magnetic field machinery utilizes the magnetic Lorentz force $\mathbf{F}_m$ (often parsed into "field" and "reluctance" components) while electric field machines use the Coulomb force $\mathbf{F}_e$ (which can be parsed into a "field" and an "elastance" component, as will be shown in Chapter 5). The term elastance was coined in the 19^{th} century by Maxwell and Heaviside and is physically defined as the inverse of capacitance [62]. This serves as a dual to magnetic reluctance as reluctance is the inverse of inductance albeit scaled by the turns N^2 (currently there is no established dual for turns in electrostatics). Switched and synchronous reluctance machines are not named variable inductance machines; therefore the same convention should be applied to elastance machines (variable capacitance). An elastance force/torque results from a system acting to minimize energy stored in the gap between the stator and rotor of a machine, i.e. the capacitance between the stator and rotor is a function of angular position. An alternative statement is that the electrostatic force/torque will act to minimize elastance.

As explained in Chapter 1, however, it is often overlooked in electromechanical energy conversion that electric fields may also create substantial force/torque to perform work. To explore the opportunities for designing a competitive electrostatic machine, Table 3.1 is provided to summarize the similarities, dualities and differences between magnetostatics and electrostatics. The relationship between the flux and the energizing source (current or voltage) is identified as the energy storage capability, inductance L and capacitance C respectively. Drawing from the table, the amount of flux attainable for a given source is limited by the capabilities of the materials and geometry involved, i.e. parameters that constitute L and C or $\mathscr{R}_m$ and $\mathscr{E}_e$. The lower the reluctance/elastance, the easier flux penetrates the space for a given source, resulting in higher energy storage capability. The reluctance/elastance perspective within the table demonstrates that both the reluctance and

elastance are only a function of geometry and the properties of the material occupying the space (gap). Assuming a switched or variable machine model, the formulae indicate torque depends on three factors:

(1) the difference between the maximum and minimum inductance/capacitance, i.e. the saliency;

(2) the angular distance over which these maxima and minima occur, i.e. the number of poles;

(3) the magnitude of the driving sources, i.e. current or voltage.

The duality introduced here is provided with the intent to inspire intuitive design techniques based on historical reluctance machine knowhow and extend it to elastance machinery. The differences between the two, however, suggest new paths to further push the performance of electrostatic machines. Based on Table 3.1, the following design concepts may be adopted:

(1) The relative permittivity ε_r of gap material can be larger than 1, to lower elastance. An electromagnetic machine has two main flux barriers — back iron and air gap. Machine designers almost always choose back iron with relative permeability μ_r as large as possible and gap material as air for shear stress consideration (see Chapter 4). However, increasing shear stress and lowering the elastance are consistent in an electrostatic machine;

(2) The pole count may be as high as dozens before leakage effects begin to dominant. Slots, windings and fill factor in an electromagnetic machine prevent it from using high pole count (this explains why usually the base speed of an electromagnetic machine is above 500 rpm for 50 Hz or 60 Hz designs.).

3.6 Duality of Electrostatic and Static Current Field

Before ending this chapter, the duality between the electrostatic and the static current field is reviewed. Without the present of the magnetic field, the current density $\mathbf{J}$ in a *lossy* material relates to the electrostatic field $\mathbf{E}$ through the well known Ohm's law

$$\mathbf{J} = \sigma \mathbf{E}, \tag{3.10}$$

Table 3.1: Duality of Magnetic Reluctance and Electric Elastance.

		Magnetostatic	**Electrostatic**
Field Perspective	*Vector Field*	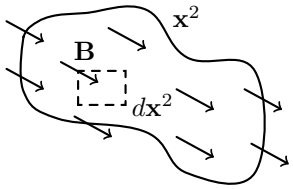	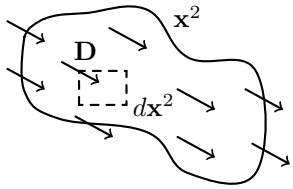
	Flux	$\mathbf{B} = \mu\mathbf{H}, \quad \varphi = \int_{x^2} \mathbf{B} \cdot d\mathbf{x}^2$	$\mathbf{D} = \varepsilon\mathbf{E}, \quad q = \int_{x^2} \mathbf{D} \cdot d\mathbf{x}^2$
	Closed Surface Integral	$\oint_{x^2} \mathbf{B} \cdot d\mathbf{x}^2 = 0$	$\oint_{x^2} \mathbf{D} \cdot d\mathbf{x}^2 = q_{enc}$
	Energy Storage Element	$L = \frac{N\varphi}{i} = \frac{\lambda}{i}$	$C = \frac{q}{e}$
Reluctance/Elastance Perspective	*Flux Path Cross Section Geometry*	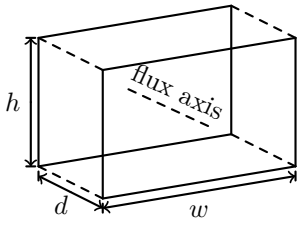	
	Reluctance or Elastance	$\mathscr{R}_m = \frac{d}{\mu_0\mu_r wh} = \frac{N^2}{L}$	$\mathscr{E}_e = \frac{d}{\varepsilon_0\varepsilon_r wh} = \frac{1}{C}$
	Circuit Diagram	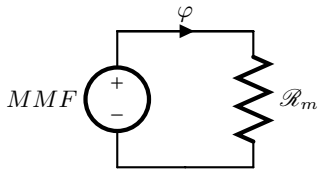	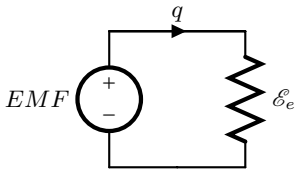
	Motive Force	$MMF = Ni = \varphi\mathscr{R}_m$	$EMF = e = q\mathscr{E}_e$
	Force	$F_m = \frac{1}{2}i^2\frac{dL(x)}{dx} = \frac{1}{2}i^2\frac{d}{dx}\frac{N^2}{\mathscr{R}_m(x)}$	$F_e = \frac{1}{2}e^2\frac{dC(x)}{dx} = \frac{1}{2}e^2\frac{d}{dx}\frac{1}{\mathscr{E}_e(x)}$
	Torque	$T_m = \frac{1}{2}i^2\frac{dL}{d\theta} \propto i^2\frac{L_{\max} - L_{\min}}{\Delta\theta}$	$T_e = \frac{1}{2}e^2\frac{dC}{d\theta} \propto e^2\frac{C_{\max} - C_{\min}}{\Delta\theta}$

where σ is the conductivity of the material in consideration. Due to eq. (3.10), like the electrostatic field, the static current field is also governed by the Laplace's equation

$$\nabla^2 \phi = 0 \tag{3.11}$$

in which ϕ represents field potential. Thus in a homogeneous medium, the conductance G between electrodes is simply obtained by swapping the permittivity ε out of the capacitance C with the conductivity σ

$$G = \frac{\sigma}{\varepsilon} C. \tag{3.12}$$

When it comes to an *inhomogeneous* environment consisting of several different dielectric materials like the synchronous machine proposed in Chapter 6, eq. (3.12) cannot be applied directly because the ratio σ/ε is not necessarily the same across these materials, which results in unparalleled discontinuities between the **J** and **D** fields. However, an effective ratio $(\sigma/\varepsilon)_{eff}$ can be assumed from the terminal perspective if necessary, since G and C are essentially lumped parameters. This ratio may differ between different pairs of electrodes or in different temperatures, frequencies, etc. Therefore in Section 5.2, the capacitance profile and the conductance profile are kept apart except for the basic trigonometric shapes, which are determined by the electrode layout directly.

3.7 Summary

An electrostatic energy conversion system is explored as a dual of electromagnetic one from the perspectives of flux linkage, energizing source, reluctance/elastance, energy, force/torque and then the principle is extended to the multi-conductor system. We can seek the common ground based on the duality between magnetostatics and electrostatics and at the same time take advantage of the differences between the two to design a competitive electrostatic machine.

4 DIELECTRIC LIQUIDS FOR ENHANCING ELECTROSTATIC FORCES

Let us change our traditional attitude to the construction of programs. Instead of imagining that our main task is to instruct a computer what to do, let us concentrate rather on explaining to human beings what we want a computer to do.

— Donald Knuth (1984)

4.1 Introduction

Electrostatic forces enhanced by dielectric liquids are investigated in depth in this chapter and are summarized in [4]. Starting from the Maxwell stress tensor, magnetic and electric shear stresses are compared to demonstrate the general gap medium requirement of an electrostatic machine. Effective electromechanical power conversion using electrostatics requires dielectric liquids whose permittivity and breakdown field strength can facilitate adequate electric shear and pressure beyond the capabilities of media such as air or vacuum.

Key dielectric properties including pressure, breakdown field strength, relative permittivity and conducitivity are measured for selected dielectric liquids with custom pressure and shear stress test stand. The best liquid candidate is demonstrated to be capable of mitigating the shear stress deficiency to only one order difference compared to the magnetic machine.

4.2 Maxwell Stress Tensor

The electrostatic force and torque determined in Section 3.4 are represented as functions of the capacitance, which is a high level lumped element. At the most fundamental level, electric and magnetic forces are described by the *Maxwell stress tensor* $\mathbf{T}$ and the *Poynting vector* $\mathbf{S}$ [36, 63, 64]. Physically, $\mathbf{T}$ is the force per unit area (or stress) acting on a surface due to local electric and magnetic fields. The Poynting vector $\mathbf{S}$ represents the directional energy flux density, i.e. power per unit area, of an electromagnetic field. Substituting Maxwell's equations into the Lorentz force equation (refer to eq. (3.1)) will eliminate any charge or current densities, allowing forces to be

written purely as field quantities. The total force acting on a surface in free space due to **T** and **S** then may be calculated by eq. (4.1). The surface integral term contributes to the Lorentz force and the volume integral term contributes to the radiation pressure.

$$\mathbf{F} = \int_{x^2} \mathbf{T} \cdot d\mathbf{x}^2 - \varepsilon_0 \mu_0 \frac{d}{dt} \int_{x^3} \mathbf{S} \cdot d\mathbf{x}^3. \tag{4.1}$$

Usually electric machines operate at quasi-static frequencies, thus the **S** term is omitted, leaving **T** as the primary contributor. An element of **T**, T_{ij} shown in eq. (4.2), is the force (per unit area) in the i^{th} direction acting on an element of surface oriented in the j^{th} direction. This implies that diagonal elements ($T_{xx},\ T_{yy},\ T_{zz}$) represent pressures, and off diagonal elements ($T_{xy},\ T_{yz},$ etc.) are shears.

$$T_{ij} \equiv \varepsilon_0 \varepsilon_r \left(E_i E_j - \frac{1}{2} \delta_{ij} E^2 \right) + \frac{1}{\mu_0 \mu_r} \left(B_i B_j - \frac{1}{2} \delta_{ij} B^2 \right). \tag{4.2}$$

In a rotary machine, the torque τ on a rotor of constant radius r is simply given by the cross product shown in equation eq. (4.3).

$$\tau = \mathbf{r} \times \mathbf{F}. \tag{4.3}$$

In this case, the pressure terms cause eccentric rotor forces and shear terms produce torque about an axis (shaft).

The terms of eq. (4.2) may be parsed into electric and magnetic components as in eq. (4.4) and eq. (4.5) [36]:

$$\text{Pressure}(i = j): \quad p_e = \frac{\varepsilon_0 \varepsilon_r}{2} E_i E_j \qquad p_m = \frac{1}{2\mu_0 \mu_r} B_i B_j, \tag{4.4}$$

$$\text{Shear}(i \neq j): \quad \sigma_e = \varepsilon_0 \varepsilon_r E_i E_j \qquad \sigma_m = \frac{1}{\mu_0 \mu_r} B_i B_j. \tag{4.5}$$

In the generic stator-gap-rotor machine as shown in Figure 4.1, either electric or magnetic fields are composed of normal ("i") and tangential ("j") components, and the reaction between them produces torque/force. Note that any electrical machine essentially facilitates normal and tangential field components regardless of magnetic/electric operation and specific configurations, e.g. induction, permanent magnet, electret, separately excited, variable capacitance (elastance), switched reluctance, DC commutated, etc. [36].

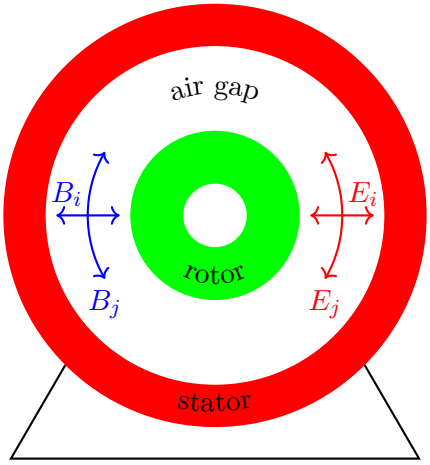

Figure 4.1: Illustration of the force or torque producing field components of the Maxwell stress tensor in the air gap of a rotating electric machine.

Magnetic Shear

Equation (4.5) indicates that for a given field B_i and B_j, the relative permeability of the gap should be as low as possible for greatest shear. Air gap in magnetic machineary naturally facilitate this as they possess unity relative permeability (if they are indeed a gas or vacuum). However, to create a large field inside the rotor-stator gap, the gap must be small and surrounded by "back-iron" of high permeability, i.e., the reluctance of the overall magnetic circuit (closed field path) must be as low as possible. This iron is a limiting factor as most electric machine steels saturate in the 1 to 2 Tesla range [10]. Additionally the amp turns to drive flux through the magnetic circuit are thermally limited, i.e. i^2R losses. Given present materials, a magnetic machine designer's role is to extract as much performance out of the $1 \sim 2\,\mathrm{T}$ limit as possible while keeping losses low. At $1.5\,\mathrm{T}$, the theorectical shear limit is $1.79\,\mathrm{MPa}$ or $260\,\mathrm{psi}$. Actual values in use today are $\sigma_e \approx 48 \sim 123\,\mathrm{kPa}$ or $7 \sim 18\,\mathrm{psi}$ for large magnetic machines (e.g., utility turbo-generators) to $\sigma_e \approx 3.4 \sim 13.8\,\mathrm{kPa}$ or $0.5 \sim 2\,\mathrm{psi}$ for small machines (e.g. integer hp induction motors) [65]. This constitutes "rule of thumb" pressure to shear ratio of $10:1$ to $100:1$ spanning from large to small machines [66].

Electric Shear

Contrary to magnetic shear, eq. (4.5) shows that electric shear is limited by the available dielectric material inside the gap. In air under ideal circumstances ($\varepsilon_r \approx 1$, $E_{bk} \approx 3\,\mathrm{MV/m}$) theoretical maximum electric shear $\sigma_e \approx 79.65\,\mathrm{Pa}$ or $0.012\,\mathrm{psi}$, a 3 to 4 order of magnitude deficiency for electrostatics compared to magnetics. Electrostatic shear stress can be enhanced by increasing the displacement field in the gap between stator and rotor surfaces. Specifically, raising the electric field strength and/or the relative permittivity of gap space can facilitate the necessary increase. This may be achieved by voiding the gap with ultra-high vacuum (UHV), or filling it with dielectric gases or liquids. Figure 4.2 shows the operational space trends based on these approaches. An additional approach to mitigate the shear stress deficiency would be to increase the stator/rotor surface area for σ_e to act on. Emerging work on increasing the surface area per unit volume of electrostatic machinery, actuators and power transfer is documented in [40, 53].

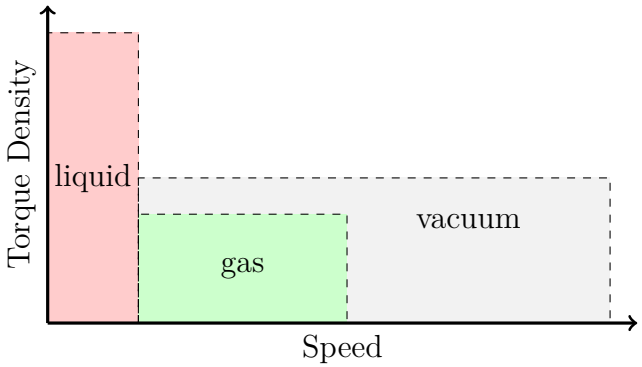

Figure 4.2: Operational space trends based on dielectric media filled in an electrostatic machine.

UHV/Dielectric Gases

Under UHV conditions, the breakdown strength is enhanced ($E_{bk} = 20 \sim 40\,\mathrm{MV/m}$ is the practical limit for many electrodes [57, 58]), typically an order of magnitude better than air or slightly more. This increase only reduces the difference between electric and magnetic shear approximately 2 orders in magnitude (given the square of the field) since the relative permittivity remains unity. The vacuum approach has been demonstrated in [43, 45, 46, 67] resulting in motors in the fractional

horsepower regime yet requiring input voltage of $10 \sim 300\,\text{kV}$. Another approach is to use gases under high pressure, to drive the breakdown strength up the Paschen's curve as in [47]. This approach has resulted in kilowatt-scale machines which utilize $200 \sim 600\,\text{kV}$. The permittivity of gases are low (near free space), as the space between the molecules dominates. In either case, the machines using these approaches produce relatively low torque, and must spin at considerable speed to develop power, often in the range of $10k \sim 500k\,\text{rpm}$ [30, 43, 45]. Additionally, it is difficult to maintain UHV or high pressure gas conditions in a rotating environment with shaft seals, let alone justify the cost for a fractional or integer horsepower machine [57].

These challenges make evident the need for greater than unity relative permittivity to increase torque for a given voltage. Dielectric liquids may facilitate this, but will hamper high speed operation due to viscous drag losses. This implies low-speed-direct-drive machines may benefit from dielectric liquids at atmospheric pressure. Low speed ($< 500\,\text{rpm}$) direct drive has always been a challenge for magnetic machinery, thus this space serves as an entry point for electrostatic technology. The study and synthesis of dielectric liquids to facilitate this machine functionality is in its infancy.

4.3 Dielectric Liquids

The analysis above indicates that competitive low speed direct drive electrostatic machinery must be designed to be filled with a dielectric liquid that possess substantially higher dielectric strength and relative permittivity compared to air/vacuum. Although not fully formed, this concept was first hinted as early as [48, 61], but safe, high performance, off-the-shelf (OTS) liquids were not available to pursue the concept. Fifty years later, there are myriad dielectric liquids available today, with vastly different chemical properties. Table 4.1 lists OTS liquids with attractive dielectric properties and theoretical limits. Dielectrics checked (✓) in Table 4.1 are investigated experimentally for their relatively balanced properties. The unselected dielectric liquids are grouped as follows: group I is excluded mainly for their potential hazard to humans and equipment. Dielectrics in group II meet the high breakdown strength and permittivity requirement; however they are relatively more conductive causing higher losses. Unfortunately, most naturally occurring liquids with high permittivity exhibit higher conductivity or are easily susceptible to electrochemical reactions/ionization due to their

Table 4.1: Dielectric Properties of Commercial Dielectric Liquids.

*	Dielectrics	Dielectric Strength	ε_r	Viscosity	Conductivity	Loss Metric	MSDS		
		E_{bk}, MV/m		μ, Pa · s	σ, S/m	$\sigma\mu/\varepsilon_r$	Health	Fire	Reactivity
✓	**Vegetable Oil**[1]	≥ 15	3.00	7.80×10^{-2}	$\approx 1 \times 10^{-11}$	/	0	1	0
✓	**FR3 Envirotemp**[2]	30	3.20	3.30×10^{-2}	3.33×10^{-12}	3.43×10^{-14}	0	1	0
	STO-50 Silicone Oil[3]	40 ~ 50	2.55	4.80×10^{-2}	1.00×10^{-12}	1.88×10^{-14}	0	1	0
✓	**Vertrel XF** ($C_5H_2F_{10}$)[4]	14 ~ 28	7.10	6.70×10^{-4}	1.0×10^{-9}	9.44×10^{-15}	1	0	1
I	**Hydrazine**[5]	/	52.0	9.70×10^{-4}	/	/	3	3	3
	Phosgene[6]	/	4.70	/	7.00×10^{-4}	/	4	0	1
	Acetone[7]	/	20.7	3.16×10^{-4}	2.00×10^{-3}	3.05×10^{-11}	1	3	0
	Bromine[8]	/	3.10	9.50×10^{-4}	1.28×10^{-8}	3.92×10^{-15}	3	0	0
	Decane[9]	192	1.99	8.59×10^{-4}	/	/	2	2	0
	Dichloromethane[10]	/	9.14	4.40×10^{-4}	4.30×10^{-4}	2.07×10^{-15}	2	1	0
	Hexane[11]	113	1.90	3.13×10^{-4}	1.00×10^{-16}	1.65×10^{-20}	2	3	0
II	**Propylene Carbonate**[12]	220	66.0	2.76×10^{-3}	1.00×10^{-4}	4.18×10^{-9}	1	1	1
	Ethylene Carbonate[13]	/	89.8	1.85×10^{-3}	1.00×10^{-6}	2.06×10^{-11}	2	1	1
	Water[14]	65 ~ 70	80.4	1.00×10^{-3}	4.00×10^{-6}	4.98×10^{-11}	0	0	0
	THESO Oil[15]	38	15.0	/	1.00×10^{-4}	/	/	/	/
III	**Air**[16]	3	≈ 1	1.82×10^{-5}	8.00×10^{-15}	1.46×10^{-19}	1	1	1
	Vacuum	∞ (theoretical)	1.00	0	0	0	1	1	1

* Checked dielectrics are tested in the experiment. Group I has hazard potential to human and equipment. Group II is relative more conductive and will give rise to conduction loss. Group III features low permittivity.

[1] [60], [68] [2] [69], [70], [71] [3] [72] [4] [73] [5] [74], [75], [76] [6] [77], [78], [79] [7] [78], [80] [8] [78], [81], [82], [83] [9] [78], [84], [85]
[10] [78], [86], [87] [11] [78], [88], [89] [12] [78], [90], [91], [92], [93] [13] [78], [94], [95] [14] [78], [96], [97] [15] [98] [16] [78], [99], [100], [101]

polar nature. In group III, air possesses not only a near unity permittivity but also much lower breakdown strength and UHV is difficult to maintain and not cost effective.

To gain greater numerical insight on the liquids' physical properties, an electromechanical "loss metric" column in Table 4.1 provides comparison. For a given electric field strength and mechanical speed, conduction losses are proportional to liquid conductivity σ while viscous drag loss is proportional to the viscosity μ. Viscosity temperature dependence was not investigated here, but can be significant for oils, especially at low temperatures. Electrostatic torque (and thus power) will be proportional to the relative permittivity ε_r. The ratio $\sigma\mu/\varepsilon_r$ represents the ratio of loss to torque properties of a liquid. The investigated dielectrics represent either oils or solvents as they have the lowest electromechanical loss metric in Table 4.1 (ranging from 9.44×10^{-15} to 3.43×10^{-14}) while being safe for humans to use.

Dielectric oils have made large strides over the last several decades thanks in large part to the HVAC and HVDC transmission industries [59]. Modern oils have dielectric strength up to $30 \sim 50\,\mathrm{MV/m}$ (or exceed, depending on the degree of chemical passivation of electrode surface), relative permittivity of $\varepsilon_r \approx 3.2$ and a volume resistivity of $30\,\mathrm{T\Omega\text{-}cm}$. Substitution of these values into eq. (4.5) yields a theoretical maximum value for σ_e = 25.49 kPa or 3.7 psi. Vertrel XF, a fluorinated hydrocarbon commercial solvent, achieves similar maximum shear of 25.2 kPa or 3.66 psi at a lower field strength of 20 MV/m given its relative permittivity of $\varepsilon_r \approx 7.1$. Additionaly Vertrel XF is 100 times less visoucs than the oils, albeit with increased conduction loss. To achieve comparable performance a UHV system would need to operate at a voltage $\sqrt{\varepsilon_r}$ greater than any liquid. Although liquid performance is impressive, it is important to remember that the achievable shear in a machine is a fraction of the pressure normal to the surface as mentioned earlier. This is due to the field component tangential to the surface typically being much smaller than the normal component. Measuring the field force capabilities of candidate liquids in a physical system is the subject of the following section.

4.4 Dielectric Liquids Test Stand

For liquid evaluation purposes, a common test fixture for all liquids is desirable. According to the Laplace's equation

$$\nabla^2\phi = 0,$$

and electric field equation

$$E_i = -\frac{\partial\phi}{\partial x_i},$$

the potential ϕ and electric field distribution for electrostatic (at least quasi-static) conditions is independent of the gap medium provided constant boundary conditions. Further, the ratio between the shear stress and pressure,

$$\frac{\sigma_e}{p_e} = 2\frac{E_j}{E_i},$$

is also independent of the medium. Thus the achievable shear stress a liquid can facilitate can be compared through the achievable pressure, an easier experiment to design. This section details the electric pressure test stand construction for intent for benchmarking dielectric liquids. A shear stress test stand is also built up to correlate the achievable shear and pressure.

Normal Pressure Test Stand

A test stand to measure electric pressure between two parallel aluminum electrodes separated by a controllable gap was assembled as shown in Figure 4.3. Circular electrodes, or "pucks," are submerged in a dielectric liquid reservoir where voltage is applied to the fully submerged lower puck while the upper puck and reservoir are at ground potential. The pucks are 76.2 mm in diameter with 5 mm radius rounded edges at the facing side to minimize the severity of fringing and breakdown. The lower puck is fixed while the upper puck is attached to a mounting plate suspended on three load cells to measure the force (pressure) pulling the pucks together. The load cells are equally spaced 120 deg apart. The mounting plate rests freely upon the load cells and its height may be adjusted by three 6-80 (i.e., 0.0125 inches/turn or 0.3175 mm/turn) fine adjustment screws as shown in Figure 4.3b. The gap may be set for any width but a 0.3175 mm gap, paired with a $0 \sim 10$ kV power supply, is used to demonstrate pressures > 1 psi (6.9 kPa), thus pushing dielectrics to their

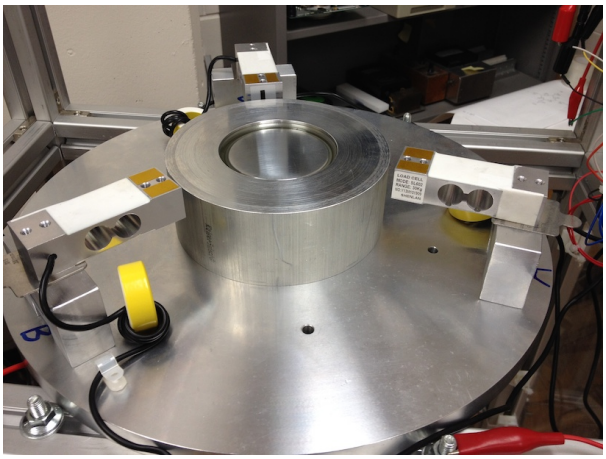

(a)

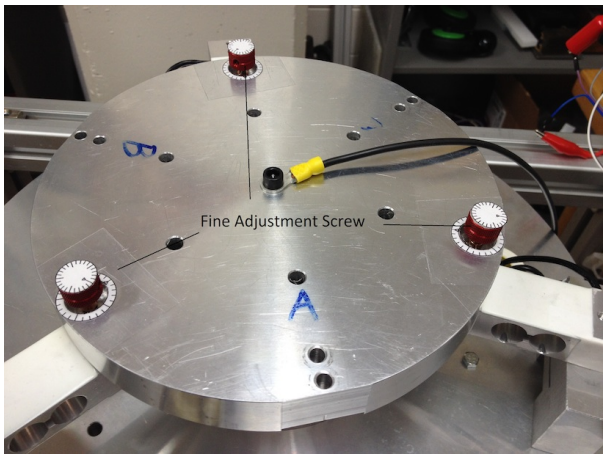

(b)

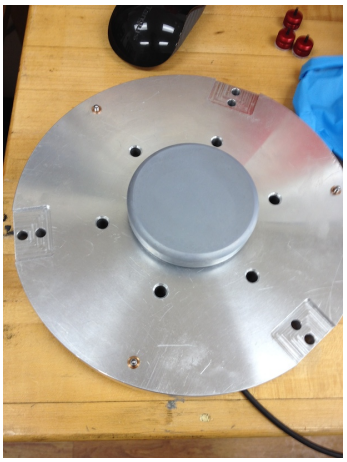

(c)

Figure 4.3: Photograph of normal pressure test stand, (a) lower puck in liquid reservoir surrounded by load cells, (b) upper puck mounting plate with adjustment screws, (c) upper puck.

limit. Referring to Figure 4.3b, the circumference of the adjustment knobs is divided into 5 main scales and each main scale is divided into 5 minor scales. Thus, the adjustment accuracy is within 6 μm, about 2% nomial gap length. The benefit of this structure is that the gap length, parallelism, and concentricity of the pucks are tunable via the incremental feedback from the three load cells.

The capacitance between the electrodes (pucks) is described in eq. (4.6) as a function of facing area A, air gap distance g, and the permittivity ε:

$$C = \frac{\varepsilon A}{g} = \frac{\varepsilon_0 \varepsilon_r \cdot \pi r^2}{g}. \tag{4.6}$$

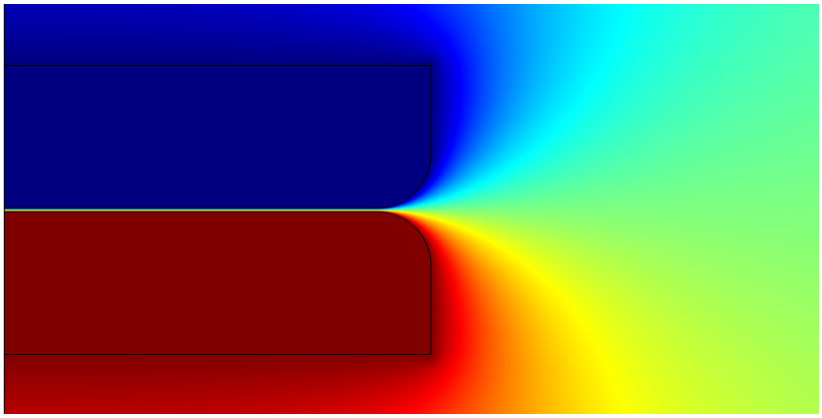

(a)

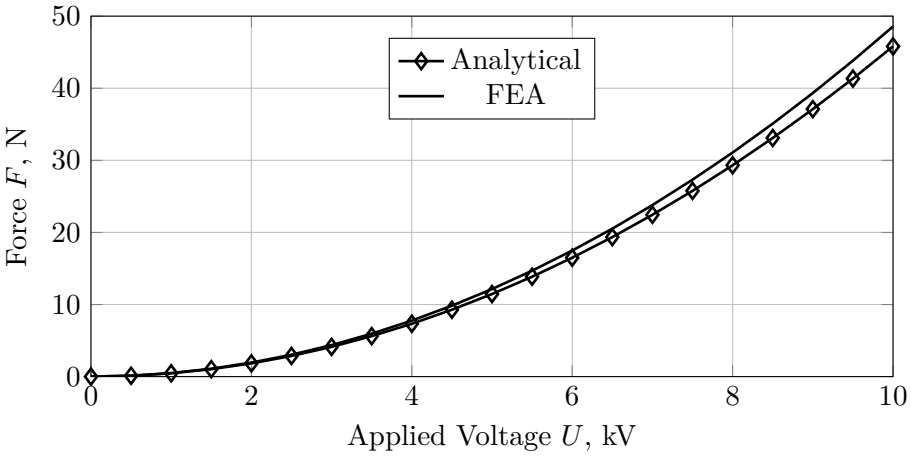

(b)

Figure 4.4: Normal pressure test stand (a) Cross section potential distribution predicted by FE for vegetable oil dielectric, Red = $+U_{max}$ = 10 kV, Blue = 0 V, (b) FE and analytical force vs. applied voltage for vegetable oil dielectric.

The force experienced by the electrodes with an applied DC voltage U is derived by taking the spatial derivative of the stored energy with respect to the air gap length:

$$F = \frac{1}{2}U^2\frac{\partial C}{\partial g} = \frac{\varepsilon_0\varepsilon_r \cdot \pi r^2 \cdot U^2}{2g^2} = \frac{\varepsilon_0\varepsilon_r \cdot \pi r^2 \cdot E^2}{2}. \tag{4.7}$$

It indicates that the compressing force is proportional to the square of the electric field between the pucks. This is in agreement with eq. (4.4) as the displacement field is defined as the product of permittivity and electric field, which leads to eq. (4.8) (consistent with eq. (4.4)):

$$F = \frac{\pi r^2 \cdot D \cdot E}{2} \text{ or } \frac{F}{\pi r^2} = \frac{D \cdot E}{2} = p_e. \tag{4.8}$$

With measured force and known electric field, this equation provides an indirect way of obtaining displacement field and enables the extraction of dielectric saturation phenomenon in the *D-E* plane, which is analogous to the *B-H* curve. Even though the electric field between the pucks is almost uniform due to the large radius to gap length ratio, field fringing still exists at the outer circumference. A finite element simulation of the potential distribution between the pucks is plotted in Figure 4.4a. This fringing is unaccounted for in the analytical derived equations eqs. (4.6)–(4.8). The difference between the analytical and FE simulation may be observed in the force vs. voltage plot in Figure 4.4b. The two correlate well, but the fringing is accounted for in the FE simulation resulting in higher force. Using the FE simulation, the effective area used in the analytical equation may be corrected by taking the ratio of the forces, i.e. the equivalent facing area is larger due to fringing.

Shear Stress Test Stand

To confirm the relationship between the achievable shear and pressure associated with dielectric liquids, a test stand to measure shear force was also built. An interleaved "comb" actuator design was selected for ease of construction and analysis. A cross section of the interleaved combs is illustrated in Figure 4.5. The capacitance between the electrodes (combs) is calculated in eq. (4.9) as a function of plate surface area A, air gap length g and the permittivity ε:

$$C = \frac{\varepsilon A}{g} = \frac{2\varepsilon_0\varepsilon_r \cdot d \cdot (n-1) \cdot x}{\delta - \delta'}, \tag{4.9}$$

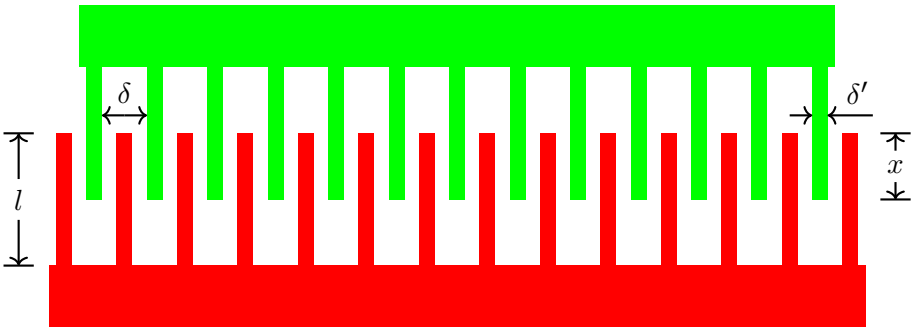

Figure 4.5: Comb-drive style electrode (half inserted, i.e. $x = 8.75\,\text{mm}$).

Table 4.2: Shear Stress Test Stand Dimensions.

Dimensions	d	δ	δ'	l	n
Value	60 mm	6 mm	2 mm	17.5 mm	27

in which, d is the depth into the paper, x is the inserted length, δ is the fin facing distance, δ' is the fin thickness and n is the total fin number. The force experienced by the electrodes with an applied DC voltage U is derived by taking the spatial derivative of the stored energy with respect to the inserted length:

$$F = \frac{1}{2}U^2\frac{\partial C}{\partial x} = U^2\frac{\varepsilon_0\varepsilon_r \cdot d \cdot (n-1)}{\delta - \delta'}. \tag{4.10}$$

The force acts to draw the combs together. Notice that eq. (4.9) only accounts the capacitance of the facing (overlapped) area. Since the aspect ratio (fin length over gap length) is large enough with respect to the partial differentiation when the electrode is half inserted, the force evaluated by eq. (4.10) is reliable for that respective position. The accuracy of eq. (4.10) as a function of overlap and the physical dimensions listed in Table 4.2 may be observed. Figure 4.6a plots the force calculated by FE simulation and analytically by eq. (4.5). When the two electrodes are inserted deeply with respect to each other, the field strength becomes saturated and so does the capacitance. When the two electrodes are apart from each other, the partial differentiation with respect to the facing area is invalid. The divergence defines a range where the experiment can be expected to correlate well with eq. (4.10). The potential distribution used for accuracy correlation is plotted in Figure 4.6b for a 2D cross section of combs filled with a vegetable base dielectric oil.

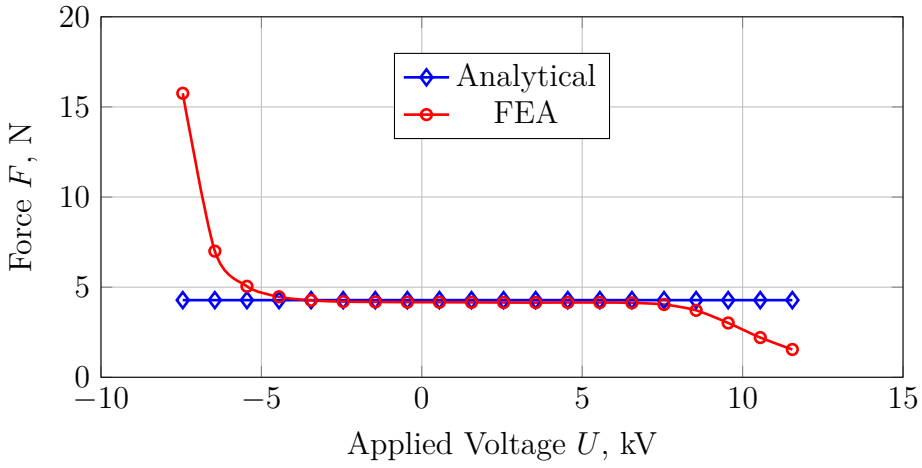

(a)

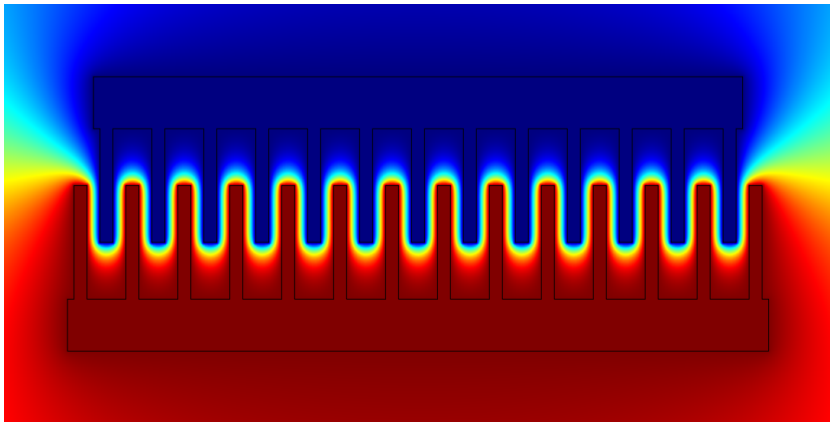

(b)

Figure 4.6: Shear stress test stand (a) Force experienced by electrodes vs. inserted length for vegetable oil dielectric, (b) Potential distribution predicted by FEA for vegetable oil dielectric with Red = $+U_{max}$ = 20 kV, Blue = 0 V.

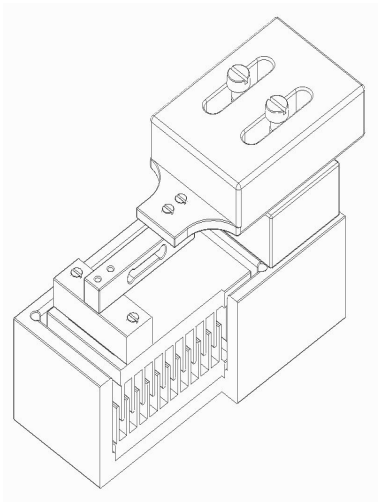

(a)

(b)

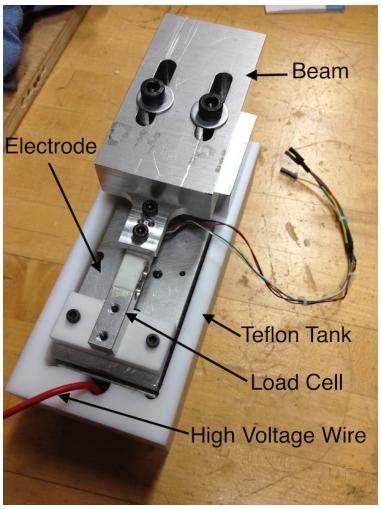

(c)

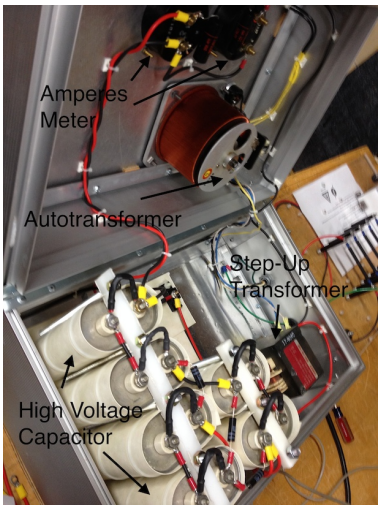

(d)

Figure 4.7: (a) CAD rendered solid model of test stand, (b) photograph of aluminum combs/-electrodes, (c) photograph of assembled test stand, (d) photograph of the adjustable high voltage multiplier.

Aspects of the completed test stand are documented in Figure 4.7. To gain perspective of the construction, Figure 4.7a illustrates a CAD rendered solid model with a cutaway of the tank. The aluminum combs reside in a tank made of Teflon that can be filled with a dielectric fluid. The bottom comb is fixed to the tank while the upper comb is suspended by a load cell beam to measure the force. With safety in mind, voltage is applied to the fully submerged lower comb while the upper comb is at ground potential. An adjustable high voltage DC supply utilizing a 3-stage half wave voltage multiplier design drives the test stand and is photographed in Figure 4.7d.

4.5 Experimental Results

Normal Pressure Measurement

Dielectric liquids vegetable oil, FR3 and Vertrel XF were poured into the pressure test stand. The electrode gap length was set to $g = 0.3175\,\text{mm}$ and DC voltage was applied across the electrodes in series with $500\,\text{M}\Omega$ current limiting resistor bank (in the event of dielectric breakdown). Force, applied voltage, and current are measured directly. The recorded data, in conjunction with the FE corrected analytical models, estimates the permittivity and conductivity of the liquid. Even though the gap can be maintained at this specified value with $U = 0$, the gap will be slightly smaller as the load cells deflect under the developed pressure when a non-zero voltage is applied. This was corrected for prior to dielectric testing by placing reference weights on the mounting plate to mimic electrostatic pressure experienced by the pucks under voltage. Then a small signal voltage was injected across the puck via an impedance analyzer to measure capacitance (and thus gap) between the pucks yielding a correction curve. This method can sense 1% change in gap distance ensuring that the corrected curve is highly accurate.

Normal force pressure is plotted as a function of electric field in Figure 4.8a for all three dielectric liquids with a UHV base line for reference. Of the three liquids, Vertrel XF is the clear choice for electrostatic machinery. Vertrel XF achieved a pressure of $\sim 2\,\text{psi}$, which is 4 ~ 5x greater than the oils, 7x greater than vacuum for the same voltage and $> 300\,\text{x}$ greater than the capability of "ideal" air. Vegetable oil and FR3 demonstrate that even modest amounts of permittivity can have

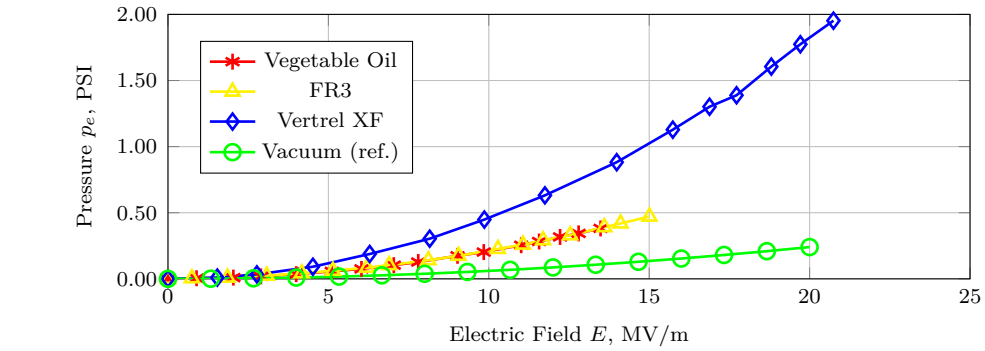

(a)

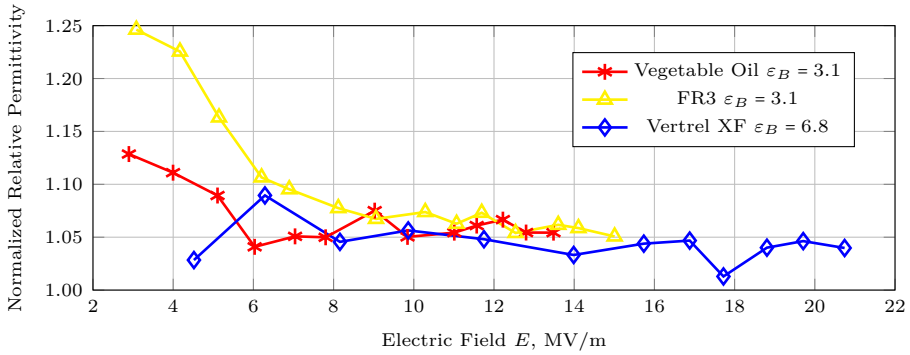

(b)

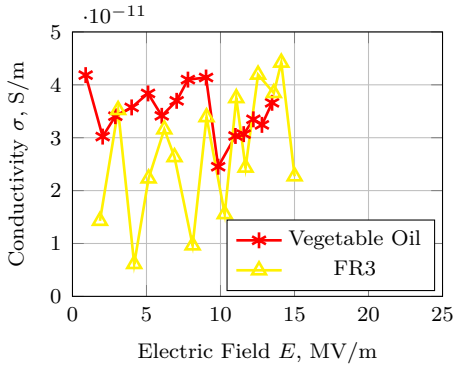

(c)

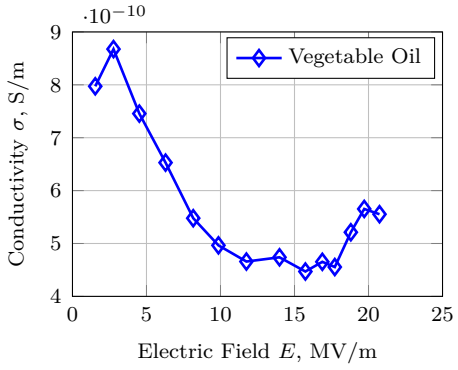

(d)

Figure 4.8: Measured normal pressure test results: (a) pressure vs. electric field, (b) normalized relative permittivity vs. electric field, (c) conductivity vs. electric field for vegetable oil and FR3, (d) conductivity vs. electric field for Vertrel XF.

a significant impact in pressure. Here the oils are able to facilitate 200% more force than vacuum for a given voltage. FR3 and vegetable oil provide nearly identical amounts of pressure but FR3 possesses greater breakdown strength, thus it is slightly better but still lags Vertrel XF significantly.

Using the measured data, the permittivity is normalized and plotted as a function of electric field in Figure 4.8b. As expected, the permittivity tends to decrease as the electric field increases, i.e. the dielectrics exhibit some degree of saturation. Machine design concepts developed for *B-H* curves may directly apply to *D-E* curves although not as pronounced; (especially for Vertrel XF) the saturation phenomenon found in material here is subtle. Actually this is good for implementing dielectrics in electrostatic actuators or machines because the dielectrics can be pushed to breakdown conditions while maintaining force capability. Contrarily, saturation in magnetic systems also cause serious loss problems, which are inherently diminished in electrostatic systems.

Figures 4.8c and 4.8d plot the calculated equivalent conductivity (with $g = 0.3175\,\text{mm}$ gap and $A = 0.00342\,\text{m}^2$ facing area) as a function of the electric field. This conductance determines leakage current in the dielectric, i.e. system conduction loss. Vegetable oil and FR3 have the same level of conductivity which is ~ 30x lower than Vertrel XF although all three are good insulators. Ultimately it will be a combination of factors that determine a liquid's merit in a particular application. The segmentation of losses (e.g. conduction loss, dielectric loss, viscous drag loss) should be studied in detail to further facilitate the ground work of competitive design of electrostatic actuators and machines.

Shear Stress Measurement

The objective of this test stand is to solidify a general relationship between the relative magnitudes of electric pressure and shear stress. The measured shear force using a vegetable oil dielectric is plotted along the FE and analytical modeled forces in Figure 4.9. All three force curves correlate with few deviations. Small deviations in the measured data are suspected to be the result of vibration interference caused by a mechanically noisy laboratory environment. For the vegetable oil, the measured relative permittivity of $\varepsilon_r = 3.0$ is well within measurement error. The highest force measured in this test stand was 4.1 N. Dividing this force by the total fin surface area of the

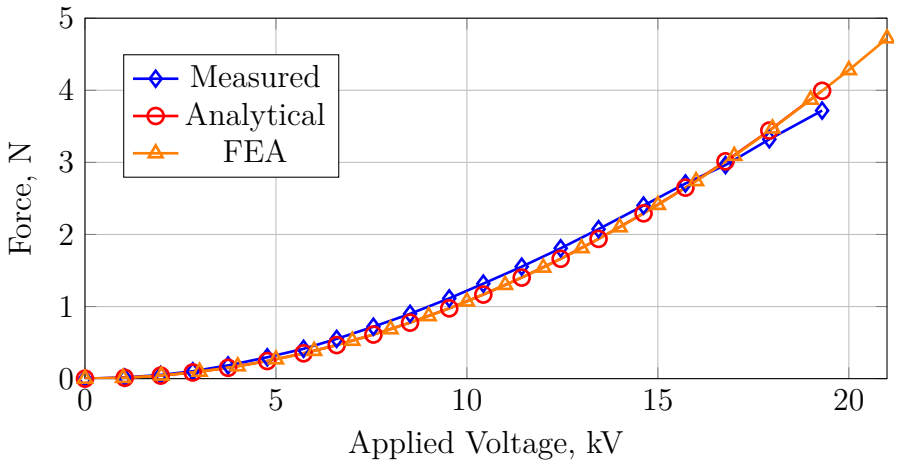

Figure 4.9: Shear force vs. applied voltage for vegetable oil dielectric.

top comb, the average achieved shear stress on the surface of the fins is 151 Pa or 0.021 psi. The average field normal to and between fin faces, i.e. away from their leading edge, is $E = 10\,\text{kV/mm}$. This calculated field strength is in line with the field predicted by the FE plot in Figure 4.6b. The resulting pressure (normal force) is 1328 Pa or 0.193 psi. The ratio of pressure to shear is $9.2:1$, which correlates with the design "rule of thumb" discussed earlier. This generally suggests that electric field forces for common electrode shapes such as a combs, exhibit similar pressure to shear ratios as magnetic machines. Although this inference is made on an isolated experimental result with a specific geometry, it establishes an initial bridge between well known design practices in magnetic machinery and emerging electrostatics.

Measurement Discussion

Table 4.3 documents the test results from both test stands. The following observation may be made:

- Significant electric pressure/shear may be generated with dielectric fluids. Vertrel XF is a promising dielectric that possesses both high breakdown strength and high permittivity at the same time. Vertrel XF achieved a pressure of ~ 2 psi, which is 7x greater than vacuum for the same voltage and 300x greater than the capability of air.

- While the tested dielectric fluids exhibit saturation, the degree is relatively small compared to

the behavior of ferromagnetic materials. Saturation effects will likely increase for dielectric fluids with increasing relative permittivity.

- The shear stress stand experimentally demonstrates (at a general level) that the normal vs tangential field design challenges magnetic machine designers face directly applies to electrostatics as well. To generate shear, there must be nomal and tangential field components and the normal component tends to dominate by an order of magnitude.

- The breakdown field strengths of the fluids do not match the values referenced in Table 4.1, they are lower. The breakdown of a fluid is highly dependent on electrode material, shape, size, surface finish, time, atomospheric conditions, etc.; thus results vary among experimental test stands.

4.6 Summary

This chapter discusses the fundamental of electric and magnetic forces and highlights their characteristics with the Maxwell stress tensor. Dielectric liquids are suggested for use in electrostatic actuators and machinery to alleviate the implementation issues associated with vacuum while simultaneously increasing force per volt via greater permittivity. This suggestion is based on an application where the incurred viscous drag of the liquid is acceptable. The increase in permittivity combined with high stator/rotor surface afforded by electrostatic machines suggests competitive macro-scale electrostatic machines may be possible in niche applications. Two test stands were constructed to evaluate electric pressure and shear between electrodes immersed in a dielectric liquid. Two dielectric oils and a commercial solvent were tested, vegetable oil, FR3, and Vertrel XF respectively. Vertrel XF achieved a pressure of ~ 2 psi, which is 7x greater than vacuum for the same voltage and 300x greater than the capability of air. The relative permittivity and saturation properties were extracted from the measured data to serve as a future machine design reference. The shear stress test stand experimentally demonstrates (at a general level) that the normal vs. tangential field design challenges magnetic machine designers face directly applies to electrostatics as well. To generate shear, there must be normal and tangential field components but the normal

Table 4.3: Measured Dielectric Properties from Both Pressure and Shear Test Stands.

	Dielectrics	Pressure Test Stand				Shear Test Stand		
		E_{bk}, MV/m	ε_r	$p_{e\,\max}$, psi	σ, S/m	E_{avg}, MV/m	ε_r	$\sigma_{e\,\max}$, psi
✓	**Vegetable Oil**	13.48	3.39	0.3814	$\approx 3.3 \times 10^{-11}$	10.1	3.08	0.021
✓	**FR3**	15.01	3.39	0.4708	$\approx 2.0 \times 10^{-11}$	9.65	3.11	0.020
✓	**Vertrel XF**	20.74	7.10	1.9524	$\approx 5.5 \times 10^{-10}$	/	/	/

component tends to dominate by $1 \sim 2$ orders of magnitude. The ratio of pressure to shear was measured to be $9.2 : 1$ for the specific electrode geometry herein. This work constitutes a first step towards modern materials capable of higher electric shear stress for the purpose of competitive macro-scale electrostatic actuators and machinery.

5 THREE PHASE ELECTROSTATIC MACHINE DQ-AXIS MODEL

Perhaps the lateness in recognition by "the establishment" was due to the nature of his contribution. It was not a new machine, not yet a new method of analysis. It was a new structure particularly well suited to facilitate analysis and application to new problems. It has been said that it was a ladder that others could climb and that it was the opening of a gate so that others could enter and cultivate the garden. Thus, it was appreciated immediately by the young engineers at the bottom of the ladder long before those at the top realized what was going on. "Park" was a household word among the young engineers and students long before any awards came.

— Charles Concordia (1996)

5.1 Introduction

Ever since Robert H. Park proposed the two reaction theory for synchronous machine [102, 103], electric machine, power electronics and power system has staged into a new era. Specifically for electric machine design, dq-axis model guides the machine designer to segregate the torque into field torque, saliency torque and induction torque, even though physically all of these three components are part of the general Lorentz force.

Specifically for the electrostatic machines, dq-axis models have been derived from field models of traveling potential wave [30] in the stationary reference frame for the induction type [50] and as equivalences of power electronic inverters or synchronous condensers in power systems for the synchronous type [104]. However, they are not developed from the physical capacitance of actual machines or with the dielectric fluid considered, both of which are crucial for machine designs and controls.

It is the intent of the author to apply the dq-axis equivalent circuit model of the electrostatic synchronous machine to the design process, i.e. to be ultimately connected with the dielectric liquid, the machine structure and the optimization routine. In this chapter, a generalized dq-axis model will be developed for both electrostatic synchronous and induction machines starting from

basic terminal equations of a three phase electrostatic synchronous machine equipped with field excitation and dampers. The dualities between three phase magnetic and electrostatic machines are then revealed by comparing the equivalent circuits and the key capacitance quantities are identified for optimization work. Furthermore, one more layer of complexity in the *dq*-axis model due to the non-ideal liquid insulation is explored. The model and torque equations are validated with FEA models of the two types of machines respectively.

5.2 *dq*-Axis Modeling of Electrostatic Synchronous Machine

Similar to a traditional electromagnetic synchronous machine, a three phase electrostatic synchronous machine equipped with field excitation and dampers can be abstracted as a set of three phase stator electrodes, two out of phase rotor electrodes and dielectric damping insulations, the latter two of which are shown separately in Figure 5.1a and Figure 5.1b. There are three reasons that they are not combined together:

- neither previous researchers nor the author has built one combining all three torque mechanisms together;
- the modern drive technologies, i.e. field oriented control and direct torque and flux control, would not require a synchronous machine physically equipped with dampers;
- the dampers are included for a more general derivation, the result of which can also be reduced to the *dq*-axis model of the electrostatic induction machine.

It is interesting that in an electromagnetic machine, a return winding is necessary for the stator phase but not for the rotor phase, while it is reversed in an electrostatic machine (return electrodes in this case) referring to Figure 5.1a. Specifically for the electrostatic induction machine, the little resistors connecting the insulation and grounded shaft surfaces in Figure 5.1b are intended to represent the equivalent lagging or leading induction effect.

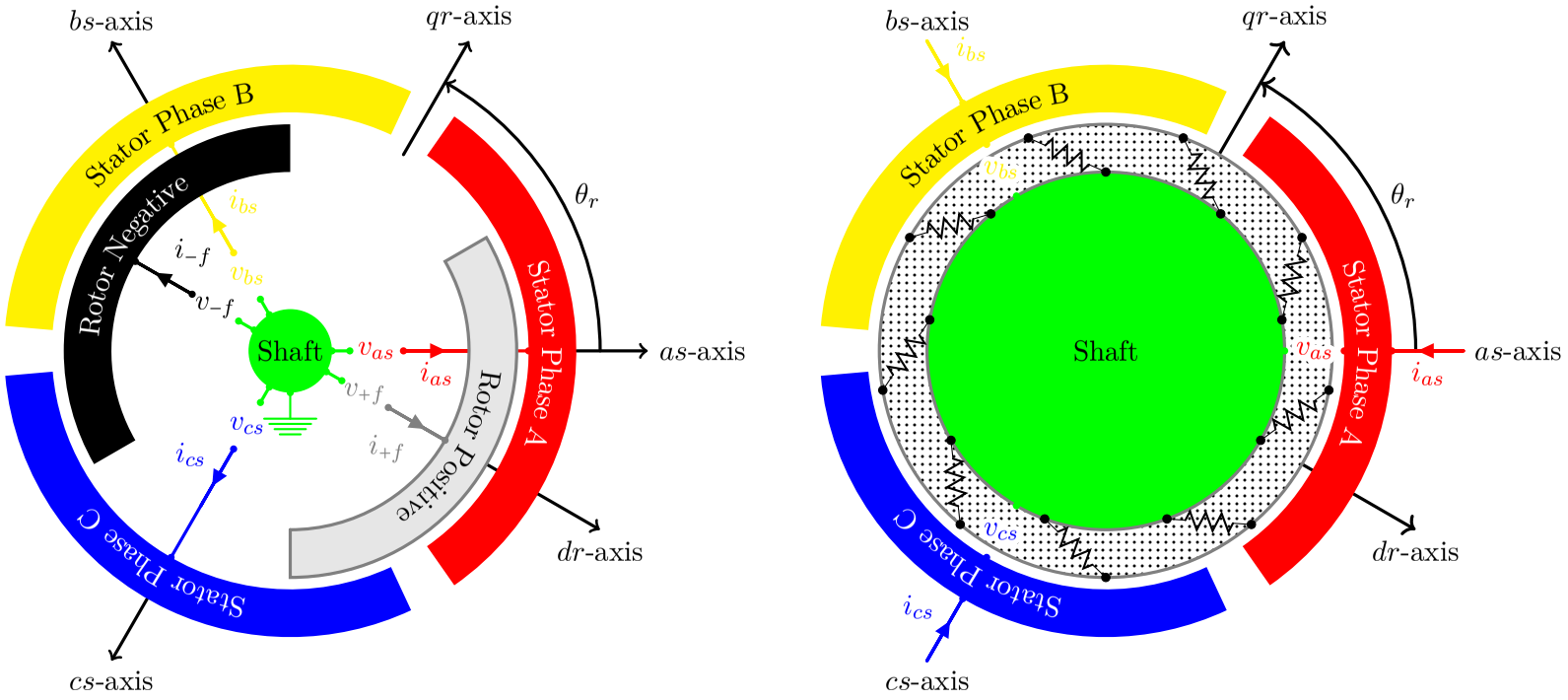

Figure 5.1: (a) The generalized model of three phase electrostatic synchronous machines with field excitation; (b) the generalized model of three phase electrostatic induction machines. Subscripts + and − stands for positive and negative electrode respectively.

Terminal Equations

Contrary to an electromagnetic machine, an electrostatic machine is voltage driven, the current is the quantity used to regulate the relevant voltages, and the charge residing in the electrode vary continuously, all of which lead to the following nine terminal equations (three stator terminals, two field terminals, four damping terminals)

$$\text{stator} \begin{cases} i_{as} = i_{lk,as} + pQ_{as} \\ i_{bs} = i_{lk,bs} + pQ_{bs} \\ i_{cs} = i_{lk,cs} + pQ_{cs} \end{cases} \quad \text{field} \begin{cases} i_{+f} = i_{lk,+f} + pQ_{+f} \\ i_{-f} = i_{lk,-f} + pQ_{-f} \end{cases} \tag{5.1}$$

$$d\text{-axis damper} \begin{cases} i_{+d} = i_{lk,+d} + pQ_{+d} \\ i_{-d} = i_{lk,-d} + pQ_{-d} \end{cases} \quad q\text{-axis damper} \begin{cases} i_{+q} = i_{lk,+q} + pQ_{+q} \\ i_{-q} = i_{lk,-q} + pQ_{-q} \end{cases}, \tag{5.2}$$

where p is the derivative operator respect to time and subscript lk denotes the leakage current. Unlike a magnetic machine where the current is confined in the wire, the electrostatic machine does have slightly complex distributive current paths due to the nonzero conductivity of the dielectric liquid residing between the electrodes. Fortunately, due to the duality between the electrostatic field and the static current field (see Section 3.6), the complexity of the dynamics added by the leakage current is manageable as will be seen later. Also notice that the damping terminals are not physically presented in Figure 5.1b. Nevertheless, the potential traveling wave generated by the polarized (induced) charges can be equivalently represented by two phase damping terminals.

The derivation process presented next follows the course notes of ECE 711 lectured in University of Wisconsin-Madison for a general electromagnetic machine. There the derivation starts from calculating the inductance value through winding functions. Correspondingly, the derivation here starts from capacitance and besides, conductance for the leakage terms in eqs. (5.1) and (5.2). Figure 5.2 shows the capacitance/conductance coupling between the terminals and the dampers are not included for simplicity (it would be combinatorial $\binom{9}{2} + 9 = 45$ coupling components as will be seen next). The relationship between charges/leakage current residing in/flowing into each terminal and the terminal voltages can be expressed as the following matrix form through those coupling

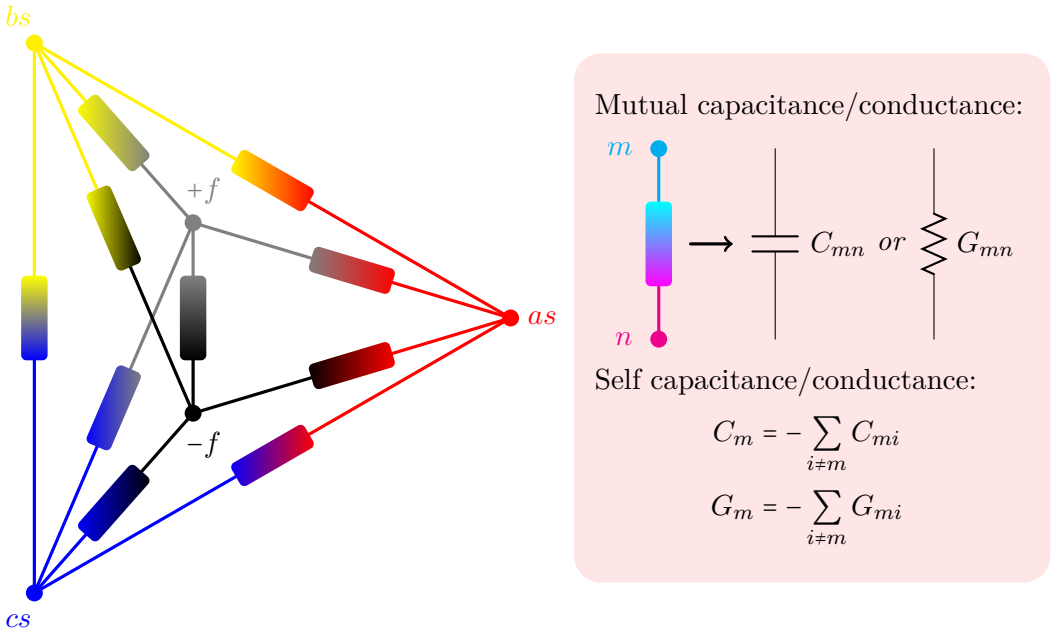

Figure 5.2: Capacitance/conductance coupling in the three phase separately excited electrostatic synchronous machine without damping terminals.

capacitance/conductance:

$$\begin{bmatrix} \kappa_{as} \\ \kappa_{bs} \\ \kappa_{cs} \\ \kappa_{+f} \\ \kappa_{+d} \\ \kappa_{+q} \\ \kappa_{-f} \\ \kappa_{-d} \\ \kappa_{-q} \end{bmatrix} = \begin{bmatrix} A_{as} & A_{asbs} & A_{ascs} & A_{as+f} & A_{as+d} & A_{as+q} & A_{as-f} & A_{as-d} & A_{as-q} \\ A_{bsas} & A_{bs} & A_{bscs} & A_{bs+f} & A_{bs+d} & A_{bs+q} & A_{bs-f} & A_{bs-d} & A_{bs-q} \\ A_{csas} & A_{csbs} & A_{cs} & A_{cs+f} & A_{cs+d} & A_{cs+q} & A_{cs-f} & A_{cs-d} & A_{cs-q} \\ A_{+fas} & A_{+fbs} & A_{+fcs} & A_{+f} & A_{+f+d} & A_{+f+q} & A_{+f-f} & A_{+f-d} & A_{+f-q} \\ A_{+das} & A_{+dbs} & A_{+dcs} & A_{+d+f} & A_{+d} & A_{+d+q} & A_{+d-f} & A_{+d-d} & A_{+d-q} \\ A_{+qas} & A_{+qbs} & A_{+qcs} & A_{+q+f} & A_{+q+d} & A_{+q} & A_{+q-f} & A_{+q-d} & A_{+q-q} \\ A_{-fas} & A_{-fbs} & A_{-fcs} & A_{-f+f} & A_{-f+d} & A_{-f+q} & A_{-f} & A_{-f-d} & A_{-f-q} \\ A_{-das} & A_{-dbs} & A_{-dcs} & A_{-d+f} & A_{-d+d} & A_{-d+q} & A_{-d-f} & A_{-d} & A_{-d-q} \\ A_{-qas} & A_{-qbs} & A_{-qcs} & A_{-q+f} & A_{-q+d} & A_{-q+q} & A_{-q-f} & A_{-q-d} & A_{-q} \end{bmatrix} \cdot \begin{bmatrix} v_{as} \\ v_{bs} \\ v_{cs} \\ v_{+f} \\ v_{+d} \\ v_{+q} \\ v_{-f} \\ v_{-d} \\ v_{-q} \end{bmatrix}, \quad (5.3)$$

where A may represent C for capacitance or G for conductance and correspondingly κ may represent Q for charge or i_{lk} for leakage current.

Capacitance/Conductance Profile Definition

As mentioned in several places, the analytical calculation of the capacitance/conductance is almost impossible even for slightly complicated systems. To circumvent this, their profiles are fabricated according to waveforms obtained from FEA. Due to the symmetrical structure, the capacitance/conductance in eq. (5.3) can be defined with a handful parameters (ignoring harmonics not contributing any steady state average torque except for the 3rd harmonics of the rotor side capacitance, which is used as an example to show how higher harmonics may disappear in the derivation) as follows.

$$\begin{aligned}
\text{stator self:} \quad & A_{as} = A_{ss0} - A_{ss2}\cos(2\theta_r), \xrightarrow{-2\pi/3} A_{bs}, \xrightarrow{+2\pi/3} A_{cs} \\
\text{rotor field self:} \quad & A_{+f} = A_{fs0} - A_{fs3}\sin(3\theta_r), \xrightarrow{+\pi} A_{-f} \\
d\text{-axis damper self:} \quad & A_{+d} = A_{ds0} - A_{ds3}\sin(3\theta_r), \xrightarrow{+\pi} A_{-d} \\
q\text{-axis damper self:} \quad & A_{+q} = A_{qs0} + A_{qs3}\sin(3\theta_r), \xrightarrow{+\pi} A_{-q} \\
\text{stator mutual:} \quad & A_{bscs} = -(A_{sm0} + A_{sm2}\cos(2\theta_r)), \xrightarrow{-2\pi/3} A_{csas}, \xrightarrow{+2\pi/3} A_{asbs} \\
\text{stator-rotor field mutual:} \quad & A_{as+f} = -(A_{sfm0} + A_{sfm1}\sin(\theta_r)), \xrightarrow{+2\pi/3} A_{bs+f}, \xrightarrow{-2\pi/3} A_{cs+f} \\
& \qquad \xrightarrow{+\pi} A_{as-f}, \xrightarrow{-\pi/3} A_{bs-f}, \xrightarrow{+\pi/3} A_{cs-f} \\
\text{stator-}d\text{-axis damper mutual:} \quad & A_{as+d} = -(A_{sdm0} + A_{sdm1}\sin(\theta_r)), \xrightarrow{+2\pi/3} A_{bs+d}, \xrightarrow{-2\pi/3} A_{cs+d} \\
& \qquad \xrightarrow{+\pi} A_{as-d}, \xrightarrow{-\pi/3} A_{bs-d}, \xrightarrow{+\pi/3} A_{cs-d} \\
\text{stator-}q\text{-axis damper mutual:} \quad & A_{as+q} = -(A_{sqm0} + A_{sqm1}\cos(\theta_r)), \xrightarrow{+2\pi/3} A_{bs+q}, \xrightarrow{-2\pi/3} A_{cs+q} \\
& \qquad \xrightarrow{+\pi} A_{as-q}, \xrightarrow{-\pi/3} A_{bs-q}, \xrightarrow{+\pi/3} A_{cs-q} \\
\text{rotor field-}d\text{-axis damper mutual:} \quad & A_{+f+d} = A_{-f-d} = -A_{fdm+0},\ A_{+f-d} = A_{-f+d} = -A_{fdm-0} \\
\text{rotor field-}q\text{-axis damper mutual:} \quad & A_{+f+q} = A_{-f-q} = -A_{fqm+0},\ A_{+f-q} = A_{-f+q} = -A_{fqm-0} \\
d\text{-}q\text{-axis damper mutual:} \quad & A_{+d+q} = A_{-d-q} = -A_{dqm+0},\ A_{+d-q} = A_{-d+q} = -A_{dqm-0} \\
\text{rotor field/damper mutual:} \quad & A_{+f-f} = -A_{fm0},\ A_{+d-d} = -A_{dm0},\ A_{+q-q} = -A_{qm0}
\end{aligned}$$

Among these definitions,

- A may represent C for capacitance or G for conductance;

- $\overset{\varphi}{\Longrightarrow} A_{xy}$ means A_{xy} is obtained by shifting the leftmost capacitance/conductance waveform a phase angle of φ. For example, $A_{bs} = A_{ss0} - A_{ss2}\cos(2\theta_r + 2\pi/3)$ and $A_{bs+f} = -(A_{sfm0} + A_{sfm1}\sin(\theta_r - 2\pi/3))$;
- $A_{yx} = A_{xy}$ is omitted since capacitance/conductance matrix is symmetrical;
- Signs and phases are manipulated that the newly introduced variables on the right hand side are positive, except for the 3rd harmonics of the rotor side self capacitance (i.e., A_{fs3}, A_{ds3} and A_{qs3}), which may be negative depending on the design. All the others can be quickly verified on mind;
- Subscripts in these newly introduced variables are self-clear and *ordered* that
  - s, f, d and q are used to identify stator, rotor field and dampers respectively;
  - s and m are used to distinguish self- and mutual-capacitance/conductance respectively;
  - $+$ and $-$ are used to differentiate pairs between rotor electrodes including dampers;
  - $0, 1, 2, 3$ represent the spatial harmonic order of the given capacitance/conductance.

Vector Form of the Stator Terminal Equations

The stator terminal equations in eq. (5.1) can be written in a compact vector form

$$i_{abcs} = i_{lk,abcs} + pQ_{abcs}, \quad \textit{where } f_{abcs} = \begin{bmatrix} f_{as} \\ f_{bs} \\ f_{cs} \end{bmatrix} \textit{ and } f \textit{ may stands for } i,\ v,\ \kappa,\ i_{lk},\ Q. \tag{5.4}$$

Substituting the first three rows in eq. (5.3) and the corresponding capacitance/conductance expressions defined in the last section into the charge vector,

$$\kappa_{abcs} = \begin{bmatrix} \kappa_{as} \\ \kappa_{bs} \\ \kappa_{cs} \end{bmatrix} = \begin{bmatrix} A_{ss0} & -A_{sm0} & -A_{sm0} \\ -A_{sm0} & A_{ss0} & -A_{sm0} \\ -A_{sm0} & -A_{sm0} & A_{ss0} \end{bmatrix} \begin{bmatrix} v_{as} \\ v_{bs} \\ v_{cs} \end{bmatrix}$$

$$
\begin{aligned}
&- A_{ss2}\begin{bmatrix} \cos(2\theta_r) & 0 & 0 \\ 0 & \cos(2\theta_r+\frac{2\pi}{3}) & 0 \\ 0 & 0 & \cos(2\theta_r-\frac{2\pi}{3}) \end{bmatrix}\begin{bmatrix} v_{as} \\ v_{bs} \\ v_{cs} \end{bmatrix} \\
&- A_{sm2}\begin{bmatrix} 0 & \cos(2\theta_r-\frac{2\pi}{3}) & \cos(2\theta_r+\frac{2\pi}{3}) \\ \cos(2\theta_r-\frac{2\pi}{3}) & 0 & \cos(2\theta_r) \\ \cos(2\theta_r+\frac{2\pi}{3}) & \cos(2\theta_r) & 0 \end{bmatrix}\begin{bmatrix} v_{as} \\ v_{bs} \\ v_{cs} \end{bmatrix} \\
&- \begin{bmatrix} A_{sfm1} & 0 & 0 \\ 0 & A_{sdm1} & 0 \\ 0 & 0 & A_{sqm1} \end{bmatrix}\begin{bmatrix} \sin(\theta_r) & \sin(\theta_r) & \cos(\theta_r) \\ \sin(\theta_r-\frac{2\pi}{3}) & \sin(\theta_r-\frac{2\pi}{3}) & \cos(\theta_r-\frac{2\pi}{3}) \\ \sin(\theta_r+\frac{2\pi}{3}) & \sin(\theta_r+\frac{2\pi}{3}) & \cos(\theta_r+\frac{2\pi}{3}) \end{bmatrix}\begin{bmatrix} v_{fr} \\ v_{dr} \\ v_{qr} \end{bmatrix} \\
&- \begin{bmatrix} A_{sfm0} & A_{sfm0} & A_{sdm0} & A_{sdm0} & A_{sqm0} & A_{sqm0} \\ A_{sfm0} & A_{sfm0} & A_{sdm0} & A_{sdm0} & A_{sqm0} & A_{sqm0} \\ A_{sfm0} & A_{sfm0} & A_{sdm0} & A_{sdm0} & A_{sqm0} & A_{sqm0} \end{bmatrix}\begin{bmatrix} v_{+f} \\ v_{-f} \\ v_{+d} \\ v_{-d} \\ v_{+q} \\ v_{-q} \end{bmatrix}, \qquad (5.5)
\end{aligned}
$$

where $v_{fr} = v_{+f} - v_{-f}$,$v_{dr} = v_{+d} - v_{-d}$ and $v_{qr} = v_{+q} - v_{-q}$. The significance of eq. (5.5) is that the balanced and the symmetrical voltages are grouped together by separating constant capacitance matrices and position dependent matrices.

Complex Vector Form of the Stator Terminal Equation

Define complex vectors

$$a = e^{j\frac{2\pi}{3}} \qquad (5.6)$$

and

$$\underline{f}_{abcs} = \frac{2}{3}(f_{as} + af_{bs} + a^2 f_{cs}). \qquad (5.7)$$

The definition of eq. (5.7) has a particular meaning in the machine analysis. In an electromagnetic machine, $\underline{i}_{abcs}$ is a traveling wave which stimulates and persists the mechanical motion. Correspondingly in an electrostatic machine, $\underline{v}_{abcs}$ is the one playing the role. Applying eq. (5.7) on the vector

form terminal eq. (5.4),

$$\underline{i}_{abcs} = \frac{2}{3}(i_{as} + a i_{bs} + a^2 i_{cs}) = \frac{2}{3}(i_{lk,as} + a\, i_{lk,bs} + a^2 i_{lk,cs}) + p\frac{2}{3}(Q_{as} + aQ_{bs} + a^2 Q_{cs})$$
$$= \underline{i}_{lk,abcs} + p\underline{Q}_{abcs}. \quad (5.8)$$

Equation (5.8) implies that $\underline{i}_{abcs}$ and $\underline{Q}_{abcs}$ are also traveling waves since the above differential equation is linear and the source $\underline{v}_{abcs}$ (from eq. (5.3) $[i_{lk,k_1}] = [G_{k_1k_2}] \cdot [v_{k_2}]$ where $k_1 \in \{as, bs, cs\}$ and $k_2 \in \{as, bs, cs, +f, +d, +q, -f, -d, -q\}$) is trigonometric. Furthermore, when the source $\underline{v}_{abcs}$ in the stationary reference frame is traveling with a constant speed in time and a constant amplitude in space, $\underline{v}_{abcs}$, $\underline{i}_{lk,abcs}$, $\underline{i}_{abcs}$ and $\underline{Q}_{abcs}$ are all constant observing from the rotor reference frame. The analysis seems to naturally falls into the rotor reference frame. Multiplying both sides of eq. (5.8) by the rotating vector $e^{-j\theta_r}$,

$$e^{-j\theta_r}\underline{i}_{abcs} = e^{-j\theta_r}\underline{i}_{lk,abcs} + e^{-j\theta_r}p\underline{Q}_{abcs} = e^{-j\theta_r}\underline{i}_{lk,abcs} + p(e^{-j\theta_r}\underline{Q}_{abcs}) + j\omega_r(e^{-j\theta_r}\underline{Q}_{abcs}), \quad (5.9)$$

and defining

$$\underline{f}^r_{qds} = f^r_{qs} - j f^r_{ds} = \underline{f}_{abcs} e^{-j\theta_r}, \quad (5.10)$$

the stator terminal eq. (5.8) turns into

$$\underline{i}^r_{qds} = \underline{i}^r_{lk,qds} + p\underline{Q}^r_{qds} + j\omega_r \underline{Q}^r_{qds}, \quad (5.11)$$

where $\omega_r = p\theta_r$. The third term in eq. (5.11) is unexpected but reasonable because the second term picks up whatever the dynamics happening in the rotor reference frame and the third term captures the remaining dynamics which is relatively stationary to the rotor reference frame due to the transformation.

To turn κ_{abcs} in eq. (5.5) into $\underline{\kappa}_{abcs}$ and then $\underline{\kappa}^r_{qds}$, each trigonometrical function in eq. (5.5) is decomposed into a sum of two complex vectors using a defined in eq. (5.6),

$$\begin{bmatrix} \kappa_{as} \\ \kappa_{bs} \\ \kappa_{cs} \end{bmatrix} = \begin{bmatrix} A_{ss0} & -A_{sm0} & -A_{sm0} \\ -A_{sm0} & A_{ss0} & -A_{sm0} \\ -A_{sm0} & -A_{sm0} & A_{ss0} \end{bmatrix} \begin{bmatrix} v_{as} \\ v_{bs} \\ v_{cs} \end{bmatrix}$$

$$
\begin{aligned}
&-\frac{A_{ss2}}{2}\left\{\begin{bmatrix} e^{j2\theta_r} & 0 & 0 \\ 0 & ae^{j2\theta_r} & 0 \\ 0 & 0 & a^2e^{j2\theta_r} \end{bmatrix}+\begin{bmatrix} e^{-j2\theta_r} & 0 & 0 \\ 0 & a^2e^{-j2\theta_r} & 0 \\ 0 & 0 & ae^{-j2\theta_r} \end{bmatrix}\right\}\begin{bmatrix} v_{as} \\ v_{bs} \\ v_{cs} \end{bmatrix} \\
&-\frac{A_{sm2}}{2}\left\{\begin{bmatrix} 0 & a^2e^{j2\theta_r} & ae^{j2\theta_r} \\ a^2e^{j2\theta_r} & 0 & e^{j2\theta_r} \\ ae^{j2\theta_r} & e^{j2\theta_r} & 0 \end{bmatrix}+\begin{bmatrix} 0 & ae^{-j2\theta_r} & a^2e^{-j2\theta_r} \\ ae^{-j2\theta_r} & 0 & e^{-j2\theta_r} \\ a^2e^{-j2\theta_r} & e^{-j2\theta_r} & 0 \end{bmatrix}\right\}\begin{bmatrix} v_{as} \\ v_{bs} \\ v_{cs} \end{bmatrix} \\
&\qquad -\frac{A_{sfm1}}{2j}\left\{\begin{bmatrix} e^{j\theta_r} \\ a^2e^{j\theta_r} \\ ae^{j\theta_r} \end{bmatrix}-\begin{bmatrix} e^{-j\theta_r} \\ ae^{-j\theta_r} \\ a^2e^{-j\theta_r} \end{bmatrix}\right\}\cdot v_{fr} \\
&\qquad -\frac{A_{sdm1}}{2j}\left\{\begin{bmatrix} e^{j\theta_r} \\ a^2e^{j\theta_r} \\ ae^{j\theta_r} \end{bmatrix}-\begin{bmatrix} e^{-j\theta_r} \\ ae^{-j\theta_r} \\ a^2e^{-j\theta_r} \end{bmatrix}\right\}\cdot v_{dr} \\
&\qquad -\frac{A_{sqm1}}{2}\left\{\begin{bmatrix} e^{j\theta_r} \\ a^2e^{j\theta_r} \\ ae^{j\theta_r} \end{bmatrix}+\begin{bmatrix} e^{-j\theta_r} \\ ae^{-j\theta_r} \\ a^2e^{-j\theta_r} \end{bmatrix}\right\}\cdot v_{qr} \\
&\qquad -\begin{bmatrix} A_{sfm0} & A_{sfm0} & A_{sdm0} & A_{sdm0} & A_{sqm0} & A_{sqm0} \\ A_{sfm0} & A_{sfm0} & A_{sdm0} & A_{sdm0} & A_{sqm0} & A_{sqm0} \\ A_{sfm0} & A_{sfm0} & A_{sdm0} & A_{sdm0} & A_{sqm0} & A_{sqm0} \end{bmatrix}\begin{bmatrix} v_{+f} \\ v_{-f} \\ v_{+d} \\ v_{-d} \\ v_{+q} \\ v_{-q} \end{bmatrix}. \qquad (5.12)
\end{aligned}
$$

Multiplying the second row of eq. (5.12) by a and the third row by a^2 and adding the result to the first row, the following complex vector is obtained:

$$
\begin{aligned}
\kappa_{as}+a\kappa_{bs}+a^2\kappa_{cs} = (A_{ss0}+A_{sm0})(v_{as}+av_{bs}+a^2v_{cs}) - (\frac{A_{ss2}}{2}+A_{sm2})e^{j2\theta_r}(v_{as}+a^2v_{bs}+av_{cs}) \\
-\frac{3A_{sfm1}}{2j}e^{j\theta_r}v_{fr}-\frac{3A_{sdm1}}{2j}e^{j\theta_r}v_{dr}-\frac{3A_{sqm1}}{2}e^{j\theta_r}v_{qr}. \qquad (5.13)
\end{aligned}
$$

Last line in eq. (5.12) vanishes in the resultant eq. (5.13) due to the identity $1+a+a^2=0$. Applying

the definition of eq. (5.7) on eq. (5.13),

$$\underline{\kappa}_{abcs} = (A_{ss0} + A_{sm0})\underline{v}_{abcs} - (\frac{A_{ss2}}{2} + A_{sm2})e^{j2\theta_r}\underline{v}^*_{abcs} + jA_{sfm1}e^{j\theta_r}v_{fr} + jA_{sdm1}e^{j\theta_r}v_{dr} - A_{sqm1}e^{j\theta_r}v_{qr}. \quad (5.14)$$

Rotating the complex vector *clockwise* by θ_r degree (eq. (5.10)),

$$\underline{\kappa}^r_{qds} = e^{-j\theta_r}\underline{\kappa}_{abcs} = (A_{ss0} + A_{sm0})\underline{v}^r_{qds} - (\frac{A_{ss2}}{2} + A_{sm2})(\underline{v}^r_{qds})^* + jA_{sfm1}v_{fr} + jA_{sdm1}v_{dr} - A_{sqm1}v_{qr}. \quad (5.15)$$

Complex Vector Form of the Rotor Terminal Equation

Since the positive and negative rotor electrodes are just π radians out of phase, rotor terminal equations in eqs. (5.1) and (5.2) can be slimmed down to

$$\text{rotor} \begin{cases} i_{fr} = i_{lk,fr} + pQ_{fr} \\ i_{dr} = i_{lk,dr} + pQ_{dr} \\ i_{qr} = i_{lk,qr} + pQ_{qr} \end{cases},$$

where $\kappa_{fr} = \kappa_{+f} - \kappa_{-f}$, $\kappa_{dr} = \kappa_{+d} - \kappa_{-d}$, $\kappa_{qr} = \kappa_{+q} - \kappa_{-q}$ and again κ may represent Q for charge or i_{lk} for leakage current. Substituting eq. (5.3) and previously defined capacitance/conductance profiles into the new condensed rotor variable κ's,

$$\begin{aligned}
\kappa_{fr} = \kappa_{+f} - \kappa_{-f} = &+ (A_{+fas} - A_{-fas})v_{as} + (A_{+fbs} - A_{-fbs})v_{bs} + (A_{+fcs} - A_{-fcs})v_{cs} \\
&+ (A_{+f+d} - A_{-f+d})v_{+d} + (A_{+f-d} - A_{-f-d})v_{-d} + (A_{+f+q} - A_{-f+q})v_{+q} \\
&+ (A_{+f-q} - A_{-f-q})v_{-q} + (A_{+f-f}v_{-f} - A_{-f+f}v_{+f}) + (A_{+f}v_{+f} - A_{-f}v_{-f}) \\
= &- 2A_{sfm1}\left(\sin(\theta_r)v_{as} + \sin(\theta_r - \frac{2\pi}{3})v_{bs} + \sin(\theta_r + \frac{2\pi}{3})v_{cs}\right) \\
&- (A_{fdm+0} - A_{fdm-0})v_{dr} - (A_{fqm+0} - A_{fqm-0})v_{qr} \\
&+ (A_{fm0} + A_{fs0})v_{fr} - A_{fs3}\sin(3\theta_r)(v_{+f} + v_{-f}), \\
\kappa_{dr} = \kappa_{+d} - \kappa_{-d} = &+ (A_{+das} - A_{-das})v_{as} + (A_{+dbs} - A_{-dbs})v_{bs} + (A_{+dcs} - A_{-dcs})v_{cs} \\
&+ (A_{+d+f} - A_{-d+f})v_{+f} + (A_{+d-f} - A_{-d-f})v_{-f} + (A_{+d+q} - A_{-d+q})v_{+q}
\end{aligned}$$

$$
\begin{aligned}
&+ (A_{+d-q} - A_{-d-q})v_{-q} + (A_{+d-d}v_{-d} - A_{-d+d}v_{+d}) + (A_{+d}v_{+d} - A_{-d}v_{-d}) \\
&= -2A_{sdm1}\left(\sin(\theta_r)v_{as} + \sin(\theta_r - \frac{2\pi}{3})v_{bs} + \sin(\theta_r + \frac{2\pi}{3})v_{cs}\right) \\
&\quad - (A_{fdm+0} - A_{fdm-0})v_{fr} - (A_{dqm+0} - A_{dqm-0})v_{qr} \\
&\quad + (A_{dm0} + A_{ds0})v_{dr} - A_{ds3}\sin(3\theta_r)(v_{+d} + v_{-d}), \\
\kappa_{qr} = \kappa_{+q} - \kappa_{-q} &= + (A_{+qas} - A_{-qas})v_{as} + (A_{+qbs} - A_{-qbs})v_{bs} + (A_{+qcs} - A_{-qcs})v_{cs} \\
&\quad + (A_{+q+f} - A_{-q+f})v_{+f} + (A_{+q-f} - A_{-q-f})v_{-f} + (A_{+q+d} - A_{-q+d})v_{+d} \\
&\quad + (A_{+q-d} - A_{-q-d})v_{-d} + (A_{+q-q}v_{-q} - A_{-q+q}v_{+q}) + (A_{+q}v_{+q} - A_{-q}v_{-q}) \\
&= -2A_{sqm1}\left(\cos(\theta_r)v_{as} + \cos(\theta_r - \frac{2\pi}{3})v_{bs} + \cos(\theta_r + \frac{2\pi}{3})v_{cs}\right) \\
&\quad - (A_{fqm+0} - A_{fqm-0})v_{fr} - (A_{dqm+0} - A_{dqm-0})v_{dr} \\
&\quad + (A_{qm0} + A_{qs0})v_{qr} + A_{qs3}\sin(3\theta_r)(v_{+q} + v_{-q}).
\end{aligned}
$$

If the negative and positive damping terminals are designed to be the same except the phase difference, which is generally true in an electrostatic induction machine, then $A_{fqm+0} = A_{fqm-0}$ and $A_{dqm+0} = A_{dqm-0}$. Applying the same decomposition process done for the stator charge/leakage current vector eq. (5.12), the above three charge/leakage current equations turn into

$$
\begin{aligned}
\kappa_{fr} &= -2A_{sfm1}\left(\sin(\theta_r)v_{as} + \sin(\theta_r - \frac{2\pi}{3})v_{bs} + \sin(\theta_r + \frac{2\pi}{3})v_{cs}\right) \\
&\quad - (A_{fdm+0} - A_{fdm-0})v_{dr} - (A_{fqm+0} - A_{fqm-0})v_{qr} + (A_{fm0} + A_{fs0})v_{fr} - A_{fs3}\sin(3\theta_r)(v_{+f} + v_{-f}) \\
&= -\frac{2A_{sfm1}}{2j}\left((e^{j\theta_r} - e^{-j\theta_r})v_{as} + (a^2e^{j\theta_r} - ae^{-j\theta_r})v_{bs} + (ae^{j\theta_r} - a^2e^{-j\theta_r})v_{cs}\right) \\
&\quad - (A_{fdm+0} - A_{fdm-0})v_{dr} + (A_{fm0} + A_{fs0})v_{fr} \\
&= -\frac{3A_{sfm1}}{2j}((\underline{v}^r_{qds})^* - \underline{v}^r_{qds}) - (A_{fdm+0} - A_{fdm-0})v_{dr} + (A_{fm0} + A_{fs0})v_{fr},
\end{aligned}
$$

$$
\begin{aligned}
\kappa_{dr} &= -2A_{sdm1}\left(\sin(\theta_r)v_{as} + \sin(\theta_r - \frac{2\pi}{3})v_{bs} + \sin(\theta_r + \frac{2\pi}{3})v_{cs}\right) \\
&\quad - (A_{fdm+0} - A_{fdm-0})v_{fr} - (A_{dqm+0} - A_{dqm-0})v_{qr} + (A_{dm0} + A_{ds0})v_{dr} - A_{ds3}\sin(3\theta_r)(v_{+d} + v_{-d}) \\
&= -\frac{2A_{sdm1}}{2j}\left((e^{j\theta_r} - e^{-j\theta_r})v_{as} + (a^2e^{j\theta_r} - ae^{-j\theta_r})v_{bs} + (ae^{j\theta_r} - a^2e^{-j\theta_r})v_{cs}\right) \\
&\quad - (A_{fdm+0} - A_{fdm-0})v_{fr} + (A_{dm0} + A_{ds0})v_{dr}
\end{aligned}
$$

$$= -\frac{3A_{sdm1}}{2j}((\underline{v}^r_{qds})^* - \underline{v}^r_{qds}) - (A_{fdm+0} - A_{fdm-0})v_{fr} + (A_{dm0} + A_{ds0})v_{dr},$$

$$\kappa_{qr} = -2A_{sqm1}\left(\cos(\theta_r)v_{as} + \cos(\theta_r - \frac{2\pi}{3})v_{bs} + \cos(\theta_r + \frac{2\pi}{3})v_{cs}\right)$$
$$- (A_{fqm+0} - A_{fqm-0})v_{fr} - (A_{dqm+0} - A_{dqm-0})v_{dr} + (A_{qm0} + A_{qs0})v_{qr} - A_{qs3}\cos(3\theta_r)(v_{+q} + v_{-q})$$
$$= -\frac{2A_{sqm1}}{2}\left((e^{j\theta_r} + e^{-j\theta_r})v_{as} + (a^2e^{j\theta_r} + ae^{-j\theta_r})v_{bs} + (ae^{j\theta_r} + a^2e^{-j\theta_r})v_{cs}\right)$$
$$+ (A_{qm0} + A_{qs0})v_{qr}$$
$$= -\frac{3A_{sqm1}}{2}((\underline{v}^r_{qds})^* + \underline{v}^r_{qds}) + (A_{qm0} + A_{qs0})v_{qr}.$$

The third harmonic terms are discarded in the above for the following reasons:

- these terms will not contribute any steady state torque due to orthogonality relations between harmonics;
- furthermore, total torque production is optimized when voltage on the positive and the negative electrodes are equally opposite maintained, i.e. $v_{+*} = -v_{-*}$;
- C_{fs3}, C_{ds3} and C_{qs3} are small comparing to the main torque contributing capacitance even if there is any transient torque could be leveraged.

Dynamic Equations

By breaking the vector form into d- and q-axis components, the intermediate dynamic equations for the electrostatic synchronous machine now become

$$\begin{cases} i^r_{qs} = i^r_{lk,qs} + pQ^r_{qs} + \omega_r Q^r_{ds} \\ i^r_{ds} = i^r_{lk,ds} + pQ^r_{ds} - \omega_r Q^r_{qs} \\ i_{fr} = i_{lk,fr} + pQ_{fr} \\ i_{dr} = i_{lk,dr} + pQ_{dr} \\ i_{qr} = i_{lk,qr} + pQ_{qr} \end{cases},$$

where

$$\begin{cases} \kappa^r_{qs} = (A_{ss0} + A_{sm0} - \dfrac{A_{ss2}}{2} - A_{sm2})v^r_{qs} - A_{sqm1}v_{qr} \\ \kappa^r_{ds} = (A_{ss0} + A_{sm0} + \dfrac{A_{ss2}}{2} + A_{sm2})v^r_{ds} - A_{sdm1}v_{dr} - A_{sfm1}v_{fr} \\ \kappa_{fr} = -3A_{sfm1}v^r_{ds} - (A_{fdm+0} - A_{fdm-0})v_{dr} + (A_{fm0} + A_{fs0})v_{fr} \\ \kappa_{dr} = -3A_{sdm1}v^r_{ds} - (A_{fdm+0} - A_{fdm-0})v_{fr} + (A_{dm0} + A_{ds0})v_{dr} \\ \kappa_{qr} = -3A_{sqm1}v^r_{qs} + (A_{qm0} + A_{qs0})v_{qr} \end{cases},$$

and again A may represent C for capacitance or G for conductance and correspondingly κ may represent Q for charge or i_{lk} for leakage current.

Further Simplification of Dynamic Equations

Even though the intermediate dynamic equations look quite close to the ones of the electromagnetic synchronous machine, the capacitance/conductance coefficients are cumbersome and may be more elegantly stated. To obtain a more compact and inviting form factor, capacitance/conductance and fractions are condensed together into the following definitions.

$$\begin{cases} A_{mqs} = A_{sqm1} \\ A_{mds} = A_{sdm1} \\ A_{mfs} = A_{sfm1} \end{cases} \qquad \begin{cases} A_{qs} = A_{ss0} + A_{sm0} - \dfrac{A_{ss2}}{2} - A_{sm2} \\ A_{ds} = A_{ss0} + A_{sm0} + \dfrac{A_{ss2}}{2} + A_{sm2} \\ A_{lqs} = A_{qs} - A_{mqs} \\ A_{lds} = A_{ds} - A_{mds} - A_{mfs} \end{cases} \tag{5.16}$$

$$\begin{cases} A_{fr} = \dfrac{1}{3}(A_{fm0} + A_{fs0}) \\ A_{dr} = \dfrac{1}{3}(A_{dm0} + A_{ds0}) \\ A_{qr} = \dfrac{1}{3}(A_{qm0} + A_{qs0}) \\ A_{mfd} = \dfrac{1}{3}(A_{fdm+0} - A_{fdm-0}) \end{cases} \qquad \begin{cases} A_{lfr} = A_{fr} - A_{mfd} - A_{mfs} \\ A_{ldr} = A_{dr} - A_{mfd} - A_{mds} \\ A_{lqr} = A_{qr} - A_{mqs} \end{cases}, \tag{5.17}$$

and current variables

$$i'_{fr} = \frac{1}{3}i_{fr}, \quad i'_{dr} = \frac{1}{3}i_{dr}, \quad i'_{qr} = \frac{1}{3}i_{qr},$$
$$i'_{lk,fr} = \frac{1}{3}i_{lk,fr}, \quad i'_{lk,dr} = \frac{1}{3}i_{lk,dr}, \quad i'_{lk,qr} = \frac{1}{3}i_{lk,qr},$$

and charge variables

$$Q'_{fr} = \frac{1}{3}Q_{fr}, \quad Q'_{dr} = \frac{1}{3}Q_{dr}, \quad Q'_{qr} = \frac{1}{3}Q_{qr},$$

In the course notes of ECE 711, primes mean stator winding turns referred and the fraction being absorbed. Although there is no direct turns ratio in an electrostatic machine, the convention of using primes remains as a general notation for condensed quantities. Finally, substituting the above defined parameters and variables into the intermediate results, the terminal equations are finally simplified as

$$\begin{matrix}\text{stator referred} \\ \text{dynamic equations in} \\ \text{the rotor reference frame}\end{matrix} \begin{cases} i^r_{qs} = i^r_{lk,qs} + pQ^r_{qs} + \omega_r Q^r_{ds} \\ i^r_{ds} = i^r_{lk,ds} + pQ^r_{ds} - \omega_r Q^r_{qs} \\ i'_{fr} = i'_{lk,fr} + pQ'_{fr} \\ i'_{dr} = i'_{lk,dr} + pQ'_{dr} \\ i'_{qr} = i'_{lk,qr} + pQ'_{qr} \end{cases}, \tag{5.18}$$

where

$$\begin{matrix}\text{stator referred charge or} \\ \text{leakage current equations in} \\ \text{the rotor reference frame} \\ A \leftarrow C,\ \kappa \leftarrow Q \ or \ A \leftarrow G,\ \kappa \leftarrow i_{lk}\end{matrix} \begin{cases} \kappa^r_{qs} = A_{lqs} v^r_{qs} + A_{mqs}(v^r_{qs} - v_{qr}) \\ \kappa^r_{ds} = A_{lds} v^r_{ds} + A_{mds}(v^r_{ds} - v_{dr}) + A_{mfs}(v^r_{ds} - v_{fr}) \\ \kappa'_{fr} = A_{lfr} v_{fr} + A_{mfs}(v_{fr} - v^r_{ds}) + A_{mfd}(v_{fr} - v_{dr}) \\ \kappa'_{dr} = A_{ldr} v_{dr} + A_{mds}(v_{dr} - v^r_{ds}) + A_{mfd}(v_{dr} - v_{fr}) \\ \kappa'_{qr} = A_{lqr} v_{qr} + A_{mqs}(v_{qr} - v^r_{qs}) \end{cases}. \tag{5.19}$$

Equivalent Circuit

According to the terminal equations and charge equations, the dq-axis equivalent circuit can be drawn as Figure 5.3. Conductance G_* is represented by resistance r_* and unsurprisingly each capacitor is parallel paired with a resistor, which is consistent with the three phase model as in eq. (5.3). When there is no damping terminals, the corresponding equivalent circuit is simplified to Figure 5.4. Comparing these to the equivalent circuit of the electromagnetic synchronous machine, beautiful dualities are established. Namely, the parallel and series connection, the voltage source and current source are interchanged respectively. Referring to Figure 5.5, even the d-axis "Y" circuit in the electromagnetic synchronous machine (reduce to the "π" circuit if no damping windings present)

becomes a d-axis "Δ" circuit in the electrostatic synchronous machine. This is not unexpected since the electrostatic field is a potential referenced field. In the electromagnetic synchronous machine, L_m is the shunt where the stator and the rotor current meet and merge, meaning the total sum of the stator and rotor current contribute to the magnetizing flux. However, in an electrostatic synchronous machine, C_{mds}, C_{mqs} and C_{mfs} are the components where the stator and rotor voltage meet and "fight," meaning the total difference of the stator and rotor voltage contribute to the "electrifying" flux. This can also be observed from the minus sign before v_{ds}^r, v_{dr} and v_{fr} in eq. (5.19).

Power & Torque

Using a similar procedure as for the electromagnetic machine, it is not difficult to show that the power input and the torque output equations for the electrostatic synchronous machine are:

$$P_e = \frac{3}{2}\left(v_{ds}^r i_{ds}^r + v_{qs}^r i_{qs}^r\right) + 3v_{fr} i_{fr}', \tag{5.20}$$

$$T_e = \frac{3P}{2}\Im\{\underline{Q}_{qds}^* \underline{v}_{qds}\} = \frac{3P}{2}\left(Q_{ds}^r v_{qs}^r - Q_{qs}^r v_{ds}^r\right), \tag{5.21}$$

where P is the pole number. With the charge defined in eq. (5.19), the torque eq. (5.21) can be expanded as

$$T_e = \frac{3P}{2}[\underbrace{(C_{ds} - C_{qs})v_{qs}^r v_{ds}^r}_{\text{elastance torque}} - \underbrace{C_{mfs} v_{qs}^r v_{fr}}_{\text{field torque}} - \underbrace{C_{mds} v_{qs}^r v_{dr} + C_{mqs} v_{ds}^r v_{qr}}_{\text{induction torque}}]. \tag{5.22}$$

Substituting the capacitance definitions back into eq. (5.22), the three torque components become

$$T_{els} = \frac{3P}{2}(C_{ss2} + 2C_{sm2})v_{qs}^r v_{ds}^r, \quad T_{fld} = -\frac{3P}{2}C_{sfm1} v_{qs}^r v_{fr}, \quad T_{ind} = \frac{3P}{2}(C_{sqm1} v_{ds}^r v_{qr} - C_{sdm1} v_{qs}^r v_{dr}).$$

These equations provide great insight to the machine designer since they reveal which capacitance is important for a particular type of machines. Specifically, for the salient synchronous machine (without damping terminals) presented in Chapter 6, C_{ss2}, C_{sm2} and C_{sfm1} determine the total torque production:

$$T_e = \frac{3P}{2}[(C_{ss2} + 2C_{sm2})v_{qs}^r v_{ds}^r - C_{sfm1} v_{qs}^r v_{fr}]. \tag{5.23}$$

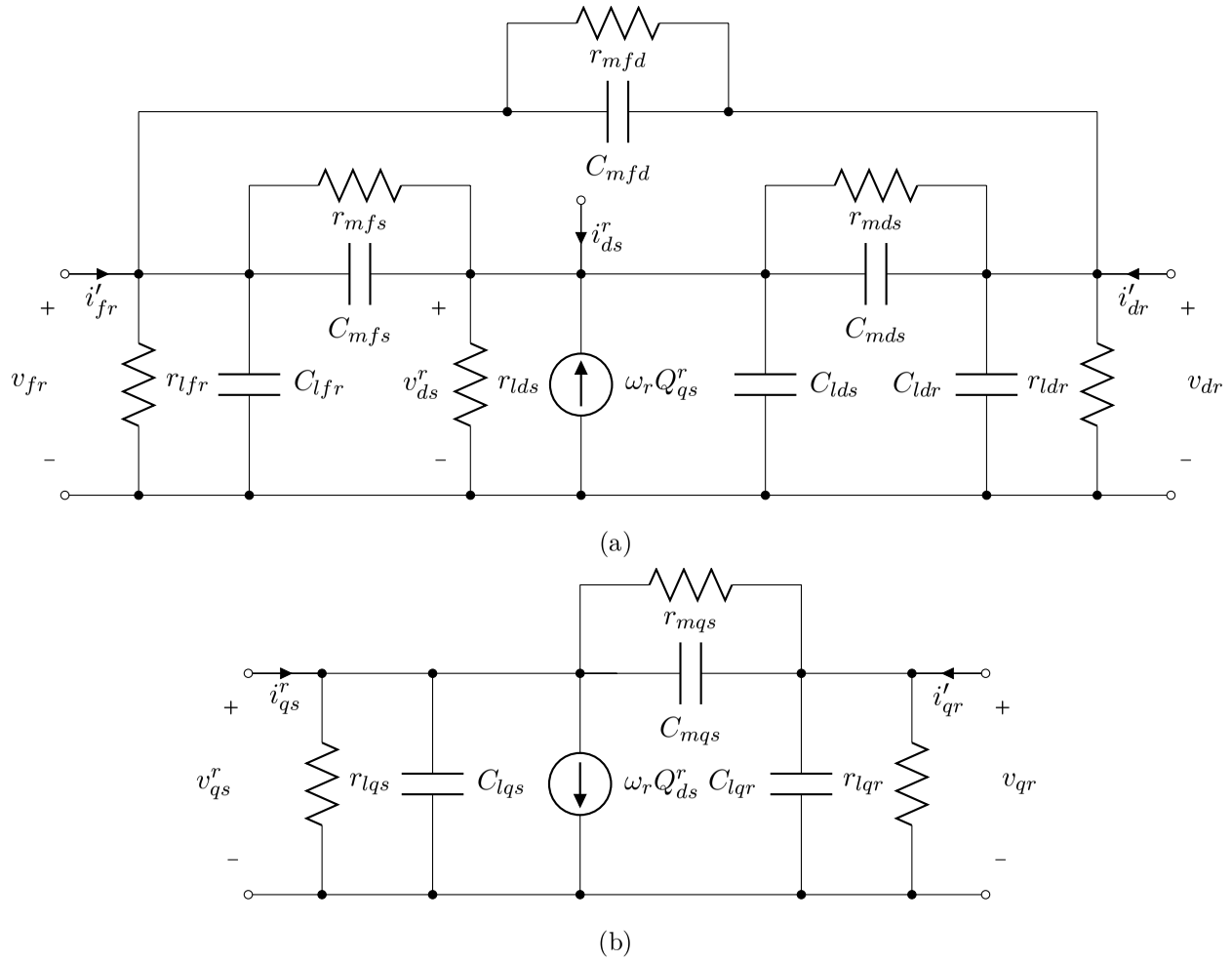

Figure 5.3: *dq*-axis equivalent circuit of the electrostatic synchronous machine with damping terminals.

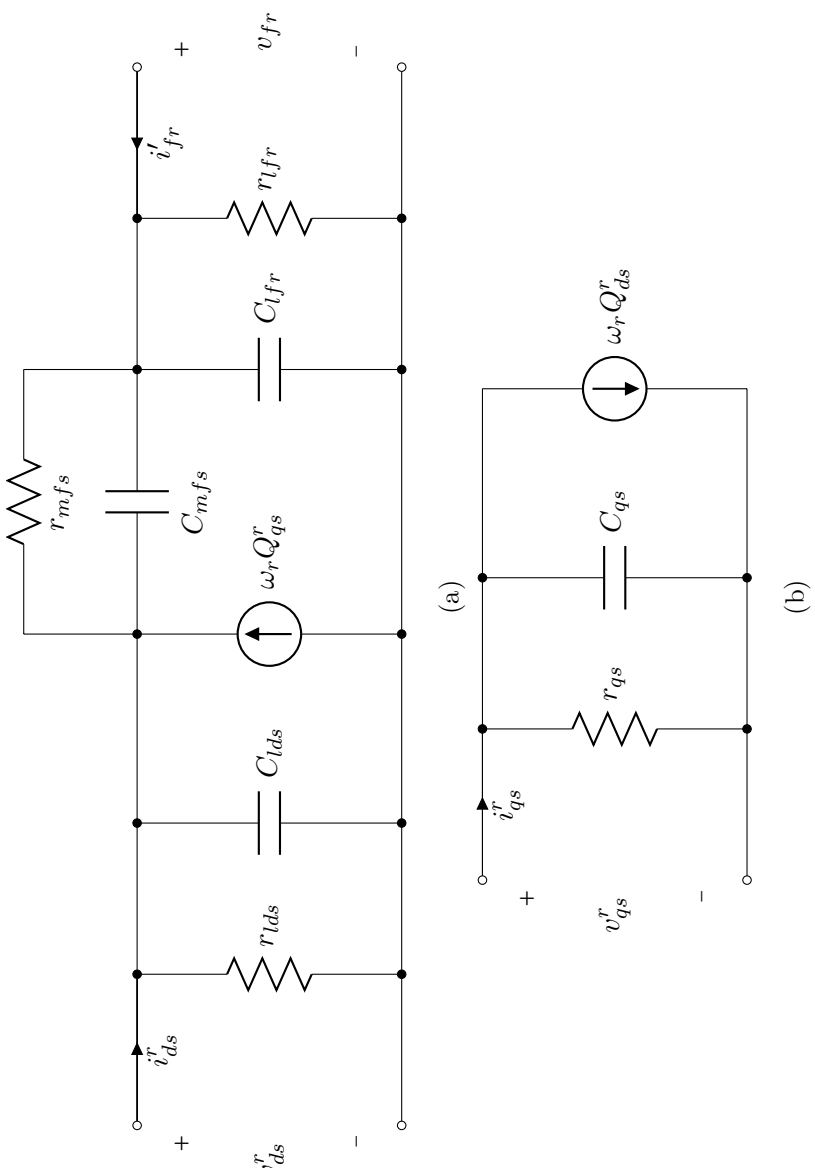

Figure 5.4: dq-axis equivalent circuit of the electrostatic synchronous machine without damping terminals.

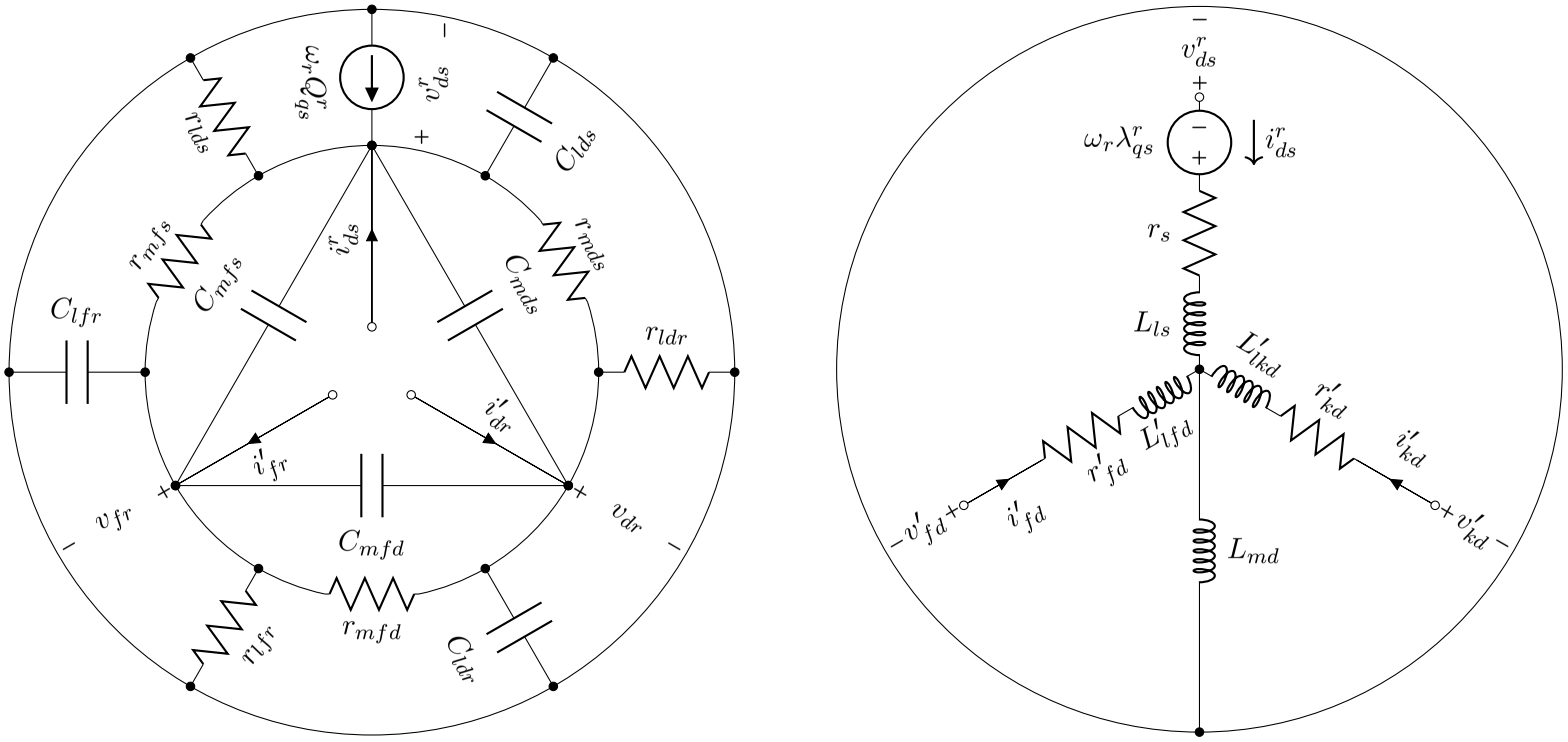

Figure 5.5: Circular layout of the d-axis circuits of the (a) electrostatic and the (b) electromagnetic [105, p. 98] synchronous machine equipped with dampers.

5.3 *dq*-Axis Modeling of Electrostatic Induction Machine

The *dq*-axis model of the electrostatic induction machine can be deduced from the previously derived one for the synchronous machine, which intentionally has the induction effect included. The reduction starts with two facts/assumptions: (1) field excitation is dismissed to allow damping terminals to come on stage for the net torque production; (2) no saliency is exhibited on the rotor, i.e. the dielectric on the rotor surface (see Figure 5.1b) is evenly coated without any discontinuities or irregular dents and cavities. The first one eliminates the dynamics from the field terminals and the second one results in the following simplification in notation because *d*- and *q*-axis are not distinguishable other than analysis necessity:

$$A_s = A_{qs} = A_{ds}, \quad A_r = A_{qr} = A_{dr}, \quad A_m = A_{mqs} = A_{mds},$$
$$A_{ls} = A_s - A_m, \quad A_{lr} = A_r - A_m.$$

The stator referred dynamic equations in the rotor reference frame for the electrostatic induction machine is then put together as

$$\begin{cases} \underline{i}^r_{qds} = \underline{i}^r_{lk,qds} + p\underline{Q}^r_{qds} + j\omega_r \underline{Q}^r_{qds} \\ \underline{i}^r_{qdr} = \underline{i}^r_{lk,qdr} + p\underline{Q}^r_{qdr} \end{cases},$$

where

$$A \leftarrow C,\ \kappa \leftarrow Q \ or\ A \leftarrow G,\ \kappa \leftarrow i_{lk},\ and \begin{cases} \underline{\kappa}^r_{qds} = A_s \underline{v}^r_{qds} - A_m \underline{v}^r_{qdr} \\ \underline{\kappa}^r_{qdr} = A_r \underline{v}^r_{qdr} - A_m \underline{v}^r_{qds} \end{cases}.$$

Notice that the fusion of the *d*- and *q*-axis easily frames the above complex vector form due to the symmetric rotor structure. It is, however, tricky and usually not necessary to do so for the synchronous machine [106]. Given the fact that the field oriented control (FOC) is typically done in the synchronous reference frame for the electromagnetic induction machine, another rotation $e^{-j(\theta_e - \theta_r)}$ is applied to obtain the final form of the *dq*-axis model of the electrostatic induction machine:

$$\begin{cases} \underline{i}^e_{qds} = \underline{i}^e_{lk,qds} + (p + j\omega_e)\underline{Q}^e_{qds} \\ \underline{i}^e_{qdr} = \underline{i}^e_{lk,qdr} + [p + j(\omega_e - \omega_r)]\underline{Q}^e_{qdr} \end{cases}, \tag{5.24}$$

where

$$A \leftarrow C,\ \kappa \leftarrow Q \ or\ A \leftarrow G,\ \kappa \leftarrow i_{lk},\ and \begin{cases} \underline{\kappa}^e_{qds} = A_s \underline{v}^e_{qds} - A_m \underline{v}^e_{qdr} \\ \underline{\kappa}^e_{qdr} = A_r \underline{v}^e_{qdr} - A_m \underline{v}^e_{qds} \end{cases} . \tag{5.25}$$

Pondering that the superscript and subscript e is nothing but a conceptual notation and by dropping it, the above model is instantly transformed into the arbitrary reference frame if necessary.

Equivalent Circuit

Just like previously, the dq-axis equivalent circuit can be drawn as Figure 5.6a except that the d- and q-axis are combined together this time. Again conductance G_* is represented by resistance r_*. Figure 5.6b, depicting its electromagnetic counterpart, is also placed side by side for a close comparison. All the dualities discussed before show up here even more apparently because the circuit is symmetrical other than the reference frame dependent speed current/voltage (the $j\omega\underline{Q}$, $j\omega\underline{\lambda}$ terms).

Other than the dualities, an interesting mismatch is that in the electromagnetic machines there is no corresponding loss component for the magnetizing branch coming from the derivation process. The reason being, the majorities of the current and the electrostatic field paths are sharing together for the electrostatic machines, while they are not for the current and the magnetic field paths of the electromagnetic ones. This indicates that the benchmark of the electrostatic machines may be easier than the electromagnetic counterparts in terms of backing out circuit components.

Power and Torque

Similarly, the power input and the torque out equations can be deduced from eqs. (5.20)–(5.22),

$$P_e = \frac{3}{2}\left(v^e_{ds} i^e_{ds} + v^e_{qs} i^e_{qs}\right), \tag{5.26}$$

$$T_e = \frac{3P}{2}\Im\{\underline{Q}^*_{qds}\underline{v}_{qds}\} = \frac{3P}{2} C_m \left(v^e_{ds} v^e_{qr} - v^e_{qs} v^e_{dr}\right). \tag{5.27}$$

Equation (5.27) intuitively shows that the net torque is directly proportional to the pole number P and the stator-rotor mutual capacitance C_m.

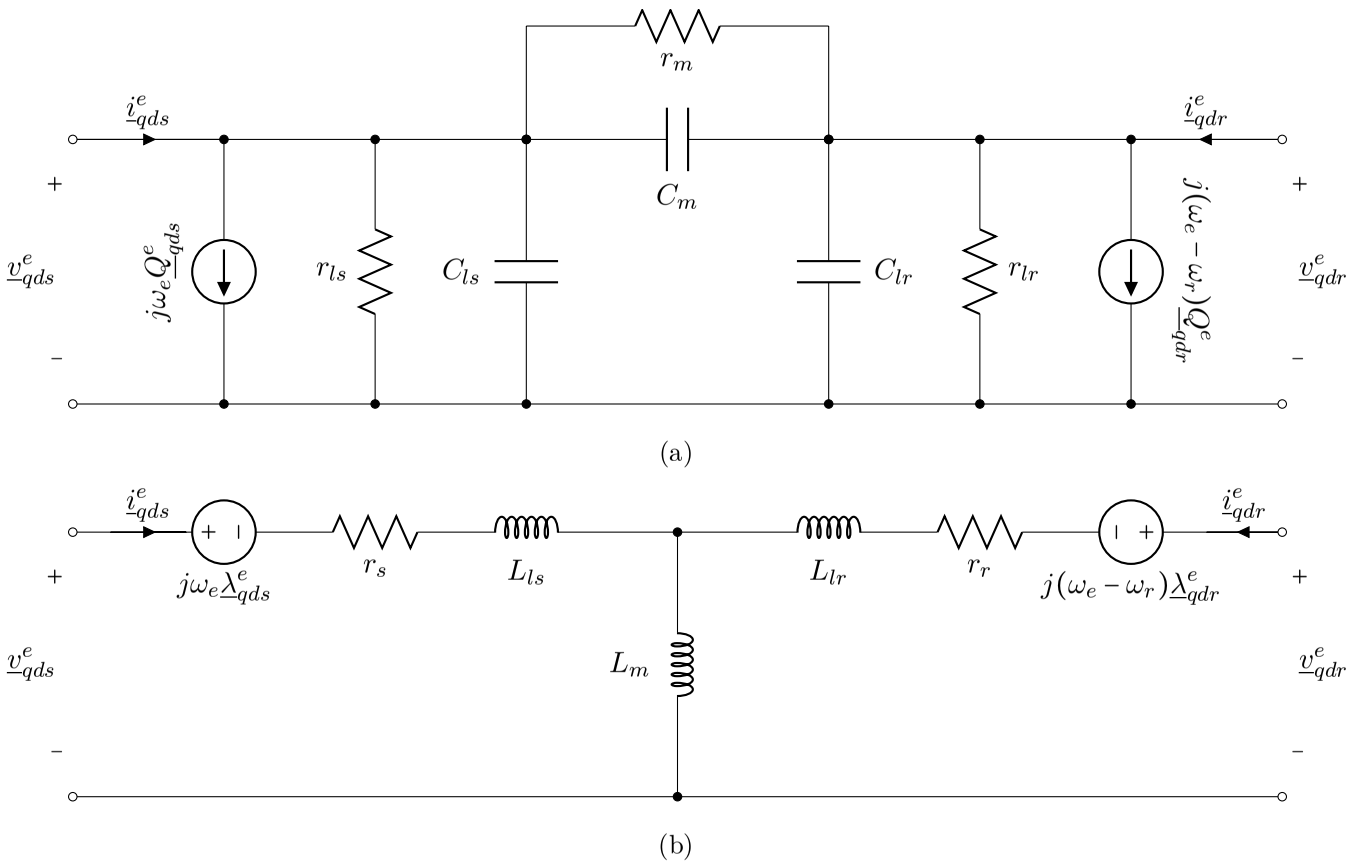

Figure 5.6: *dq*-axis equivalent circuits of the (a) electrostatic and the (b) electromagnetic [105, p. 62] induction machine.

5.4 Steady State Analysis

Steady state analysis is carried out next for both the synchronous and the induction machines to find out the characteristic torque profiles. Dualities are further discovered.

Synchronous Machine

For the synchronous machine, steady state current, voltage and charge are DC in the rotor (i.e. synchronous) reference frame. Therefore, the p terms in the dynamic equations varnish to zero. There still should be leakage current flowing in/out the dampers, however the corresponding dynamic equations are discarded here because (1) they contribute zero net torque and (2) the machine presented in the next Chapter is not equipped with dampers. All of these lead to the following steady state equations

$$\begin{array}{c}\text{stator referred}\\ \text{steady state equation in}\\ \text{the rotor reference frame}\end{array}\left\{\begin{array}{l} I_{qs} = \dfrac{V_{qs}}{r_{qs}} + \dfrac{V_{ds}}{X_{ds}} - \dfrac{V_{fr}}{X_{mfs}} \\ I_{ds} = \dfrac{V_{ds}}{r_{ds}} - \dfrac{V_{fr}}{r_{mfs}} - \dfrac{V_{qs}}{X_{qs}} \\ I_{fr} = \dfrac{V_{fr}}{r_{fr}} - \dfrac{V_{ds}}{r_{mfs}} \end{array}\right. , \tag{5.28}$$

where $X_* = 1/(\omega_r C_*)$, the superscript r's and primes are dropped and lower case dynamic variables are changed to upper case steady state variables for simplicity and elucidation. The corresponding vector diagram is plotted in Figure 5.7. For the purpose of keeping the meaning of the torque angle γ, it is defined as the angle between q-axis and the vector $\underline{V}_{qds}$, while it is the angle between q-axis and the vector $\underline{I}_{qds}$ in the electromagnetic synchronous machine. Substituting the relationship

$$v_{ds}^r = -V_s \sin\gamma, \quad v_{qs}^r = V_s \cos\gamma,$$

into eq. (5.23), the torque equation in the steady state becomes

$$T_e = -\frac{3P}{2}[(C_{ss2} + 2C_{sm2})V_s^2 \sin\gamma\cos\gamma + C_{sfm1}V_s V_{fr}\cos\gamma], \tag{5.29}$$

where V_s is the amplitude of the stator voltage vector. The meaning of the torque angle γ is self explained. The two torque components in eq. (5.29) are plotted as functions of the torque angle γ

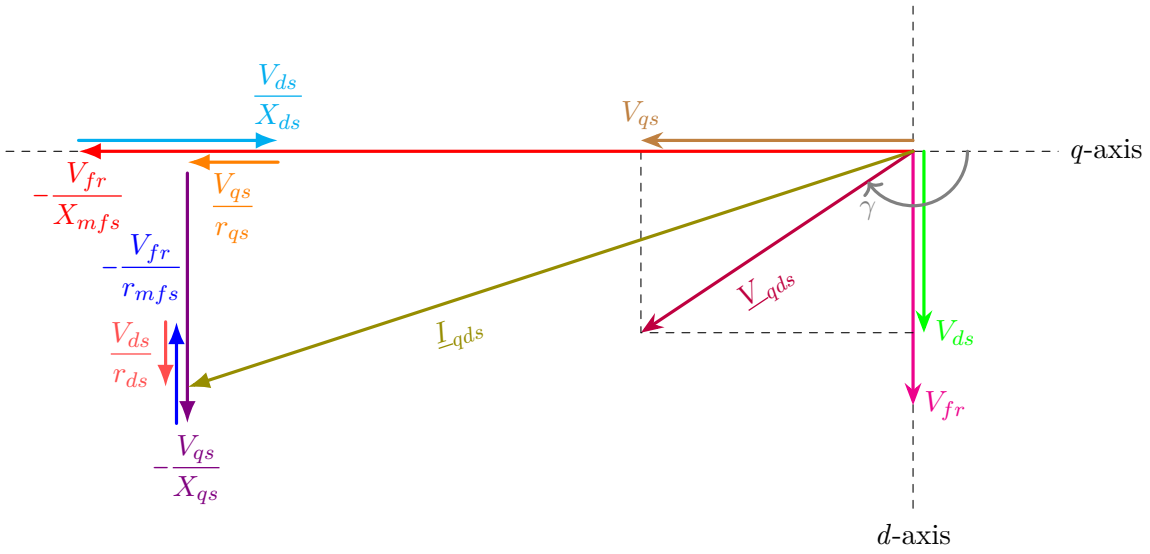

Figure 5.7: Steady state complex vector diagram of the salient electrostatic synchronous machine. The state depicted is in the motoring mode.

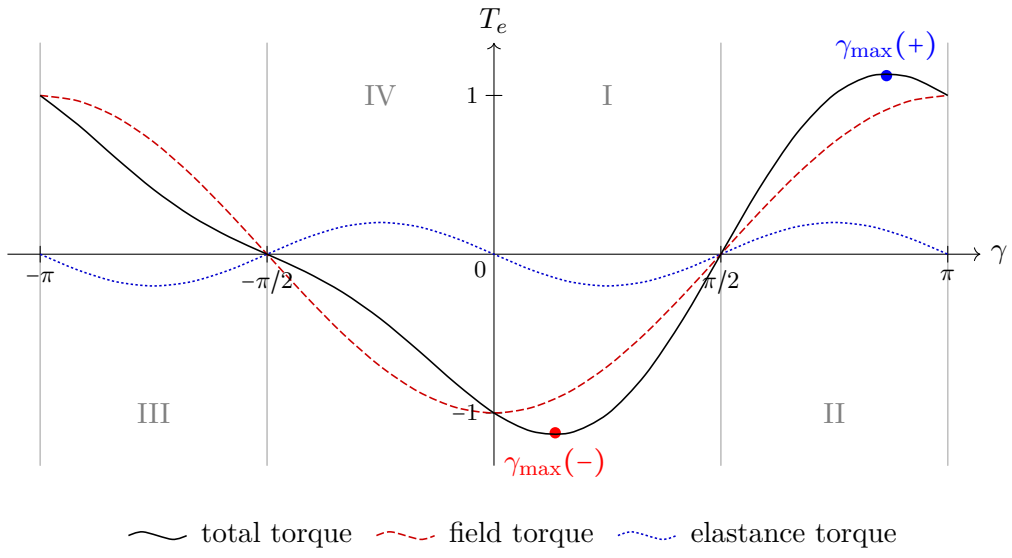

Figure 5.8: Torque components as functions of the torque angle γ in a salient electrostatic synchronous machine. They are normalized to the total torque when $\gamma = 0$.

in Figure 5.8. By differentiating eq. (5.29) with respect to γ and setting the differential to zero, the maximum torque angle is solved as

$$\gamma_{\max} = -\arcsin\left[\frac{C_{sfm1}V_{fr} \pm \sqrt{C_{sfm1}^2 V_{fr}^2 + 8(C_{ss2}+2C_{sm2})^2 V_s^2}}{4(C_{ss2}+2C_{sm2})V_s}\right]. \tag{5.30}$$

The maximum torque is then calculated by substituting eq. (5.30) into eq. (5.29). The two values showing up in eq. (5.30) correspond to the generating torque (take minus sign) and motoring torque (take plus sign) respectively.

Another duality emerging in Figure 5.8 is that the generating mode occurs in the first and the fourth quadrants and the motoring mode occurs in the second and the third quadrants, while they are switched for the electromagnetic synchronous machine.

In the case of a non-salient synchronous machine (without damping terminals), A_{ss2} and A_{sm2} vanish to zero (i.e. $A_{ds} = A_{qs} = A_s$). Assuming $r_{mfs} >> r_s$, an equivalent steady state circuit and the corresponding vector diagram may be obtained as Figure 5.9 and Figure 5.10. Furthermore, T_{fld} is the only torque component. The maximum torque occurs when $\gamma = 0$ or π and the corresponding torque is

$$T_e = \mp\frac{3P}{2}C_{sfm1}V_sV_{fr}. \tag{5.31}$$

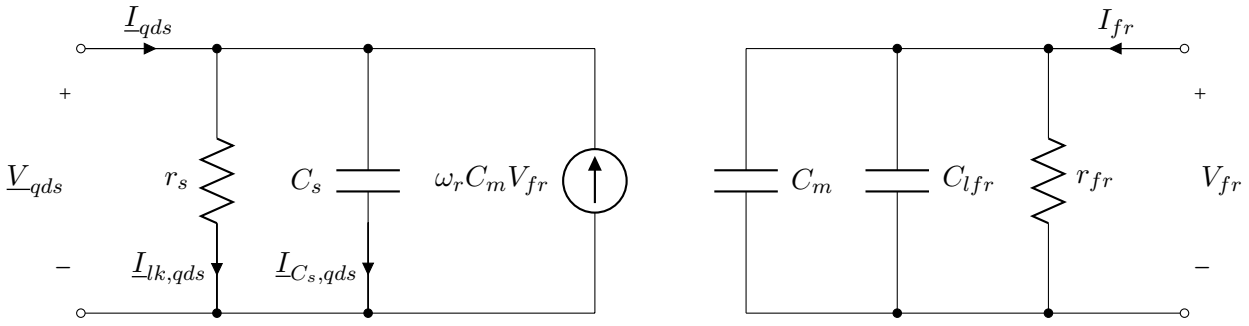

Figure 5.9: Steady state equivalent circuit of the non-salient electrostatic synchronous machine, where $C_m = C_{sfm1}$ for simplicity.

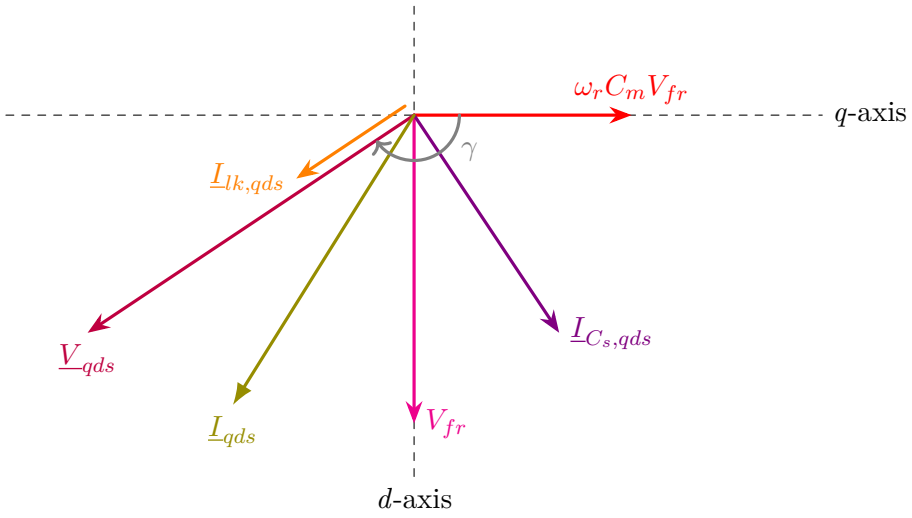

Figure 5.10: Steady state complex vector diagram of the non-salient electrostatic synchronous machine. The state depicted is in the motoring mode.

Induction Machine

For the induction machine, two ways are possible to get the steady state equations, i.e. by dropping the p terms as before or setting ω_e to zero in eq. (5.24). The latter one is more intuitive since it is essentially transforming the equations back to the stationary reference frame. All the complex vectors can then be replaced by the steady state phasors with the tilde notation

$$\begin{cases} \widetilde{I}_s = \left(\dfrac{\widetilde{V}_s}{r_s} - \dfrac{\widetilde{V}_r}{r_m}\right) + \left(\dfrac{\widetilde{V}_s}{-jX_s} - \dfrac{\widetilde{V}_r}{-jX_m}\right) \\ \widetilde{I}_r = \left(\dfrac{\widetilde{V}_r}{r_r} - \dfrac{\widetilde{V}_s}{r_m}\right) + \left(\dfrac{s\widetilde{V}_r}{-jX_r} - \dfrac{s\widetilde{V}_s}{-jX_m}\right) \end{cases}, \tag{5.32}$$

where $s = (\omega_e - \omega_r)/\omega_e$ is the well known slip and $X_* = 1/(\omega_e C_*)$.

Unfortunately, it may be impossible to draw a steady state per phase equivalent circuit as the traditional induction machine because the existence of the leakage component r_m. (Even though it may be large enough to be ignored, but the story will be more complete to live with it.) That being said, the steady state torque equation can still be derived and will be shown next. Reorganizing and factoring out $\widetilde{V}_s$ and $\widetilde{V}_r$, eq. (5.32) turns into

$$\begin{cases} (G_s + j\omega_e C_s)\,\widetilde{V}_s - (G_m + j\omega_e C_m)\,\widetilde{V}_r = \widetilde{I}_s \\ (G_m + js\omega_e C_m)\,\widetilde{V}_s - (G_r + js\omega_e C_r)\,\widetilde{V}_r = 0 \end{cases},$$

where the conductance and the capacitance are recycled for purpose will be seen later. Also notice that $\widetilde{I}_r$ is set to zero, which is generally true for the coating type induction machine. The stator and the rotor voltage can be solved as

$$\widetilde{V}_s = \frac{G_r + js\omega_e C_r}{(G_s + j\omega_e C_s)(G_r + js\omega_e C_r) - (G_m + j\omega_e C_m)(G_m + js\omega_e C_m)}\widetilde{I}_s \tag{5.33}$$

and

$$\widetilde{V}_r = \frac{G_m + js\omega_e C_m}{(G_s + j\omega_e C_s)(G_r + js\omega_e C_r) - (G_m + j\omega_e C_m)(G_m + js\omega_e C_m)}\widetilde{I}_s. \tag{5.34}$$

Substituting these back to the torque eq. (5.27),

$$\begin{aligned}
T_e &= -\frac{3P}{2}C_m\Im\{\underline{v}^*_{qdr}\underline{v}_{qds}\} = -\frac{3P}{2}C_m\Im\{\widetilde{V}_r^*\widetilde{V}_s\} \\
&= -\frac{3P}{2}C_m|\widetilde{I}_s|^2\frac{\Im\{[(G_m - js\omega_e C_m)(G_r + js\omega_e C_r)]\}}{|(G_s + j\omega_e C_s)(G_r + js\omega_e C_r) - (G_m + j\omega_e C_m)(G_m + js\omega_e C_m)|^2} \\
&= -\frac{3P}{2}C_m|\widetilde{I}_s|^2\frac{s\omega_e(C_r G_m - C_m G_r)}{|(G_s + j\omega_e C_s)(G_r + js\omega_e C_r) - (G_m + j\omega_e C_m)(G_m + js\omega_e C_m)|^2},
\end{aligned}$$

and finally replacing $\widetilde{I}_s$ with $\widetilde{V}_s$,

$$T_e = \frac{3P}{2}|\widetilde{V}_s|^2\frac{s\omega_e C_m(C_m G_r - C_r G_m)}{G_r^2 + s^2\omega_e^2 C_r^2}. \tag{5.35}$$

As a function of the slip s, eq. (5.35) has the same form as the traditional induction machine torque formula except for swapping the current source family with the voltage source family. Therefore, the shape of the torque-speed curve is identical to the well known one.

Notice that it is equivalent to set $G_m = 0$ in eq. (5.35), had r_m been ignored previously. The physical significance of r_m is now unveiled: the electrostatic induction torque may contradict with the excitation in direction depending on the selected material properties. Furthermore, comparing eq. (5.35) to eq. (A.1), an underlying connection between the circuit model and the field model is revealed. More details can be found in Appendix A.

5.5 Summary

A *dq*-axis model of the synchronous electrostatic machine with field excitation and dampers is derived. From the machine design perspective, three coupling capacitance are identified as crucial

for optimizing the torque production, i.e. the fundamental component of the stator-rotor field mutual capacitance C_{sfm1}, the second order harmonic of the stator self capacitance C_{ss2} and the second order harmonic of the stator mutual capacitance C_{sm2}. The first one is directly proportional to the field torque and the last two are directly proportional to the elastance torque.

6 SEPARATELY EXCITED THREE PHASE SYNCHRONOUS ELECTROSTATIC MACHINE DESIGN

The designer of electrical machinery usually endeavours, in his primary calculations, to follow a rational scheme, based on sound physical assumptions; but in many secondary matters he is compelled to resort to methods of an empirical or imperfectly reasoned nature, which in some instances have little relation to facts. In reality he relies on his experience to bring the performance of the machine sufficiently near to his purpose to be within the limits of toleration permitted to him.

— Frederick Carter (1926)

6.1 Introduction

As pointed out in [54], a three phase electrostatic synchronous machine with field excitation may be comparable with PM machines in terms of the volumetric and the specific torque densities. However, the previous manufacturing approach (3D printing plus metal plating) is not fully applicable to a three phase electrostatic machine because the nickel plating process, though claimed as selective, does not allow galvanic insulation between pegs (phases). Furthermore, limited by the state of the art technology, the plating thickness is not controllable, resulting in unevenly distributed gap distance.

To circumvent these manufacturing difficulties and uncertainties, a new viable machine structure based on the mature PCB manufacturing is proposed and its electrical design, including design consideration and scalability, are elaborated in this chapter.

6.2 Proposed Machine Topology

The machine topology is finalized as a result of design consideration even though it is presented here first. An axial flux style three phase synchronous electrostatic machine is proposed here using printed circuit boards (PCB) as the main torque producing components, whose schematic is shown

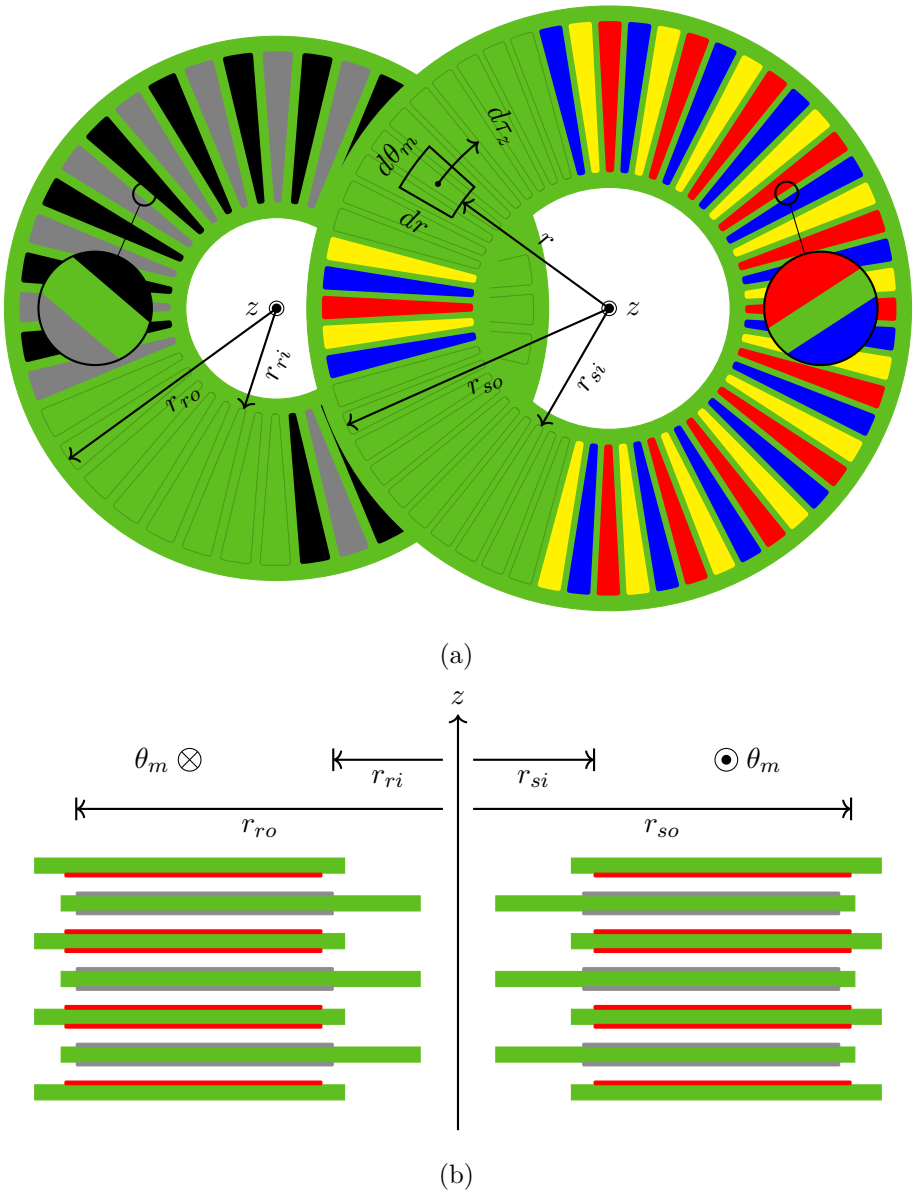

Figure 6.1: Electrical schematic layout of the stator (right) and rotor (left) PCB. (a) Axial view with stator and rotor plates apart from each other ($P = 20$). The integration element is also displayed here for calculating the torque next (b) circumferential view to show the relative relation between the trace radius ($N = 3$).

in Figure 6.1. Three sets of traces are consecutively and symmetrically laid out on the stator and two on the rotor. They are fed with three phase and a bipolar DC voltages respectively. To maximize the space usage, the clearance between the traces next to each other, determined by the breakdown strength of the gap medium, are constant as highlighted in the spied area in Figure 6.1a. Depending on the torque requirement, more plates may be added and cascaded in the axial direction as in Figure 6.1b. These plates are double sided and two layered except for the end ones (in axial direction). Notice that the traces are staggered so that no two edges are against each other directly and therefore the likelihood of breakdown events is reduced.

Now, if walking circumferentially along the plates at a constant radius or axially along the shaft at a constant angle, one may see a repeating structure like Figure 6.2. In the axial direction, the thickness of the stator and rotor substrates are t_{bs} and t_{br} respectively, where subscript "b" emulates the meaning of "back-iron," the thickness of the copper traces are t_{cs} and t_{cr} respectively, where subscript "c" simply stands for "copper," and the minimum gap distance between the stator and rotor traces is denoted as g. In the circumferential direction, the duty ratios d_s and d_r are defined as the angular span of the traces over the period. Due to the aforementioned constant clearance between traces, d_s and d_r relate to the radius r through the following if balanced excitation conditions are assumed

$$\frac{1-3d_s}{3}\cdot\frac{2\pi r}{P}=\frac{\sqrt{3}V_{sp}}{E_{\max}},\quad \frac{1-2d_r}{2}\cdot\frac{2\pi r}{P}=\frac{2V_{rp}}{E_{\max}}, \tag{6.1}$$

where V_{sp} and V_{rp} are the peak stator and rotor voltages on the traces and $E_{\max}$ is the maximum allowable field strength in the fluid and is only a fraction of the breakdown strength. Clearly, the gap distance has to meet the following condition

$$g\geq\frac{V_{sp}+V_{rp}}{E_{\max}}. \tag{6.2}$$

For the detailed prototype structure, one may jump to Chapter 8.

6.3 Torque Estimation — Asymptotical Approach

Traditionally, the design of either electromagnetic machines or electrostatic machines has been done by calculating the torque producing inductance or capacitance. However, as will be explained

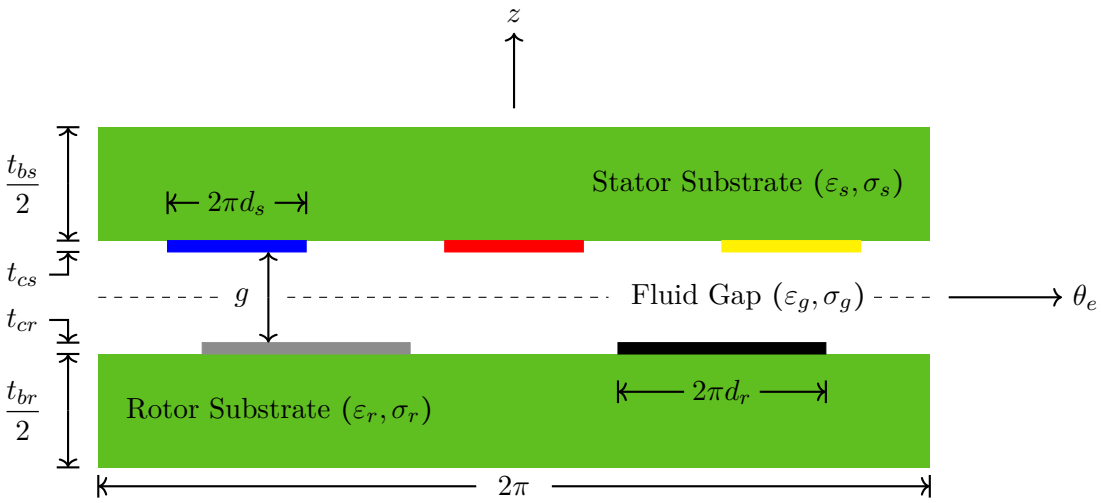

Figure 6.2: 2D schematic view of a separately excited three phase synchronous electrostatic machine with key dimensions called out.

in Section 7.2, the solution of an electrostatic field governed by the Laplace's equation is usually complicated and often analytically unavailable. Chapter 7 gives a general analytical solution to the PCB based design through capacitances, but it does not guide the design process intuitively from the torque perspective.

A generic and easy to implement design approach is proposed here to circumvent such difficulty. The torque is first estimated in this section, then the design procedure and scalability are discussed in the next two sections.

Ideal Case with Sinusoidal Traveling Wave

It starts with the ideal model assuming the stator and rotor surface are excited with pure sinusoidal traveling waves $\widetilde{V}_s$ and $\widetilde{V}_r$ (peak) as in Figure 6.3a. J. R. Melcher showed that the average shear stress (i.e., force per unit area) at radius r is simply

$$\bar{\sigma}_e(r) = -\frac{\varepsilon_g P^2}{2r^2 \sinh(Pg/r)} \left|\widetilde{V}_s\right| \left|\widetilde{V}_r\right| \cos(\gamma) \tag{6.3}$$

for a gap with thickness of g and permittivity of ε_g [36, p. 4.4]. The angle γ, known as the torque angle, is already introduced in Section 5.4. To find the maximum achievable torque, the cosine term is dropped out by simply setting γ to π . Now referring to Figure 6.1a, the total torque generated in

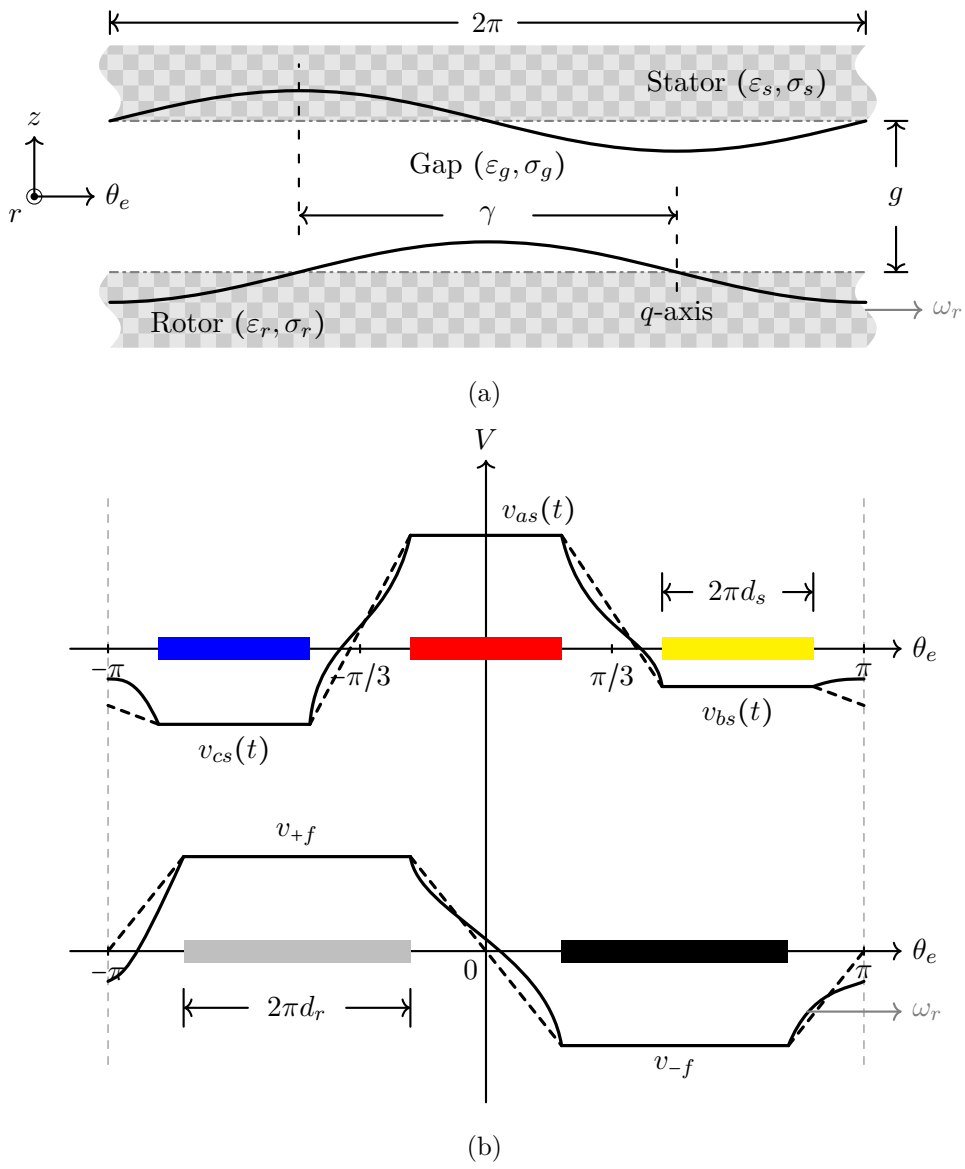

Figure 6.3: Potential wave model based electrostatic machine design. (a) ideal sinusoidal traveling wave (b) linear approximation (dashed line) of the stator and rotor potential distribution (solid line).

N cascaded rotor plates ($2N$ fluid gaps) may be obtained by integrating over the active overlapping area,

$$T_{e,\max} = 2N \int d\tau_z = 2N \int_{r_{si}}^{r_{ro}} \int_0^{2\pi} r\, \bar{\sigma}_e(r)\,|_{\gamma=\pi} \cdot r d\theta_m \cdot dr \tag{6.4}$$

where r_{si} and r_{ro} are the inner radius of the stator traces and the outer radius of the rotor traces. The above integration can be evaluated directly since $\left|\widetilde{V}_s\right|$ and $\left|\widetilde{V}_r\right|$ are constant in the ideal case,

$$T_{e,\max} = 2N \cdot \pi \varepsilon_g P^2 \cdot \left|\widetilde{V}_s\right| \left|\widetilde{V}_r\right| \cdot \int_{r_{si}}^{r_{ro}} \frac{1}{\sinh(Pg/r)} dr.$$

Practical Case with Discrete Traces

In reality $\widetilde{V}_s$ and $\widetilde{V}_r$, achieved by those symmetrically arranged discrete traces, are functions of the radius for two reasons:

- as mentioned above, a constant clearance (distance, not angle) between the stator or rotor traces is necessary for optimal space usage;
- the potential over the circumferential span of the traces are constant as the solid line shown in Figure 6.3b. This is analog to the concentrated winding in the traditional magnetic machines. However, there is no distributed plates here to at least emulate the sinusoidal electromotive force (EMF).

Naturally, it leads to evaluating the fundamental component of the stator and rotor potential distribution. To avoid finding the exact solution of the potential distribution between the traces, a linear distribution is assumed as the dashed line in Figure 6.3b. It will be shown later that this approximation is accurate enough for the preliminary design.

The potential distribution is a function of each single variables defined in Figure 6.2. The linear approximation not only decouples the gap region from the substrate but also separates the stator and rotor field distribution, therefore the relative angle between them does not affect the final result. Torque angle $\gamma = 0$ is depicted here. From the plot, it is not hard to derive the field distribution in

piece-wise functions from left to right via d_s for the stator field

$$\begin{cases} \dfrac{v_{cs}(t)-v_{bs}(t)}{2\pi(1/3-d_s)}\theta_e + v_{cs}(t) + \dfrac{1/3+d_s/2}{1/3-d_s}[v_{cs}(t)-v_{bs}(t)] & \theta_e \in [-\pi, -\dfrac{2\pi}{3}-\pi d_s) \\ v_{cs}(t) & \theta_e \in [-\dfrac{2\pi}{3}-\pi d_s, -\dfrac{2\pi}{3}+\pi d_s) \\ \dfrac{v_{as}(t)-v_{cs}(t)}{2\pi(1/3-d_s)}\theta_e + v_{as}(t) + \dfrac{d_s/2}{1/3-d_s}[v_{as}(t)-v_{cs}(t)] & \theta_e \in [-\dfrac{2\pi}{3}+\pi d_s, -\pi d_s) \\ v_{as}(t) & \theta_e \in [-\pi d_s, \pi d_s) \\ \dfrac{v_{bs}(t)-v_{as}(t)}{2\pi(1/3-d_s)}\theta_e + v_{bs}(t) - \dfrac{1/3-d_s/2}{1/3-d_s}[v_{bs}(t)-v_{as}(t)] & \theta_e \in [\pi d_s, \dfrac{2\pi}{3}-\pi d_s) \\ v_{bs}(t) & \theta_e \in [\dfrac{2\pi}{3}-\pi d_s, \dfrac{2\pi}{3}+\pi d_s) \\ \dfrac{v_{cs}(t)-v_{bs}(t)}{2\pi(1/3-d_s)}\theta_e + v_{cs}(t) - \dfrac{2/3-d_s/2}{1/3-d_s}[v_{cs}(t)-v_{bs}(t)] & \theta_e \in [\dfrac{2\pi}{3}+\pi d_s, \pi) \end{cases}$$

and via d_r for the rotor field

$$\begin{cases} \dfrac{v_{+f}-v_{-f}}{2\pi(1/2-d_r)}\theta_e + v_{+f} + \dfrac{1/4+d_r/2}{1/2-d_r}[v_{+f}-v_{-f}] & \theta_e \in [-\pi, -\dfrac{\pi}{2}-\pi d_r) \\ v_{+f} & \theta_e \in [-\dfrac{\pi}{2}-\pi d_r, -\dfrac{\pi}{2}+\pi d_r) \\ \dfrac{v_{-f}-v_{+f}}{2\pi(1/2-d_r)}\theta_e + v_{-f} - \dfrac{1/4-d_r/2}{1/2-d_r}[v_{-f}-v_{+f}] & \theta_e \in [-\dfrac{\pi}{2}+\pi d_r, \dfrac{\pi}{2}-\pi d_r) \\ v_{-f} & \theta_e \in [\dfrac{\pi}{2}-\pi d_r, \dfrac{\pi}{2}+\pi d_r) \\ \dfrac{v_{+f}-v_{-f}}{2\pi(1/2-d_r)}\theta_e + v_{+f} - \dfrac{3/4-d_r/2}{1/2-d_r}[v_{+f}-v_{-f}] & \theta_e \in [\dfrac{\pi}{2}+\pi d_r, \pi) \end{cases} .$$

By applying Fourier decomposition on these waveforms, the fundamental components of the stator and rotor excitation are obtained as

$$\left|\widetilde{V}_s\right| = \frac{9\sqrt{3}}{2\pi^2}\cdot\frac{\cos\left(\pi d_s+\pi/6\right)}{1-3d_s}\cdot V_{sp}, \quad \left|\widetilde{V}_r\right| = \frac{8}{\pi^2}\cdot\frac{\cos(\pi d_r)}{1-2d_r}\cdot V_{rp}. \tag{6.5}$$

Eventually, substituting eqs. (6.1), (6.3) and (6.5) into eq. (6.4), the maximum torque may be estimated if $V_{sp}, V_{rp}, E_{\max}, r_{si}, r_{ro}, P, g$ and ε_g are known.

As might be expected, there are two other extreme approximations that may be profitable to the designers. Referring to Figure 6.4, the first one fills the gap region with zero potential and results in a lower bound of the torque production $T^L_{e,\max}$. The second one keeps up the trace potential to the gap region and gives an upper bound $T^U_{e,\max}$. Following the above procedure, the fundamental

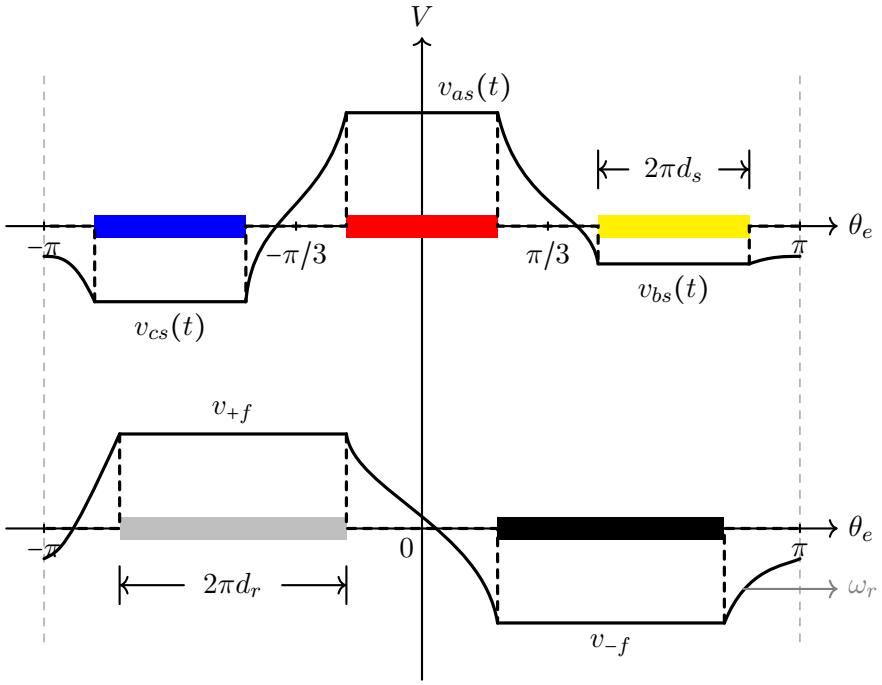

(a)

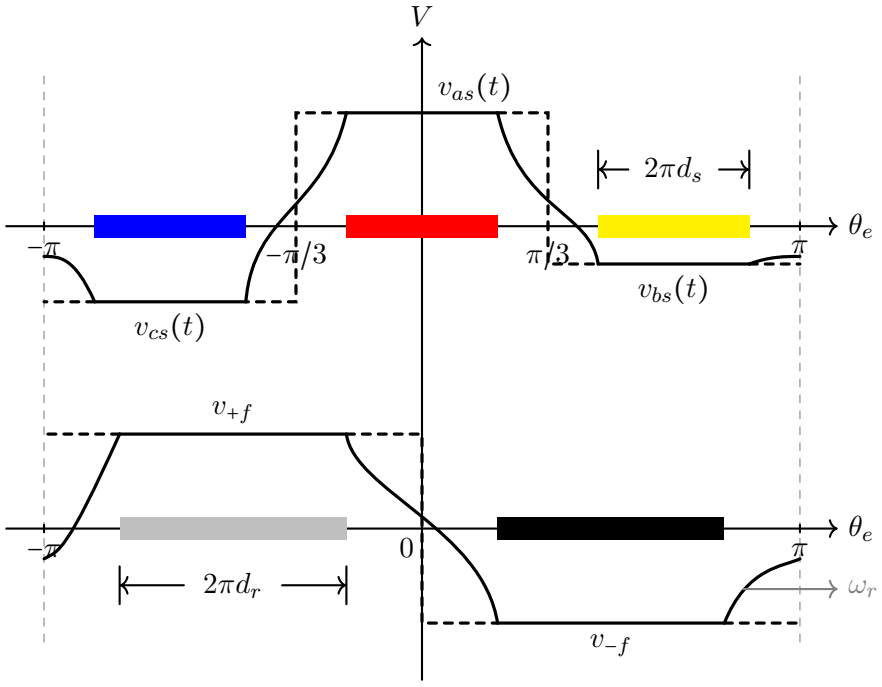

(b)

Figure 6.4: Extreme approximation of the potential distribution. (a) under estimation (b) over estimation.

Table 6.1: Fundamental Components of the Potential Traveling Wave and Torque Estimation with Different Approximation Methods.

Methods		**Lower Bound**	**Linear Approximation**	**Upper Bound**
Stator Fund. Component $\lvert\widetilde{V}_s\rvert$		$\frac{3}{\pi}\sin(\pi d_s)\cdot V_{sp}$	$\frac{9\sqrt{3}}{2\pi^2}\cdot\frac{\cos(\pi d_s+\pi/6)}{1-3d_s}\cdot V_{sp}$	$\frac{3\sqrt{3}}{2\pi}\cdot V_{sp}$
Rotor Fund. Component $\lvert\widetilde{V}_r\rvert$		$\frac{4}{\pi}\sin(\pi d_r)\cdot V_{rp}$	$\frac{8}{\pi^2}\cdot\frac{\cos(\pi d_r)}{1-2d_r}\cdot V_{rp}$	$\frac{4}{\pi}\cdot V_{rp}$
Torque Notation		$T^L_{e,\max}$	$T^1_{e,\max}$	$T^U_{e,\max}$
Typical	Max. Torque Est. $T_{e,\max}$	$2N\cdot\pi\varepsilon_g P^2\cdot V_{sp}V_{rp}\cdot\int_{r_{si}}^{r_{ro}} f(r,P,g,d_s,d_r)dr$		
Analysis with Finite	Duty Ratio d_s, d_r	$d_s=\frac{1}{3}-\frac{\sqrt{3}V_{sp}}{E_{\max}}\cdot\frac{P}{2\pi r},\quad d_r=\frac{1}{2}-\frac{2V_{rp}}{E_{\max}}\cdot\frac{P}{2\pi r}$		
Radius r	Integrand $f(r,P,g,d_s(r),d_r(r))$	$\frac{12}{\pi^2}\cdot\frac{\sin(\pi d_s)\sin(\pi d_r)}{\sinh(Pg/r)}$	$\frac{36\sqrt{3}}{\pi^4}\cdot\frac{\cos(\pi d_s+\pi/6)\cos(\pi d_r)}{(1-3d_s)(1-2d_r)}\frac{1}{\sinh(Pg/r)}$	$\frac{6\sqrt{3}}{\pi^2}\cdot\frac{1}{\sinh(Pg/r)}$
Asymptotical	Max. Torque Est. $T_{e,\max}$	$2N\cdot\pi\varepsilon_g P^3 g\cdot V_{sp}V_{rp}\cdot\int_{r'_{si}}^{r'_{ro}} f(r',d_s,d_r)dr$		
Analysis as	Duty Ratio d_s, d_r	$d_s=\frac{1}{3}-\frac{\sqrt{3}}{4\pi r'},\quad d_r=\frac{1}{2}-\frac{1}{2\pi r'}$		
$r'\to\infty$	Integrand $f(r',d_s(r'),d_r(r'))$	$\frac{12}{\pi^2}\cdot\frac{\sin(\pi d_s)\sin(\pi d_r)}{\sinh(1/r')}$	$\frac{36\sqrt{3}}{\pi^4}\cdot\frac{\cos(\pi d_s+\pi/6)\cos(\pi d_r)}{(1-3d_s)(1-2d_r)}\frac{1}{\sinh(1/r')}$	$\frac{6\sqrt{3}}{\pi^2}\cdot\frac{1}{\sinh(1/r')}$

components of the stator and rotor traveling wave may also be derived. They are summarized and documented in Table 6.1 together with the linear approximation.

Observing that the potential falls off the trace edge dramatically and tends to stay in the lowest energy state, the linear distribution approximation is believed to result in an over estimation of the fundamental components. It is likely that the linear approximation proposed here is a tighter upper bound. Correspondingly, it is denoted as $T^1_{e,\max}$.

Asymptotical Analysis

Rewrite the torque upper bound here

$$T^U_{e,\max} = \frac{12\sqrt{3}}{\pi} \cdot N\varepsilon_g P^2 \cdot V_{sp}V_{rp} \cdot \int_{r_{si}}^{r_{ro}} \frac{1}{\sinh(Pg/r)} dr,$$

It would be much more convenient to get rid of the integral. Using the Taylor series expansion of the hyperbolic sine function $\sinh(x) = x + x^3/3! + x^5/5! + \cdots$, it is not hard to prove that

$$\frac{1}{\sinh(Pg/r)} \sim \frac{r}{Pg}$$

as $r \to \infty$, where "$\sim$" means asymptotically approaching. Therefore we have

$$T^U_{e,\max} \sim \frac{6\sqrt{3}}{\pi} \cdot \frac{N\varepsilon_g P}{g} \cdot V_{sp}V_{rp} \cdot (r^2_{ro} - r^2_{si}) \tag{6.6}$$

as $r_{ro} \to \infty$. This is for the upper bound, what about the lower bound and the linear approximation? Without loss of generality, lower bound case will be derived as an example. First, rewrite d_s and d_r as explicit functions of r from eq. (6.1),

$$d_s = \frac{1}{3} - \frac{\sqrt{3}V_{sp}}{E_{\max}} \cdot \frac{P}{2\pi r} = \frac{1}{3} - \frac{\sqrt{3}}{4\pi}\frac{Pg}{r}, \quad d_r = \frac{1}{2} - \frac{2V_{rp}}{E_{\max}} \cdot \frac{P}{2\pi r} = \frac{1}{2} - \frac{1}{2\pi}\frac{Pg}{r}, \tag{6.7}$$

where $E_{\max}$ is replaced by g based on the conclusion from Section 6.4. Since $d_s \in (0, 1/3)$ and $d_r \in (0, 1/2)$, the following condition has to be met

$$\frac{3\sqrt{3}}{4\pi} < \frac{r}{Pg} < \infty.$$

Substitute eq. (6.7) into the lower bound torque equation and do a change of variable $r' = r/Pg$

$$T^L_{e,\max} = 2N \cdot \pi\varepsilon_g P^2 \cdot V_{sp}V_{rp} \cdot \int_{r_{si}}^{r_{ro}} \frac{12}{\pi^2} \cdot \frac{\sin\left[\pi\left(\frac{1}{3} - \frac{\sqrt{3}}{4\pi}\frac{Pg}{r}\right)\right]\sin\left[\pi\left(\frac{1}{2} - \frac{1}{2\pi}\frac{Pg}{r}\right)\right]}{\sinh\left(\frac{Pg}{r}\right)} dr$$

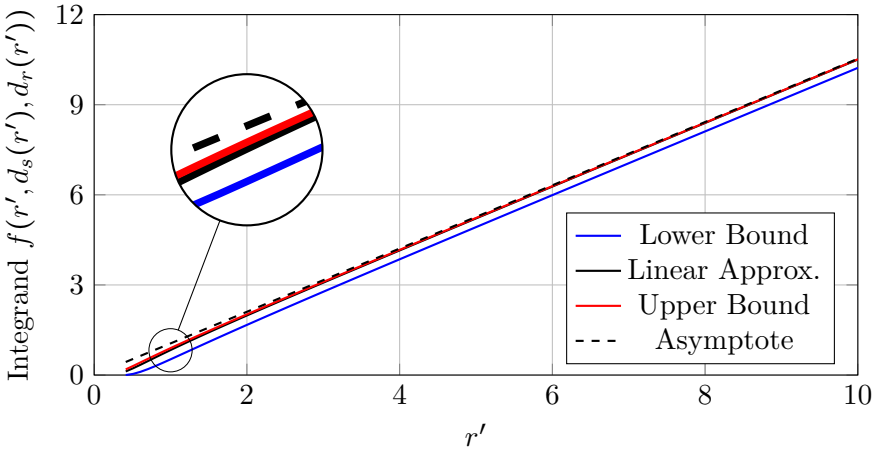

Figure 6.5: Integrand value versus unitless radius. Asymptote is a straight line with a slope of $6\sqrt{3}/\pi^2$.

$$= 2N \cdot \pi\varepsilon_g P^3 g \cdot V_{sp} V_{rp} \cdot \int_{r'_{si}}^{r'_{ro}} \frac{12}{\pi^2} \cdot \frac{\sin\left[\pi\left(\frac{1}{3} - \frac{\sqrt{3}}{4\pi}\frac{1}{r'}\right)\right]\sin\left[\pi\left(\frac{1}{2} - \frac{1}{2\pi}\frac{1}{r'}\right)\right]}{\sinh\left(\frac{1}{r'}\right)} dr',$$

where $r'_{si} = r_{si}/Pg$ and $r'_{ro} = r_{ro}/Pg$. The other two torque estimations look similar to the above equation except for the integrand part (see Table 6.1). Figure 6.5 plots all three integrands for $r' \geq 3\sqrt{3}/4\pi$. Obviously, no matter which method is used, they are all asymptotically the same as $6\sqrt{3}r'/\pi^2$ as $r' \to \infty$. (They can be proved, but it will not look too much different from the one for $T^U_{e,\max}$.) Therefore,

$$T_{e,\max} \sim T^A_{e,\max} = \frac{6\sqrt{3}}{\pi} \cdot \frac{N\varepsilon_g P}{g} \cdot V_{sp} V_{rp} \cdot (r_{ro}^2 - r_{si}^2) \tag{6.8}$$

as $r_{ro} \to \infty$, where superscript "A" simply means asymptote.

As a side note, when r' goes higher, the difference between the upper bound and the lower bound is gradually decreasing, thus the torque estimation method proposed here has very high accuracy when it comes to big size machines with small fluid gaps. However, mechanically, it is hard to maintain a small gap with a big diameter plate. Therefore, the proposed method could only be used for preliminary design.

It is worth mentioning that the torque derived in this section only corresponds to the field torque in Section 5.4. Unlike the large permeability contrast in the magnetic machines between the back iron and air, the permittivity contrast is quite small in the proposed machine between FR-4 and

the fluid, which results in a saliency ratio close to one. Therefore, it is reasonable to leave out the elastance torque. If correlating eq. (6.8) with eq. (5.31), we would obtain the asymptote for the maximum of the mutual capacitance as

$$C_{m,\max}^{A} = \frac{\sqrt{3}}{\pi} \cdot \frac{2N\varepsilon_g(r_{ro}^2 - r_{si}^2)}{g} \approx 0.551 \, \frac{2N\varepsilon_g(r_{ro}^2 - r_{si}^2)}{g}, \tag{6.9}$$

which indicates the mutual capacitance is almost determined by the total facing area, gap length and fluid permittivity and about 55.1% of facing area is effective.

Another aspect in the interest of machine designers is the developed shear stress. It has been discussed in Chapter 4 from the dielectric standpoint. Here, we will give another look from the geometric point of view. Equation (6.3) gives the average shear stress at radius r, therefore, the maximum average shear stress over the whole facing area is

$$\bar{\sigma}_{e,\max} = \frac{1}{r_{ro} - r_{si}} \int_{r_{si}}^{r_{ro}} \sigma_e(r)|_{\gamma=\pi} \, dr = \frac{\varepsilon_g P^2}{2(r_{ro} - r_{si})} \int_{r_{si}}^{r_{ro}} \frac{|\widetilde{V}_s||\widetilde{V}_r|}{r^2 \sinh(Pg/r)} dr.$$

Going through the same derivation for $T_{e,\max}^{A}$, one would reach the following asymptote for the maximum average shear stress

$$\bar{\sigma}_{e,\max}^{A} = \frac{3\sqrt{3}}{\pi^2} \cdot \frac{\varepsilon_g P V_{sp} V_{rp}}{g} \cdot \frac{\ln(r_{ro}/r_{si})}{r_{ro} - r_{si}}. \tag{6.10}$$

Again, this may be correlated with eq. (4.5). Perhaps a more interesting thing to check is the "pressure to shear stress ratio." Before that, we have to derive the pressure equation. According to J. R. Melcher's work, the pressure (i.e. normal force per unit area) for the rotor surface at radius r may be derived as

$$\begin{aligned} \bar{p}_{e,r}(r) &= \frac{\varepsilon_g P^2}{4r^2} \left| \coth(Pg/r)\widetilde{V}_r - \frac{1}{\sinh(Pg/r)} \widetilde{V}_s \right|^2 \\ &= \frac{\varepsilon_g P^2}{4r^2} \left\{ \left[\coth(Pg/r) \left|\widetilde{V}_r\right| \right]^2 + \left[\frac{1}{\sinh(Pg/r)} \left|\widetilde{V}_s\right| \right]^2 + \frac{2\coth(Pg/r)}{\sinh(Pg/r)} \left|\widetilde{V}_r\right| \left|\widetilde{V}_s\right| \sin(\gamma) \right\} \end{aligned} \tag{6.11}$$

and for the stator as

$$\begin{aligned} \bar{p}_{e,s}(r) &= \frac{\varepsilon_g P^2}{4r^2} \left| \coth(Pg/r)\widetilde{V}_s - \frac{1}{\sinh(Pg/r)} \widetilde{V}_r \right|^2 \\ &= \frac{\varepsilon_g P^2}{4r^2} \left\{ \left[\coth(Pg/r) \left|\widetilde{V}_s\right| \right]^2 + \left[\frac{1}{\sinh(Pg/r)} \left|\widetilde{V}_r\right| \right]^2 + \frac{2\coth(Pg/r)}{\sinh(Pg/r)} \left|\widetilde{V}_r\right| \left|\widetilde{V}_s\right| \sin(\gamma) \right\}. \end{aligned} \tag{6.12}$$

Table 6.2: Summary of Asymptotes for Torque, Mutual Capacitance, Shear Stress, Pressure to Shear Ratio and Torque Density.

Asymptote for	Derived Equation	Proportionality
$T_{e,\max}$	$\frac{6\sqrt{3}}{\pi} \cdot \frac{N\varepsilon_g P}{g} \cdot V_{sp} V_{rp} \cdot (r_{ro}^2 - r_{si}^2)$	$\propto N, \varepsilon_g, P, V_{sp}, V_{rp}, r^2, g^{-1}$
$C_{m,\max}$	$\frac{\sqrt{3}}{\pi} \cdot \frac{2N\varepsilon_g (r_{ro}^2 - r_{si}^2)}{g}$	$\propto N, \varepsilon_g, r^2, g^{-1}$
$\bar{\sigma}_{e,\max}$	$\frac{3\sqrt{3}}{\pi^2} \cdot \frac{\varepsilon_g P V_{sp} V_{rp}}{g} \cdot \frac{\ln(r_{ro}/r_{si})}{r_{ro} - r_{si}}$	$\propto \varepsilon_g, P, V_{sp}, V_{rp}, g^{-1}$ $\propto r^{-1}$
$\left(\frac{p_e}{\sigma_e}\right)_{\min}$	$\frac{r}{Pg}$	$\propto r, P^{-1}, g^{-1}$
$\left(\frac{T_e}{V_{active}}\right)_{\max}$	$\frac{6\sqrt{3}}{\pi^2} \cdot \frac{\varepsilon_g P \cdot V_{sp} V_{rp}}{g(t_{bs} + t_{br} + 2t_{cs} + 2t_{cr} + 2g)} \cdot \left[1 - \left(\frac{r_{si}}{r_{ro}}\right)^2\right]$	$\propto \varepsilon_g, P, V_{sp}, V_{rp}, g^{-1} l_g^{-1}$ $\propto [1 - (r_{si}/r_{ro})^2]$

These indicate that the pressure on the stator or the rotor has a non-zero average content and an AC content which is a function of the torque angle γ. Obviously, when $\gamma = 0$ or π, this machine arrives at the minimum pressure to shear stress ratio

$$\left(\frac{\bar{p}_{e,r}}{\bar{\sigma}_e}\right)_{\min} = \frac{1}{2}\left[\frac{\cosh^2(Pg/r)}{\sinh(Pg/r)}\frac{|\widetilde{V}_r|}{|\widetilde{V}_s|} + \frac{1}{\sinh(Pg/r)}\frac{|\widetilde{V}_s|}{|\widetilde{V}_r|}\right] \geq \coth(Pg/r) \sim \frac{r}{Pg} \tag{6.13}$$

for the rotor side and

$$\left(\frac{\bar{p}_{e,s}}{\bar{\sigma}_e}\right)_{\min} = \frac{1}{2}\left[\frac{\cosh^2(Pg/r)}{\sinh(Pg/r)}\frac{|\widetilde{V}_s|}{|\widetilde{V}_r|} + \frac{1}{\sinh(Pg/r)}\frac{|\widetilde{V}_r|}{|\widetilde{V}_s|}\right] \geq \coth(Pg/r) \sim \frac{r}{Pg} \tag{6.14}$$

for the stator side. The equal sign in eqs. (6.13) and (6.14) happens when $|\widetilde{V}_s| = |\widetilde{V}_r|\cosh(Pg/r)$ and $|\widetilde{V}_r| = |\widetilde{V}_s|\cosh(Pg/r)$ respectively. Since they have the same minimum value, we will denote it as

$$\left(\frac{p_e}{\sigma_e}\right)^A_{\min} = \frac{r}{Pg}. \tag{6.15}$$

Eventually, for a machine to be competitive, probably the most important factor is the torque density. Referring to Figures 6.1 and 6.2, the active volume of this machine is

$$V_{active} = \pi r_{ro}^2 \cdot 2Nl_g,$$

where $l_g = (t_{bs} + t_{br})/2 + t_{cs} + t_{cr} + g$ is the stacking length for one fluid gap. Therefore the asymptote for the maximum active torque density is

$$\left(\frac{T_e}{V_{active}}\right)^A_{\max} = \frac{6\sqrt{3}}{\pi^2} \cdot \frac{\varepsilon_g P \cdot V_{sp} V_{rp}}{g(t_{bs} + t_{br} + 2t_{cs} + 2t_{cr} + 2g)} \cdot \left[1 - \left(\frac{r_{si}}{r_{ro}}\right)^2\right]. \tag{6.16}$$

Lastly, Table 6.2 documents the derived asymptote and the corresponding proportionality for ease of referencing.

6.4 Design Considerations

All of the design variables will be explored in this section based on the derived torque equations. Power electronics and mechanical design considerations are also incorporated here. Sweep analysis is also done for most of the design variables on the prototype machine presented in Chapter 8. Other than the swept parameter, all the others are kept the same as in Table 8.1. Both of the models presented in this chapter (upper bound, linear approximation and lower bound) and the next chapter (analytical methods assuming zero thickness and non-zero thickness electrode) are included for the purpose of demonstrating the capabilities and limitations of each model. The computational time for each model is documented in the next chapter since it is more relevant there.

Plate Number N and Liquid Permittivity ε_g

These are quite straightforward, i.e. more plates and higher permittivity liquid could produce more torque. Figure 6.6 also shows that the torque production of the machine is linearly proportional to the the dielectric constant of the liquid.

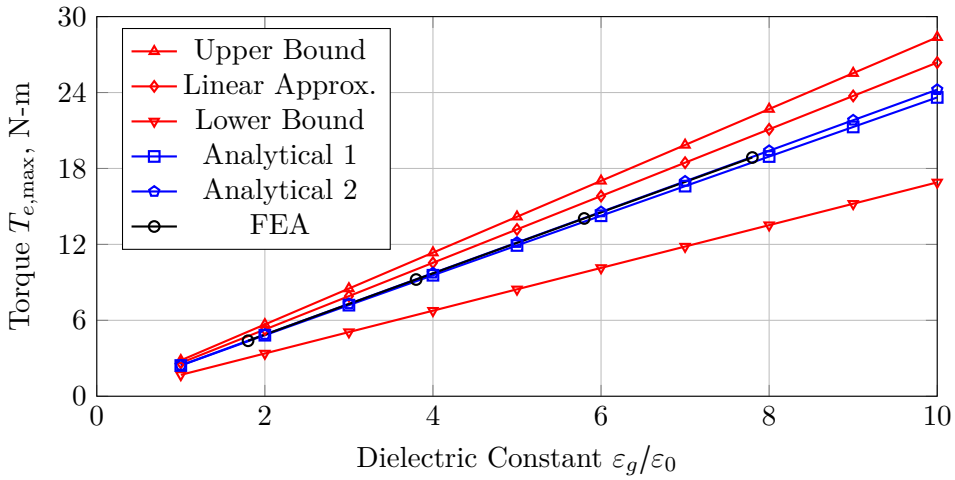

Figure 6.6: Sweep analysis of the fluid dielectric constant $\varepsilon_g/\varepsilon_0$ for parameters in Table 8.1.

Electrode Duty Ratio d_s, d_r

It seems reasonable to substitute eq. (6.1) into eq. (6.5) to obtain even simpler relations

$$\left|\widetilde{V}_s\right| = \frac{3r}{\pi} \cdot \cos\left(\pi d_s + \frac{\pi}{6}\right) \cdot E_{\max}, \quad \left|\widetilde{V}_r\right| = \frac{4r}{\pi} \cdot \cos(\pi d_r) \cdot E_{\max},$$

both of which imply to minimize the duty ratio or trace width to maximize their fundamental components. However, the peak voltage V_{sp} and V_{rp} in this case may be way beyond the capability of the drive circuitry. Usually, this works in the opposite way, i.e. first determine V_{sp} and V_{rp} based on the power electronics capability especially for such high voltage and then find the optimal duty ratios according to eq. (6.5). Figure 6.7 plots $\left|\widetilde{V}_s\right|/V_{sp}$ and $\left|\widetilde{V}_r\right|/V_{rp}$ as functions of d_s and d_r respectively. It shows the fundamental components actually increase as the traces become wider when the peak voltage is fixed. Therefore at a specific radius r, the torque per unit area requires d_s and d_r to be as large as possible based on eq. (6.3). This essentially explains eq. (6.1) presented at the beginning (since eq. (6.1) is not used in the torque derivation, this is not a circular reasoning).

Additionally, the plot also suggests that when $d_s \geq 1/6$ and $d_r \geq 1/4$, which is generally true due to mechanical limitation on the PCB manufacturing, the lower and upper bound could result less than 42% and 73% relative error respectively. This indicates these bounds could be used as part of a first pass design tool.

Lastly, it is interesting to see when $d_s = 0$ and $d_r = 0$, the linear approximation still gives non-zero

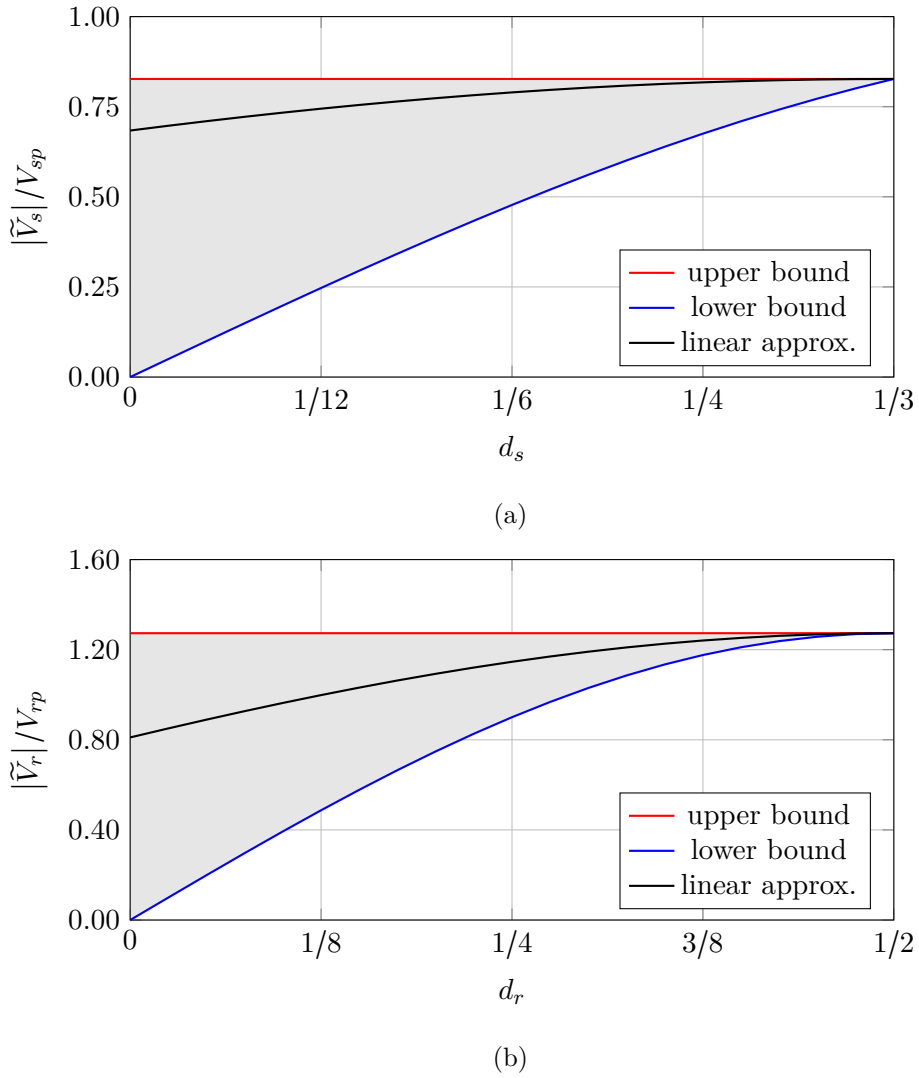

Figure 6.7: Stator and rotor fundamental components estimation as functions of electrode duty ratios.

fundamental components. Indeed, zero width electrode is valid and exists in the mathematical realm even though not true in the physical world, where it should vanish to the lower bound directly.

Gap Length g and Voltages V_{sp}, V_{rp}

Either observing from eq. (6.8), eq. (6.10) or Figure 6.8, one would find that more torque desire less gap length g. Due to the breakdown limitation, it would take the lowest possible value

$$g = \frac{V_{sp} + V_{rp}}{E_{\max}}. \tag{6.17}$$

If viewing this problem from another angle, a natural question to ask is how to divide the voltage between V_{sp} and V_{rp}. With the inequality of arithmetic and geometric means, all the torque equations in Table 6.1 and eq. (5.29) suggest that $V_{sp} = V_{rp}$ to get the maximum torque output. Interestingly, this is also consistent with eq. (6.11) where extract the tangential field out of the total electric field as much as possible would require $V_{sp} = V_{rp}$. Even for the power electronics design, one would like to use the same voltage output level on the stator and rotor to split the design difficulty.

Pole Number P and Active Area $[r_{si}, r_{ro}]$

There is no doubt that increasing r_{ro} would increase the torque. Although eq. (6.10) indicates that the shear stress will be reduced when r_{ro} goes up, the rate of area expanding is faster. It is the inner radius r_{si} that needs to be carefully selected simply because it relates to the pole number P. As P goes higher, r_{si} also needs to be raised high enough so that the minimum trace width meets the PCB manufacturing requirement, which is assumed as δ here. The optimal P will be derived next.

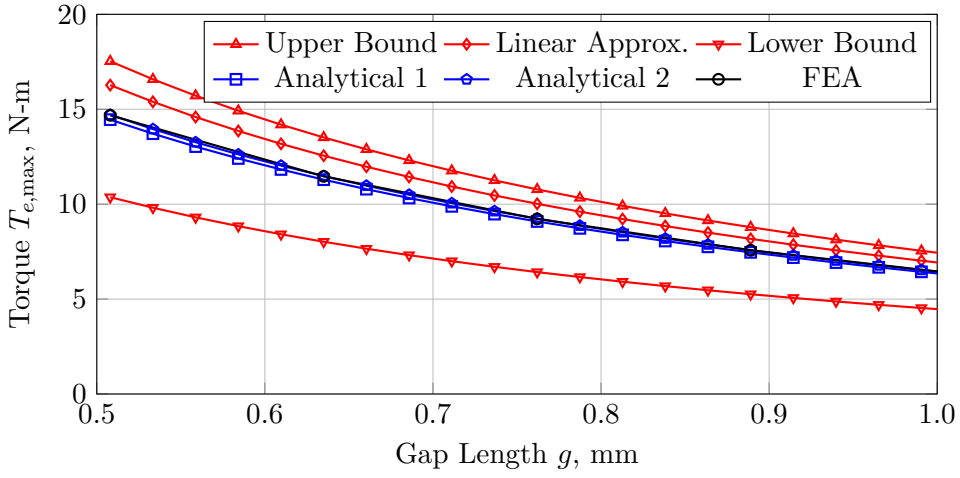

Figure 6.8: Sweep analysis of the gap length g for parameters in Table 8.1.

First, the stator board has more non-plated area than the rotor boards due to

$$3 \cdot \frac{\sqrt{3}V_{sp}}{E_{\max}} > 2 \cdot \frac{2V_{rp}}{E_{\max}}$$

assuming $V_{sp} = V_{rp}$, therefore the narrowest active trace is on the stator. Second, To meet the PCB design requirement, we have

$$\frac{2\pi r_{si}}{3P} - \frac{\sqrt{3}V_{sp}}{E_{\max}} \geq \delta.$$

To maximize the torque production, the equal sign should be taken and substitute eq. (6.7) for $E_{\max}$,

$$r_{si} = \frac{3P}{2\pi}\left(\delta + \frac{\sqrt{3}V_{sp}g}{V_{sp}+V_{rp}}\right) = \frac{3P}{2\pi}\left(\delta + \frac{\sqrt{3}}{2}g\right).$$

Substituting the above equation into eq. (6.8),

$$T^A_{e,\max} = \frac{6\sqrt{3}}{\pi} \cdot \frac{N\varepsilon_g P}{g} \cdot V_{sp}V_{rp} \cdot \left\{ r_{ro}^2 - P^2\left[\frac{3}{2\pi}\left(\delta + \frac{\sqrt{3}}{2}g\right)\right]^2 \right\}. \tag{6.18}$$

With $N, \varepsilon_g, g, V_{sp}, V_{rp}, r_{ro}$ and δ fixed, it is not hard to obtain the optimal P as

$$P_{opt} = \arg\max_P T^A_{e,\max} = \left\lfloor \frac{2\pi r_{ro}}{3\sqrt{3}(\delta + \sqrt{3}g/2)} \right\rfloor \quad or \quad \left\lceil \frac{2\pi r_{ro}}{3\sqrt{3}(\delta + \sqrt{3}g/2)} \right\rceil. \tag{6.19}$$

If $\delta = 0$, i.e. no restriction from the manufacturing side, then

$$P_{opt} = \arg\max_P T^A_{e,\max}\big|_{\delta=0} = \left\lfloor \frac{4\pi r_{ro}}{9g} \right\rfloor \quad or \quad \left\lceil \frac{4\pi r_{ro}}{9g} \right\rceil. \tag{6.20}$$

Notice that eq. (6.19) are derived using the torque asymptote and so does eq. (6.20). In reality, d_s and d_r are also affected negatively when P goes up, therefore eqs. (6.19) and (6.20) may be viewed as the upper bound of the optimal P and could be used as a starting point in the optimization routine. For the sweep analysis in Figure 6.9, it also shows that the maximum torque of the prototype machine peaks at $P \approx 120$ instead of 196 or 197 based on eq. (6.20).

All the Rest $t_{bs}, t_{br}, t_{cs}, t_{cr}, \varepsilon_s, \varepsilon_r$

These variables are isolated out in the torque estimation using potential wave model. It is rational to do so without considering these variables in the first place because torque production simply desires 1) thinner electrode 2) lower substrate permittivity. The former one is due to less side area

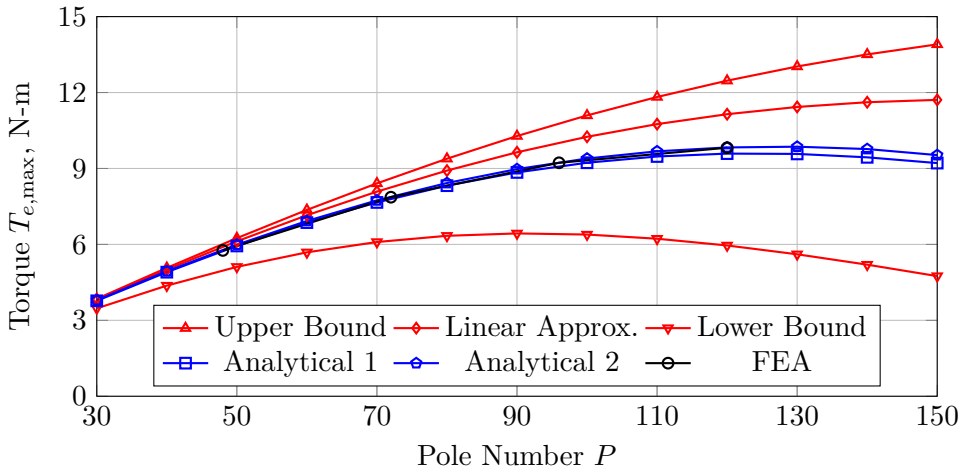

Figure 6.9: Sweep analysis of the pole number P for parameters in Table 8.1.

coupling with the other side of the gap, which reduces the capacitance at the misalignment position and thus increases the stator-rotor coupling capacitance. It is also an observation from the previous work in [54]. The latter one was investigated through a series of FE simulations, the results of which are shown in Figure 6.10. The left column was conducted with air dielectric and the right one was with Vertrel XF. The first row, which studied the same rectangular structure fully plated with metal as in [54], is used as the control group. The rest are treatment group and only plate the surface of the substrate partially. Specifically, the width of the electrode is the same as that of the substrate in the second and the third rows, while the fourth and the fifth rows have wider substrates. Furthermore, The relative permittivity of the substrate were manipulated as 1.0 and 3.0 among the two rows. Figure 6.11 plotted the corresponding percentage of torque increment/decrement. From the torque production perspective, the following two observations may be made:

- a higher permittivity ratio between the dielectric liquid and the substrate material is preferred;
- a wider substrate extended beyond the edge of the metal plating is preferred.

These two can be understood if a close attention is paid to the magnified areas in Figure 6.10. First of all, either elastance, field or induction torque mechanism, which is directly proportional to the AC component of the coupling capacitance (refer to eq. (5.22)), prefers a large capacitance variation, i.e. a large difference between the maximum capacitance and the minimum capacitance.

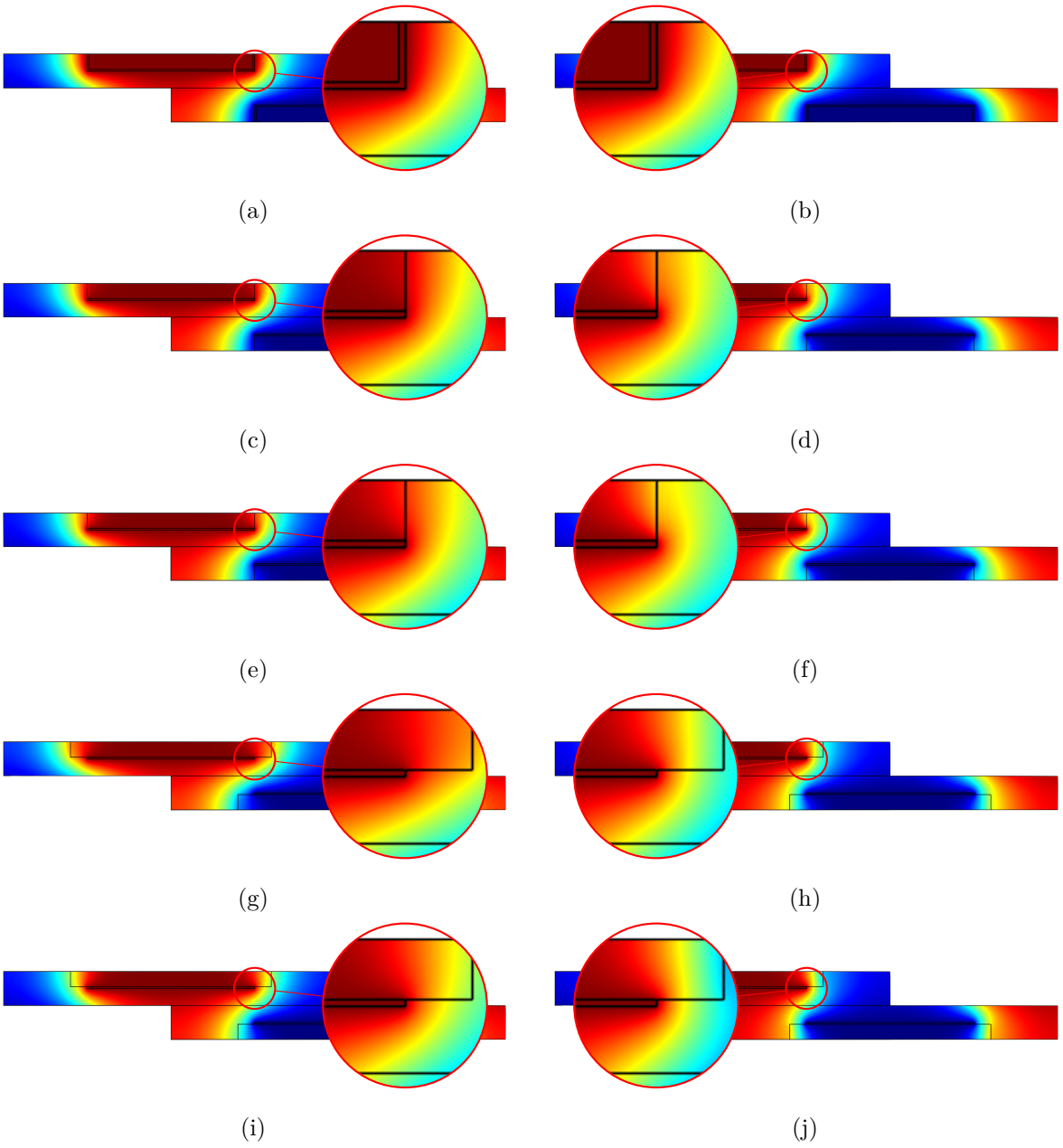

Figure 6.10: Potential distribution of different cases simulated for investigating the electrostatic flux barrier. (a) fully plated, $\varepsilon_{r,g}$ = 1.0; (b) fully plated, $\varepsilon_{r,g}$ = 7.1; (c) partially plated, $\varepsilon_{r,g}$ = 1.0, $\varepsilon_{r,s}$ = 3.0; (d) partially plated, $\varepsilon_{r,g}$ = 7.1, $\varepsilon_{r,s}$ = 3.0; (e) partially plated, $\varepsilon_{r,g}$ = 1.0, $\varepsilon_{r,s}$ = 1.0; (f) partially plated, $\varepsilon_{r,g}$ = 7.1, $\varepsilon_{r,s}$ = 1.0; (g) partially plated, wider base, $\varepsilon_{r,g}$ = 1.0, $\varepsilon_{r,s}$ = 3.0; (h) partially plated, wider base, $\varepsilon_{r,g}$ = 7.1, $\varepsilon_{r,s}$ = 3.0; (i) partially plated, wider base, $\varepsilon_{r,g}$ = 1.0, $\varepsilon_{r,s}$ = 1.0; (j) partially plated, wider base, $\varepsilon_{r,g}$ = 7.1, $\varepsilon_{r,s}$ = 1.0.

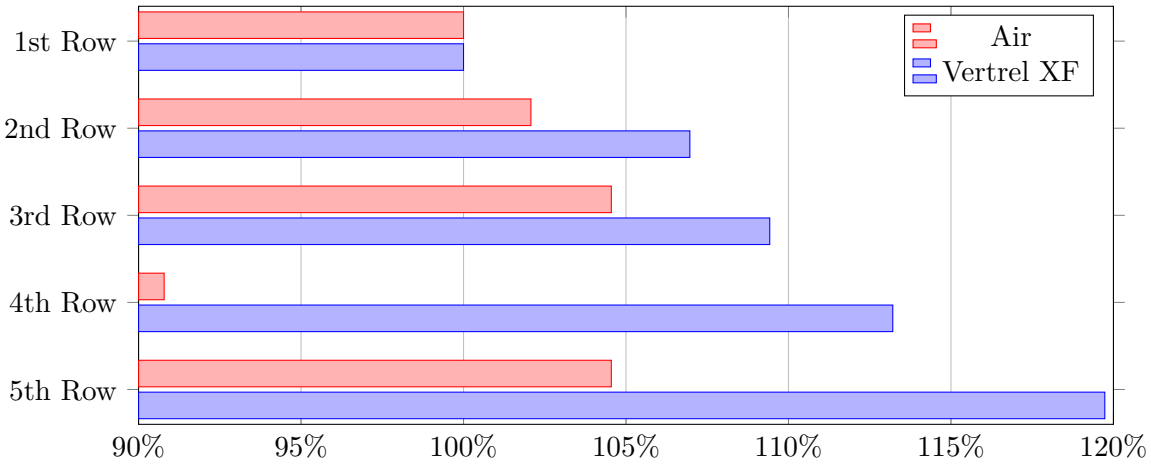

Figure 6.11: Percentage of torque enhancement corresponding to FE simulation of manipulating the flux barriers in Figure 6.10.

Since the electrostatic induction is well accepted as a near field effect, the maximum capacitance is substantially determined by the facing area and the distance of the electrodes and is vaguely influenced by the back substrate material. However, the minimum capacitance, though being small in magnitude, can be considerably regulated by the facing dielectric material in the misaligned position. The key is to increase the equivalent elastance, which is similar to manipulating the reluctance in an electromagnetic machine. Based on the elastance equation $\mathscr{E}_e = d/\varepsilon_0\varepsilon_r wh$ introduced in Chapter 3, two approaches are possible: (1) increasing the flux path length; (2) lowering the permittivity of the material in the flux path. Turning the substrates being fully plated into partially plated is a direct application of (1), where the flux has to go further penetrating through the substrate instead of terminating on the side of the substrate. (2) is realized by making the substrate wider, which takes places where originally are occupied by the dielectric liquid. The PCB design proposed here is an extreme application of (2), which is also consistent with (1).

As for the thickness of the substrate t_{bs} and t_{br}, it is almost independent of the torque production since the trace layout at the two sides of the PCB boards are symmetrical. It is more relevant to the mechanical integrity, which will be discussed later.

6.5 Scalability

Scalability is an indicator of whether the candidate machine keeps up its performance or not when the size changes. Based on the previous asymptotical analysis result eq. (6.16), we know that the electrostatic machine in the proposed form factor can maintain its torque density simply by scaling up the voltage and dimensions at the same rate and using the same pole number and dielectric liquid. Actually, when all the dimensions in Figure 6.2 are augmented with the same ratio, the capacitance coupling per fluid gap per unit depth will not change (this concept is illustrated in [54] and also see Appendix B.). Therefore the torque scales up cubicly because of the increased applied voltage and radius. We have to be careful here though. The above analysis is based on the assumption that the thickness of the plates are mechanically sufficient to shoulder the pressure and it is scalable, which will be discussed below.

Mechanical Scalability

Of course the plates are double sided and the pressure are balanced out in a perfect world. In order to see how the machine is constrained mechanically, we will assume the worst scenario, i.e. only one side of the plate is experiencing the load. The pressure eqs. (6.11) and (6.12) are re-organized using the unitless radius $r' = r/Pg$ as

$$\begin{aligned}
\bar{p}_{e,r}(r) &\le \frac{\varepsilon_g P^2}{4r^2}\left[\coth(Pg/r)\left|\widetilde{V}_r\right| + \frac{1}{\sinh(Pg/r)}\left|\widetilde{V}_s\right|\right]^2 && \text{since } \sin(\gamma) \le 1 \\
&< \frac{\varepsilon_g P^2}{4r^2}\left[\coth(Pg/r)\frac{4}{\pi}V_{rp} + \frac{1}{\sinh(Pg/r)}\frac{3\sqrt{3}}{2\pi}V_{sp}\right]^2 && \text{use upper bound for } V_{sp}, V_{rp} \\
&= \frac{\varepsilon_g V_{sp}^2}{4g^2}\left\{\frac{1}{r'}\left[\frac{4}{\pi}\coth(1/r') + \frac{3\sqrt{3}}{2\pi}\frac{1}{\sinh(1/r')}\right]\right\}^2 && r' = \frac{r}{Pg} \text{ and } V_{sp} = V_{rp}
\end{aligned}$$

for the rotor and similarly

$$\bar{p}_{e,s}(r) < \frac{\varepsilon_g V_{sp}^2}{4g^2}\left\{\frac{1}{r'}\left[\frac{3\sqrt{3}}{2\pi}\coth(1/r') + \frac{4}{\pi}\frac{1}{\sinh(1/r')}\right]\right\}^2$$

for the stator. The brace parts (including the square) are only functions of r' and are unitless. They are plotted in Figure 6.12. Of course the pressure at lower r' is not as high as shown in the plot since d_r and d_s in this case would be very small and so do $\left|\widetilde{V}_r\right|$ and $\left|\widetilde{V}_s\right|$. The key point here is the

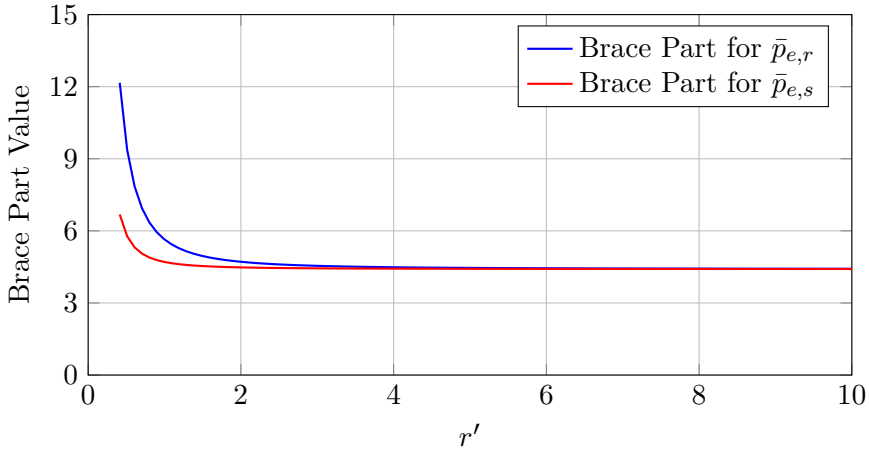

Figure 6.12: Brace part of the pressure versus unitless radius r'.

pressure will not go higher as the radius goes up, at most staying up to a constant. Therefore, the worst situation of the mechanical constraint would be the entire rotor or stator plate is getting an uniformly distributed pressure, which is documented in [107] and also shown in Figure 6.13. The maximum deflection of the plate under the given pressure p is

$$(\Delta z)_{\max} = \alpha \frac{p \cdot r_o^4}{E \cdot t_b^3},$$

where α is a variable coefficient depending on the ratio of r_o/r_i, E is the Young's modulus of elasticity, r_o is the outer radius of the plate and t_b is the thickness of the plate. This deflection would decrease the effective gap length and thus increase the possibility of breakdown events, which is one of the reasons why $E_{\max}$ is set at a small fraction of the dielectric strength of the liquid. Since the redundancy is already built in, as long as the ratio of the maximum deflection to the designed gap length

$$\frac{(\Delta z)_{\max}}{g} = \alpha \frac{p \cdot r_o^4}{E \cdot t^3 g} \tag{6.21}$$

is kept within an acceptable limit, the machine is in its comfortable work region. From the standpoint of the scalability, eq. (6.21) implies that, when r_o, t and g scale up synchronously, the ratio will stay bounded if the pressure p is kept the same or less. The pressure equations above tell us exactly that it meets the requirement if V_{sp}/g is kept constant, which is consistent with the torque scalability analysis. Therefore, the proposed machine is as good as traditional magnetic machines in terms of

Figure 6.13: Annular plate with a uniformly distributed pressure p over the entire plate [107] (a) rotor plate: outer edge free, inner edge fixed (b) stator plate: outer edge fixed, inner edge free.

the torque scaling, i.e. they are both proportional to the active volume.

Another way to increase the torque is to add more plates, i.e. increase N, when the dielectric liquid ε_g and $E_{\max}$, peak voltages V_{sp} and V_{rp} are constrained. Based on the prototype machine presented in Chapter 8, the number of plates in one stack may be limited mechanically, however we may build more than one stack on the same shaft to accommodate the increasing N.

Electrical Scalability

The active part of this machine itself is not very much constrained from the electrical point of view. Since the pole number is high, the current on each trace sector is actually very small, which is much lower than the capability of the trace width. It is the bus trace that has to be carefully designed to carry the total current. Ignoring stray losses, we have the following power conservation equation

$$3V_{s,rms}I_{s,rms}\cos\theta = T_e \cdot \omega_{rm} + \frac{3V_{s,rms}^2}{r_s}, \tag{6.22}$$

where $\cos\theta$ is the input power factor and the rest variables are self clear. The current $I_{s,rms}$ is the one actually flowing in the bus trace. As mentioned at the beginning of this section, the capacitance will increase linearly as the diameter and the thickness per fluid gap scale up the same ratio. Because of the duality between the electrostatic field and the static current field, the same applies to the conductance $1/r_s$. Therefore, for the same operating speed and torque angle, the equivalent circuit model show in Figure 5.9 is unchanged and so does the power factor. In addition, both terms in the right hand side of eq. (6.22) scale up cubicly. Consequently, the stator current scales up quadratically for the same speed, which may also be confirmed from Figure 5.9. On the other hand,

Table 6.3: Trend of Machine Parameters when both the radius and thickness of the machine scale up a factor of k. Speed is kept constant.

Parameters	Proportionality	Constant $E_{\max}, N, \varepsilon_g$ and ω_{rm}, Scale Up Trend	Ref. Equation
Capacitance	$C \propto N \cdot \varepsilon_g \cdot r^2 \cdot g^{-1}$	k	eq. (6.9)
Conductance	$G \propto N \cdot \sigma_g \cdot r^2 \cdot g^{-1}$	k	eq. (6.9)
Voltage	$V \propto E_{\max} \cdot g$	k	eq. (6.17)
Torque	$T \propto N \cdot \varepsilon_g \cdot V^2 \cdot r^2 \cdot g^{-1}$	k^3	eq. (6.8)
Current	$I \propto V \cdot Z^{-1}$	k^2	eq. (6.22)
Power	VI	k^3	eq. (6.22)

since both the thickness and the width of the trace scale up, the area of the cross section of the current path is also quadratically increasing. In the end, the current density is kept the same, which indicates that no special trace routing or extra cooling is needed when the machine scales up.

Similar analysis could be carried out for the rotor side. Therein the current is leakage and the torque and speed are out of the loop, the conclusion is the same as the stator side. Table 6.3 summarizes the scaling law discussed above.

Chemical Scalability

Lastly, what really makes this machine attractive is the torque density is directly proportional to the permittivity of the dielectric liquid. Although the performance of state of the art dielectric liquid only matches air cooled PM machines as will be shown in Chapter 8, there has never had any demand for such high permittivity and high breakdown strength in the market. The research on developing these special liquids is promising.

6.6 Summary

A torque estimation model for the three phase electrostatic synchronous machine based on the traveling wave analysis is presented. The upper and lower bound of the torque production are also derived and they are asymptotically the same, which further verify the effectiveness of the proposed model. Then the design considerations are investigated for the key design parameters and the scalability of the machine is discussed in terms of mechanical strength, voltage, current, torque and power. It turns out that the torque density of the proposed machine has the same scaling law as the traditional magnetic machine, which enlightens that it may extends its advantages to large size applications.

7 ANALYTICALLY DETERMINED FIELD SOLUTION FOR ELECTROSTATIC MACHINES

Simple can be harder than complex: You have to work hard to get your thinking clean to make it simple. But it's worth it in the end because once you get there, you can move mountains.

— Steve Jobs (1998)

7.1 Introduction

The optimization of the electrical performance of electric machines requires solving the governing field. Historically, researchers have been pursuing analytical solutions for two reasons

- the design becomes much easier with an analytical expression. However, most of the time the exact expression does not exist;
- the design duration may be cut down significantly comparing to a numerical approach. Usually, the solution is a trade off between accuracy and time.

The first part has been achieved indirectly by the asymptotical design approach presented in Chapter 6. This chapter tries to deal with the second part. The solution shown here is not in a close form, but it is determined analytically. Its performance is benchmarked against FEA.

7.2 State of the Art Review

Solving electrostatic field analytically is not as easy as solving magnetostatic field. It could be boiled down to

- magnetostatic field is determined by the current, which is usually confined within wires. Biot-Savart law may be used to calculate the field distribution when the current is given;
- electrostatic field is determined by the voltage. However, there is no physical law so far to calculate the field distribution based on the given voltage;

- what about charge? Coulomb's law does work in this case, however the charge distribution is still unknown until we solve it.

Even so, numerous brilliant methods have been proposed in the literature, although most of them are not generic or systematic and usually only apply to their own special structures/cases. They are reviewed and categorized next based on the fundamental concepts.

Conformal Mapping

Conformal mapping is the most popular technique when it comes to solving electrostatic field, due to its ability of transforming complex geometries into regular ones. However, when the structure has more than a few vertices, a non-close form Schwarz-Christoffel mapping needs to be carried out. The process is documented in [108] for a magnetic machine and the author also tried to use it to solve the field in a single phase electrostatic machine. Typically, electric machines tend to have small gap length, which results in a large aspect ratio (periodic length over gap length). The direct implementation of the Schwarz-Christoffel mapping on a small aspect ratio structure is numerically unstable. T. A. Driscoll proposed to triangulate such structure into small pieces so that each single of them has an accepted aspect ratio [109–111]. However this approach is discarded in the three phase machine case due to the following three reasons:

- For the three phase machine proposed here in this work, it contains five electrodes, the mapping of which could be cumbersome. In addition, after the conformal mapping process, one still needs to solve the field distribution in the transformed coordinates. Several typical situations with three electrodes are considered in [112], but it is not a generic solution or at least not be able to be carried over to our case.

- Boundary conditions, including periodic and symmetric, are not well taken into account in T. A. Driscoll's algorithm. The former one is indirectly solved in [108] by having few more repeating structures in the computation loop, which however would increase the time cost, and the latter one has not been considered yet.

- Conformal mapping usually works for one uniform material. When it comes to multiple materials, the common approach for the two electrode case is to average out the permittivity in the capacitance calculation [113] or empirically approximate the material boundary [114], both of which are not intuitive and accurate.

For more technical details on this approach, one may refer to R. Schinzinger's book *Conformal Mapping: Methods and Applications* [115] and T. A. Driscoll's book *Schwarz-Christoffel Mapping* [116].

Separation of Variables

Separation of variables is a commonly used method in the magnetostatic field calculation. Therein the magnetic structure with non-zero thickness in the gap direction could be treated mathematically as a zero thickness one [117]. However it does not apply to the electrostatic field if one tries to match the excitation boundary and the slot region at the same time. X. Ma proposed a branch and cut type of strategy called rectangular boundary division method to circumvent the difficulties of matching boundaries [118]. The implementation, which is well documented in [119], requires solving the boundary conditions using variational method. It is therefore essentially like a FE approach although it starts with close form expressions.

D. Homentcovschi reconsidered the boundary conditions [120]. Instead of unilaterally matching the potential distribution, he also developed the boundary conditions for the charge distribution. Solving both of them together turns out to be a known mathematical problem. He then extended his work to non-periodic structures in [121] for microstrip transmission lines, which may be of interest to the design of linear type of electrostatic machines in the future.

Given the fact that D. Homentcovschi's method is relatively generic and numerically robust comparing to the other methods, we will use it to solve for the three phase machine proposed in Chapter 6 with constraints specifically imposed by electrostatic machines. It is also the first time applied to any kind of electrical machines.

Since D. Homentcovschi's method only applies to zero thickness electrodes, Section 7.3 will first derive the solution for the same zero thickness assumption, then Section 7.4 will derive the solution

for the non-zero thickness situation by approximating the physical electrode with multiple zero thickness electrodes.

7.3 Field Solution for Zero Thickness Electrodes

Conformal Mapping

By assuming the electrode thickness is zero, the model depicted in Figure 6.2 may be simplified as Figure 7.1a and it is further conformally mapped into polar coordinate as shown in Figure 7.1b using the analytical function (in order to be consistent with Chapter 5 after mapping, phase B and C, rotor positive and negative are swapped respectively in Figure 7.1a. From the capacitance perspective, it does not make any difference)

$$\zeta = e^{-j\frac{2\pi}{L}z}, \tag{7.1}$$

where $z = x + jy$ and $\zeta = re^{j\theta}$ are the rectangular and polar coordinates in the complex plane respectively. It is straightforward to get the following relations

$$r_1 = \exp\left(-\frac{\pi(g+t_{br})}{L}\right),\ r_2 = \exp\left(-\frac{\pi g}{L}\right),\ r_3 = \exp\left(\frac{\pi g}{L}\right),\ r_4 = \exp\left(\frac{\pi(g+t_{bs})}{L}\right)$$

and

$$\alpha_{s,i} = -\frac{2\pi}{L}x_{a_{s,i}},\ \beta_{s,i} = -\frac{2\pi}{L}x_{b_{s,i}},\ \alpha_{r,i} = -\frac{2\pi}{L}x_{a_{r,i}},\ \beta_{r,i} = -\frac{2\pi}{L}x_{b_{r,i}}.$$

Notice that eq. (7.1) maps $y = 0$ into the unit circle in the polar coordinate system (see Figure 7.1). However, for this analytical method to work, it is not necessary to do so. See Appendix B for the justfication. Furthermore, as explained above, the minus sign in eq. (7.1) is selected so that Figure 7.1b is consistent with Figure 5.1a.

Now that the problem is transformed into the polar coordinate system, conformal mapping ensures that the capacitance matrix is conformal along the mapping process. Indeed the method proposed by D. Homentcovschi can be used under the rectangular coordinate (exponential function to hyperbolic function), however, for the ease of sanity check and most importantly solving eqs. (7.5)–(7.8) naturally falls into the polar coordinate, it is still conducted in the original form presented in [120].

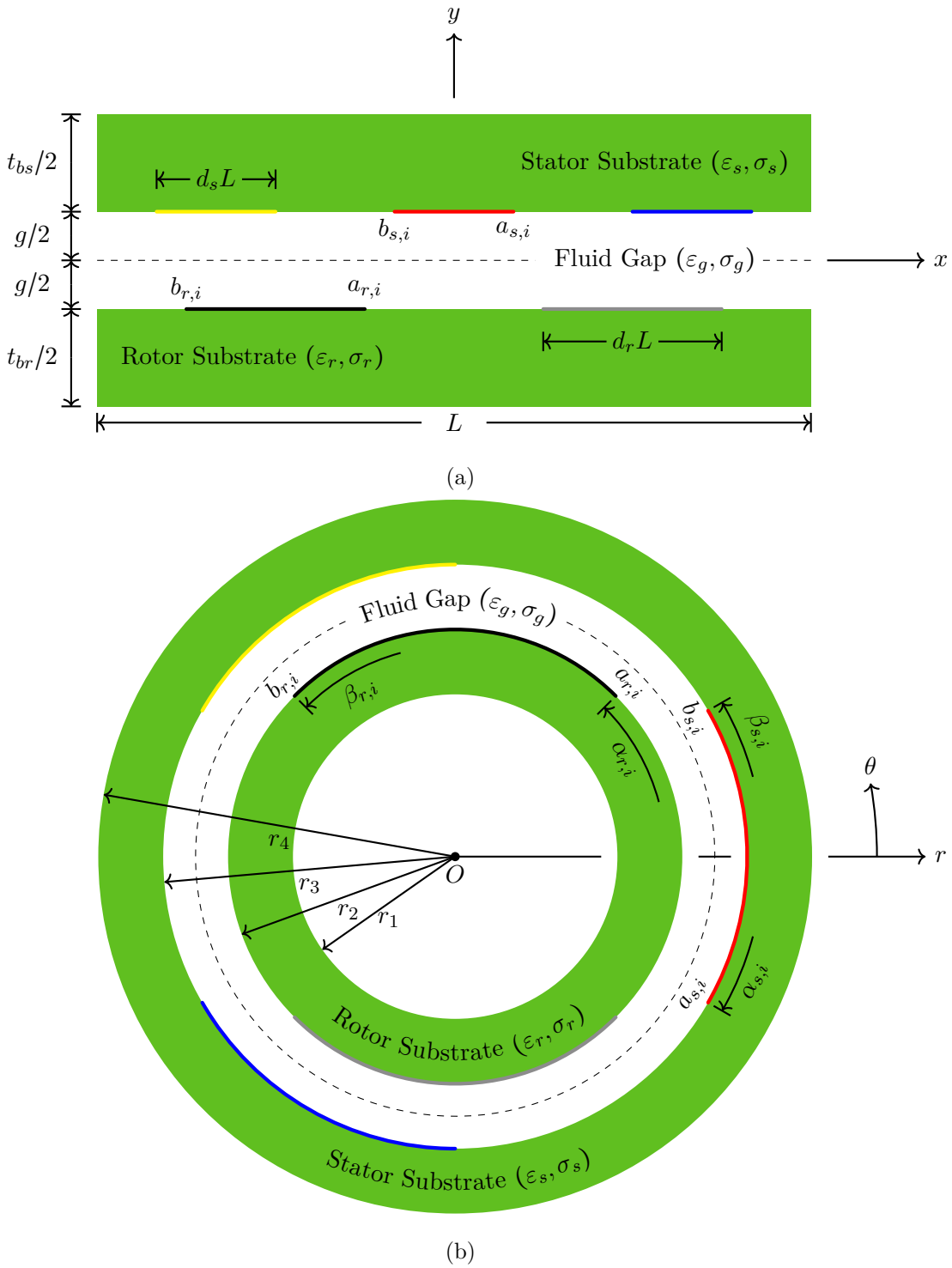

Figure 7.1: Redrawing of Figure 6.2 with zero thickness electrodes in (a) rectangular coordinate (b) polar coordinate. Dashed lines correspond to $y = 0$ and $r = 1$ respectively.

General Solution

Using the method of separation of variables, the general solution of the 2D Laplace's equation in the polar coordinate is obtained as

$$\phi(r,\theta) = \tau \ln(r) + \lambda + \sum_{n=1}^{\infty} \left[A_n \cos(n\theta) + B_n \sin(n\theta)\right] \cdot \left(C_n r^n + D_n r^{-n}\right),$$

where $\tau, \lambda, A_n, B_n, C_n, D_n$ are constants to be determined. The Fourier series automatically ensures the periodic condition at $x = \pm L/2$ in the $x - y$ coordinate, which is also another natural reason to use the $r - \theta$ coordinate. What is left to be determined are these coefficients to satisfy the boundary conditions at $r = r_1, r_2, r_3, r_4$.

The nice thing about the method of separation of variables is that different solutions, each of which satisfies a small set of the boundary conditions that are complement together, can be superimposed together. Here, the field solution in the rotor substrate, fluid gap and stator substrate are denoted as ϕ_{br}, ϕ_g and ϕ_{bs} corresponding to the call-out dimensions respectively. Based on the Neumann boundary conditions at $r = r_1$ and r_4, and the continuous boundary conditions at $r = r_2$ and r_3, the intermediate general field solution for each region can be obtained as

$$\phi_{br}(r,\theta) = \Gamma_{br} + \sum_{n=1}^{\infty} S_n^+(r, r_1, r_2) \left[A'_{br,n} \cos(n\theta) + B'_{br,n} \sin(n\theta)\right], \tag{7.2}$$

$$\phi_{bs}(r,\theta) = \Gamma_{bs} + \sum_{n=1}^{\infty} S_n^+(r, r_4, r_3) \left[A'_{bs,n} \cos(n\theta) + B'_{bs,n} \sin(n\theta)\right], \tag{7.3}$$

and

$$\begin{aligned}\phi_g(r,\theta) = (\Gamma_{bs} - \Gamma_{br}) R_0^-(r, r_2, r_3) + \Gamma_{br} &+ \sum_{n=1}^{\infty} R_n^-(r, r_3, r_2) \left[A'_{br,n} \cos(n\theta) + B'_{br,n} \sin(n\theta)\right] \\ &+ \sum_{n=1}^{\infty} R_n^-(r, r_2, r_3) \left[A'_{bs,n} \cos(n\theta) + B'_{bs,n} \sin(n\theta)\right]\end{aligned} \tag{7.4}$$

where

$$R_0^-(r, r_a, r_b) = \frac{\ln\left(\frac{r}{r_a}\right)}{\ln\left(\frac{r_b}{r_a}\right)}, \; R_n^{\pm}(r, r_a, r_b) = \frac{\left(\frac{r}{r_a}\right)^n \pm \left(\frac{r_a}{r}\right)^n}{\left(\frac{r_b}{r_a}\right)^n - \left(\frac{r_a}{r_b}\right)^n}, \; S_n^{\pm}(r, r_a, r_b) = \frac{\left(\frac{r}{r_a}\right)^n \pm \left(\frac{r_a}{r}\right)^n}{\left(\frac{r_b}{r_a}\right)^n + \left(\frac{r_a}{r_b}\right)^n}.$$

The prime notation is used in eqs. (7.2)–(7.4) to follow D. Homentcovschi's convention [120].

Notice that

$$R_0^-(r_a, r_a, r_b) = 0,\ R_n^-(r_a, r_a, r_b) = 0,\ S_n^-(r_a, r_a, r_b) = 0,$$

$$R_0^-(r_b, r_a, r_b) = 1,\ R_n^-(r_b, r_a, r_b) = 1,\ S_n^+(r_b, r_a, r_b) = 1,$$

and

$$\frac{\partial}{\partial r} R_n^{\pm}(r, r_a, r_b) = \frac{n}{r} R_n^{\mp}(r, r_a, r_b),\ \frac{\partial}{\partial r} S_n^{\pm}(r, r_a, r_b) = \frac{n}{r} S_n^{\mp}(r, r_a, r_b).$$

Boundary Conditions

Now the coefficients are narrowed down to Γ's, A_n's and B_n's, which are up to the voltage level and location of the electrodes at the interface r_2 and r_3. The traditional method of separation of variables usually fails here since it assumes the boundary conditions at r_2 and r_3 are homogeneous. However, these electrodes are not at the same potential and most importantly are discretely distributed. This is where D. Homentcovschi's method stands out.

Following D. Homentcovschi's approach, these coefficients should satisfy

$$\Gamma_{br} + \sum_{n=1}^{\infty} \left[A_{br,n}\cos(n\theta) + B_{br,n}\sin(n\theta)\right] = \phi_{br-g,i} - \sum_{n=1}^{\infty} \eta_{br}(n) \left[A_{br,n}\cos(n\theta) + B_{br,n}\sin(n\theta)\right],$$
$$\text{for } \theta \in (\alpha_{r,i}, \beta_{r,i}),\ i \in (1, N_r) \quad (7.5)$$

$$-\gamma_{br} + \sum_{n=1}^{\infty} \left[A_{br,n}\sin(n\theta) - B_{br,n}\cos(n\theta)\right] = (\varepsilon_1 + \varepsilon_2)^{-1} \left(\sum_{l=1}^{i} q_{br-g,l} - \frac{\theta}{2\pi} \sum_{l=1}^{N_r} q_{br-g,l}\right) +$$
$$\sum_{n=1}^{\infty} \frac{\varepsilon_2}{\varepsilon_1 + \varepsilon_2} \cdot \frac{2 r_2^n r_3^n}{r_3^{2n} - r_2^{2n}} [1 + \eta_{bs}(n)] \left[A_{bs,n}\sin(n\theta) - B_{bs,n}\cos(n\theta)\right],$$
$$\text{for } \theta \in (\beta_{r,i}, \alpha_{r,i+1}),\ i \in (1, N_r) \quad (7.6)$$

$$\Gamma_{bs} + \sum_{n=1}^{\infty} \left[A_{bs,n}\cos(n\theta) + B_{bs,n}\sin(n\theta)\right] = \phi_{bs-g,i} - \sum_{n=1}^{\infty} \eta_{bs}(n) \left[A_{bs,n}\cos(n\theta) + B_{bs,n}\sin(n\theta)\right],$$
$$\text{for } \theta \in (\alpha_{s,i}, \beta_{s,i}),\ i \in (1, N_s) \quad (7.7)$$

$$-\gamma_{bs} + \sum_{n=1}^{\infty} \left[A_{bs,n}\sin(n\theta) - B_{bs,n}\cos(n\theta)\right] = (\varepsilon_2 + \varepsilon_3)^{-1} \left(\sum_{l=1}^{i} q_{bs-g,l} - \frac{\theta}{2\pi} \sum_{l=1}^{N_s} q_{bs-g,l}\right) +$$
$$\sum_{n=1}^{\infty} \frac{\varepsilon_2}{\varepsilon_2 + \varepsilon_3} \cdot \frac{2 r_2^n r_3^n}{r_3^{2n} - r_2^{2n}} [1 + \eta_{br}(n)] \left[A_{br,n}\sin(n\theta) - B_{br,n}\cos(n\theta)\right],$$

$$\text{for } \theta \in (\beta_{s,i}, \alpha_{s,i+1}),\ i \in (1, N_s) \quad (7.8)$$

Among these conditions,

- Coefficients A_n's and B_n's relate to the primed ones through

$$\left(A'_{br,n} - jB'_{br,n}\right) = (A_{br,n} - jB_{br,n})[1 + \eta_{br}(n)],$$

and

$$\left(A'_{bs,n} - jB'_{bs,n}\right) = (A_{bs,n} - jB_{bs,n})[1 + \eta_{bs}(n)].$$

- Variables $\eta_{br}(n), \eta_{bs}(n)$ are defined as

$$\eta_{br}(n) = \frac{\delta_{br}(n)}{1 - \delta_{br}(n)}, \quad \delta_{br}(n) = \frac{2\varepsilon_1}{\varepsilon_1 + \varepsilon_2} \cdot \frac{r_1^{2n}}{r_1^{2n} + r_2^{2n}} + \frac{2\varepsilon_2}{\varepsilon_1 + \varepsilon_2} \cdot \frac{r_2^{2n}}{r_2^{2n} - r_3^{2n}},$$

and

$$\eta_{bs}(n) = \frac{\delta_{bs}(n)}{1 - \delta_{bs}(n)}, \quad \delta_{bs}(n) = \frac{2\varepsilon_2}{\varepsilon_2 + \varepsilon_3} \cdot \frac{r_2^{2n}}{r_2^{2n} - r_3^{2n}} + \frac{2\varepsilon_3}{\varepsilon_2 + \varepsilon_3} \cdot \frac{r_3^{2n}}{r_3^{2n} + r_4^{2n}}.$$

- Charge $q_{br-g,l}, q_{bs-g,l}$ are the total amount on the l-th electrodes at the br-g and bs-g interface respectively, which relate to Γ_{br}, Γ_{bs} through

$$\sum_{l=1}^{N_r} q_{br-g,l} = -\sum_{l=1}^{N_s} q_{bs-g,l} = -2\pi\varepsilon_2 \cdot \frac{\Gamma_{br} - \Gamma_{bs}}{\ln(r_2/r_3)}. \quad (7.9)$$

- Constants γ_{br}, γ_{bs} define the starting points of charge counting.

- Voltages $\phi_{br-g,i}, \phi_{bs-g,i}$ are from the i-th rotor and stator electrodes.

- Integers N_r, N_s are the number of the rotor and stator electrodes.

Analytical Solution

D. Homentcovschi indicated that the left hand side of eqs. (7.5) and (7.6) or eqs. (7.7) and (7.8) may be viewed as the expansion of the following complex variable function on the unit circle

$$F(\zeta) = \Gamma - j\gamma + \sum_{n=1}^{\infty} (A_n - jB_n)\zeta^n, \quad |\zeta| \le 1.$$

Therefore, eq. (7.5) or eq. (7.7) defines the real part of $F(\zeta)$ and eq. (7.6) or eq. (7.8) the imaginary part. The problem of determining the function $F(\zeta)$ based on these real and imaginary parts is known as the Volterra problem [120, 122]. By applying Schwartz's formula,

$$F(\zeta) = \frac{H(\zeta)}{2\pi}\left\{-\sum_{i=1}^{N}\int_{\overbrace{a_i b_i}} \frac{\zeta'+\zeta}{\zeta'-\zeta}\cdot\frac{f_i(\theta')}{|H(\zeta')|}\cdot\frac{d\zeta'}{\zeta} + \sum_{i=1}^{N}\int_{\overbrace{b_i a_{i+1}}} \frac{\zeta'+\zeta}{\zeta'-\zeta}\cdot\frac{g_i(\theta')}{|H(\zeta')|}\cdot\frac{d\zeta'}{\zeta}\right\} - \Im\left[\frac{\Gamma - j\gamma}{jH(0)}\right]\cdot H(\zeta), \tag{7.10}$$

where θ' is the angle of ζ', $f_i(\theta')$ and $g_i(\theta')$ are defined as the right hand side of eqs. (7.5) and (7.6) or eqs. (7.7) and (7.8) respectively.

D. Homentcovschi further indicated that the unknown coefficients A_n's and B_n's and the constants Γ's and γ's are in fact the Maclaurin expansion coefficients of the function $F(\zeta)$. Matching the coefficient of ζ^n on the two sides of the eq. (7.10), one would obtain an infinite linear system for the determination of these unknowns [120].

Numerical Implementation

Obviously, one can not solve an infinite linear system with nowadays computers. Thanks to the quickly decaying property of η's defined previously as $n \to \infty$, the numerical solutions (especially for the resultant capacitances) converges quickly without considering too many higher harmonics. In fact, η's could be used as an index for selecting maximum harmonic order for a trade off between the accuracy and time.

The implementation detail is almost the same as what D. Homentcovschi documented in [120] and thus it is omitted here except for few things the author modified or added:

- Γ and γ are added in the $\mathbf{x}$ vector. Originally, these two constants may be substituted into the obtained linear system directly, however it is not obvious and not easy to implement in the computer program.

- Correspondingly, the Maclaurin expansion of ζ^0 is added into the linear system. However, the coefficients of the real part of this added equation are all zeros, which results in the matrix $\mathbf{R}$ not being full rank. This is where eq. (7.9) comes in to fill the gap.

- There are two linear systems in our case since it is three layered and has two $F(\zeta)$'s to match. Notice that $q_{br-g,l}$ and $q_{bs-g,l}$ are linearly dependent according to eq. (7.9). After adding eq. (7.9) into the two linear systems, the $\mathbf{R}$ matrix of the full system is not full rank. The trick is to swap one of the linear equation from eq. (7.9) with any equation in the compatibility conditions to make $\mathbf{R}$ invertible.

7.4 Field Solution for Non-Zero Thickness Electrodes

When it comes to non-zero thickness electrodes, D. Homentcovschi's method collapses at the side boundaries. However, this may be circumvented via approximating the real electrodes with volume by two or more zero thickness electrode lines because of

- the electrode thickness is much smaller than its width, which is also in favor of the torque production as discussed in Chapter 6;
- it is relatively easy to adapt D. Homentcovschi's method to a multi-layer structure.

Conformal Mapping

With the electrode thickness considered, the model depicted in Figure 6.2 may be conformally mapped into polar coordinate as shown in Figure 7.2b using the same analytical function as in eq. (7.1). Notice that the side boundaries are omitted and only two lines are used here for approximating each of the non-zero thickness electrodes. Figure 7.2a, same as Figure 6.2 except for the phasing part, is added here for the ease of reading.

It is straightforward to get the following relations

$$r_1 = \exp\left(-\frac{\pi(g+2t_{cr}+t_{br})}{L}\right),\ r_2 = \exp\left(-\frac{\pi(g+2t_{cr})}{L}\right),\ r_3 = \exp\left(-\frac{\pi g}{L}\right),$$

$$r_4 = \exp\left(\frac{\pi g}{L}\right),\ r_5 = \exp\left(\frac{\pi(g+2t_{cs})}{L}\right),\ r_6 = \exp\left(\frac{\pi(g+2t_{cs}+t_{bs})}{L}\right).$$

The angle α's and β's are still the same as before.

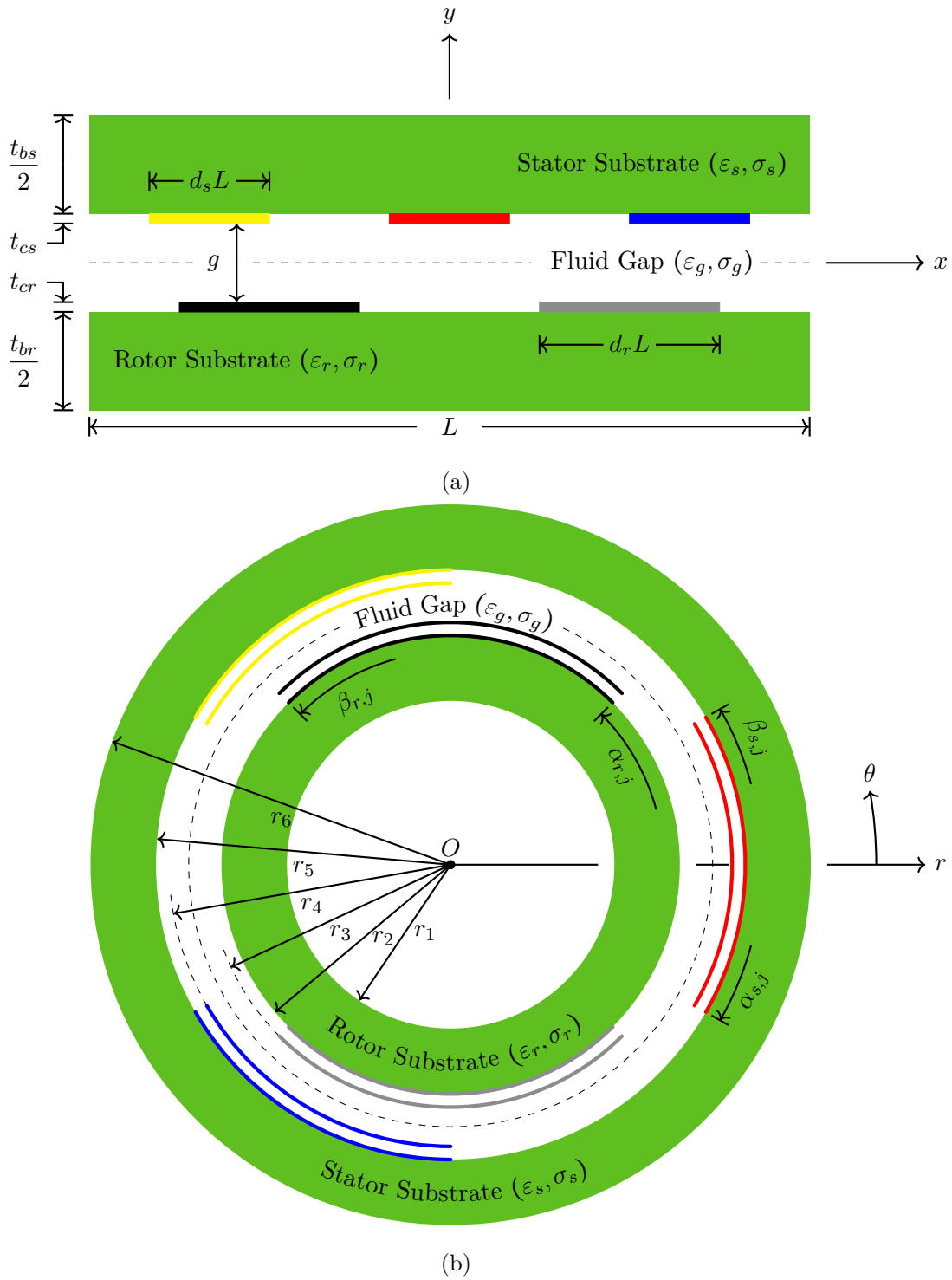

Figure 7.2: Redrawing of Figure 6.2 with non-zero thickness electrodes in (a) rectangular coordinate (b) polar coordinate. Dashed lines correspond to $y = 0$ and $r = 1$ respectively.

General Solution

There are five layers now in the formulated structure. Their field solution are denoted as $\phi_{br}, \phi_{cr}, \phi_g, \phi_{cs}$ and ϕ_{bs} corresponding to the call-out dimensions respectively. Based on the Neumann boundary conditions at $r = r_1$ and r_6, and the continuous boundary conditions at $r = r_2, r_3, r_4$ and r_5, the intermediate general field solution may be obtained as

$$\phi_{br}(r,\theta) = \Gamma_{br} + \sum_{n=1}^{\infty} S_n^+(r, r_1, r_2)\left[A'_{br,n}\cos(n\theta) + B'_{br,n}\sin(n\theta)\right], \tag{7.11}$$

$$\phi_{bs}(r,\theta) = \Gamma_{bs} + \sum_{n=1}^{\infty} S_n^+(r, r_6, r_5)\left[A'_{bs,n}\cos(n\theta) + B'_{bs,n}\sin(n\theta)\right], \tag{7.12}$$

$$\begin{aligned}\phi_{cr}(r,\theta) = (\Gamma_{br} - \Gamma_{cr})R_0^-(r, r_3, r_2) + \Gamma_{cr} &+ \sum_{n=1}^{\infty} R_n^-(r, r_3, r_2)\left[A'_{br,n}\cos(n\theta) + B'_{br,n}\sin(n\theta)\right] \\ &+ \sum_{n=1}^{\infty} R_n^-(r, r_2, r_3)\left[A'_{cr,n}\cos(n\theta) + B'_{cr,n}\sin(n\theta)\right],\end{aligned} \tag{7.13}$$

$$\begin{aligned}\phi_{cs}(r,\theta) = (\Gamma_{bs} - \Gamma_{cs})R_0^-(r, r_4, r_5) + \Gamma_{cs} &+ \sum_{n=1}^{\infty} R_n^-(r, r_5, r_4)\left[A'_{cs,n}\cos(n\theta) + B'_{cs,n}\sin(n\theta)\right] \\ &+ \sum_{n=1}^{\infty} R_n^-(r, r_4, r_5)\left[A'_{bs,n}\cos(n\theta) + B'_{bs,n}\sin(n\theta)\right],\end{aligned} \tag{7.14}$$

and

$$\begin{aligned}\phi_g(r,\theta) = (\Gamma_{cs} - \Gamma_{cr})R_0^-(r, r_3, r_4) + \Gamma_{cr} &+ \sum_{n=1}^{\infty} R_n^-(r, r_4, r_3)\left[A'_{cr,n}\cos(n\theta) + B'_{cr,n}\sin(n\theta)\right] \\ &+ \sum_{n=1}^{\infty} R_n^-(r, r_3, r_4)\left[A'_{cs,n}\cos(n\theta) + B'_{cs,n}\sin(n\theta)\right].\end{aligned} \tag{7.15}$$

Boundary Conditions

Now the coefficients are narrowed down to Γ's, A_n's and B_n's, which are up to the voltage level and location of the electrodes at the interface r_2, r_3, r_4 and r_5. Again, following D. Homentcovschi's approach, these coefficients should satisfy

$$\Gamma_{br} + \sum_{n=1}^{\infty}\left[A_{br,n}\cos(n\theta) + B_{br,n}\sin(n\theta)\right] = \phi_{br-cr,i} - \sum_{n=1}^{\infty}\eta_{br}(n)\left[A_{br,n}\cos(n\theta) + B_{br,n}\sin(n\theta)\right],$$
$$\text{for } \theta \in (\alpha_{r,i}, \beta_{r,i}),\ i \in (1, N_r) \tag{7.16}$$

$$-\gamma_{br}+\sum_{n=1}^{\infty}\left[A_{br,n}\sin(n\theta)-B_{br,n}\cos(n\theta)\right]=(\varepsilon_1+\varepsilon_2)^{-1}\left(\sum_{l=1}^{i}q_{br-cr,l}-\frac{\theta}{2\pi}\sum_{l=1}^{N_r}q_{br-cr,l}\right)+$$
$$\sum_{n=1}^{\infty}\frac{\varepsilon_2}{\varepsilon_1+\varepsilon_2}\cdot\frac{2r_2^nr_3^n}{r_3^{2n}-r_2^{2n}}\left[1-\eta_{cr}(n)\right]\left[A_{cr,n}\sin(n\theta)-B_{cr,n}\cos(n\theta)\right],$$
$$\text{for } \theta\in(\beta_{r,i},\alpha_{r,i+1}),\ i\in(1,N_r) \quad (7.17)$$

$$\Gamma_{bs}+\sum_{n=1}^{\infty}\left[A_{bs,n}\cos(n\theta)+B_{bs,n}\sin(n\theta)\right]=\phi_{bs-cs,i}-\sum_{n=1}^{\infty}\eta_{bs}(n)\left[A_{bs,n}\cos(n\theta)+B_{bs,n}\sin(n\theta)\right],$$
$$\text{for } \theta\in(\alpha_{s,i},\beta_{s,i}),\ i\in(1,N_s) \quad (7.18)$$

$$-\gamma_{bs}+\sum_{n=1}^{\infty}\left[A_{bs,n}\sin(n\theta)-B_{bs,n}\cos(n\theta)\right]=(\varepsilon_4+\varepsilon_5)^{-1}\left(\sum_{l=1}^{i}q_{bs-cs,l}-\frac{\theta}{2\pi}\sum_{l=1}^{N_s}q_{bs-cs,l}\right)+$$
$$\sum_{n=1}^{\infty}\frac{\varepsilon_4}{\varepsilon_4+\varepsilon_5}\cdot\frac{2r_4^nr_5^n}{r_5^{2n}-r_4^{2n}}\left[1-\eta_{cs}(n)\right]\left[A_{cs,n}\sin(n\theta)-B_{cs,n}\cos(n\theta)\right],$$
$$\text{for } \theta\in(\beta_{s,i},\alpha_{s,i+1}),\ i\in(1,N_s) \quad (7.19)$$

$$\Gamma_{cr}+\sum_{n=1}^{\infty}\left[A_{cr,n}\cos(n\theta)+B_{cr,n}\sin(n\theta)\right]=\phi_{cr-g,i}+\sum_{n=1}^{\infty}\eta_{cr}(n)\left[A_{cr,n}\cos(n\theta)+B_{cr,n}\sin(n\theta)\right],$$
$$\text{for } \theta\in(\alpha_{r,i},\beta_{r,i}),\ i\in(1,N_r) \quad (7.20)$$

$$-\gamma_{cr}+\sum_{n=1}^{\infty}\left[A_{cr,n}\sin(n\theta)-B_{cr,n}\cos(n\theta)\right]=(\varepsilon_2+\varepsilon_3)^{-1}\left(\sum_{l=1}^{i}q_{cr-g,l}-\frac{\theta}{2\pi}\sum_{l=1}^{N_r}q_{cr-g,l}\right)+$$
$$\sum_{n=1}^{\infty}\frac{\varepsilon_2}{\varepsilon_2+\varepsilon_3}\cdot\frac{2r_2^nr_3^n}{r_3^{2n}-r_2^{2n}}\left[1+\eta_{br}(n)\right]\left[A_{br,n}\sin(n\theta)-B_{br,n}\cos(n\theta)\right]+$$
$$\sum_{n=1}^{\infty}\frac{\varepsilon_3}{\varepsilon_2+\varepsilon_3}\cdot\frac{2r_3^nr_4^n}{r_4^{2n}-r_3^{2n}}\left[1-\eta_{cs}(n)\right]\left[A_{cs,n}\sin(n\theta)-B_{cs,n}\cos(n\theta)\right],$$
$$\text{for } \theta\in(\beta_{r,i},\alpha_{r,i+1}),\ i\in(1,N_r) \quad (7.21)$$

$$\Gamma_{cs}+\sum_{n=1}^{\infty}\left[A_{cs,n}\cos(n\theta)+B_{cs,n}\sin(n\theta)\right]=\phi_{cs-g,i}+\sum_{n=1}^{\infty}\eta_{cs}(n)\left[A_{cs,n}\cos(n\theta)+B_{cs,n}\sin(n\theta)\right],$$
$$\text{for } \theta\in(\alpha_{s,i},\beta_{s,i}),\ i\in(1,N_s) \quad (7.22)$$

$$-\gamma_{cs}+\sum_{n=1}^{\infty}\left[A_{cs,n}\sin(n\theta)-B_{cs,n}\cos(n\theta)\right]=(\varepsilon_3+\varepsilon_4)^{-1}\left(\sum_{l=1}^{i}q_{cs-g,l}-\frac{\theta}{2\pi}\sum_{l=1}^{N_s}q_{cs-g,l}\right)+$$

$$\sum_{n=1}^{\infty} \frac{\varepsilon_4}{\varepsilon_3+\varepsilon_4} \cdot \frac{2r_4^n r_5^n}{r_5^{2n}-r_4^{2n}}[1+\eta_{bs}(n)]\left[A_{bs,n}\sin(n\theta)-B_{bs,n}\cos(n\theta)\right]+$$
$$\sum_{n=1}^{\infty} \frac{\varepsilon_4}{\varepsilon_3+\varepsilon_4} \cdot \frac{2r_3^n r_4^n}{r_4^{2n}-r_3^{2n}}[1-\eta_{cr}(n)]\left[A_{cr,n}\sin(n\theta)-B_{cr,n}\cos(n\theta)\right],$$
$$\text{for } \theta \in (\beta_{s,i}, \alpha_{s,i+1}),\ i \in (1, N_s) \quad (7.23)$$

Among these conditions,

- Coefficients A_n's and B_n's relate to the primed ones through

$$\left(A'_{br,n}-jB'_{br,n}\right) = (A_{br,n}-jB_{br,n})[1+\eta_{br}(n)],$$
$$\left(A'_{bs,n}-jB'_{bs,n}\right) = (A_{bs,n}-jB_{bs,n})[1+\eta_{bs}(n)],$$
$$\left(A'_{cr,n}-jB'_{cr,n}\right) = (A_{cr,n}-jB_{cr,n})[1-\eta_{cr}(n)],$$
$$\left(A'_{cs,n}-jB'_{cs,n}\right) = (A_{cs,n}-jB_{cs,n})[1-\eta_{cs}(n)].$$

- Variables $\eta_{br}(n), \eta_{bs}(n), \eta_{cr}(n)$ and $\eta_{cs}(n)$ are defined as

$$\eta_{br}(n) = \frac{\delta_{br}(n)}{1-\delta_{br}(n)}, \quad \delta_{br}(n) = \frac{2\varepsilon_1}{\varepsilon_1+\varepsilon_2} \cdot \frac{r_1^{2n}}{r_1^{2n}+r_2^{2n}} + \frac{2\varepsilon_2}{\varepsilon_1+\varepsilon_2} \cdot \frac{r_2^{2n}}{r_2^{2n}-r_3^{2n}},$$
$$\eta_{bs}(n) = \frac{\delta_{bs}(n)}{1-\delta_{bs}(n)}, \quad \delta_{bs}(n) = \frac{2\varepsilon_4}{\varepsilon_4+\varepsilon_5} \cdot \frac{r_4^{2n}}{r_4^{2n}-r_5^{2n}} + \frac{2\varepsilon_5}{\varepsilon_4+\varepsilon_5} \cdot \frac{r_5^{2n}}{r_5^{2n}+r_6^{2n}},$$
$$\eta_{cr}(n) = \frac{\delta_{cr}(n)}{1+\delta_{cr}(n)}, \quad \delta_{cr}(n) = \frac{2\varepsilon_2}{\varepsilon_2+\varepsilon_3} \cdot \frac{r_2^{2n}}{r_3^{2n}-r_2^{2n}} + \frac{2\varepsilon_3}{\varepsilon_2+\varepsilon_3} \cdot \frac{r_3^{2n}}{r_4^{2n}-r_3^{2n}},$$
$$\eta_{cs}(n) = \frac{\delta_{cs}(n)}{1-\delta_{cs}(n)}, \quad \delta_{cs}(n) = \frac{2\varepsilon_3}{\varepsilon_3+\varepsilon_4} \cdot \frac{r_3^{2n}}{r_4^{2n}-r_3^{2n}} + \frac{2\varepsilon_4}{\varepsilon_3+\varepsilon_4} \cdot \frac{r_4^{2n}}{r_5^{2n}-r_4^{2n}}.$$

- Charge $q_{br-cr,l}, q_{bs-cs,l}, q_{cr-g,l}$ and $q_{bs-g,l}$ are the total amout on the l-th electrodes at the *br-cr*, *bs-cs*, *cr-g* and *cs-g* interface respectively, which relate to $\Gamma_{br}, \Gamma_{bs}, \Gamma_{cr}$ and Γ_{cs} through

$$\sum_{l=1}^{N_r} q_{br-cr,l} = -2\pi\varepsilon_2 \cdot \frac{\Gamma_{br}-\Gamma_{cr}}{\ln(r_2/r_3)}, \quad \sum_{l=1}^{N_r} q_{cr-g,l} = 2\pi\varepsilon_2 \cdot \frac{\Gamma_{br}-\Gamma_{cr}}{\ln(r_2/r_3)} - 2\pi\varepsilon_3 \cdot \frac{\Gamma_{cr}-\Gamma_{cs}}{\ln(r_3/r_4)}, \quad (7.24)$$
$$\sum_{l=1}^{N_s} q_{bs-cs,l} = -2\pi\varepsilon_4 \cdot \frac{\Gamma_{bs}-\Gamma_{cs}}{\ln(r_4/r_5)}, \quad \sum_{l=1}^{N_s} q_{cs-g,l} = 2\pi\varepsilon_3 \cdot \frac{\Gamma_{cr}-\Gamma_{cs}}{\ln(r_3/r_4)} + 2\pi\varepsilon_4 \cdot \frac{\Gamma_{bs}-\Gamma_{cs}}{\ln(r_4/r_5)}. \quad (7.25)$$

- Constants $\gamma_{br}, \gamma_{bs}, \gamma_{cr}$ and γ_{cs} define the starting points of charge counting.

- Voltages $\phi_{br-g,i}, \phi_{bs-g,i}, \phi_{cr-g,i}$ and $\phi_{cs-g,i}$ are from the corresponding i-th rotor and stator electrodes.

- Integers N_r, N_s are the number of the rotor and stator electrodes.

Analytical Solution

The derivation for the analytical solution is similar to zero thickness case except for having two more linear systems in the computation loop. It is therefore dropped here.

Numerical Implementation

The numerical implementation is also similar except for the following changes:

- One more equation has to be swapped out from the full matrix $\mathbf{R}$ to keep it invertible due to eqs. (7.24) and (7.25).
- The condition number of the full matrix $\mathbf{R}$ in this case may be relatively high because the field coupling every other row(s) is weak, however this is not destructive. It would lower the accuracy of the capacitance evaluation, but only to a not noticeable amount. For the data shown in this thesis using this proposed analytical approach, the relative accuracy of the capacitance evaluation drops from 10^{-15} to 10^{-12}.

7.5 Comparison Study with FEA

The correctness of these two analytical methods assuming zero and non-zero thickness are verified with the FE results. Figures 7.3 and 7.4 document an example case, where phase A is aligned with the q-axis and the potential on the traces are set to

$$v_{as} = 1.0\,\mathrm{V}, \quad v_{bs} = -0.5\,\mathrm{V}, \quad v_{cs} = -0.5\,\mathrm{V}, \quad v_{+f} = 1.0\,\mathrm{V}, \quad v_{-f} = -1.0\,\mathrm{V}.$$

These two analytical approach are also implemented in the sweep analysis in the last Chapter with harmonic order counted to 10. They are labelled as “Analytical 1” and “Analytical 2” respectively. The corresponding computational time, including the approximation method proposed in Chapter 6 and FEA, are documented in Table 7.1. Several observations may be made

- With the thickness of the electrode considered, it is definitely more accurate than without. However the computational time is more than two times higher;

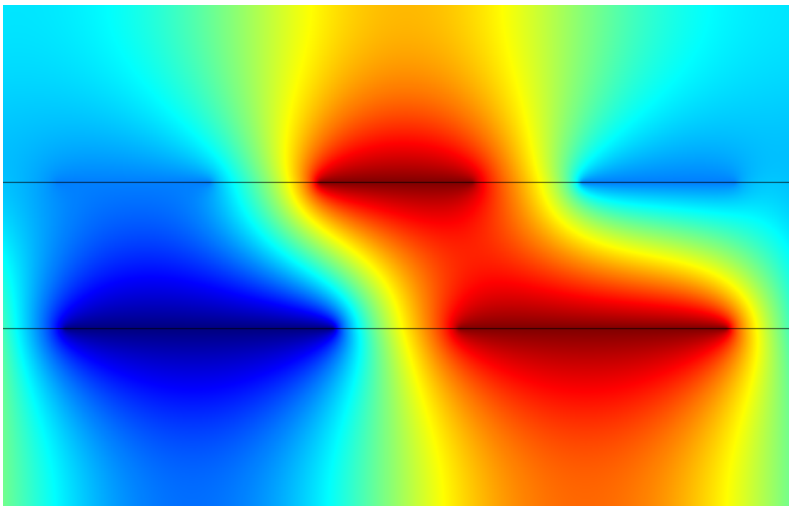

(a)

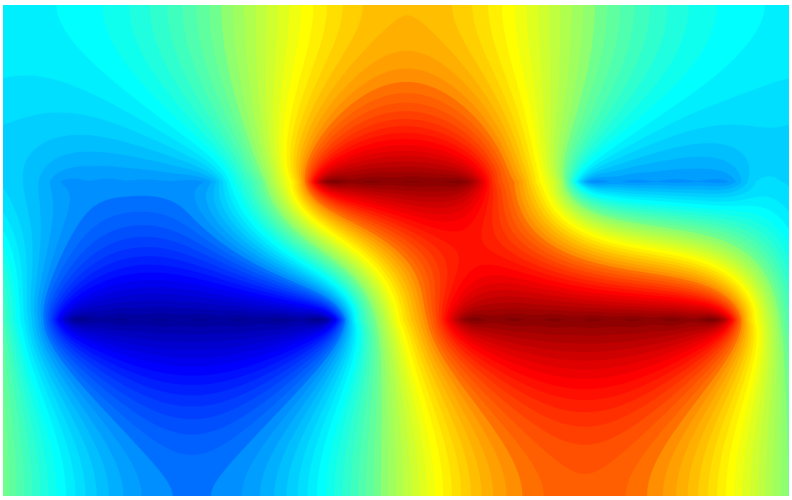

(b)

Figure 7.3: Potential distribution of the designed machine at mean radius assuming electrodes of zero thickness. (a) FEA (b) analytical.

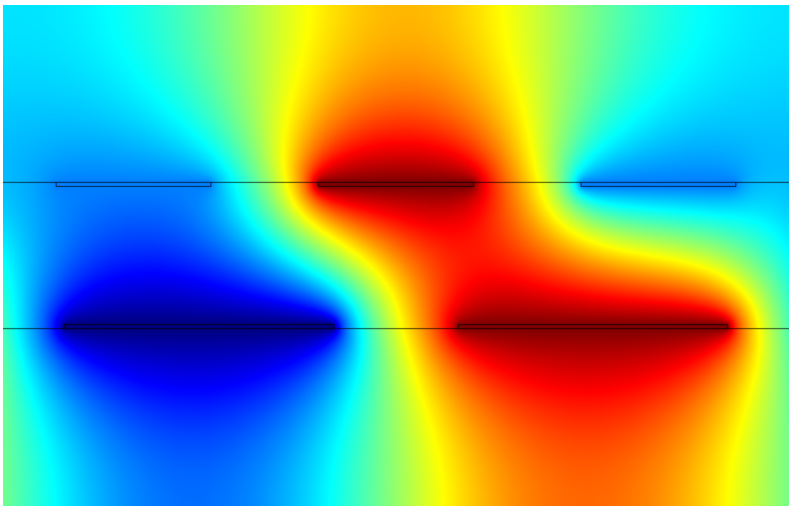

(a)

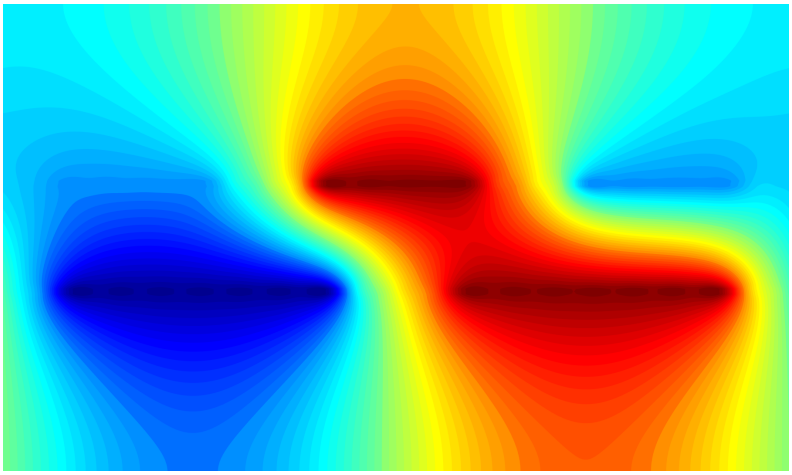

(b)

Figure 7.4: Potential distribution of the designed machine at mean radius assuming electrodes of non-zero thickness. (a) FEA (b) analytical.

Table 7.1: Summary of Computational Time for Different Torque Evaluation Methods

Sweep for	Result in Plot	Linear Approx. Time/Case, hrs	Analytical 1 Time/Case, hrs	Analytical 2 Time/Case, hrs	FEA Time/Case, hrs
$\varepsilon_g/\varepsilon_0$	Figure 6.6	3.3E-7	0.1	0.24	9.1
g	Figure 6.8	1.1E-7	0.1	0.24	9.2
P	Figure 6.9	3.6E-7	0.1	0.24	11.7

- For the FEA, the computational time depends on the size of the model, which is why the time consumption is higher for pole number sweeping;
- To take advantages of each method, they may be implemented at different design optimization stage of the proposed machine, i.e. use the linear approximation at the early phase to instantly size the machine, the analytical method to quickly determine the circuit parameters and the FEA to tune the details especially for the inactive region.

It is also worth to mention that these analytical methods are implemented in the Matlab environment. The computational time could be significantly reduced by using Fortran.

7.6 Summary

An analytical capacitance evaluation model is derived. It is further refined by visioning the physical geometry as mathematically solvable geometry. The model could also be modified to solve the static current field at the same time by simply swapping dielectric permittivity with electrical conductivity. Furthermore, thanks to the simplicity and scalability of the applied fundamental method, it may be extended to other electrostatic machine topologies, i.e. single/multi-phase, axial/radial flux, etc.

8 EXPERIMENTAL RESULTS

Ours is a life of constant reruns. We're always circling back to where we'd started, then starting all over again. Even if we don't run extra laps that day, we surely will come back for more of the same another day soon.

— Joe Henderson

8.1 Introduction

This chapter presents a prototype machine and the corresponding experimental results. The experiment consists of two main parts: 1) identifing the equivalent circuit parameters via short and open circuit tests and 2) benchmarking its torque performance by sweeping the excitation. The results are also compared to the designed and simulated ones to validate the models in Chapters 5–7, i.e. *dq*-axis, machine design and analytical capacitance calculation models.

8.2 Prototype Machine

An axial flux style three phase synchronous electrostatic machine (SEM) using printed circuit boards (PCB) as the main torque producing components is built here and shown in Figures 8.1 and 8.2. It is designated as *SEM 1* throughout this chapter and its design details will be presented below.

Mechanical Design

SEM 1 consists of 7 stator boards and 6 rotor boards (i.e., $N = 6$), all of which are double sided and two layered except for the stator end ones. Three sets of traces are consecutively and symmetrically laid out on the stator and two on the rotor as shown in Figure 8.3. Balanced three phase stator voltages are fed from the back side of SEM 1. A bipolar DC voltage is applied on the rotor through a slip ring and a hollow shaft. The spacers shown in Figure 8.1a serve two purposes: 1) maintaining mechanical space between the stator and rotor boards and 2) transmitting voltage and current through the whole stack. The stator-rotor gap is filled with a dielectric liquid

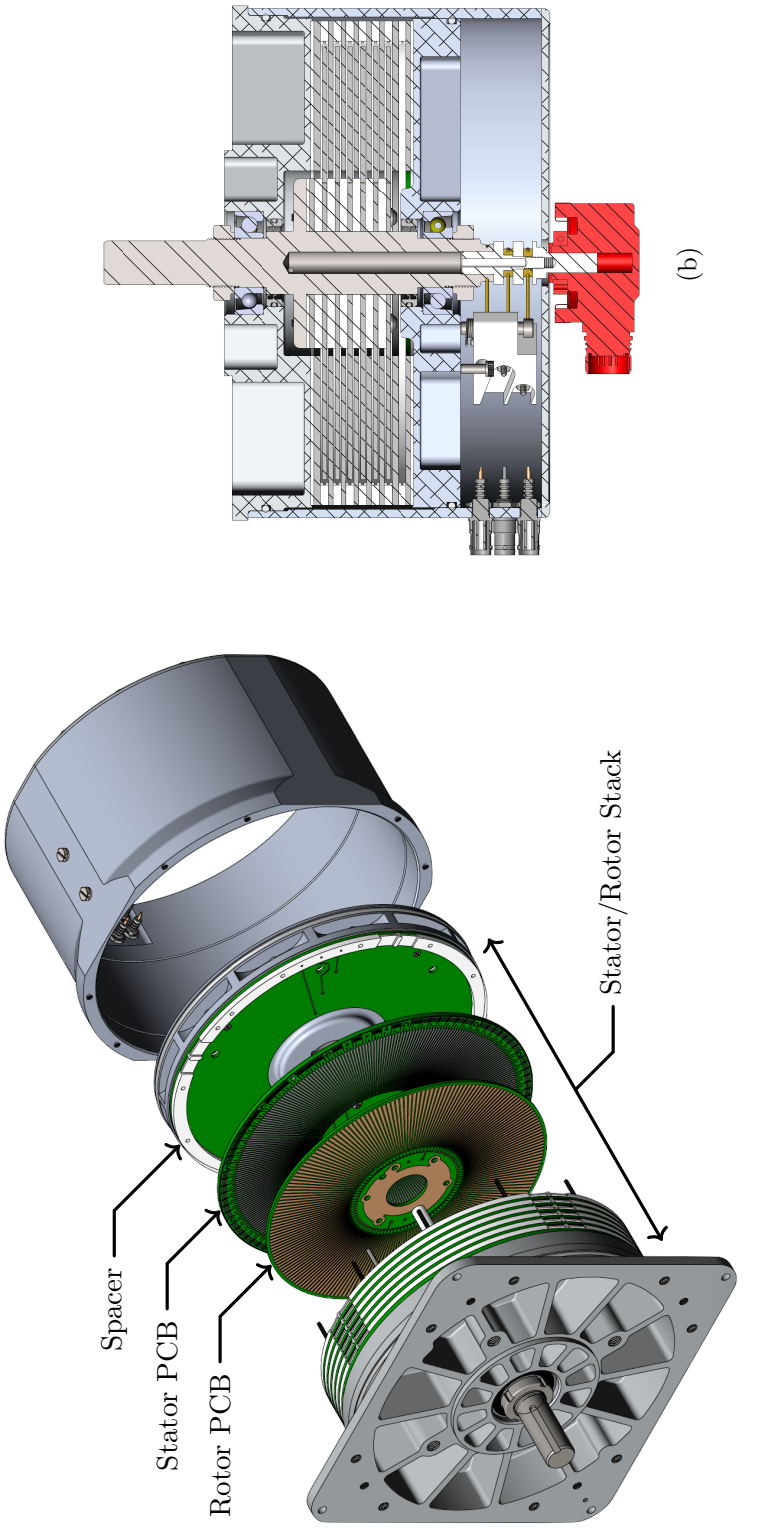

Figure 8.1: CAD Gallery of SEM 1. (a) Exploded view (b) section view.

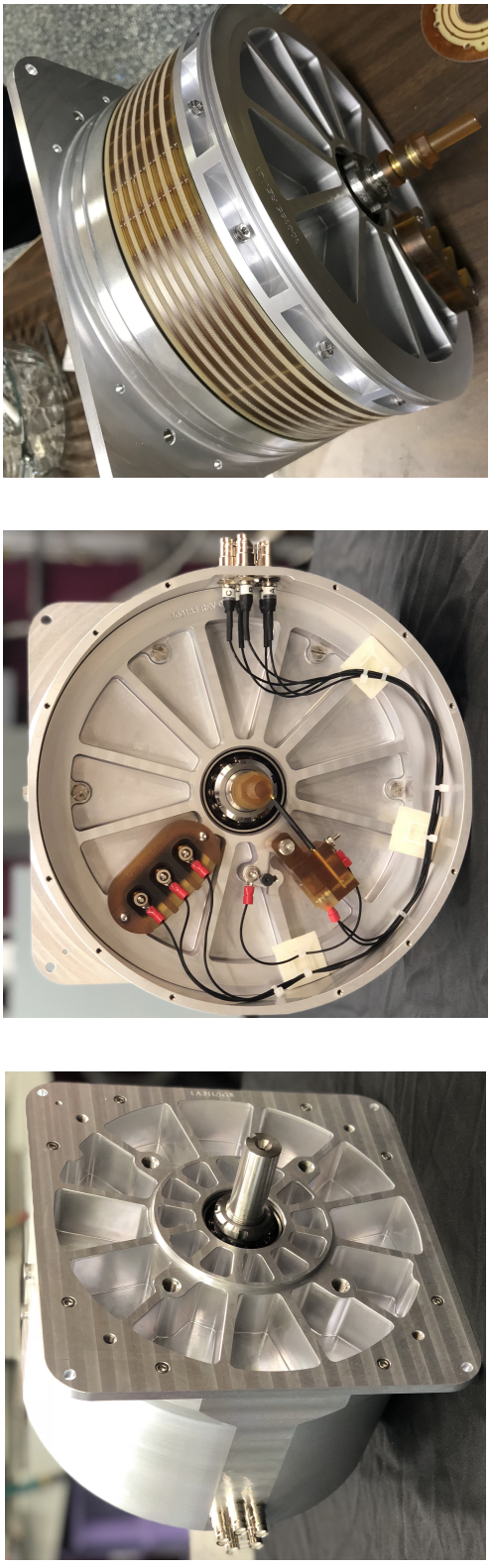

(a) (b) (c)

Figure 8.2: Photographs of SEM 1. (a) Front view (b) back view (c) without case.

(a)

(b)

Figure 8.3: Photograph of the (a) stator and (b) rotor PCB boards used in SEM 1 machine.

Table 8.1: SEM 1 Prototype Machine Dimensions and Parameters.

Parameters	Notation	Value	Unit	Parameters	Notation	Value	Unit
substrate thickness	t_{cs}, t_{cr}	90	mil	machine effective length	$2Nl_g$	37.41	mm
electrode thickness	c_{cs}, c_{cr}	1	oz	number of rotor plates	N	6	—
minimum gap	g	30	mil	number of stator plates	$N+1$	7	—
stack length per gap	l_g	3.12	mm	pole number	P	96	—
stator inner radius	r_{si}	47.46	mm	total weight	—	12.20	kg
stator outer radius	r_{so}	110.00	mm	total volume	—	5.20	L
rotor inner radius	r_{ri}	44.92	mm	machine outer diameter	—	10.25	in
rotor outer radius	r_{ro}	107.46	mm	machine axial length	—	6.50	in
stator trace clearance	$2\pi r d_s/P$	0.69	mm	stator peak voltage	V_s	4	kV
rotor trace clearance	$2\pi r d_r/P$	0.80	mm	rotor peak voltage	V_{fr}	8	kV

called *HT101* possessing a dielectric constant of 3.8 and a breakdown strength of 20 kV/mm. The mechanical enclosure of SEM 1 and the liquid HT101 are provided by the start-up company *C-Motive Technologies*. The concept of using PCBs has been demonstrated in a single phase switched elastance (variable capacitance) machine by this company in [55], therefore the peripheral mechanical details are skipped here.

The design parameters of SEM 1 are listed in Table 8.1. Notice that the pole number P and stator inner radius r_{si} are not designed according to the optimal value shown in eq. (6.19). The thought was: 1) presented in Chapter 6, the clearance between the active traces are constant, which leads to the trace width at the inner radius very small. The minimum trace width (≈ 10 mil) used in SEM 1 is bigger than the manufacturing capability $\delta \approx 5$ mil for cost reduction and 2) the misalignment issue would be severe at higher pole count considering first time trying.

Drive Circuit

The drive circuit of SEM 1 is temporarily implemented using relatively mature and easy to implement techniques given its requirement for high voltage (HV) at a moderate power level. The stator side is excited with a voltage source inverter (VSI) and a step up transformer with a three phase LC filter

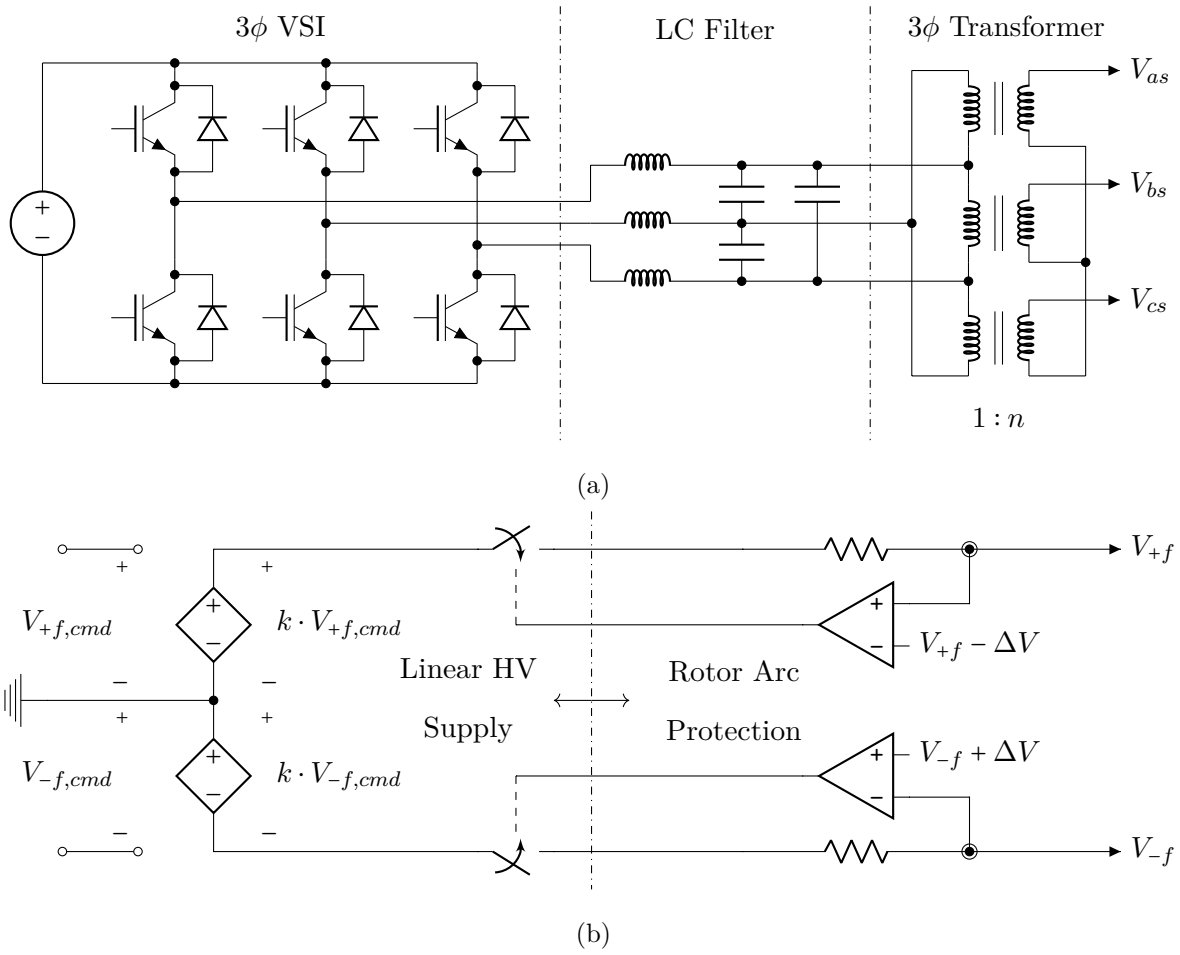

Figure 8.4: Schematic of the drive circuit at the (a) stator side and (b) rotor side.

in between as shown in Figure 8.4a. The transformer is in Δ-Y connection for a balanced output. Aside from the 30° difference between the secondary and primary of the transformer, the voltage is modulated with a standard space vector pulse width modulation. The rotor side is fed with two linear HV supplies, whose output can be manipulated by the commands with a transformation ratio $k = 1000$. To protect the PCB boards from potential damage caused by arcing, HV resistors ($500\,\mathrm{k\Omega}$) are added in series at the supply output for limiting the transient current. Furthermore, the voltages at the rotor terminals are sensed and compared to preset thresholds, the result of which are used to disable the linear supplies if breakdown happens.

8.3 Short Circuit Back-MMF Test

Circuit Setup

Just like the open circuit back-EMF test in the magnetic machines, here we do the short circuit back-MMF test to identify the coupling capacitance between the stator and the rotor, i.e. C_m. Given the fact that the to be measured current is very small and at mA level, the back-MMF measurement is indirectly done by voltage measurement using regular 10X probes. Therein SEM 1 is connected with three phase Y connected 75 Ω load resistance. Referring to Figure 8.5, the leakage resistance r_s and stator reactance $1/\omega_r C_s$ is much larger than 75 Ω. Hence it is almost like a short circuit to the machine and almost all of the current still flow into the load resistance, i.e. $\underline{I}_s \approx \omega_r C_m V_{fr}$.

Experimental Results

Figure 8.6 plots the measured average (over three phase) fundamental peak current $\bar{I}_{s,pk}$ as a function of the rotor excitation $V_{fr} = V_{+f} - V_{-f}$ for different mechanical speed n_r. Theoretically, the slope of each line should be $\omega_r C_m$, where $\omega_r = 2\pi n_r P/60$. By averaging the curve fitting results, one may back out the mutual capacitance $C_m = 2.028$ nF. Notice that the fitted slope for each line is proportional to the speed, i.e. almost no current flows in the $r_s//C_s$ branch as the frequency goes up, which validates the above short circuit proof.

Figure 8.7 shows the waveform quality of the back-MMF at $V_{fr} = 4.2$ kV and $n_r = 300$ rpm. The spikes in the time domain is due to the radiation noise from the dynamometer switching at 10 kHz.

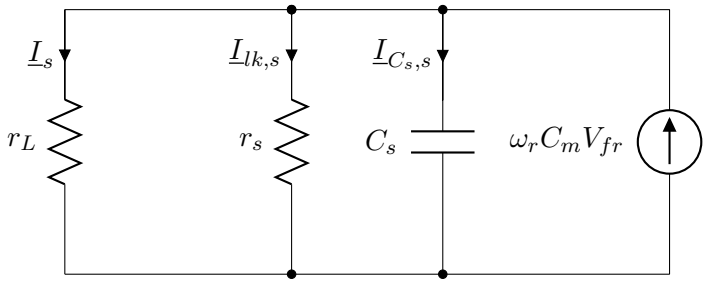

Figure 8.5: Single phase diagram of the short circuit test. $r_L = 75\,\Omega$.

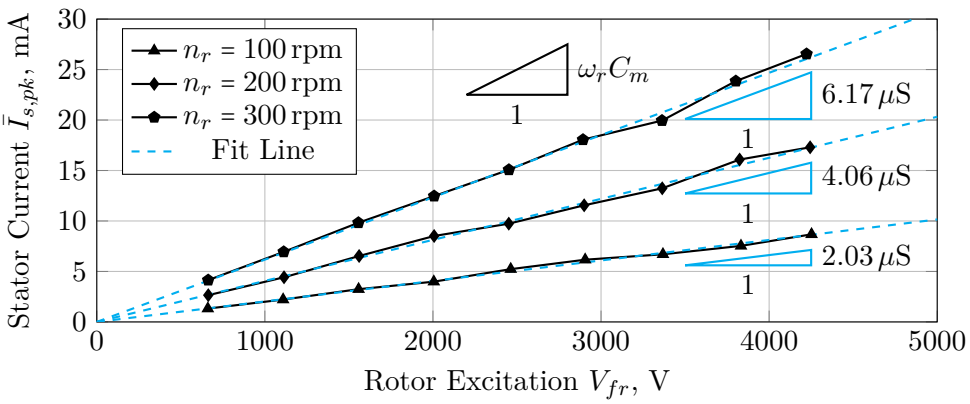

Figure 8.6: Short circuit peak current as a function of the rotor excitation. Fit line $\bar{I}_{s,pk} = k \cdot V_{fr}$.

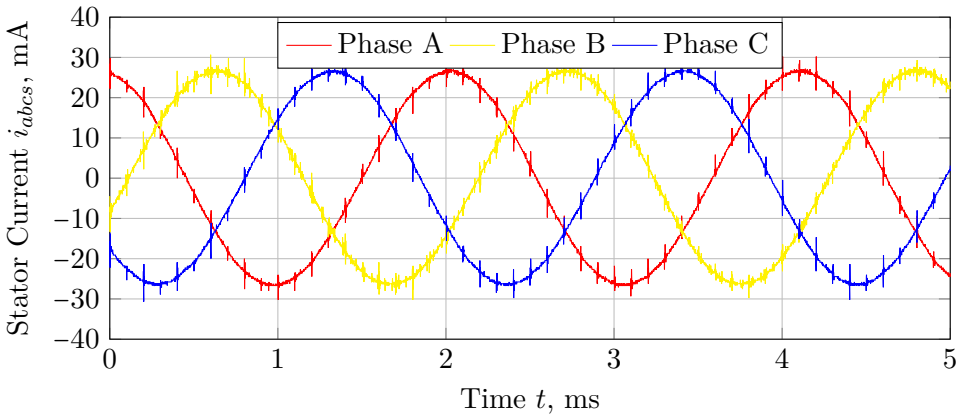

(a)

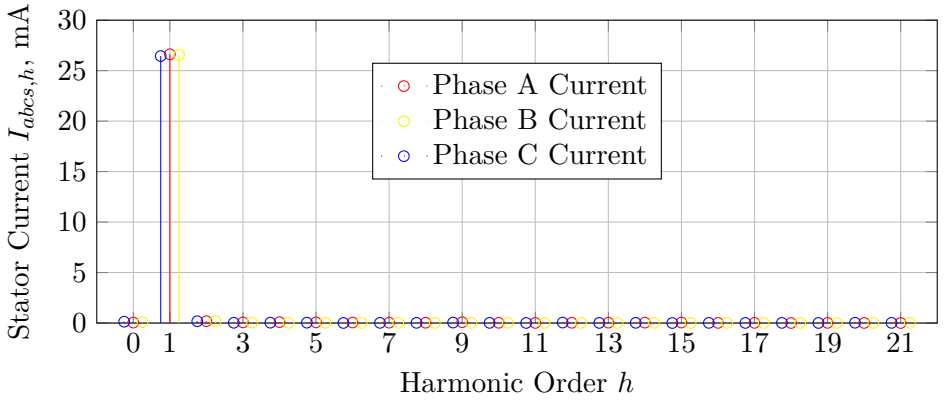

(b)

Figure 8.7: Measured back-MMF in the (a) time domain (10 kHz spikes/noise is from the dynamometer) and (b) frequency domain for V_{fr} = 4.2 kV and n_r = 300 rpm.

Other than that, the harmonic content of the waveform is almost zero as shown in Figure 8.7b. The total harmonic distortion (THD) is 0.88% up to 51st harmonic for the presented waveform and less than 3% for all the data points shown in Figure 8.6. This indicates that this machine may be suitable for potential servo applications.

8.4 Open Circuit Voltage Test

Circuit Setup

Just like the short circuit test in the magnetic machines to measure the characteristic current, here we do the open circuit test to measure the characteristic voltage and identify the synchronous capacitance, i.e. C_s.

Experimental Resutls

Figure 8.8 plots the measured stator fundamental peak voltage $V_{s,pk}$ as a function of the rotor excitation V_{fr} for different mechanical speed n_r. Notice that the voltages are different between phases and the difference becomes larger as the speed goes up. However the average of them for different speeds are almost the same. It is due to the leakage path in the inactive area, where the routing of the traces could not be done symmetrically with two layer PCB boards. Different excitation frequency would change the proximity effect among these routing traces and redistribution only happens among the phases, therefore the average voltage is not a function of the speed.

Since the mutual capacitance C_m is known, we may use it to calculate the internal current $\omega_r C_m V_{fr}$. By Ohm's law, the division of the open circuit voltage and the corresponding internal current should be the equivalent impedance of the r_s and C_s parallel branch. Figure 8.9 plots this impedance as a function of the electrical frequency $f_e = n_r P/60$, the curve fitting of which could be used to back out r_s and C_s. However, as will be seen later, the leakage resistance r_s is about $1 \sim 2$ orders higher than $r_s//C_s$. From the mathematical point of view, it is not accurate or not even feasible to back out r_s from here. Therefore the curve fitting in the plot only counts for C_s. The result is $C_s = 13.8\,\text{nF}$. It is much larger than C_m, which causes the power factor of SEM 1 is

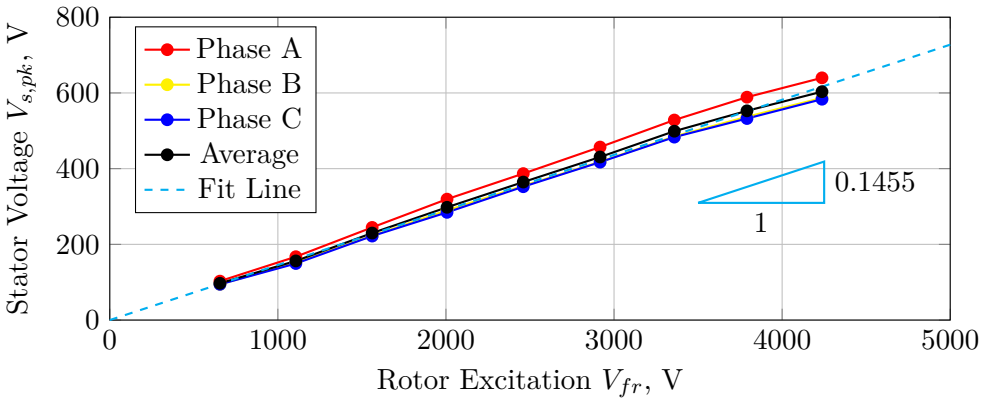

(a) n_r = 100 rpm

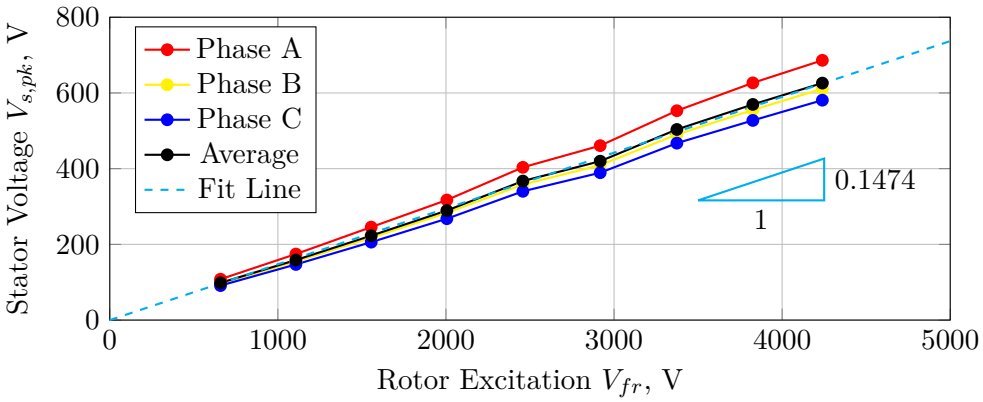

(b) n_r = 200 rpm

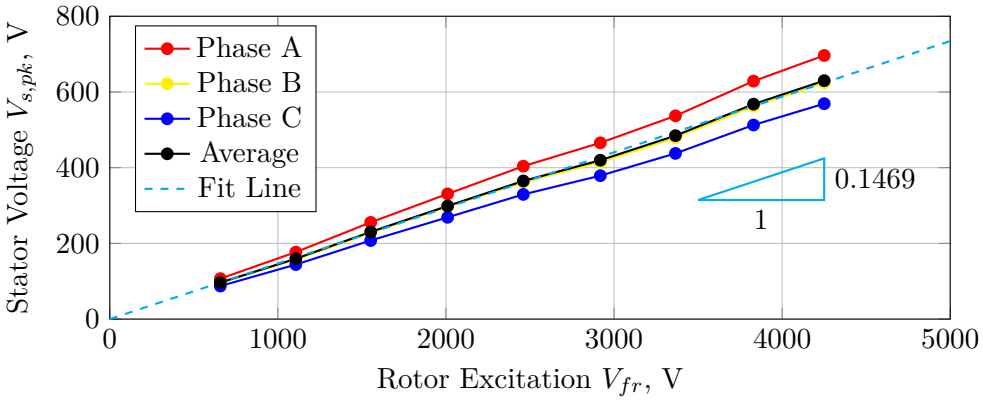

(c) n_r = 300 rpm

Figure 8.8: Open circuit voltage as a function of the rotor excitation. Fit line $\bar{V}_{s,pk} = k \cdot V_{fr}$, where $k = |\omega_r r_s C_m / (1 + j\omega_r r_s C_s)|$ theorectically.

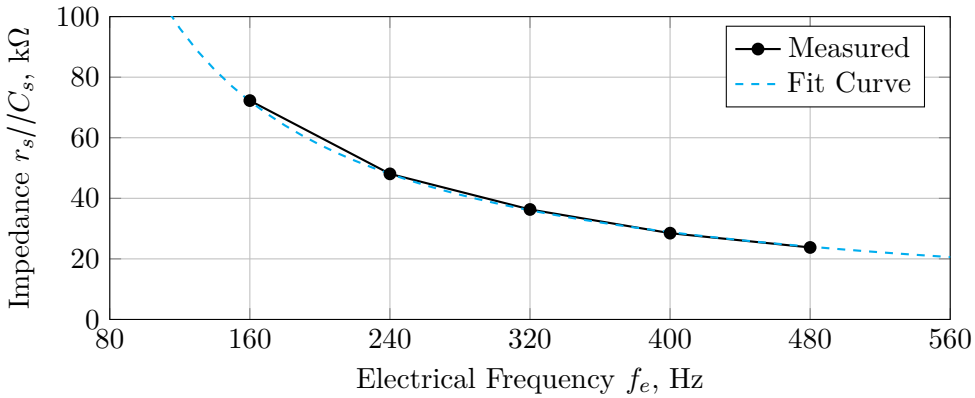

Figure 8.9: Internal impedance of the machine as a function of the electrical frequency. Fit curve $X_s = k/2\pi f_e$, where $k = 1/C_s$ theorectically.

relatively low as will be seen later. Being a high pole count machine for the most torque production, SEM 1 also possesses a significantly large amount of leakage. This should be taken into account in the future design.

8.5 Loss Mechanism

The loss of this machine is mainly from the stator leakage resistance r_s, the rotor leakage resistance r_{fr} and the mechanical friction. These loss mechanisms will be benchmarked next.

Stator Leakage Loss

The stator leakage loss could be measured by exciting the stator with three phase voltages at standstill with the rotor held at zero voltage at the same time and measuring the current of each phase. The total power going into the machine should be consumed by the stator leakage in this condition. Figure 8.10 plots the measured three phase power as a function of the stator excitation voltage $\bar{V}_s$ with $f_e = 480\,\text{Hz}$, the slope of which should be $3/r_s$ based on the above analysis. The curve fitting result gives $r_s = 1.70\,\text{M}\Omega$.

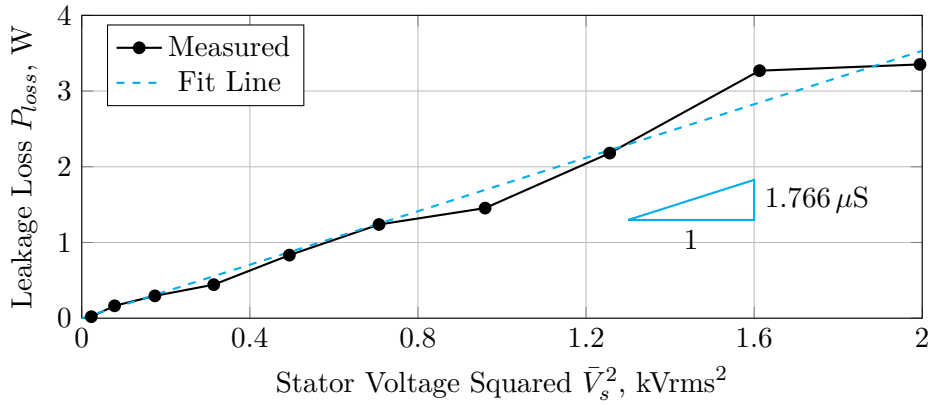

Figure 8.10: Stator leakage loss as a function of the excitation voltage. Fit line $P_{loss} = 3\bar{V}_s^2/r_s$.

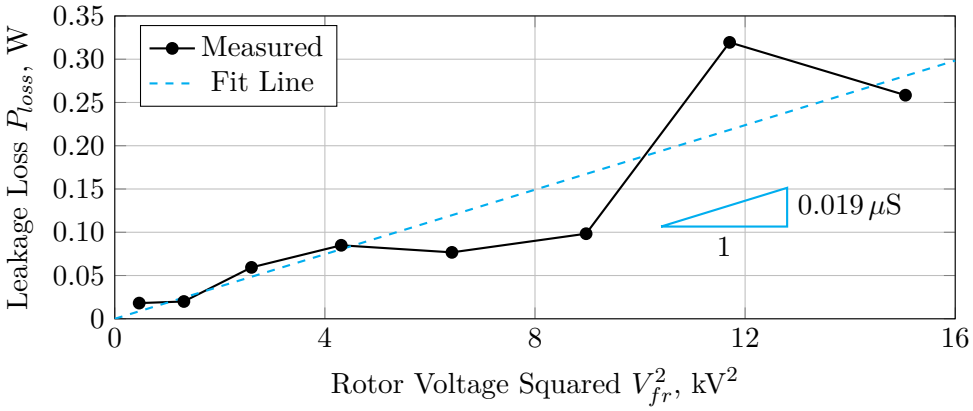

Figure 8.11: Rotor leakage loss as a function of the excitation voltage. Fit line $P_{loss} = V_{fr}^2/r_{fr}$.

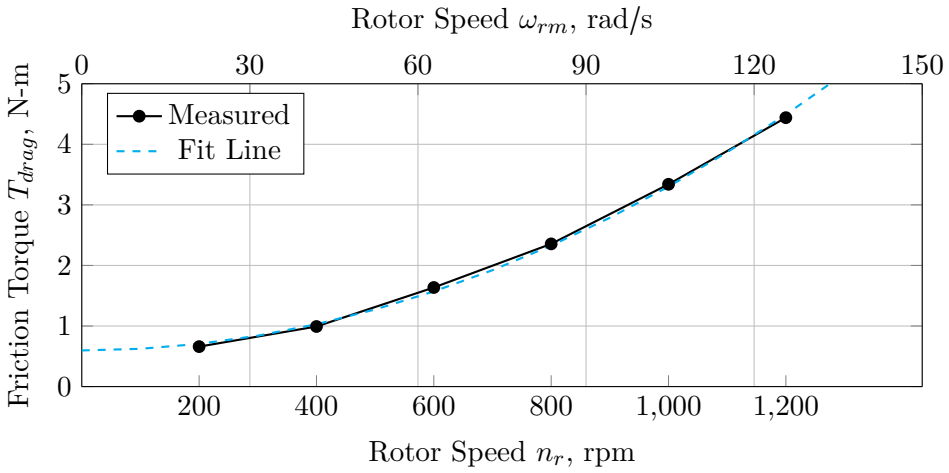

Figure 8.12: Friction torque as a function of the rotor mechanical speed. Fit line $T_{drag} = \beta\omega_{rm}^2 + T_0$.

Rotor Leakage Loss

The rotor leakage loss could be measured in a similar way, i.e. by exciting the rotor with symmetrical voltages at standstill with the stator terminals held at zero voltage at the same time and measuring the rotor current. The total power going into the machine should be consumed by the rotor leakage in this condition. Figure 8.11 plots the measured DC power as a function of the rotor excitation voltage $\bar{V}_{fr}$, the slope of which should be $1/r_{fr}$ based on the above analysis. The curve fitting result gives $r_{fr} = 52.6\,\mathrm{M\Omega}$. (The probes for measuring the rotor terminal voltages have an internal resistance of $100\,\mathrm{M\Omega}$, which is also included in the current calculating.) Notice that this value is more than one order higher than r_s, which may be because the DC conductivity is significantly lower than the AC one for the dielectric materials used here, i.e. FR4 and HT101.

Friction Loss

The friction loss includes bearing friction, seal friction, slip ring friction and viscosity drag due to the dielectric liquid. The corresponding torque is measured through the torque transducer coupled with the dynamometer. Figure 8.12 documents the test results for a speed sweep. The curve fitting result gives $T_{drag} = 2.47 \times 10^{-4}\omega_{rm}^2 + 0.5698\,[\text{N-m}]$. Clearly SEM 1 has a relatively big friction torque at nearly zero speed, which is about 6% of the full torque. It should be improved in the future for a better efficiency. Furthermore, the drag torque ramps up quickly as the speed goes up, which indicates that it is more realistic to run SEM 1 below 300 rpm or under for the liquid currently used in SEM 1. Therefore the speed of the machine in the tests presented here are no more than 300 rpm.

8.6 Torque Test

The torque test is conducted in two paths: 1) keep the torque angle $\gamma = \pi$ and sweep the excitation V_s and V_{fr} and 2) keep the excitation V_s and V_{fr} constant and sweep the torque angle γ, which verify T_e is proportional to $V_s V_{fr}$ and $\cos(\gamma)$ respectively.

At the time of testing, the VSI drive circuit faced noise issue and could not output more than 2 kV without tripping the protection circuit. The theoretical torque value at this voltage level is

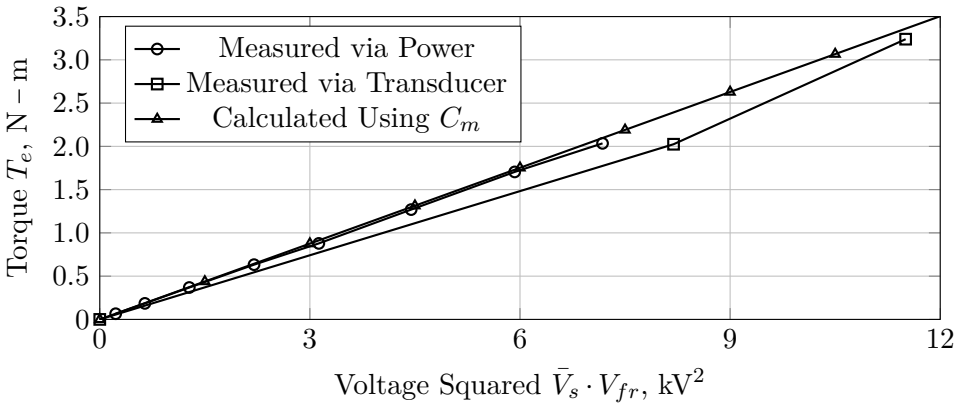

Figure 8.13: Measured electrostatic torque as a function of the excitation $\bar{V}_s V_{fr}$ at $n_r = 300\,\text{rpm}$.

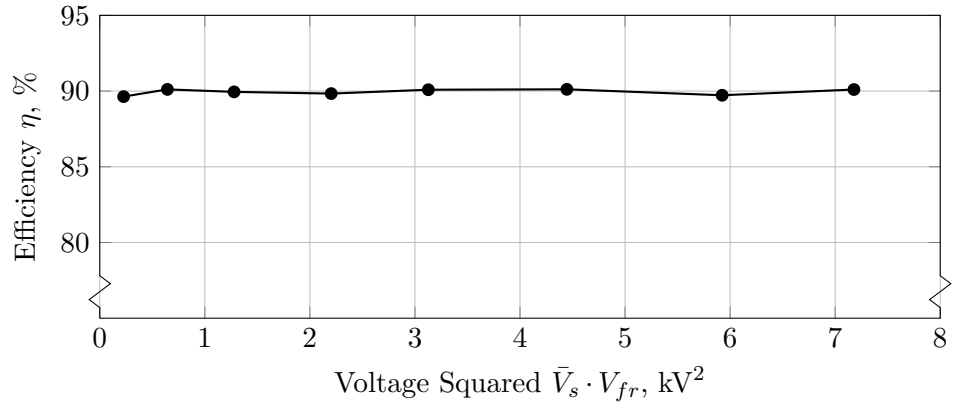

Figure 8.14: The efficiency as a function of the excitation $\bar{V}_s V_{fr}$ at $n_r = 300\,\text{rpm}$.

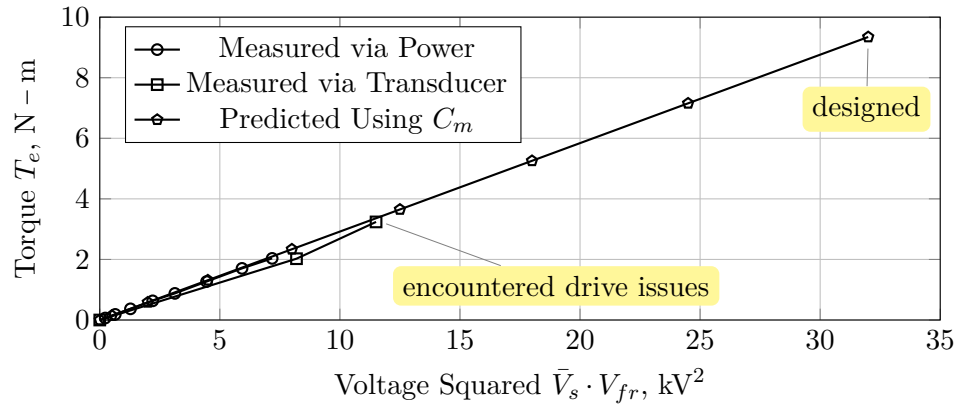

Figure 8.15: Predicted electrostatic torque as a function of the excitation $\bar{V}_s V_{fr}$.

close to the torque transducer's resolution. In order to have a better comparison, the torque value presented next are calculated through power, i.e. dividing the total gap power (measured stator input power subtract the stator leakage loss) by the rotor mechanical speed (this is exactly how torque is derived in the dq-axis model).

Torque vs. Voltage

Figure 8.13 shows the measured torque as a function of the excitation $\bar{V}_s V_{fr}$ at $n_r = 300\,\text{rpm}$. It is overlaid with the calculated torque using eq. (5.31) and the mutual capacitance C_m measured from the short circuit test. It also includes three measured data points from the torque transducer after the drive circuitry has been modified and improved. (However the stator PCB boards are broken when we tried to get more torque data at even higher voltages. Therefore the stator side should also paired with an arc protection like Figure 8.4b for the rotor in the future.) Although these points are still around the resolution range of the torque transducer, they are very close to the trend.

Figure 8.14 presents the corresponding efficiency data at each work point excluding the friction loss. Regardless the excitation level, the efficiency is alwasy around 95%, which is consistent with the circuit model since both the torque and the leakage loss are proportional to squared voltage. (For this test, the stator peak to peak voltage is maintained roughly the same as the rotor excitation V_{fr}, therefore $\bar{V}_s V_{fr} \approx 2\bar{V}_s^2$.)

Figure 8.15 extends the torque line to the designed full excitation, i.e. $V_s = 4\,\text{kV}$ and $V_{fr} = 8\,\text{kV}$. It shows the obtained torque value either calculated by power method or measured through the torque transducer are right on the trend. At full excitation, the predicted torque is 9.35 N-m.

Torque vs. γ

Figure 8.16 plots the torque as a function of the torque angle γ under different excitation level. The angle γ was commanded at $-260, -240, -210, -180, -150, -120$ and -100 electrical degrees respectively. This plot shows that the torque production of the proposed machine is proportional to $\cos(\gamma)$, as derived in Chapter 5.

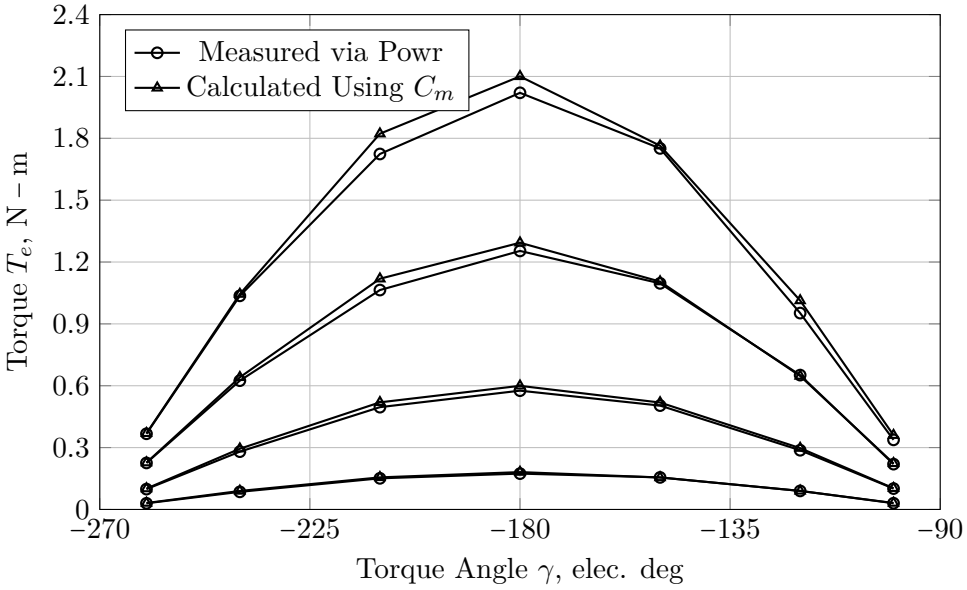

Figure 8.16: Measured electrostatic torque as a function of the torque angle γ at $n_r = 300\,\text{rpm}$.

8.7 Equivalent Model Summary

Equivalent Circuit

The equivalent circuit, including the rotor side, is presented in Figure 8.17 and the corresponding circuit parameters are documented in Table 8.2. The resistance r_s and r_{fr} could be predicted by the capacitance/conductance model and the field model, however it is omitted here since the conductivity of the dielectric materials seems varies a lot between AC and DC excitation as seen from the measured data. The behavior of these materials should be studied further in the future.

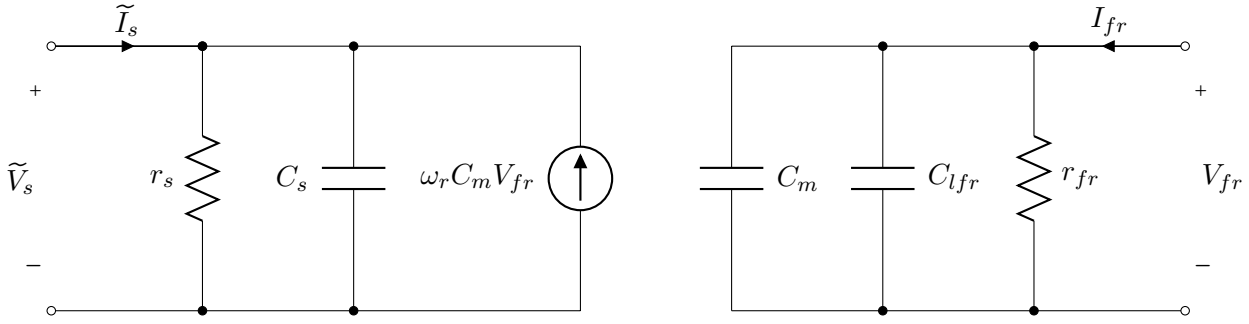

Figure 8.17: The equivalent circuit model of SEM 1.

Table 8.2: Summary of SEM 1 Circuit Parameters Obtained Using Different Models.

Parameters	r_s, MΩ	C_s, nF	C_m, nF	C_{lfr}, nF	r_{fr}, MΩ
Predicted via Chapter 6, Torque Model	—	—	2.17	—	—
Predicted via Chapter 7, Capacitance Model	—	11.1	2.01	3.02	—
Predicted via 2D FEA, Field Model	—	11.0	2.00	3.01	—
Measured, Circuit Model	1.70	13.8	2.03	3.41	52.6

Other than that, the models proposed in Chapters 6 and 7 are reliable to predict the mutual capacitance C_m. For the synchronous capacitance C_s, the proposed models could estimate for the active region, which is about ~ 80% of the total. The rest may be simulated using 3D FEA given the complexity of the routing. Furthermore, it may be reduced in the future design if multi-layer boards are used.

Weight and Volume

The distribution of the weight and volume of SEM 1 are displayed as pie charts in Figure 8.18. The total weight and volume of this machine is 12.2 kg and 5.2 L. The corresponding designed torque densities are 0.76 N-m/kg and 1.79 N-m/L. It can be seen that the active parts (everything but case and hardware) of SEM 1 is only ~ 50% of the total weight and volume, which indicates that there is room for future mechanical optimization in SEM 1 to further pushing the torque density limit. If only the active parts are counted, the torque densities would be 1.68 N-m/kg and 3.37 N-m/L.

Model Based Efficiency and Power Factor Map

Assuming the drive of this machine could output its full capacity, the efficiency map of SEM 1 in the T-ω plane may be predicted using the measured circuit parameters. Figures 8.19 and 8.20 display the efficiency map of SEM 1 under maximum torque per volt control (i.e. $\gamma = 0$) and $V_{fr} = 8$ kV. Notice that the first one excludes the friction losses and therefore it shows the electrical efficiency of SEM 1. The efficiency is at its highest around 300 rpm rotor speed and 3 N-m torque output. It

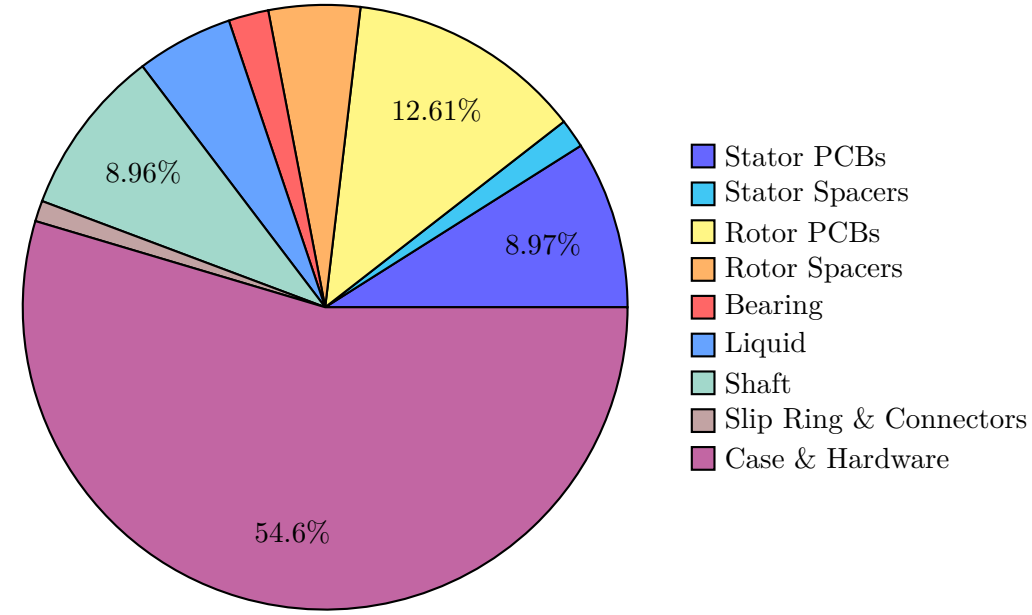

(a)

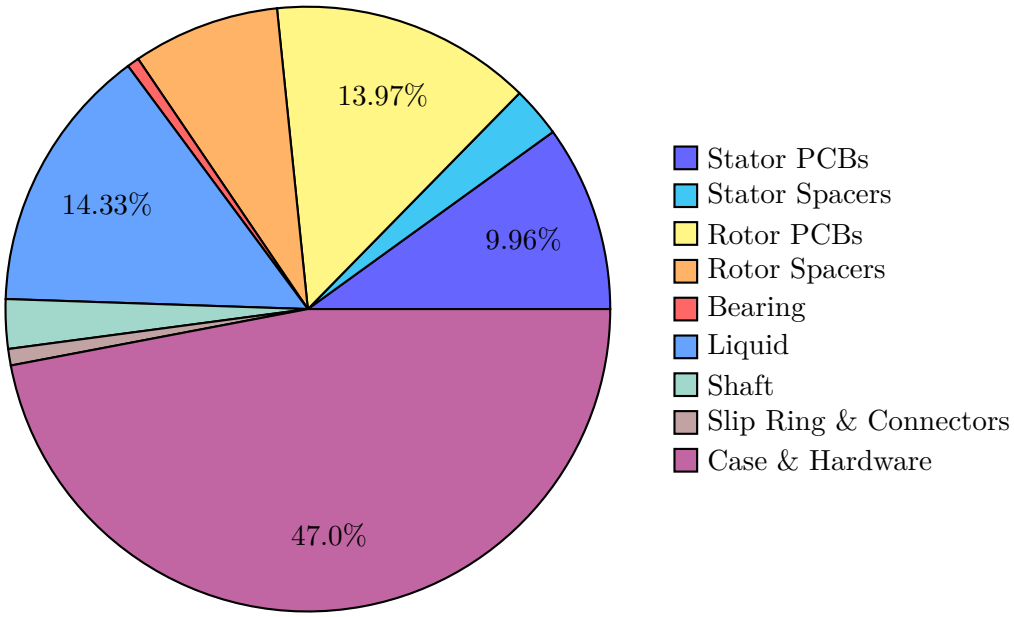

(b)

Figure 8.18: The weight and volume distribution of SEM1 (a) weight, 100% = 12.2 kg (b) volume, 100% = 5.2 L.

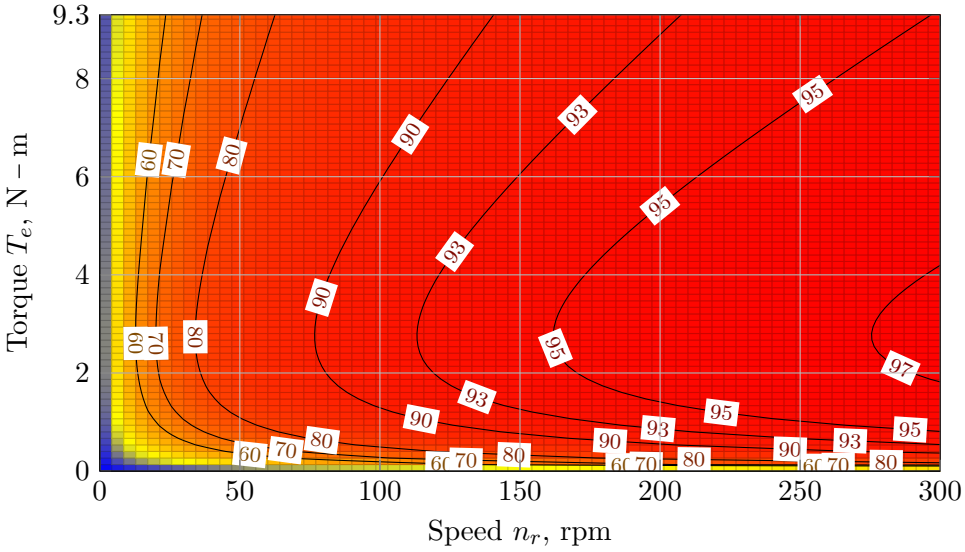

Figure 8.19: Predicted efficiency map for SEM 1 under maximum torque per volt control without counting friction losses.

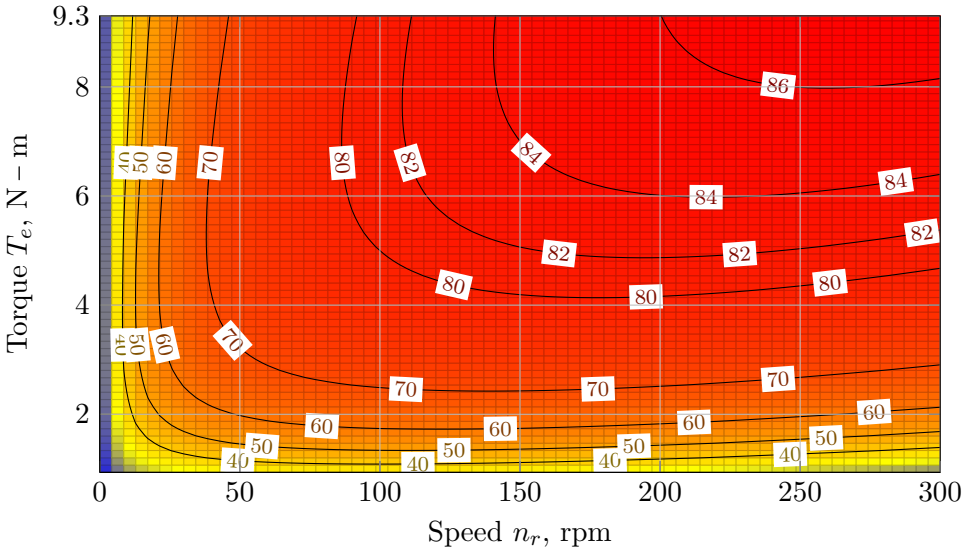

Figure 8.20: Predicted efficiency map for SEM 1 under maximum torque per volt control with friction losses counted.

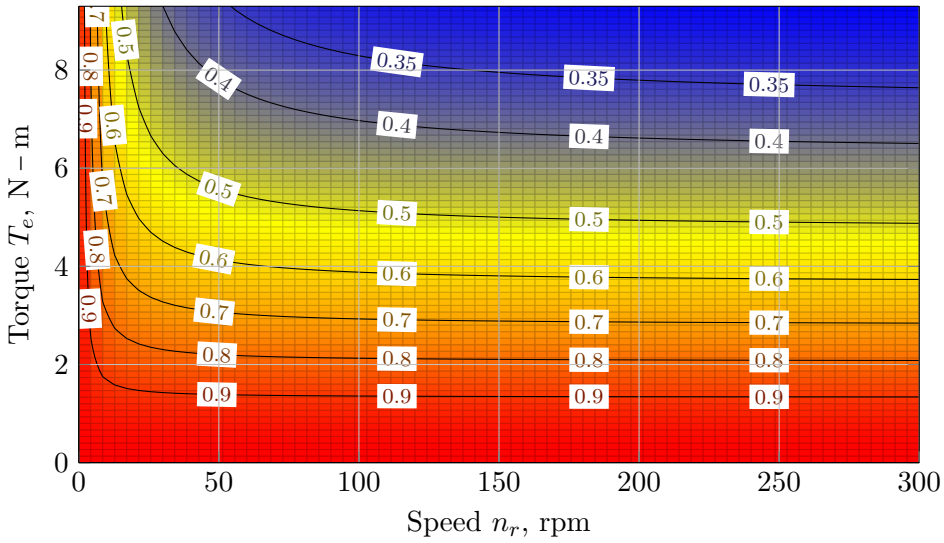

Figure 8.21: Predicted power factor map for SEM 1 under maximum torque per volt control.

does not peak at higher torque output because the leakage losses tends to dominant. The second map includes all losses and the efficiency generally drops more than 10% comparing to the first one, which indicates the need for further improvement on the mechanical design. The peak efficiency now shifts to the high torque output corner since friction losses dominant.

The corresponding power factor is also calculated and displayed in Figure 8.21. When either the speed or the torque output is low, the power factor of SEM 1 is relatively high due to the relatively low leakage reactive current through the C_s branch. As also stated previously, a trade off between C_s and C_m should be done in the future design to have a better power factor looking into the machine.

A major application this machine is targeting at is position and hold due to its low power consumption at the stall condition. Based on the model, the standstill loss is ploted as a function of the output torque in Figure 8.22. Notice that the solid line is assuming the stator leakage resistance is still 1.70 MΩ as under AC excitations. However, based on the measured rotor leakage resistance, it may be one order of magnitude lower. The dashed line predicts the loss with r_s = 17 MΩ, which is significantly smaller.

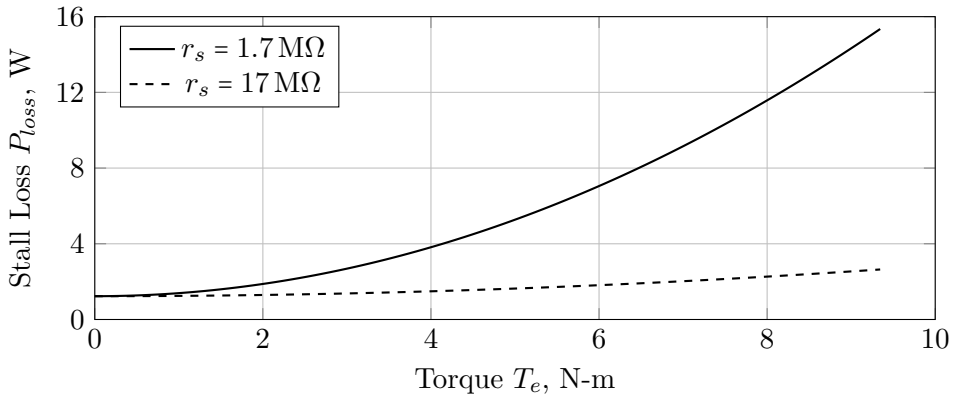

Figure 8.22: Predicted stall loss as a function of the torque output under maximum torque per volt control and V_{fr} = 8 kV.

9 CONTRIBUTIONS AND RECOMMENDED FUTURE WORK

While it is impossible to tell when this industrial revolution will be consummated, there can be no doubt that the future belongs to aluminium, and that in times to come it will be the chief means of increasing human performance.

— Nikola Tesla (1900)

The research work has been done so far demonstrated the benefit of utilizing the dielectric liquid as the essential insulating medium for enhancing electrostatic shear stresses and the research goal of approaching the volumetric and the specific torque densities of traditional magnetic machines of similar ratings have been achieved. Along the way the design tools including both FE and the analytical analysis have been validated experimentally. A detailed summary of contributions is presented in Section 9.1, in light of which the suggested future work are presented in Section 9.2.

9.1 Summary of Contributions

The contributions are summarized as bullet points in the following and a comparison with prior electrostatic machines is made at the end.

Contributions

1. Utilizing Dielectric Liquid As Essential Insulating and Force Enhancing Medium (work presented in Chapter 4 and [4]):

- A pressure and a shear stress test stands were constructed to evaluate maximum dielectric pressure and shear stress a liquid can achieve prior to use in a machine;
- Commercialized off the shelf dielectric insulating liquids were benchmarked in terms of the relative permittivity, breakdown strength and electrical conductivity;
- Vertrel XF exhibiting 2 psi of pressure and withstanding 20 kV/mm, was identified as a promising insulating medium for high performance electrostatic machine in low speed applications.

2. Theoretical Framework for Single Phase Electrostatic Machines (work presented in [4, 54, 123]):

- The duality of the magnetic reluctance and the electric elastance was established;
- An ad-hoc analytical capacitance calculation method for cylindrical peg style machine was developed;
- The capacitance profile was proved to be configurable via different peg layout techniques;
- A semi-analytical method incorporating conformal mapping techniques with FE analysis to optimize single phase electrostatic machine was developed. The optimum ratios between the key geometric parameters are documented as look up tables in Appendix C.

3. Radial Flux Machine Prototyping and Experimental Demonstration (work presented in [4, 54, 123]):

- Both a single phase and a three phase elastance machine were prototyped in the lab and were in well agreement with the analytical and FE analysis;
- The additive manufacturing approach was proved to be able to prototype a single phase electrostatic machine in one week;
- Both specific torque density and volumetric torque density were increased over prior work by 2 orders of magnitude to be competitive with the level of an electromagnetic induction machine of similar ratings.

4. Theoretical dq-Axis Framework for Three Phase Electrostatic Machines (work presented in Chapter 5 and [124]):

- A generalized *dq*-axis model was developed for the three phase electrostatic machine, which embraces all three torque production mechanisms, i.e. field, elastance and induction torque;
- The resistive saliency of the machine is also incorporated into the *dq*-axis model;
- Key capacitances are identified for the purpose of optimizing the electrostatic machine with field excitation;

- The duality between the dq-axis model of the electromagnetic and the electrostatic synchronous machine was established.

5. Field Torque Model of Three Phase Electrostatic Machines (work presented in Chapter 6):

- A generalized field torque model was developed for the three phase electrostatic machine, which relates the torque production to several key geometric parameters;
- The upper and lower bounds of the torque production are derived for quickly sizing of the machine;
- The scalability of the machine is discussed in terms of capacitance, conductance, voltage, current, torque and power;
- The design guidelines are presented for maximizing the torque production.

6. Generalized Capacitance/Conductance Evaluation for Electrostatic Machines (work presented in Chapter 7):

- A generalized analytical method based on separation of variables is developed for evaluating the capacitance coupling of electrostatic machines;
- The method is extended to cover 2D structures;
- The model may be applied to various types of electrostatic machines, i.e. radial flux, axial flux, single phase, multi-phase etc.;
- The model may be modified to evaluate the conductance coupling by simply swapping the permittivities with conductivities.

7. Axial Flux Machine Prototyping and Experimental Demonstration (work presented in Chapter 8):

- An axial flux three phase electrostatic machine with field excitation using PCB boards as the main torque producing components is prototyped in the lab and were in well agreement with the analytical and FE analysis;

- The PCB manufacturing approach was proved to be reliable in terms of mechanical integrity and accuracy;
- Both specific torque density and volumetric torque density were increased over prior work by 1 order of magnitude to be competitive with the level of air cooled permanent magnet machines of similar ratings.

Benchmark of Contributions with Previous Electrostatic Machines

To put this work into perspective, Table 2.1 is remade here with the inclusion of SEM 1 and presented in Table 9.1. Again, gray highlighted work are ludois group affiliated. With a particular attention on the metric column of torque per volt squared, being relatively low in this metric is the major reason that prohibited the previous researchers from making further efforts on the electrostatic machines. The usage of the dielectric liquid improves this metric at least two orders of magnitude, which is as predicted in Chapter 4. The transition from single phase to three phase structure adds another one order of magnitude.

Benchmark of Contributions with Magnetic Machines

Table 9.2 compares this work with OTS magnetic machines with comparable ratings. The at least three magnitudes superiority over the previous electrostatic machines built by others helped the prototyped machine SEM 1 in this research to outnumber the specific torque density of air cooled permanent magnet machines of similar ratings. Even the volumetric torque density is close to the selected BLDC machine. As for the stall loss, SEM 1 improves about one order over previous work and is superior than any magnetic machines in the table.

9.2 Recommended Future Work

Even though SEM 1 shows great potential in terms of torque density and stall loss, the electrostatic machine still need significant engineering efforts for it to become mature. These efforts are suggested as and not limited to the following:

Table 9.1: Key Metrics of Rotational Electrostatic Machines Built by Notable Prior Researchers and the Author.

Metric	**Insulation Medium**	**Power**, W	**Speed**, rpm	**Maximum Torque**, N-m	**Voltage**, kV	**Torque per Volt^2**, N-m/kV^2	Type †	Year	Scale ‡
J. G. Trump [43]	UHV	5.5E+1	3.6E3	1.5E-1	7.3E+1	2.7E-5	Sync	1933	L
N. J. Felici [47]	HPG	5.0E+2	7.5E2	6.4E+0	2.5E+2	1.0E-4	Sync	1947	L
R. A. Vanslette [48]	HPG	1.0E-2	1.5E3	7.5E-5	4.0E+0	4.7E-6	Hyst	1965	L
B. Bollée [51]	Air	1.0E-4	2.0E2	4.8E-6	2.2E-1	9.9E-5	Sync	1969	L
B. Bollée [51]	Air	2.0E-4	6.0E2	3.2E-6	2.2E-1	6.6E-5	Indu	1969	L
P. T. Krein [50]	Air	2.0E-1	5.4E2	3.5E-3	1.2E+1	2.4E-5	Coro	1982	L
S. F. Bart et al. [29]	Air	7.9E-7	1.0E4	7.5E-10	1.0E-1	7.5E-8	Indu	1989	S
T. Niino et al. [28]	Air	3.6E-3	2.0E2	6.9E-4	1.8E+0	2.1E-4	Sync	1995	S
S. F. Nagle et al. [30]	Air	5.8E-2	2.7E5	2.0E-6	9.0E-2	2.5E-4	Indu	2005	S
Shinsei Corp. [56]	UHV	1.0E+2	1.0E4	1.0E-1	1.0E+2	1.0E-5	DC	2007	L
B. Ge et al. [54]	Liquid	2.0E+1	5.0E2	1.2E+0	7.0E+0	2.0E-2	Swit	2016	L
G. Reitz et al. [55]	Liquid	3.0E+1	5.0E2	2.0E+0	9.0E+0	2.5E-2	Swit	2017	L
SEM 1 Chapter 8	Liquid	2.9E+2	3.0E2	9.3E+0	8.0E+0	1.5E-1	Sync§	2018	L

† Sync — Synchronous Machine, Hyst — Hysteresis Machine, Indu — Induction Machine, Coro — Corona Machine, DC — DC Machine, Swit — Switched Machine. ‡ L — Macro Scale, S — MEMS Scale. § Synchronous Machine with Field Excitation.

Table 9.2: Comparison of SEM 1 with Selected Machines of Comparable Ratings.

Machine Model	# of	Power	Volume	Weight	T_{pk}	T_{avg}	Loss†	Pk./Avg. Torque Density			
	Phase	[kW]	[L]	[kg]	[N-m]	[N-m]	[W]	volumetric		specific	
Bodine 34R6BFPP [2]	3	0.15	1.36	4.10	—	0.84	51.5	—	0.62	—	0.20
Leeson ZSP6-0602 [2]	1	0.25	2.73	7.71	—	1.37	—	—	0.50	—	0.18
Rel Tork 2-124SR-24 [3]	4	1.10	2.25	9.10	—	3.56	53.0	—	1.58	—	0.39
BLWS235D-160V-3k [4]	4	0.16	0.25	1.25	—	0.50	12.7	—	2.00	—	0.40
EMJ-04APB22 [4]	3	0.40	0.35	2.51	—	1.27	3.70	—	3.63	—	0.51
Previous Work [125] [1]	1	0.02	3.30	7.17	0.90	0.45	10.0	0.27	0.14	0.13	0.06
Previous Work [54] [1]	1	0.02	1.23	1.70	1.15	0.38	7.75	0.93	0.31	0.68	0.22
Chapter 8 Work [5]	3	0.29	5.2	12.2	—	9.35	1.27	—	1.79	—	0.76

† at 0.5 N-m stall torque condition. [1] switching elastance machine. [2] magnetic induction machine.

[3] magnetic switched reluctance machine. [4] permanent magnet machine. [5] electrostatic synchronous machine.

1. Development of the Drive:

- The most urgent and relevant further development may be the drive, especially for applications in kilowatt scale, where there is a mismatch between the requirement and the OTS drive in terms of the voltage and current level. The emerging of HV silicon carbide devices may fill the gap.

- By duality, this machine pairs with a current source inverter (CSI) ideally. Given the fact that CSI is relatively immature at low power level comparing to its widely used cousin VSI, the development of CSI is compelling.

2. Improving on the Dielectric Liquid:

- As mentioned in Chapter 6, what really makes the electrostatic machine attractive is the torque density is directly proportional to the permittivity of the dielectric liquid. The maximum dielectric constant of common liquids is more than 100. Although dielectric constant is not the only metric that matter, there has never had any demand for this application in the market. The research on developing these special liquids is promising.

- The performance of the liquid may be enhanced by suspending ferroelectric nano-particles like barium titanate within them. The resultant colloidal suspension increases the dielectric constant of the liquid according to the Maxwell-Wagner polarization model [126].

- Chapter 4 investigated the dielectric liquid mainly from the electrical perspective, more benchmark work should be done on the mechanical and chemical properties, including viscosity, thermal conductivity, reactivity, etc.

3. Improving on the Electrical Performance:

- Based on the leakage resistance measured in Chapter 8, the DC and AC properties of the dielectric materials should be studied thoroughly in order to model the machine and predict the performance more accurately.

- As mentioned in several places, a trade off between the power factor and torque or C_s and C_m may be carried out in the future design depending on the application requirement and drive capabiliy.
- Multi-layer PCB boards may be implemented in the future design to optimize the trace routing for reducing the coupling between phases in the inactive region and eventually balancing the three phase leakage paths.
- In order to improve the reliability of the machine, arc protection should be added at both stator and rotor sides. The breakdown behavior in the machine should be studied in order to improve the protection circuit.

4. Improving on the Mechanical Performance:

- Currently in SEM 1, there are lots of mechanical redundancies (PCB board thickness, shaft diameter, etc.) built in, which are more than needed. By taking these off or even developing new structures, the weight and volume may be further reduced.
- Aside from the liquid viscous drag, the friction torque from the seals and bearings is high in SEM 1 comparing to magnetic machines of similar shaft sizes. This at least may be reduced by new designs given the fact that it is the first time trying.
- The slip ring, which serves for field excitation, may be replaced through inductive or capacitive power transfer. They have been demonstrated to provide field power for magnetic synchronous machines in [127–129].

5. Hydrodynamic Analysis:

- The hydrodynamic performance of this machine directly determines the viscous drag. The corresponding research may help to find the pathway to reduce the loss and thus push the speed limit.

A MAPPING FIELD MODEL TO CIRCUIT MODEL FOR ELECTROSTATIC INDUCTION MACHINE

The purpose of this appendix is twofold:

- validate the correctness of the steady state dq-axis model of the electrostatic induction machine in Section 5.4 through the field solution of an ideal induction machine;
- prove that the dielectric liquid as the gap medium will not experience any electrostatic force to flow in both induction and synchronous machines.

The second one, an important conjecture from the first one, may be usually taken for granted, but it is a life-saver in terms of segregating fluid dynamics and electrodynamics although one may selfishly desire any positive electrostatic force to counteract the viscous drag.

A.1 Field Solution of An Ideal Electrostatic Induction Machine

The derivation starts from the torque equation of an ideal electrostatic induction machine, as shown in Figure A.1. It has P poles, a depth into the paper of d, and consists a gap material $(\varepsilon_g, \sigma_g)$ and a rotor material $(\varepsilon_r, \sigma_r)$. The outermost peripheral (stator side) is energized with a pure traveling

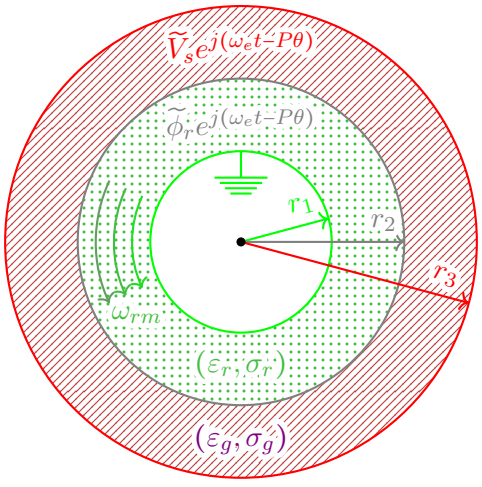

Figure A.1: An ideal electrostatic induction machine modeled with the stator traveling wave.

wave $\Re[\widetilde{V}_s e^{j(\omega_e t - P\theta)}]$ with an electrical angular speed of ω_e. The innermost peripheral is connected to ground. The rotor itself is rotating at a mechanical speed of ω_{rm}, which together with the slip frequency of the induced traveling wave (rotor reference frame) results in electrical speed of ω_e in the stator reference frame.

The result is documented by J. R. Melcher in his grand work *Continuum Electromechanics* [36, p. 5.49] for the translational version of Figure A.1. Following the same procedure, the total torque for the rotary type of interest here is

$$T = \frac{\pi P^2 \cdot d \cdot \varepsilon_g h_P^2(r_2, r_3) f_P(r_1, r_2) \left|\widetilde{V}_s\right|^2 s\omega_e(\varepsilon_g\sigma_r - \varepsilon_r\sigma_g)}{[\sigma_r f_P(r_1, r_2) - \sigma_g f_P(r_3, r_2)]^2 + s^2\omega_e^2[\varepsilon_r f_P(r_1, r_2) - \varepsilon_g f_P(r_3, r_2)]^2}, \tag{A.1}$$

where

$$f_n(x, y) = -\frac{\left(\frac{x}{y}\right)^n + \left(\frac{y}{x}\right)^n}{\left(\frac{x}{y}\right)^n - \left(\frac{y}{x}\right)^n}, \quad h_n(x, y) = -\frac{2}{\left(\frac{x}{y}\right)^n - \left(\frac{y}{x}\right)^n},$$

and s is the slip defined in Section 5.4. Functions f and h are tweaked to be unit-less to make the result more explicit. As an intermediate result, the induced rotor surface potential is a function of the excitation voltage $\widetilde{V}_s$:

$$\widetilde{\phi}_r = \frac{h_P(r_2, r_3)(\sigma_g + js\omega_e\varepsilon_g)}{[\sigma_r f_P(r_1, r_2) - \sigma_g f_P(r_3, r_2)] + js\omega_e[\varepsilon_r f_P(r_1, r_2) - \varepsilon_g f_P(r_3, r_2)]}\widetilde{V}_s. \tag{A.2}$$

This potential $\widetilde{\phi}_r$ is actually identical to $\widetilde{V}_r$ defined in Section 5.4 by careful examinations:

- Once $\widetilde{V}_s$ and $\widetilde{\phi}_r$ (or $\widetilde{V}_r$) are determined, the resultant torque is fixed according to

  $$T = -\pi P^2 \cdot d \cdot \varepsilon_g h_P(r_2, r_3) \cdot \Re[j(\widetilde{V}_s^*)\widetilde{\phi}_r]$$

  from J. R. Melcher's derivation and

  $$T = -\frac{3P}{2} C_m \cdot \Re[j(\widetilde{V}_s^*)\widetilde{V}_r]$$

  from eq. (5.27).

- Had the rotor been wound type, r_2 would be the ideal peripheral for the rotor excitation $\widetilde{\phi}_r$ and $\widetilde{V}_r$ by symmetry based on Figure A.1 and Figure 5.6a respectively.

A.2 Mapping Field Solution to Circuit Model

Notice that eq. (A.1) contains a variable s and eq. (A.2) is a complex one. Comparing eqs. (A.1) and (A.2) to eqs. (5.33)–(5.35), four circuit parameters defined in Section 5.3 may be backed out as

$$\begin{cases} C_m = \dfrac{2\pi P d}{3}\varepsilon_g h_P(r_2, r_3) \\ G_m = \dfrac{2\pi P d}{3}\sigma_g h_P(r_2, r_3) \end{cases} \quad and \quad \begin{cases} C_r = \dfrac{2\pi P d}{3}[\varepsilon_g f_P(r_3, r_2) - \varepsilon_r f_P(r_1, r_2)] \\ G_r = \dfrac{2\pi P d}{3}[\sigma_g f_P(r_3, r_2) - \sigma_r f_P(r_1, r_2)] \end{cases}. \tag{A.3}$$

These equations may be used for the initial sizing of an electrostatic induction machine. One may use eqs. (A.1) and (A.3) to find the rough optimum pole number for maximum torque production as we did in Chapter 6. The stator side leakage information is still unknown due to the forced boundary condition at $r = r_3$ and the field distribution outside r_3 is up to the outer structure.

A.3 Net Torque on the Fluid

A natural question to ask whether or not there is any net torque on the fluid. If there is a positive torque, then it would help to counteract the viscous drag. Unfortunately, it turns out the torque only happens at the material interface. The proof is simple. Consider the fluid gap interface at any radius $r_{23} \in (r_2, r_3)$. The displacement field in the radial direction $\widetilde{D}_r$ should be continuous at this interface (i.e. $\widetilde{D}_r^{r_{23}^-} = \widetilde{D}_r^{r_{23}^+}$) because the fluid is uniform. Then, according to J. R. Melcher, the torque developed at the interface should be

$$T_e = 2\pi r_{23} \cdot d \cdot r_{23} \cdot \frac{1}{2}\Re\left[jP\widetilde{\phi}_{23}\left(\widetilde{D}_r^{r_{23}^-} - \widetilde{D}_r^{r_{23}^+}\right)\right] = 0,$$

where $\widetilde{\phi}_{23}$ is the potential at the interface. This conclusion also applies to the synchronous machines since the topology look the same from the gap perspective.

This appendix serves for proving the electric potential, charge, capacitance and energy are conformal for the mapping used in Chapter 7 (eq. (7.1)):

$$\zeta = r_0 \exp\left(-j\frac{2\pi}{L}z\right)$$

where L is the periodic length, r_0 is the radius of the circle that $y = 0$ is mapped into, $z = x + jy$ and $\zeta = re^{j\theta}$ are the rectangular and polar coordinates respectively.

B.1 Conformal Mapping

The x and y coordinates relate to r and θ coordinates through the following equations:

$$r = r_0 \exp\left(\frac{2\pi}{L}y\right) \tag{B.1}$$

$$\theta = -\frac{2\pi}{L}x, \tag{B.2}$$

which then lead to the following first order derivatives:

$$\frac{\partial r}{\partial x} = 0, \quad \frac{\partial r}{\partial y} = r_0\frac{2\pi}{L}\exp\left(\frac{2\pi}{L}y\right), \tag{B.3}$$

and

$$\frac{\partial \theta}{\partial x} = -\frac{2\pi}{L}, \quad \frac{\partial \theta}{\partial y} = 0. \tag{B.4}$$

It is not hard to check that $\zeta(z)$ is analytical (harmonic) using eq. (B.3) and eq. (B.4), which is a basic requirement for conformal mapping [115].

B.2 Electric Potential and Field

The electric potential ϕ is conformal, i.e.,

$$\phi(r(x,y),\theta(x,y)) = \phi(x,y), \tag{B.5}$$

since Laplace's equation governs the field distribution. The electric field is simply the spatial derivative of the electric potential:

$$E_x = -\frac{\partial \phi}{\partial x} = -\frac{\partial \phi}{\partial r}\frac{\partial r}{\partial x} - \frac{\partial \phi}{\partial \theta}\frac{\partial \theta}{\partial x} = E_r\frac{\partial r}{\partial x} + rE_\theta\frac{\partial \theta}{\partial x} = -r_0\frac{2\pi}{L}\exp\left(\frac{2\pi}{L}y\right)E_\theta, \tag{B.6}$$

and

$$E_y = -\frac{\partial \phi}{\partial y} = -\frac{\partial \phi}{\partial r}\frac{\partial r}{\partial y} - \frac{\partial \phi}{\partial \theta}\frac{\partial \theta}{\partial y} = E_r\frac{\partial r}{\partial y} + rE_\theta\frac{\partial \theta}{\partial y} = r_0\frac{2\pi}{L}\exp\left(\frac{2\pi}{L}y\right)E_r. \tag{B.7}$$

Equations (B.6) and (B.7) establish the electric field link between the two coordinate systems.

B.3 Force and Torque

To establish the torque relationship, the Maxwell stress tensor $\mathbf{T}$ is used to compute the total force experienced by the rotor at both coordinate systems,

$$F_z = \oint T_{xy}\cdot da = d\cdot\int_{-\frac{L}{2}}^{\frac{L}{2}} \varepsilon_0\varepsilon_r\cdot E_xE_y\cdot dx, \quad at\ y = y', \tag{B.8}$$

$$F_\zeta = \oint T_{\theta r}\cdot da = d\cdot\int_{-\pi}^{\pi} \varepsilon_0\varepsilon_r\cdot E_\theta E_r\cdot r'\cdot d\theta, \quad at\ r = r' = r_0\exp(2\pi y'/L), \tag{B.9}$$

where d is the depth into the paper. Substituting the electric field relationship from the above, we have

$$F_z = d\cdot\int_{-\pi}^{\pi}\varepsilon_0\varepsilon_r\cdot\left[r_0\frac{2\pi}{L}\exp\left(\frac{2\pi}{L}y'\right)\right]^2\cdot E_\theta E_r\cdot\left(\frac{L}{2\pi}\right)\cdot d\theta = \frac{2\pi r'}{L}F_\zeta. \tag{B.10}$$

Therefore, $F_\zeta|_{r=r'}$ is not necessarily equaling to $F_z|_{y=y'}$. Only when $2\pi r' = L$ and r' is in the domain under consideration, the total force is conformal. Another way to understand this is that both the electric field E_θ and E_r are shrunk by a factor of r' according to eqs. (B.6) and (B.7), however, the integration length is only elongated by a factor of r'. Actually, the torque in the $r-\theta$ coordinate relates to the force in the $x-y$ coordinate through

$$T_\zeta = r'\cdot F_\zeta = \frac{L}{2\pi}F_z. \tag{B.11}$$

The above derivation also accommodates a multi-row machine, as presented in Chapter 6 and [54]. Without loss of generality, two radii r_1' and r_2' are assumed to be the torque producing surfaces. Returning to eq. (B.8), the force for a multi-row machine can be re-derived as

$$\begin{aligned} F_z &= d\cdot\oint_{\Gamma_{z,1}}\varepsilon_0\varepsilon_r\cdot E_xE_y\cdot dl_z + d\cdot\oint_{\Gamma_{z,2}}\varepsilon_0\varepsilon_r\cdot E_xE_y\cdot dl_z \\ &= d\cdot\oint_{\Gamma_{\zeta,1}}\varepsilon_0\varepsilon_r\cdot\left(\frac{2\pi r_1'}{L}\right)E_rE_\theta\cdot dl_\zeta + d\cdot\oint_{\Gamma_{\zeta,2}}\varepsilon_0\varepsilon_r\cdot\left(\frac{2\pi r_2'}{L}\right)E_rE_\theta\cdot dl_\zeta \\ &= \frac{2\pi r_1'}{L}F_{\zeta,1} + \frac{2\pi r_2'}{L}F_{\zeta,2}, \end{aligned} \tag{B.12}$$

where Γ_1 and Γ_2 are the integration paths defined by the two force producing surfaces. In general, the total force equals the summation of the force in the converted model scaled by $2\pi r_i'/L$

$$F_z = \sum_i \frac{2\pi r_i'}{L} F_{\zeta i}, \tag{B.13}$$

and torque is simply the summation over all the rows

$$\frac{L}{2\pi} F_z = \sum_i r_i' F_{\zeta,i} = T_\zeta. \tag{B.14}$$

If $L/2\pi$ is taken as the moment arm in the rectangular coordinate, then the above shows that torque is conformal along the mapping process.

B.4 Charge and Capacitance

For a two electrode system, capacitance is usually defined as charge held by the electrode per unit voltage. In a multi-conductor system, which is much more complex, capacitance is defined as a matrix link between charge and voltage

$$Q_i = \sum_i C_{ik} V_k, \tag{B.15}$$

where Q_i is the charge on the i-th conductor, V_k is the charge on the k-th conductor and C_{ik} is the capacitance between the i- and k-th conductors.

As we already claimed in the above, electric potential of the electrode, i.e. V, does not change after conformal mapping. If the charge Q on each electrode also does not change, then the capacitance matrix will hold along the mapping process.

Since capacitance is independent of the charge and voltage associated with the electrodes, an electrostatic condition is assumed in the remaining of this section. Free surface charge density σ_f is

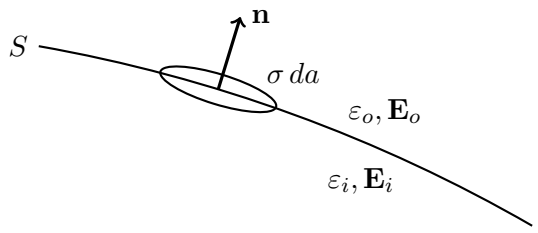

Figure B.1: Electric field boundary conditions at the material interface.

defined on a surface S with a unit normal vector $\mathbf{n}$ directed from inside to outside of the surface and electric field $\mathbf{E}_i$ and $\mathbf{E}_o$, permittivity ε_i and ε_o are associated at each side as shown in Figure B.1. Recall the boundary condition derived from Gauss's Law,

$$(\varepsilon_o \mathbf{E}_o - \varepsilon_i \mathbf{E}_i) \cdot \mathbf{n} = \sigma_f. \tag{B.16}$$

In an electrostatic condition, the electric field inside the electrode is zero and the free charge density is exactly the charge density σ on the electrode (no bound charges). Thus, the above equation becomes

$$\varepsilon_o \mathbf{E}_o \cdot \mathbf{n} = \varepsilon_o |\mathbf{E}_o| = \sigma. \tag{B.17}$$

The simplification above is based on the electric field is perpendicular to the surface of an equal potential conductor. Then the total charge residing on the surface of an electrode equals to the surface integral of the charge density,

$$Q = \oint_S \sigma \cdot da = \oint_S \varepsilon_o \mathbf{E}_o \cdot \mathbf{n} \cdot da = \varepsilon_o \oint_S |\mathbf{E}_o| \cdot da = d \cdot \varepsilon_o \oint_\Gamma |\mathbf{E}_o| \cdot dl. \tag{B.18}$$

In the $r - \theta$ coordinate, the above equation is expanded as

$$\begin{aligned} Q_\zeta &= d \cdot \varepsilon_o \oint_{\Gamma_\zeta} |\mathbf{E}_{o\zeta}| \cdot dl_\zeta \\ &= d \cdot \varepsilon_o \oint_{\Gamma_z} \left(\frac{L}{2\pi r}\right) |\mathbf{E}_{oz}| \cdot \left(\frac{2\pi r}{L}\right) dl_z \\ &= d \cdot \varepsilon_o \oint_{\Gamma_z} |\mathbf{E}_{oz}| \cdot dl_z \\ &= Q_z. \end{aligned} \tag{B.19}$$

The above shows that the total charge resides on the surface of the electrode does not change after applying conformal mapping. Furthermore, from the derivation, even the local total charge residing on the surface of part of the electrode does not change. In addition, the above derivation is independent of the applied voltage, thus the capacitance matrix should hold along the conformal mapping process.

B.5 Energy

Since the capacitance and potential associated with the electrode do not change after mapping, the total energy of the system shall not change.

C LOOKUP TABLE OF FORCE MAP SIMULATED VIA FEA FOR SINGLE PHASE ELECTROSTATIC MACHINE DESIGN

Figures C.2–C.9 are the lookup tables generated from the simulation via FEA. The simulation was carried out with a fixed periodic length l = 10 mm and a vacuum dielectric. The geometric definitions in Figure C.1 are given here for convenient referencing.

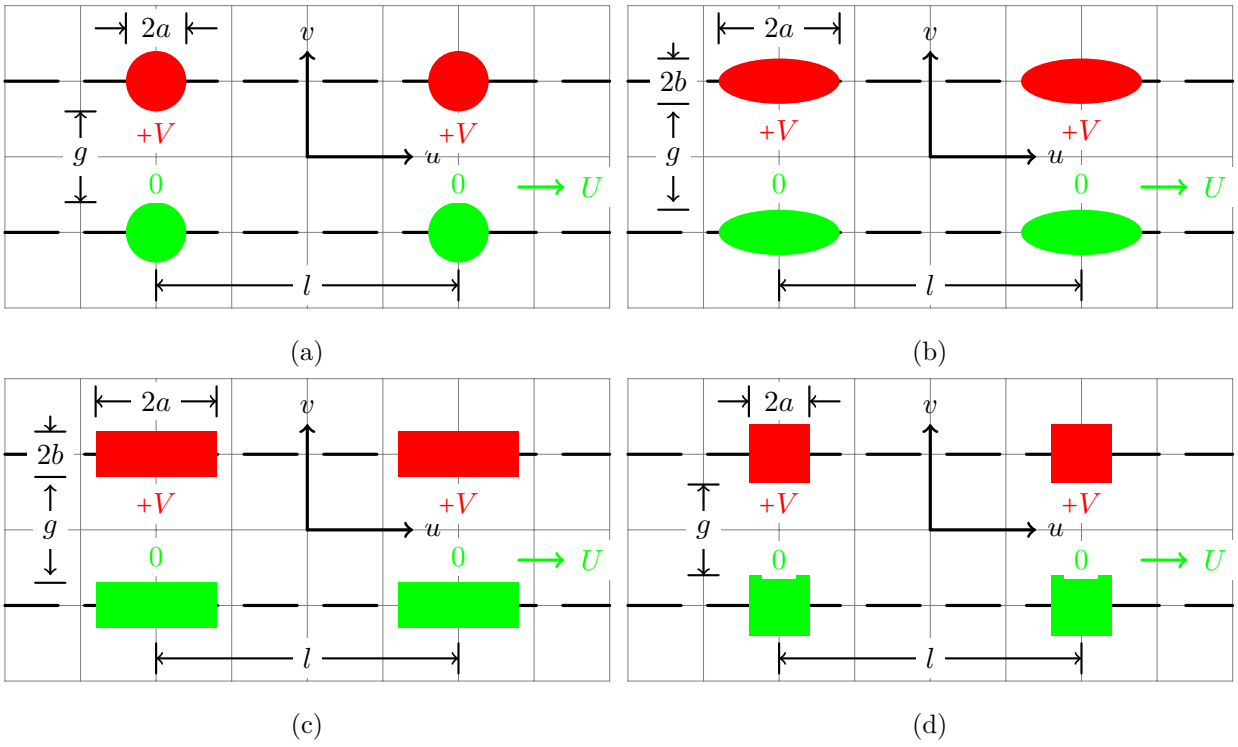

Figure C.1: Translational machine geometric definitions with 2-norm electrodes: (a) circular pole; (b) elliptical pole and ∞-norm electrodes: (a) rectangular pole; (b) square pole. (Red represents stator and green represents rotor.)

Pole radius a/l \ Gap g/l	0.04	0.06	0.08	0.10	0.12	0.14	0.16	0.18	0.20	0.22	0.24	0.26	0.28	0.30	0.32	0.34	0.36	0.38	0.40
0.40	0.18	0.25	0.30	0.33	0.34	0.34	0.34	0.32	0.31	0.29	0.27	0.25	0.24	0.22	0.20	0.18	0.16	0.15	0.14
0.39	0.18	0.25	0.30	0.33	0.34	0.34	0.34	0.33	0.31	0.30	0.28	0.26	0.24	0.22	0.20	0.18	0.17	0.15	0.14
0.38	0.18	0.25	0.30	0.33	0.34	0.35	0.34	0.33	0.32	0.30	0.28	0.26	0.24	0.22	0.20	0.19	0.17	0.15	0.14
0.37	0.18	0.25	0.30	0.33	0.35	0.35	0.34	0.33	0.32	0.30	0.28	0.26	0.24	0.23	0.21	0.19	0.17	0.16	0.14
0.36	0.18	0.25	0.30	0.33	0.35	0.35	0.35	0.34	0.32	0.31	0.29	0.27	0.25	0.23	0.21	0.19	0.18	0.16	0.14
0.35	0.18	0.25	0.30	0.33	0.35	0.35	0.35	0.34	0.33	0.31	0.29	0.27	0.25	0.23	0.21	0.20	0.18	0.16	0.15
0.34	0.18	0.25	0.30	0.34	0.35	0.36	0.35	0.34	0.33	0.31	0.30	0.28	0.26	0.24	0.22	0.20	0.18	0.17	0.15
0.33	0.18	0.25	0.30	0.34	0.35	0.36	0.36	0.35	0.34	0.32	0.30	0.28	0.26	0.24	0.22	0.20	0.19	0.17	0.15
0.32	0.18	0.25	0.31	0.34	0.36	0.36	0.36	0.35	0.34	0.32	0.31	0.29	0.27	0.25	0.23	0.21	0.19	0.17	0.16
0.31	0.18	0.25	0.31	0.34	0.36	0.37	0.37	0.36	0.35	0.33	0.31	0.29	0.27	0.25	0.23	0.21	0.19	0.18	0.16
0.30	0.18	0.25	0.31	0.34	0.37	0.37	0.37	0.36	0.35	0.34	0.32	0.30	0.28	0.26	0.24	0.22	0.20	0.18	0.16
0.29	0.18	0.26	0.31	0.35	0.37	0.38	0.38	0.37	0.36	0.34	0.32	0.30	0.28	0.26	0.24	0.22	0.20	0.19	0.17
0.28	0.18	0.26	0.31	0.35	0.37	0.38	0.39	0.38	0.37	0.35	0.33	0.31	0.29	0.27	0.25	0.23	0.21	0.19	0.17
0.27	0.18	0.26	0.32	0.36	0.38	0.39	0.39	0.39	0.37	0.36	0.34	0.32	0.30	0.28	0.26	0.24	0.22	0.20	0.18
0.26	0.18	0.26	0.32	0.36	0.38	0.40	0.40	0.39	0.38	0.37	0.35	0.33	0.31	0.29	0.26	0.24	0.22	0.20	0.19
0.25	0.18	0.26	0.32	0.36	0.39	0.41	0.41	0.40	0.39	0.38	0.36	0.34	0.32	0.30	0.27	0.25	0.23	0.21	0.19
0.24	0.18	0.26	0.32	0.37	0.40	0.41	0.42	0.41	0.40	0.39	0.37	0.35	0.33	0.31	0.28	0.26	0.24	0.22	0.20
0.23	0.18	0.26	0.33	0.37	0.41	0.42	0.43	0.43	0.42	0.40	0.38	0.36	0.34	0.32	0.30	0.27	0.25	0.23	0.21
0.22	0.18	0.26	0.33	0.38	0.41	0.43	0.44	0.44	0.43	0.41	0.40	0.38	0.35	0.33	0.31	0.28	0.26	0.24	0.22
0.21	0.18	0.27	0.33	0.39	0.42	0.44	0.45	0.45	0.44	0.43	0.41	0.39	0.37	0.34	0.32	0.30	0.27	0.25	0.23
0.20	0.18	0.27	0.34	0.39	0.43	0.45	0.46	0.46	0.46	0.44	0.43	0.41	0.38	0.36	0.34	0.31	0.29	0.26	0.24
0.19	0.18	0.27	0.34	0.40	0.44	0.46	0.47	0.48	0.47	0.46	0.44	0.42	0.40	0.37	0.35	0.33	0.30	0.28	0.26
0.18	0.18	0.27	0.34	0.40	0.44	0.47	0.49	0.49	0.49	0.47	0.46	0.44	0.41	0.39	0.37	0.34	0.32	0.29	0.27
0.17	0.18	0.27	0.35	0.41	0.45	0.48	0.50	0.50	0.50	0.49	0.47	0.45	0.43	0.41	0.38	0.36	0.33	0.31	0.28
0.16	0.17	0.27	0.35	0.41	0.46	0.49	0.51	0.51	0.51	0.50	0.49	0.47	0.45	0.42	0.40	0.37	0.35	0.32	0.30
0.15	0.17	0.27	0.35	0.41	0.46	0.50	0.52	0.53	0.53	0.52	0.50	0.49	0.46	0.44	0.41	0.39	0.36	0.34	0.31
0.14	0.17	0.26	0.35	0.41	0.46	0.50	0.52	0.54	0.54	0.53	0.52	0.50	0.48	0.46	0.43	0.40	0.38	0.35	0.32
0.13	0.17	0.26	0.34	0.41	0.47	0.50	0.53	0.54	0.55	0.54	0.53	0.51	0.49	0.47	0.45	0.42	0.39	0.37	0.34
0.12	0.16	0.26	0.34	0.41	0.46	0.51	0.53	0.55	0.55	0.55	0.54	0.53	0.51	0.48	0.46	0.43	0.41	0.38	0.35
0.11	0.16	0.25	0.33	0.40	0.46	0.50	0.53	0.55	0.56	0.56	0.55	0.53	0.52	0.49	0.47	0.44	0.42	0.39	0.36
0.10	0.15	0.24	0.33	0.40	0.45	0.50	0.53	0.55	0.56	0.56	0.55	0.54	0.52	0.50	0.48	0.45	0.43	0.40	0.37
0.09	0.15	0.24	0.32	0.39	0.44	0.49	0.52	0.54	0.55	0.56	0.55	0.54	0.52	0.50	0.48	0.46	0.43	0.41	0.38
0.08	0.14	0.23	0.30	0.37	0.43	0.47	0.51	0.53	0.54	0.55	0.54	0.53	0.52	0.50	0.48	0.46	0.43	0.41	0.38
0.07	0.13	0.21	0.29	0.35	0.41	0.45	0.49	0.51	0.53	0.53	0.53	0.52	0.51	0.49	0.48	0.45	0.43	0.41	0.38
0.06	0.12	0.20	0.27	0.33	0.39	0.43	0.46	0.49	0.50	0.51	0.51	0.50	0.49	0.48	0.46	0.44	0.42	0.40	0.38
0.05	0.11	0.18	0.25	0.31	0.36	0.40	0.43	0.45	0.47	0.48	0.48	0.48	0.47	0.46	0.44	0.42	0.40	0.38	0.36

Figure C.2: Force map for circular shape electrode.

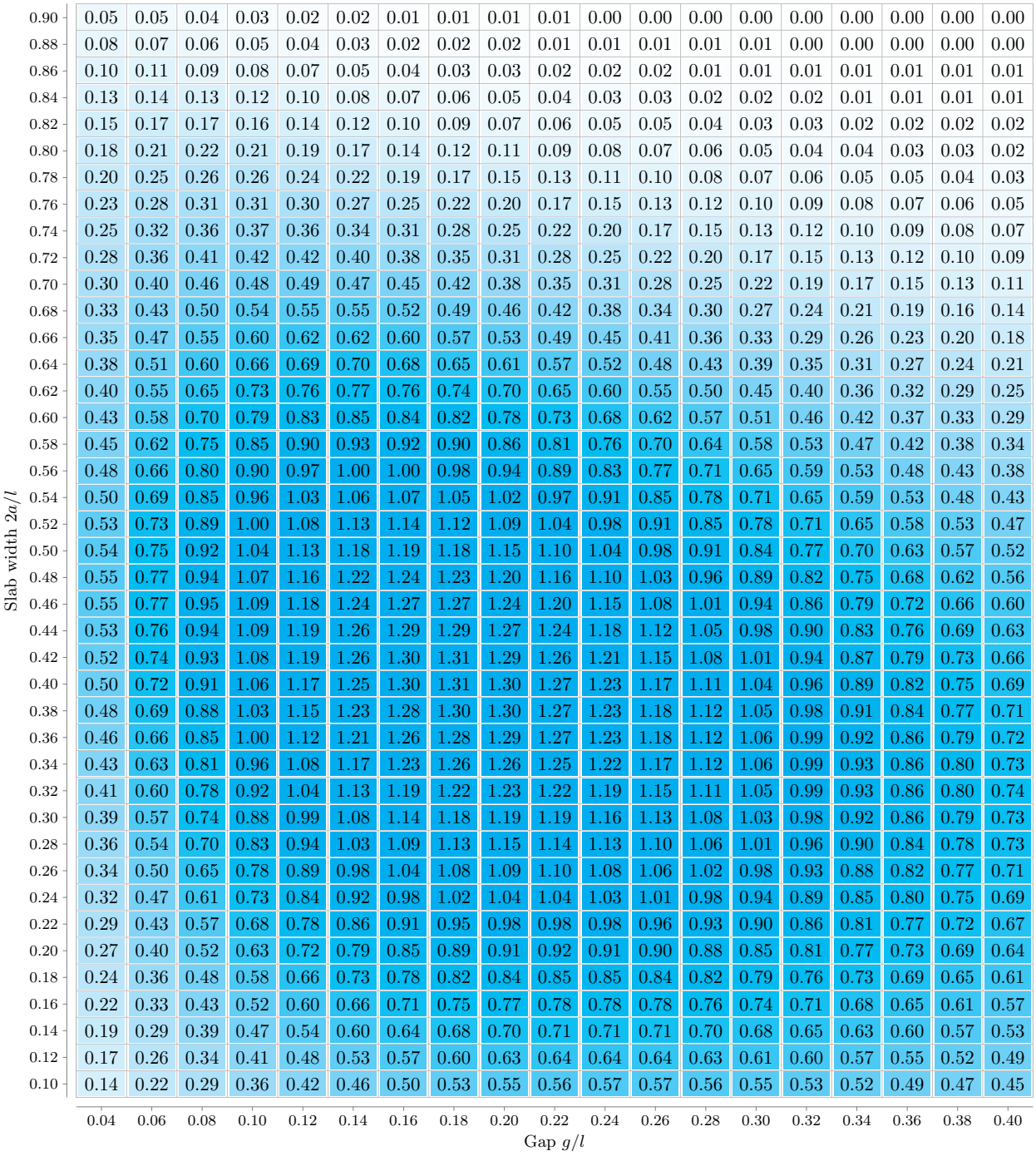

Figure C.3: Force map for rectangular shape electrode with $2b/g = 0.1$.

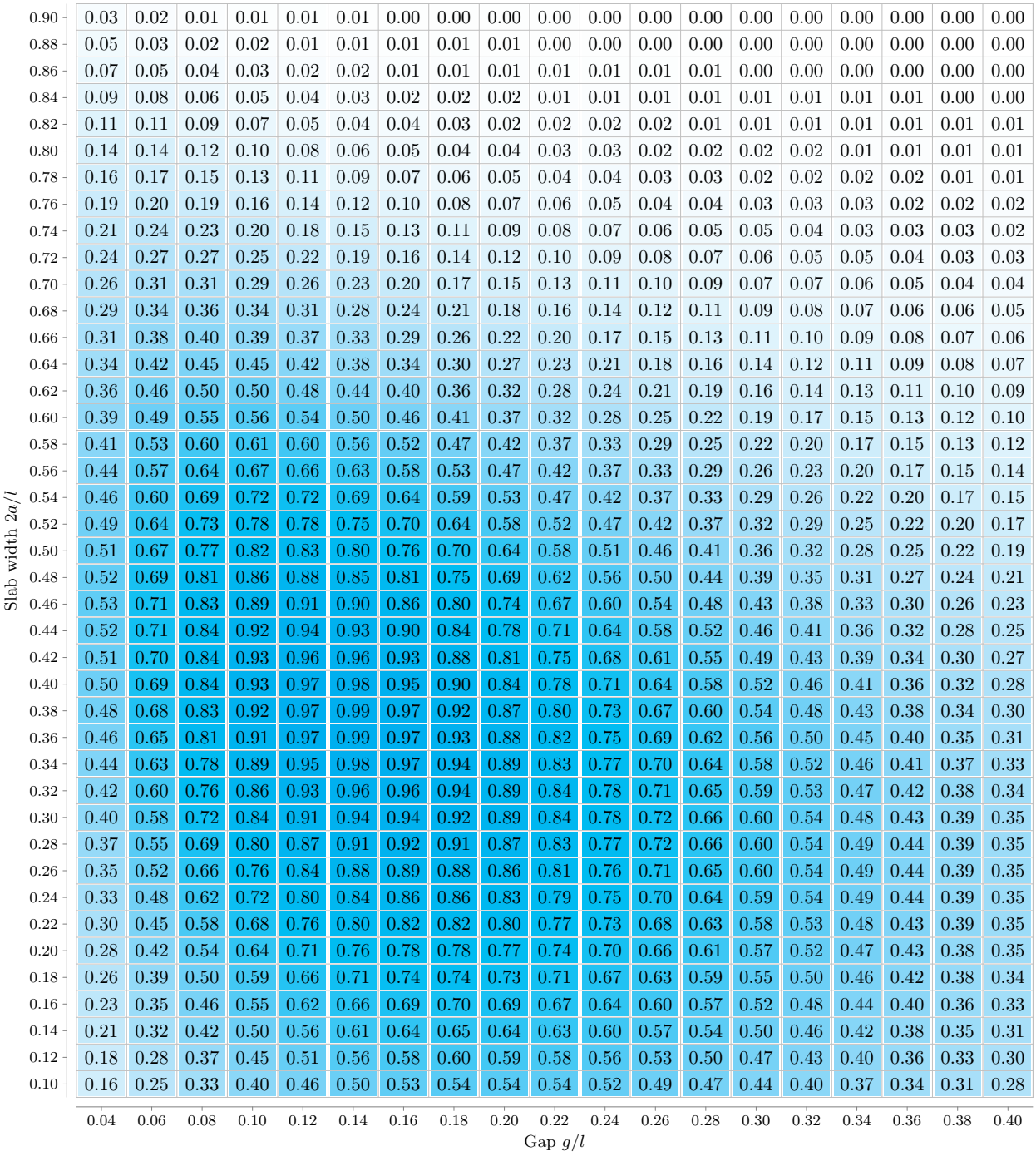

Figure C.4: Force map for rectangular shape electrode with $2b/g = 1.0$.

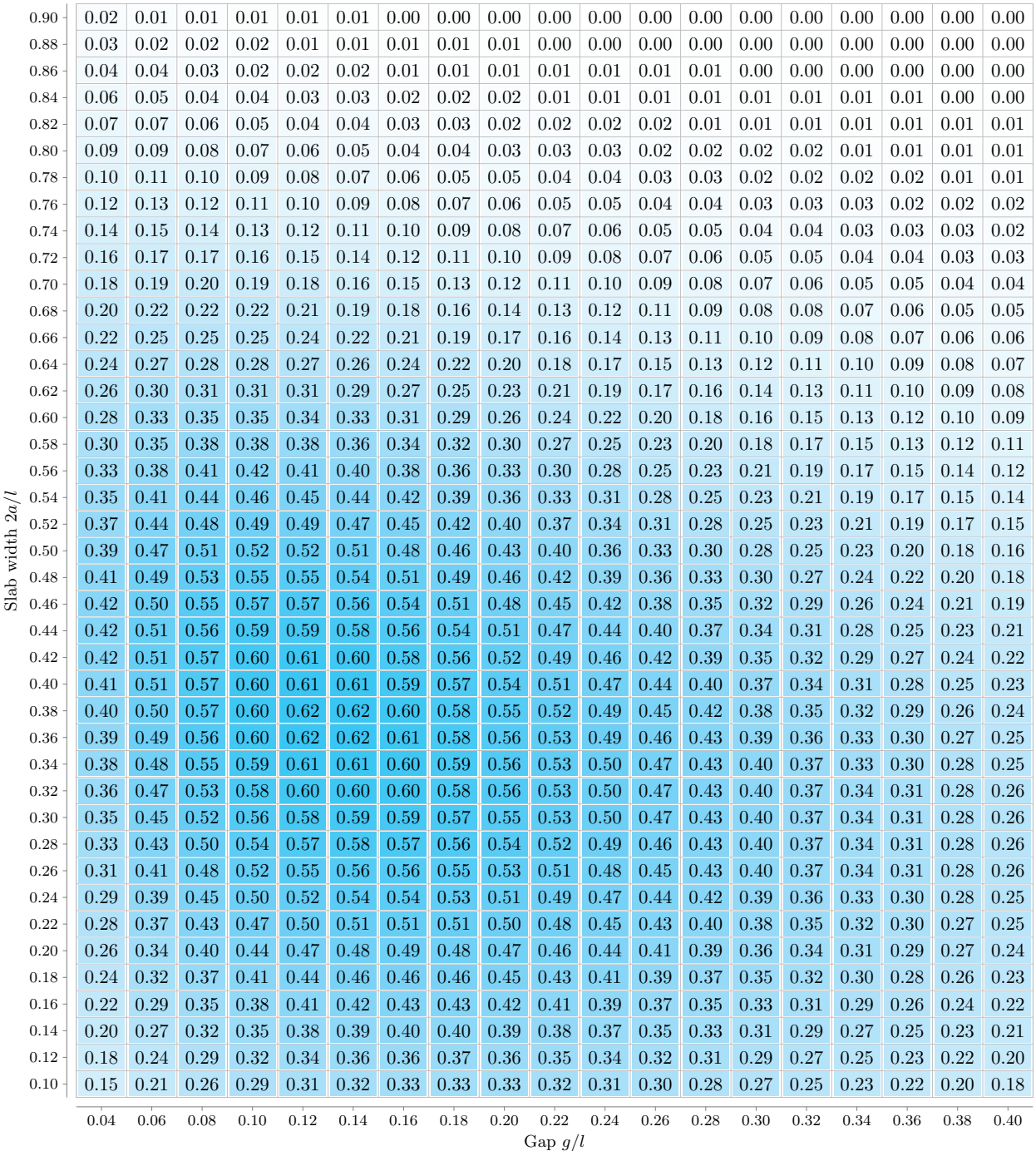

Figure C.5: Force map for rectangular shape electrode with $2b/g = 10.0$.

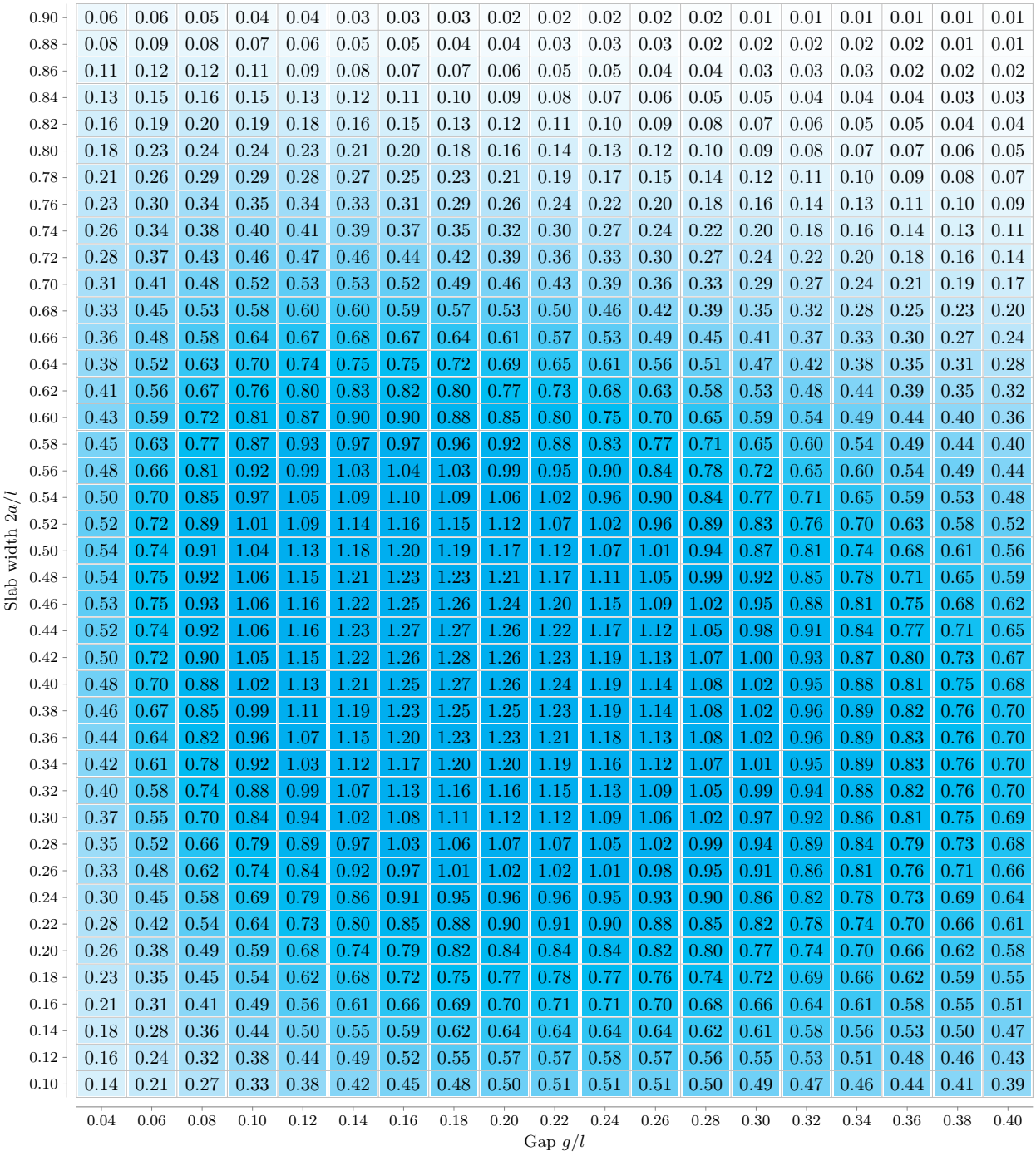

Figure C.6: Force map for elliptical shape electrode with $2b/g = 0.1$.

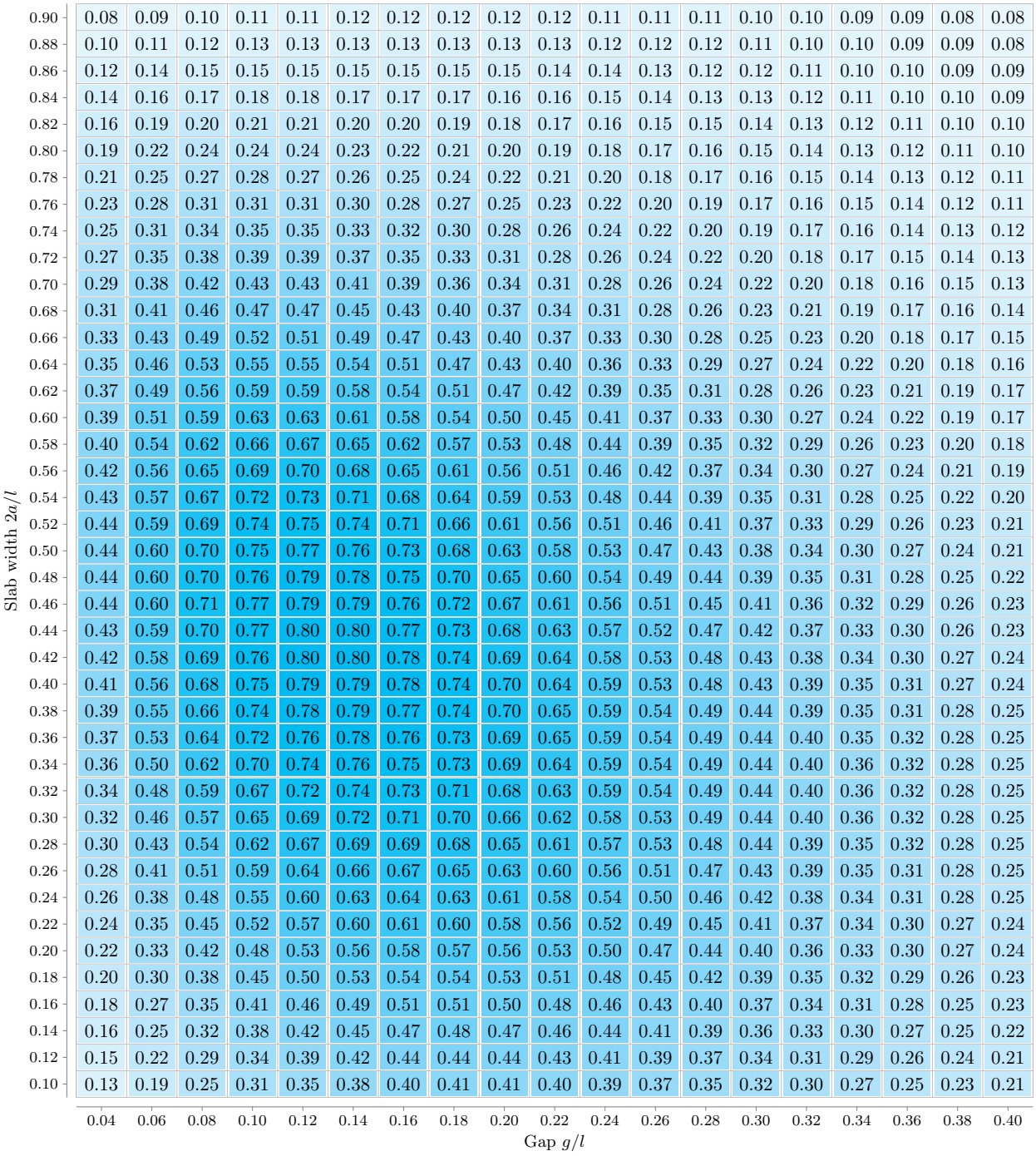

Figure C.7: Force map for elliptical shape electrode with $2b/g = 1.0$.

Slab width $2a/l$ \ Gap g/l	0.04	0.06	0.08	0.10	0.12	0.14	0.16	0.18	0.20	0.22	0.24	0.26	0.28	0.30	0.32	0.34	0.36	0.38	0.40
0.90	0.19	0.25	0.29	0.32	0.33	0.34	0.34	0.33	0.32	0.30	0.29	0.27	0.25	0.24	0.22	0.20	0.19	0.17	0.16
0.88	0.19	0.25	0.29	0.32	0.34	0.34	0.34	0.33	0.32	0.30	0.29	0.27	0.25	0.24	0.22	0.20	0.19	0.17	0.15
0.86	0.19	0.25	0.30	0.32	0.34	0.34	0.34	0.33	0.32	0.30	0.29	0.27	0.25	0.24	0.22	0.20	0.18	0.17	0.15
0.84	0.20	0.26	0.30	0.32	0.34	0.34	0.34	0.33	0.32	0.30	0.29	0.27	0.25	0.23	0.22	0.20	0.18	0.17	0.15
0.82	0.20	0.26	0.30	0.32	0.34	0.34	0.34	0.33	0.32	0.30	0.29	0.27	0.25	0.23	0.22	0.20	0.18	0.17	0.15
0.80	0.20	0.26	0.30	0.32	0.34	0.34	0.34	0.33	0.32	0.30	0.29	0.27	0.25	0.23	0.22	0.20	0.18	0.17	0.15
0.78	0.20	0.26	0.30	0.32	0.34	0.34	0.34	0.33	0.32	0.30	0.28	0.27	0.25	0.23	0.22	0.20	0.18	0.17	0.15
0.76	0.20	0.26	0.30	0.32	0.33	0.34	0.33	0.33	0.31	0.30	0.28	0.27	0.25	0.23	0.21	0.20	0.18	0.17	0.15
0.74	0.21	0.26	0.30	0.32	0.33	0.34	0.33	0.32	0.31	0.30	0.28	0.26	0.25	0.23	0.21	0.20	0.18	0.17	0.15
0.72	0.21	0.26	0.30	0.32	0.33	0.33	0.33	0.32	0.31	0.30	0.28	0.26	0.25	0.23	0.21	0.20	0.18	0.16	0.15
0.70	0.21	0.26	0.30	0.32	0.33	0.33	0.33	0.32	0.31	0.29	0.28	0.26	0.24	0.23	0.21	0.19	0.18	0.16	0.15
0.68	0.21	0.26	0.29	0.32	0.33	0.33	0.33	0.32	0.31	0.29	0.28	0.26	0.24	0.23	0.21	0.19	0.18	0.16	0.15
0.66	0.21	0.26	0.29	0.31	0.32	0.33	0.32	0.32	0.30	0.29	0.27	0.26	0.24	0.22	0.21	0.19	0.18	0.16	0.15
0.64	0.21	0.26	0.29	0.31	0.32	0.32	0.32	0.31	0.30	0.29	0.27	0.26	0.24	0.22	0.21	0.19	0.18	0.16	0.15
0.62	0.21	0.26	0.29	0.31	0.32	0.32	0.32	0.31	0.30	0.28	0.27	0.25	0.24	0.22	0.20	0.19	0.17	0.16	0.15
0.60	0.21	0.25	0.29	0.30	0.31	0.32	0.31	0.31	0.30	0.28	0.27	0.25	0.24	0.22	0.20	0.19	0.17	0.16	0.14
0.58	0.21	0.25	0.28	0.30	0.31	0.31	0.31	0.30	0.29	0.28	0.26	0.25	0.23	0.22	0.20	0.19	0.17	0.16	0.14
0.56	0.21	0.25	0.28	0.30	0.31	0.31	0.31	0.30	0.29	0.28	0.26	0.25	0.23	0.21	0.20	0.18	0.17	0.16	0.14
0.54	0.20	0.25	0.28	0.29	0.30	0.30	0.30	0.29	0.28	0.27	0.26	0.24	0.23	0.21	0.20	0.18	0.17	0.15	0.14
0.52	0.20	0.24	0.27	0.29	0.30	0.30	0.30	0.29	0.28	0.27	0.25	0.24	0.23	0.21	0.19	0.18	0.17	0.15	0.14
0.50	0.20	0.24	0.27	0.28	0.29	0.30	0.29	0.29	0.28	0.26	0.25	0.24	0.22	0.21	0.19	0.18	0.16	0.15	0.14
0.48	0.20	0.24	0.26	0.28	0.29	0.29	0.29	0.28	0.27	0.26	0.25	0.23	0.22	0.20	0.19	0.18	0.16	0.15	0.14
0.46	0.19	0.23	0.26	0.27	0.28	0.28	0.28	0.28	0.27	0.26	0.24	0.23	0.22	0.20	0.19	0.17	0.16	0.15	0.14
0.44	0.19	0.23	0.25	0.27	0.28	0.28	0.28	0.27	0.26	0.25	0.24	0.23	0.21	0.20	0.19	0.17	0.16	0.15	0.13
0.42	0.18	0.22	0.25	0.26	0.27	0.27	0.27	0.27	0.26	0.25	0.24	0.22	0.21	0.20	0.18	0.17	0.16	0.14	0.13
0.40	0.18	0.22	0.24	0.25	0.26	0.27	0.27	0.26	0.25	0.24	0.23	0.22	0.21	0.19	0.18	0.17	0.15	0.14	0.13
0.38	0.17	0.21	0.23	0.25	0.26	0.26	0.26	0.26	0.25	0.24	0.23	0.22	0.20	0.19	0.18	0.16	0.15	0.14	0.13
0.36	0.17	0.20	0.23	0.24	0.25	0.26	0.25	0.25	0.24	0.24	0.22	0.21	0.20	0.19	0.17	0.16	0.15	0.14	0.13
0.34	0.16	0.20	0.22	0.24	0.24	0.25	0.25	0.25	0.24	0.23	0.22	0.21	0.20	0.18	0.17	0.16	0.15	0.14	0.13
0.32	0.16	0.19	0.21	0.23	0.24	0.24	0.24	0.24	0.23	0.23	0.22	0.20	0.19	0.18	0.17	0.16	0.15	0.13	0.12
0.30	0.15	0.18	0.21	0.22	0.23	0.24	0.24	0.23	0.23	0.22	0.21	0.20	0.19	0.18	0.17	0.15	0.14	0.13	0.12
0.28	0.14	0.18	0.20	0.21	0.22	0.23	0.23	0.23	0.22	0.22	0.21	0.20	0.19	0.17	0.16	0.15	0.14	0.13	0.12
0.26	0.14	0.17	0.19	0.21	0.22	0.22	0.22	0.22	0.22	0.21	0.20	0.19	0.18	0.17	0.16	0.15	0.14	0.13	0.12
0.24	0.13	0.16	0.18	0.20	0.21	0.21	0.22	0.22	0.21	0.21	0.20	0.19	0.18	0.17	0.16	0.15	0.14	0.13	0.12
0.22	0.12	0.15	0.18	0.19	0.20	0.21	0.21	0.21	0.21	0.20	0.19	0.18	0.17	0.16	0.15	0.14	0.13	0.12	0.11
0.20	0.11	0.15	0.17	0.18	0.19	0.20	0.20	0.20	0.20	0.19	0.19	0.18	0.17	0.16	0.15	0.14	0.13	0.12	0.11
0.18	0.11	0.14	0.16	0.18	0.19	0.19	0.20	0.20	0.19	0.19	0.18	0.18	0.17	0.16	0.15	0.14	0.13	0.12	0.11
0.16	0.10	0.13	0.15	0.17	0.18	0.19	0.19	0.19	0.19	0.18	0.18	0.17	0.16	0.15	0.14	0.14	0.13	0.12	0.11
0.14	0.09	0.12	0.15	0.16	0.17	0.18	0.18	0.18	0.18	0.18	0.17	0.17	0.16	0.15	0.14	0.13	0.12	0.11	0.11
0.12	0.09	0.12	0.14	0.15	0.16	0.17	0.18	0.18	0.18	0.17	0.17	0.16	0.16	0.15	0.14	0.13	0.12	0.11	0.10
0.10	0.08	0.11	0.13	0.15	0.16	0.17	0.17	0.17	0.17	0.17	0.16	0.16	0.15	0.14	0.14	0.13	0.12	0.11	0.10

Figure C.8: Force map for elliptical shape electrode with $2b/g = 10.0$.

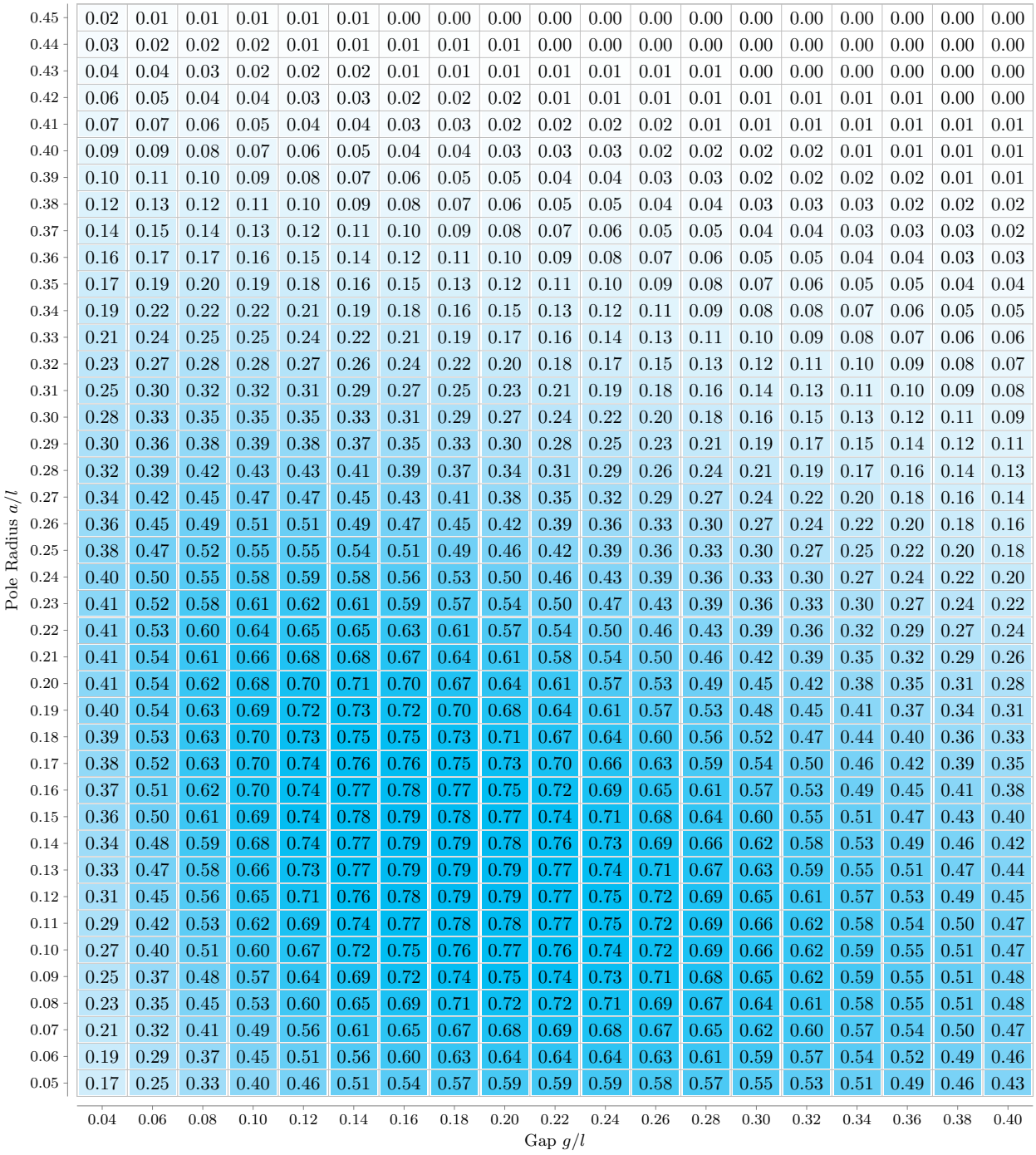

Figure C.9: Force map for square shape electrode.

BIBLIOGRAPHY

[1] A. Chiba, K. Kiyota, N. Hoshi, M. Takemoto, and S. Ogasawara, "Development of a Rare-Earth-Free SR Motor With High Torque Density for Hybrid Vehicles," *IEEE Transactions on Energy Conversion*, vol. 30, no. 1, pp. 175–182, Mar. 2015.

[2] A. Chiba, "Rare-Earth-Free AC Motors -an Alternative Approach Advances," in *2011 IEEE International Electric Machines Drives Conference (IEMDC) Invited Lecture*, May 2011.

[3] Y. Kano, "Recent technical trends in SRM and FSM," in *Power Electronics Conference (IPEC-Hiroshima 2014 - ECCE-ASIA), 2014 International*, May 2014, pp. 2004–2010.

[4] B. Ge and D. C. Ludois, "Dielectric liquids for enhanced field force in macro scale direct drive electrostatic actuators and rotating machinery," *IEEE Transactions on Dielectrics and Electrical Insulation*, vol. 23, no. 4, pp. 1924–1934, Aug. 2016.

[5] M. A. White, "Sustainable Approaches to Advanced Materials Research," *Physics in Canada*, vol. 68, no. 1, 2012.

[6] "Neodymium Prices," http://www.metalprices.com/metal/neodymium/neodymium-metal-china, Jun. 2014.

[7] BGS, "Risk List 2015: Current Supply Risk for Chemical Elements or Element Groups which are of Econoic Value," British Geological Survey, Tech. Rep., 2015.

[8] "Copper Prices," http://www.lme.com/metals/non-ferrous/copper, Jun. 2014.

[9] J. D. McFarland, "On the design of rare-earth-free and reduced rare-earth permanent magnet machines for high-performance traction applications," Ph.D. dissertation, University of Wisconsin-Madison, 2015.

[10] T. A. Lipo, *Introduction to AC Machine Design*, 2nd ed. Madison, WI: University of Wisconsin-Madison, Aug. 2007.

[11] "Electric Motors | WEG," https://www.weg.net/catalog/weg/US/en/Electric-Motors/c/US_MT.

[12] SIMENS, "SINAMICS Inverters for Single Axis Drives and SIMOTICS Motors," 2015.

[13] "SLA Materials," http://www.forecast3d.com/sla_materials.html, 2016.

[14] A. E. Fitzgerald, C. K. Jr, and S. Umans, *Electric Machinery*, 6th ed. Boston, MA: McGraw-Hill, Jul. 2002.

[15] O. Jefimenko, *Electrostatic Motors: Their History, Types and Principles of Operation*, 1st ed. Beltsville, MD: Integrity Research Institute, Mar. 2011.

[16] C. A. S. Hall, J. G. Lambert, and S. B. Balogh, "EROI of different fuels and the implications for society," *Energy Policy*, vol. 64, pp. 141–152, Jan. 2014.

[17] M. A. Elsayed, R. Matthews, and N. D. Mortimer, "Carbon and energy balances for a range of biofuel options," Sheffield Hallam University, Tech. Rep. B/B6/00784/REP, Mar. 2003.

[18] R. Feynman, "There's plenty of room at the bottom," *Journal of Microelectromechanical Systems*, vol. 1, no. 1, pp. 60–66, Mar. 1992.

[19] ——, "Infinitesimal machinery," *Journal of Microelectromechanical Systems*, vol. 2, no. 1, pp. 4–14, Mar. 1993.

[20] W. S. Trimmer, Ed., *Micromechanics and MEMS: Classic and Seminal Papers to 1990*, 1st ed. New York: Wiley-IEEE Press, Jan. 1997.

[21] P. Chapman and P. Krein, "Micromotor technology: Electric drive designer's perspective," in *Conference Record of the 2001 IEEE Industry Applications Conference, 2001. Thirty-Sixth IAS Annual Meeting*, vol. 3, Sep. 2001, pp. 1978–1983 vol.3.

[22] A. Yamamoto, K. Ichiyanagi, T. Higuchi, H. Imamizu, R. Gassert, M. Ingold, L. Sache, and H. Bleuler, "Evaluation of MR-compatibility of Electrostatic Linear Motor," in *Proceedings of the 2005 IEEE International Conference on Robotics and Automation*, Apr. 2005, pp. 3658–3663.

[23] L.-S. Fan, Y.-C. Tai, and R. Muller, "IC-processed electrostatic micro-motors," in *Electron Devices Meeting, 1988. IEDM '88. Technical Digest., International*, Dec. 1988, pp. 666–669.

[24] Y. C. Tai, L. S. Fan, and R. S. Muller, "IC-processed micro-motors: Design, technology, and testing," in *IEEE Micro Electro Mechanical Systems, 1989, Proceedings, An Investigation of Micro Structures, Sensors, Actuators, Machines and Robots*, Feb. 1989, pp. 1–6.

[25] L.-S. Fan, Y.-C. Tai, and R. Muller, "Integrated movable micromechanical structures for sensors and actuators," *IEEE Transactions on Electron Devices*, vol. 35, no. 6, pp. 724–730, Jun. 1988.

[26] R. X. Gao and J. Fang, "Design and performance evaluation of linear and rotary surface-driven electrostatic microactuators," in *Proceedings IEEE Conference on Industrial Automation and Control Emerging Technology Applications*, May 1995, pp. 572–579.

[27] R. X. Gao, J. Fang, B. Rao, and R. O. Warrington, "Miniaturized surface-driven electrostatic actuators: Design and performance evaluation," *IEEE/ASME Transactions on Mechatronics*, vol. 2, no. 1, pp. 1–7, Mar. 1997.

[28] T. Niino, T. Higuchi, and S. Egawa, "Dual excitation multiphase electrostatic drive," in *, Conference Record of the 1995 IEEE Industry Applications Conference, 1995. Thirtieth IAS Annual Meeting, IAS '95*, vol. 2, Oct. 1995, pp. 1318–1325 vol.2.

[29] S. F. Bart and J. H. Lang, "Electroquasistatic induction micromotors," in *IEEE Micro Electro Mechanical Systems, 1989, Proceedings, An Investigation of Micro Structures, Sensors, Actuators, Machines and Robots*, Feb. 1989, pp. 7–12.

[30] S. Nagle, C. Livermore, L. Frechette, R. Ghodssi, and J. H. Lang, "An electric induction micromotor," *Journal of Microelectromechanical Systems*, vol. 14, no. 5, pp. 1127–1143, Oct. 2005.

[31] S. C. Jacobsen, R. H. Price, J. E. Wood, T. H. Rytting, and M. Rafaelof, "The wobble motor: Design, fabrication and testing of an eccentric-motion electrostatic microactuator," in *1989*

International Conference on Robotics and Automation Proceedings, May 1989, pp. 1536–1546 vol.3.

[32] T. Furuhata, T. Hirano, L. H. Lane, R. E. Fontana, L. S. Fan, and H. Fujita, "Outer rotor surface-micromachined wobble micromotor," in *[1993] Proceedings IEEE Micro Electro Mechanical Systems*, Feb. 1993, pp. 161–166.

[33] F. J. Santana, J. M. Monzón, S. García-Alonso, and J. A. Montiel-Nelson, "Lumped parametric model for an electrostatic induction micromotor using GA," in *2009 35th Annual Conference of IEEE Industrial Electronics*, Nov. 2009, pp. 4029–4033.

[34] A. Ketabi and M. J. Navardi, "Optimization of Variable-Capacitance Micromotor Using Genetic Algorithm," *Journal of Microelectromechanical Systems*, vol. 20, no. 2, pp. 497–504, Apr. 2011.

[35] W. Trimmer and K. Gabriel, "Design considerations for a practical electrostatic micro-motor," *Sensors and Actuators*, vol. 11, no. 2, pp. 189–206, 1987.

[36] J. R. Melcher, *Continuum Electromechanics*, 1st ed. Cambridge, Mass: The MIT Press, Jun. 1981.

[37] F. J. Santana, J. M. Monzón-Verona, S. García-Alonso, and J. A. Montiel-Nelson, "Analysis of spatial harmonics in a polyphase electrostatic induction micromotor," in *The XIX International Conference on Electrical Machines - ICEM 2010*, Sep. 2010, pp. 1–6.

[38] S. F. Bart, T. A. Lober, R. T. Howe, J. H. Lang, and M. F. Schlecht, "Design considerations for micromachined electric actuators," *Sensors and Actuators*, vol. 14, no. 3, pp. 269–292, Jul. 1988.

[39] S. Kumar, D. Cho, and W. Carr, "Electric levitation bearings for micromotors," in *, 1991 International Conference on Solid-State Sensors and Actuators, 1991. Digest of Technical Papers, TRANSDUCERS '91*, Jun. 1991, pp. 882–885.

[40] J. E. Colgate, H. Matsumoto, and W. Wannasuphoprasit, "Linear electrostatic actuators: Gap maintenance via fluid bearings," *Robotics and Computer-Integrated Manufacturing*, vol. 10, no. 5, pp. 365–376, Oct. 1993.

[41] L. Frechette, S. Nagle, R. Ghodssi, S. Umans, M. Schmidt, and J. Lang, "An electrostatic induction micromotor supported on gas-lubricated bearings," in *The 14th IEEE International Conference on Micro Electro Mechanical Systems, 2001. MEMS 2001*, Jan. 2001, pp. 290–293.

[42] M. T. Hou, M.-X. Huang, and C.-M. Chang, "Nested folded-beam suspensions with low longitudinal stiffness for comb-drive actuators," *Journal of Micromechanics and Microengineering*, vol. 24, no. 12, p. 125022, 2014.

[43] J. G. Trump, "Vacuum electrostatic engineering," Ph.D. dissertation, Massachusetts Institute of Technology, 1933.

[44] S. F. Philp, "The Vacuum-Insulated, Varying-Capacitance Machine," *IEEE Transactions on Electrical Insulation*, vol. EI-12, no. 2, pp. 130–136, Apr. 1977.

[45] "Shinsei high power electrostatic motor," http://www.shinsei-motor.com/English/techno/, 2007.

[46] R. O'Donnell, N. Schofield, A. Smith, and J. Cullen, "Design Concepts for High-Voltage Variable-Capacitance DC Generators," *IEEE Transactions on Industry Applications*, vol. 45, no. 5, pp. 1778–1784, Sep. 2009.

[47] N. J. Felici, "Ten years of research on electrostatics at the University of Grenoble 1942-1952," *British Journal of Applied Physics*, vol. 4, p. 62, Jan. 1953.

[48] R. Vanslette, "Torque Generation Using Ferroelectric Materials," *IEEE Transactions on Aerospace and Electronic Systems*, vol. AES-1, no. 2, pp. 124–128, Oct. 1965.

[49] M. A. Lieberman and A. J. Lichtenberg, *Principles of Plasma Discharges and Materials Processing*, 2nd ed. John Wiley & Sons, Apr. 2005.

[50] P. T. Krein, "Nonideal Effects in Electrostatic Induction Motors," Ph.D. dissertation, University of Illinois Urbana-Champaign, 1982.

[51] B. Bollée, "Electrostatic Motors," *Philips Technical Review*, vol. 30, pp. 178–194, 1969.

[52] D. C. Ludois, "Varying capacitance rotating electrical machine," U.S. Patent US9 184 676 B2, Nov., 2015, international Classification H02N1/08, H02N1/00; Cooperative Classification H02N1/00, H02N1/006, H02N1/08, H02N1/002.

[53] D. Ludois, M. Erickson, and J. Reed, "Aerodynamic Fluid Bearings for Translational and Rotating Capacitors in Noncontact Capacitive Power Transfer Systems," *IEEE Transactions on Industry Applications*, vol. 50, no. 2, pp. 1025–1033, Mar. 2014.

[54] B. Ge, A. N. Ghule, and D. C. Ludois, "A 3D Printed Fluid Filled Electrostatic Rotating Machine Designed with Conformal Mapping Methods," *IEEE Transactions on Industry Applications*, vol. PP, no. 99, pp. 1–1, 2017.

[55] G. Reitz, B. Butrymowicz, J. Reed, B. Ge, and D. C. Ludois, "A switched elastance electrostatic machine constructed from sustainable elements for rotational actuators," in *2017 IEEE Energy Conversion Congress and Exposition (ECCE)*, Oct. 2017, pp. 2389–2395.

[56] T. Sashida, "Electrostatic motor," European Union Patent EP2 040 366 A1, Mar., 2009, international Classification H02N1/00; Cooperative Classification H02N1/004; European Classification H02N1/00B1.

[57] D. Alpert, D. A. Lee, E. M. Lyman, and H. E. Tomaschke, "Initiation of Electrical Breakdown in Ultrahigh Vacuum," *Journal of Vacuum Science & Technology*, vol. 1, no. 2, pp. 35–50, Nov. 1964.

[58] S. Giere, M. Kurrat, and U. Schumann, "HV dielectric strength of shielding electrodes in vacuum circuit-breakers," in *20th International Symposium on Discharges and Electrical Insulation in Vacuum, 2002*, 2002, pp. 119–122.

[59] I. Fofana, "50 years in the development of insulating liquids," *IEEE Electrical Insulation Magazine*, vol. 29, no. 5, pp. 13–25, Sep. 2013.

[60] I. Fernández, A. Ortiz, F. Delgado, C. Renedo, and S. Pérez, "Comparative evaluation of alternative fluids for power transformers," *Electric Power Systems Research*, vol. 98, pp. 58–69, May 2013.

[61] N. Felici, "Electrostatic generators," *Electronics and Power*, vol. 11, no. 5, pp. 169–171, May 1965.

[62] O. Heaviside, *Electrical Papers*. Macmillan and Company, 1894.

[63] D. J. Griffiths, *Introduction to Electrodynamics*, 4th ed. Boston: Addison-Wesley, Oct. 2012.

[64] J. D. Jackson, *Classical Electrodynamics Third Edition*, 3rd ed. New York: Wiley, Aug. 1998.

[65] T. J. E. Miller, *Speed's Electric Motors*. Magna Physics, 2004.

[66] J. Pyrhonen, T. Jokinen, and V. Hrabovcova, *Design of Rotating Electrical Machines*, 1st ed. Chichester, West Sussex, United Kingdom ; Hoboken, NJ: Wiley, Feb. 2009.

[67] T. Sashida, "Electrostatic motor," U.S. Patent US8 278 797 B2, Oct., 2012, u.S. Classification 310/309; International Classification H02N1/00; Cooperative Classification H02N1/004; European Classification H02N1/00B1.

[68] "Crisco vegetable oil MSDS," https://www.lakeland.edu/PDFs/MSDS/1764/Vegetable%20Shortening%20(Crisco)%20No%20Date.pdf, 2016.

[69] "Environment FR3 fluid brochure," http://www.nttworldwide.com/docs/fr3brochure.pdf, 2016.

[70] C. P. Systems, *Cooper Power Systems Envirotemp FR3 Vegetable Oil Based Insulating Dielectric Fluid*. DIANE Publishing, May 2002.

[71] "FR3 MSDS," http://www.cooperindustries.com/content/dam/public/powersystems/resources/MSDS/98082_MSDS.pdf, 2016.

[72] "STO-50 Silicone Transformer Oil," http://www.clearcoproducts.com/pdf/specialty/NP-STO-50%20%20Silicone%20Transformer%20Oil.pdf, 2016.

[73] "Dupont Vertrel XF specialty fluid," http://www2.dupont.com/Vertrel/en_US/assets/downloads/pdf/k05113.pdf, 2016.

[74] T. J. Bruno and P. D. N. Svoronos, *CRC Handbook of Basic Tables for Chemical Analysis, Third Edition*. CRC Press, Dec. 2010.

[75] M. M. Safarov, A. V. Kartavchenko, and M. A. Zaripova, "Viscosity and density of aqueous solutions of hydrazine and phenylhydrazine as functions of temperature at atmospheric pressure," *Journal of Engineering Physics and Thermophysics*, vol. 68, no. 2, pp. 252–254, Mar. 1995.

[76] "Hydrazine MSDS," http://www.sciencelab.com/msds.php?msdsId=9924279, 2016.

[77] H. Schlundt and A. F. O. Germann, "The Dielectric Constant of Liquid Phosgene," *The Journal of Physical Chemistry*, vol. 29, no. 3, pp. 353–355, Jan. 1924.

[78] J. G. Speight, *Lange's Handbook of Chemistry, 70th Anniversary Edition*, 16th ed. New York: McGraw-Hill Education, Jan. 2005.

[79] "Phosgene MSDS," http://www.vdmchemical.com/vdm/images/vdm/MSDS/phosgene.pdf, 2016.

[80] "Acetone MSDS," http://www.sciencelab.com/msds.php?msdsId=9927062, 2016.

[81] A. I. Anderson, "The dielectric constant of liquid bromine," *Proceedings of the Physical Society*, vol. 40, pp. 62–70, Dec. 1927.

[82] "Absolute or dynamic viscosity of some common fluids," http://www.engineeringtoolbox.com/absolute-viscosity-liquids-d_1259.html, 2016.

[83] "Bromine MSDS," https://www.sciencelab.com/msds.php?msdsId=9927659, 2016.

[84] A. L. Lee and R. T. Ellington, "Viscosity of n-Decane in the Liquid Phase." *Journal of Chemical & Engineering Data*, vol. 10, no. 4, pp. 346–348, Oct. 1965.

[85] "N-Decane MSDS," http://www.sciencelab.com/msds.php?msdsId=9923666, 2016.

[86] "Methylene chloride," http://bts.chimie.encpb.free.fr/09_10/cours/gene/chapitre_02/02_04_dichloromethane.pdf, 2016.

[87] "Methylene chloride MSDS," http://www.sciencelab.com/msds.php?msdsId=9926060, 2016, msds.

[88] B. Salvage, "The Dielectric Breakdown of some Simple Organic Liquids," *Proceedings of the IEE - Part IV: Institution Monographs*, vol. 98, no. 1, pp. 15–22, Oct. 1951.

[89] "Hexanes MSDS," http://www.sciencelab.com/msds.php?msdsId=9927187, 2016.

[90] J. Kolb, S. Kono, S. Xiao, B. Goan, X. Lu, C. Bickes, M. Laroussi, R. Joshi, K. Schoenbach, and E. Schamiloglu, "Water and propylene carbonate as storage and switching media in pulsed power systems," in *Pulsed Power Conference, 2003. Digest of Technical Papers. PPC-2003. 14th IEEE International*, vol. 1, Jun. 2003, pp. 715–718 Vol.1.

[91] C. Wohlfarth, "Viscosity of propylene carbonate," in *Supplement to IV/18*, ser. Landolt-Börnstein - Group IV Physical Chemistry, M. D. Lechner, Ed. Springer Berlin Heidelberg, 2008, no. 25, pp. 202–204.

[92] R. Bartnikas, *Electrical Insulating Liquids*. ASTM International, 1994.

[93] "Propylene Carbonate MSDS," http://www.sciencelab.com/msds.php?msdsId=9927238, 2016.

[94] "Jeffsol alkylene carbonates brochure," http://www.huntsman.com/performance_products/Media%20Library/global/files/jeffsol_alkylene_carbonates_brochure.pdf, 2016.

[95] "Ethylene Carbonate MSDS," http://www.sciencelab.com/msds.php?msdsId=9923969, 2016.

[96] W. M. Haynes, Ed., *CRC Handbook of Chemistry and Physics, 95th Edition*, 95th ed. Boca Raton, Fla.: CRC Press, Jun. 2014.

[97] "Water MSDS," https://www.sciencelab.com/msds.php?msdsId=9927321, 2016.

[98] W. M. Moeny, "Development of a High Dielectric Constant Insulating Oil," in *2005 IEEE Pulsed Power Conference*, Jun. 2005, pp. 1141–1142.

[99] P. B. Sankar, "Measurement of air breakdown voltage and electric field using standad sphere gap method," MTech, National Institute of Technology Rourkela, Jun. 2011.

[100] S. D. Pawar, P. Murugavel, and D. M. Lal, "Effect of relative humidity and sea level pressure on electrical conductivity of air over Indian Ocean," *Journal of Geophysical Research: Atmospheres*, vol. 114, no. D2, p. D02205, Jan. 2009.

[101] "Air MSDS," http://airgas.com/msds/001002.pdf, 2016.

[102] R. Park, "Two-reaction theory of synchronous machines generalized method of analysis-part I," *American Institute of Electrical Engineers, Transactions of the*, vol. 48, no. 3, pp. 716–727, Jul. 1929.

[103] ——, "Two-reaction theory of synchronous machines-II," *American Institute of Electrical Engineers, Transactions of the*, vol. 52, no. 2, pp. 352–354, Jun. 1933.

[104] F. A. Rengifo, L. Romeral, J. Cusidó, and J. J. Cárdenas, "New Model of a Converter-Based Generator Using Electrostatic Synchronous Machine Concept," *IEEE Transactions on Energy Conversion*, vol. 29, no. 2, pp. 344–353, Jun. 2014.

[105] D. W. Novotny and T. A. Lipo, *Vector Control and Dynamics of AC Drives*, 1st ed. Oxford : New York: Clarendon Press, Sep. 1996.

[106] M. W. Degner and C. M. Wolf, "Transient analysis of asymmetric AC systems using complex vectors," in *2017 IEEE International Electric Machines and Drives Conference (IEMDC)*, May 2017, pp. 1–8.

[107] W. C. Young, R. G. Budynas, and A. M. Sadegh, *Roark's Formulas for Stress and Strain, 8th Edition*, 8th ed. New York: McGraw-Hill Education, Dec. 2011.

[108] T. C. O'Connell and P. T. Krein, "A Schwarz-Christoffel-Based Analytical Method for Electric Machine Field Analysis," *IEEE Transactions on Energy Conversion*, vol. 24, no. 3, pp. 565–577, Sep. 2009.

[109] T. Driscoll and S. Vavasis, "Numerical Conformal Mapping Using Cross-Ratios and Delaunay Triangulation," *SIAM Journal on Scientific Computing*, vol. 19, no. 6, pp. 1783–1803, Nov. 1998.

[110] T. A. Driscoll, "Algorithm 756: A MATLAB Toolbox for Schwarz-Christoffel Mapping," *ACM Trans. Math. Softw.*, vol. 22, no. 2, pp. 168–186, Jun. 1996.

[111] ——, "Algorithm 843: Improvements to the Schwarz-Christoffel Toolbox for MATLAB," *ACM Trans. Math. Softw.*, vol. 31, no. 2, pp. 239–251, Jun. 2005.

[112] W. Wang, W. Ma, Q. Wang, and H. Ren, "Conformal mapping for multiple terminals," *Scientific Reports*, vol. 6, p. 36918, Nov. 2016.

[113] V. F. hanna, "Finite boundary corrections to coplanar stripline analysis," *Electronics Letters*, vol. 16, no. 15, pp. 604–606, Jul. 1980.

[114] C. Wan and J. X. Zheng, "Accurate solution of periodic microstrips for digital applications," *IEEE Transactions on Microwave Theory and Techniques*, vol. 51, no. 3, pp. 1003–1008, Mar. 2003.

[115] R. Schinzinger and P. A. A. Laura, *Conformal Mapping: Methods and Applications*. Mineola, NY: Dover Publications, Nov. 2003.

[116] T. A. Driscoll and L. N. Trefethen, *Schwarz-Christoffel Mapping*, 1st ed. Cambridge ; New York: Cambridge University Press, Jun. 2002.

[117] Y. Huang, B. Ge, J. Dong, H. Lin, J. Zhu, and Y. Guo, "3-D Analytical Modeling of No-Load Magnetic Field of Ironless Axial Flux Permanent Magnet Machine," *IEEE Transactions on Magnetics*, vol. 48, no. 11, pp. 2929–2932, Nov. 2012.

[118] M. Xikui, Q. Xiuying, and Q. Yuanren, "An approach for analysing the effect of conductor-strip-thickness on quasi-TEM characteristics of printed multiconductor strip lines," *IEEE Transactions on Magnetics*, vol. 29, no. 2, pp. 1653–1655, Mar. 1993.

[119] M. Nakajima and E. Yamashita, "Rectangular boundary division method and its applications (invited review article)," *International Journal of Microwave and Millimeter-Wave Computer-Aided Engineering*, vol. 3, no. 3, pp. 205–220, Jul. 1993.

[120] D. Homentcovschi, G. Ghione, C. Naldi, and R. Oprea, "Analytic determination of the capacitance matrix of planar or cylindrical multiconductor lines on multilayered substrates," *IEEE Transactions on Microwave Theory and Techniques*, vol. 43, no. 2, pp. 363–373, Feb. 1995.

[121] D. Homentcovschi and R. Oprea, "Analytically determined quasi-static parameters of shielded or open multiconductor microstrip lines," *IEEE Transactions on Microwave Theory and Techniques*, vol. 46, no. 1, pp. 18–24, Jan. 1998.

[122] D. Homentcovschi, "Electrostatic field of a system of aligned electrodes," *Journal of Electrostatics*, vol. 26, no. 2, pp. 187–200, 1991.

[123] B. Ge and D. C. Ludois, "Design Concepts for a Fluid-Filled Three-Phase Axial-Peg-Style Electrostatic Rotating Machine Utilizing Variable Elastance," *IEEE Transactions on Industry Applications*, vol. 52, no. 3, pp. 2156–2166, May 2016.

[124] B. Ge, A. N. Ghule, and D. C. Ludois, "A dq-axis framework for electrostatic synchronous machines and charge oriented control," in *2017 IEEE Energy Conversion Congress and Exposition (ECCE)*, Oct. 2017, pp. 2396–2403.

[125] B. Ge and D. C. Ludois, "A 1-phase 48-pole axial peg style electrostatic rotating machine utilizing variable elastance," in *2015 IEEE International Electric Machines Drives Conference (IEMDC)*, May 2015, pp. 604–610.

[126] D. J. Klingenberg, "Particle Polarization and Nonlinear Effects in Electrorheological Suspensions," *MRS Bulletin*, vol. 23, no. 08, pp. 30–34, Aug. 1998.

[127] D. C. Ludois, J. K. Reed, and K. Hanson, "Capacitive Power Transfer for Rotor Field Current in Synchronous Machines," *IEEE Transactions on Power Electronics*, vol. 27, no. 11, pp. 4638–4645, Nov. 2012.

[128] J. Dai, S. Hagen, D. C. Ludois, and I. P. Brown, "Synchronous Generator Brushless Field Excitation and Voltage Regulation via Capacitive Coupling Through Journal Bearings," *IEEE Transactions on Industry Applications*, vol. 53, no. 4, pp. 3317–3326, Jul. 2017.

[129] C. Stancu, T. Ward, K. M. Rahman, R. Dawsey, and P. Savagian, "Separately Excited Synchronous Motor With Rotary Transformer for Hybrid Vehicle Application," *IEEE Transactions on Industry Applications*, vol. 54, no. 1, pp. 223–232, Jan. 2018.